GFZ

Helmholtz-Zentrum
POTSDAM

HELMHOLTZ-ZENTRUM POTSDAM
DEUTSCHES
GEOFORSCHUNGSZENTRUM

Andreas Reinicke

Mechanical and Hydraulic Aspects of Rock-Proppant Systems

Laboratory Experiments and Modelling Approaches

Scientific Technical Report STR11/09

www.gfz-potsdam.de

HELMHOLTZ
GEMEINSCHAFT

Impressum

Helmholtz-Zentrum Potsdam
Deutsches
GeoForschungsZentrum

D-14473 Potsdam

Gedruckt in Potsdam
Oktober 2011

ISSN 1610-0956

Die vorliegende Arbeit
in der Schriftenreihe
Scientific Technical Report (STR) des GFZ
ist in elektronischer Form erhältlich unter
www.gfz-potsdam.de > Neuestes
> Neue Publikationen des GFZ

Andreas Reinicke

Mechanical and Hydraulic Aspects of Rock-Proppant Systems

Laboratory Experiments and Modelling Approaches

Scientific Technical Report STR11/09

Institut für Geowissenschaften &
Department 3.2: Geomechanik und Rheologie
Deutsches GeoForschungsZentrum GFZ

Mechanical and Hydraulic Aspects of Rock-Proppant Systems
Laboratory Experiments and Modelling Approaches

Dissertation
zur Erlangung des akademischen Grades
"doctor rerum naturalium"
(Dr. rer. nat.)
in der Wissenschaftsdisziplin Geologie

eingereicht an der Mathematisch-Naturwissenschaftlichen Fakultät
der Universität Potsdam

vorgelegt von
Andreas Reinicke
Potsdam, den 8. Oktober 2009

Scientific Technical Report STR 11/09
DOI: 10.2312/GFZ.b103-11098

Deutsches GeoForschungsZentrum GFZ

[…] tellurem intus exquirente cura multiplici modo […]

Der Mensch ist ja auf vielerlei Art bemüht,
das Innere der Erde zu durchforschen.

Plinius Maior, *Naturalis historia* (1. Jh. n. Chr

DOI: 10.2312/GFZ.b103-11098

Acknowledgments

I would like to express my gratitude to all those who made it possible for me to complete this thesis and helped me overcome problems and challenges en route.

The Federal Ministry for Environment and Nature Conservation (BMU) and the GFZ German Research Centre for Geosciences shall be recognized for supporting and funding the work for this thesis.

I strongly want to express my gratitude to my supervisors, Prof. Dr. Georg Dresen and Dr. Ernst Huenges, for their helpful guidance through my studies, countless valuable discussions and the motivating support they gave me.

It is very important for me to mention several colleagues at the GFZ. These are Dr. Sergei Stanchits for his help with the acoustic emission recordings and analysis; PD Dr. Günter Zimmermann for improving my understanding of reservoir stimulation and petrophysics; Dr. Guido Blöcher for always being available for valuable discussions and new - problem solving - ideas. His support for the numerical modelling presented in this study was vital; Dr. Harald Milsch for his excellent support in the laboratory at the long-term flow cell; Dr. Erik Rybacki who was always willing to listen to my problems; Dimitri Naumov who helped me make use of the analytical modelling approach for 3D stress calculation; Dipl.-Ing. Michael Naumann, whose ideas led to the eventual design of the bidirectional flow cell; Stefan Gehrmann who prepared the thin sections and was of great help in sample preparation; and Liane Liebeskind, whose collaboration at the MTS press was of great help to me.

Many others helped me, but I cannot mention all of them here. Nevertheless, I would like to express my appreciation to Dr. Tobias Backers (GeoFrames GmbH) who supported my work through a number of fruitful discussions and so improved my understanding of rock mechanics; to Dr. Björn Legarth (NAM BV) who introduced me into the fascinating field of formation damage and fracture face skin and to Dr. Axel Makurat (Royal Dutch Shell) who supported this thesis with innovative ideas and valuable discussions. I am particularly obliged to Dr. David Bruhn for fruitful discussions and his mental support. Wolfram von Stilfried deserves to be acknowledged for his contributions to the 2D modelling of rock-proppant systems. My especial appreciation goes to Anja Scholz (GeoEnergy GmbH) who supported me by creating and evaluating GBs of data. I want to thank Rita Hamlischer for lots of helpful organisation and all the time we spend with friendly chats.

I would also like to mention those who read through this thesis and commented on it, such as my supervisors, Günter Zimmermann, Tobias Backers, Erik Rybacki, James Faulds, and Malte Forstat.

My heartfelt thanks go out to my dear parents, who made it possible for me to study, who always believed in me, and who have always given me their full support – far beyond my studies.

I thank my brother for many interesting debates on computer science. What began as a game when we were children, has helped to avoid not a few technical emergencies in recent years.

I thank my friends for their honest sympathy and their understanding when instead of to the park for a barbeque, I was drawn to the library.

Most of all, I thank my wife Heike in so many infinite ways, that listing them all at the end of a single thesis would be impossible – thanks, coach!

Zusammenfassung

In Reservoiren werden hydraulische Stimulationsmaßnamen zur Kompensation von Reservoirschädigungen sowie zur Erhöhung der Produktivität des Reservoirs durchgeführt. Zur hydraulischen Stimulation wird ein Fluid in das Reservoir gepumpt, so dass ein Riss entstehen und sich solange ausbreiten kann, bis der Druck unter den Rissfortleitungsdrucks fällt. Im Allgemeinen steht die neu erzeugte Rissfläche nicht für die Förderung von Reservoirfluiden zur Verfügung, da der Riss sich wieder schließt. Um dies zu verhindern, werden Stützmittel, so genannte *Proppants,* mit dem Fluid in den Riss transportiert. Obwohl die hydraulische Stimulation Chancen zur Kompensation von Reservoirschädigungen bietet, birgt sie gleichzeitig das Risiko einer Schädigung in Form einer Permeabilitätsveränderung in der direkten Umgebung des hydraulisch erzeugten Risses. Diese Art der Reservoirschädigung wird als *Fracture Face Skin* (FFS) bezeichnet.

Als ein zentrales Ergebnis dieser Arbeit kann ein neuer Schädigungsmechanismus vorgestellt werden: der *mechanisch induzierte Fracture Face Skin*. Dieser neuartige Mechanismus resultiert aus der mechanischen Wechselwirkung zwischen den Proppants und dem Reservoirgestein. Durch steigende mechanische Spannung, die auf dem *Gesteins-Proppant-System* lastet, werden die Proppants in die Gesteinsmatrix eingedrückt (*Proppant Embedment*). Dies führt einerseits zur Zerstörung von Quarzkörnern, andererseits auch zur Zerstörung von Proppants, so dass Feinstmaterial entsteht, welches den Fluidzufluss beeinträchtigen kann. Um eine nachhaltige Langzeitförderung aus einem Reservoir zu gewährleisten, muss es daher Ziel sein, die hydraulisch-mechanischen Wechselwirkungen im Gesteins-Proppant-System zu verstehen.

Zur Untersuchung der hydraulisch-mechanischen Wechselwirkungen sind Laborexperimente mit drei Messständen durchgeführt worden. Durch die hierbei eingesetzten Messzellen konnte der *mechanisch induzierte FFS* lokalisiert werden und quantifiziert werden, außerdem ist sein Einfluss auf die Langzeitförderung aus Reservoiren analysiert worden.

Die Laborexperimente zeigen, dass die mechanische Schädigung an der Rissfläche die Permeabilität bis zu 90 % reduzieren kann. Dabei setzt die Schädigung unmittelbar mit der initialen Belastung der Probe im Kontaktbereich zwischen Gestein und Proppants ein. Für mechanische Spannungen unterhalb von 35 MPa, die auf dem Gesteins-Proppant-System lasten, ist die mechanische Schädigung an der Rissfläche lokalisiert. Mittels optischer Untersuchungen wurde ergänzend die Zerstörung von Quarzkörnern, die Produktion von Feinstmaterial und daraus resultierend auch die Blockierung von Poren in der Rissfläche als Ursache für den *mechanisch induzierten FFS* identifiziert. Wird das System mit höheren Spannungen belastet, tritt mechanische Schädigung innerhalb der Proppant Packung ein. In der Konsequenz kann sich die Risspermeabilität deutlich reduzieren.

Die Spannungsverteilungen im Gesteins-Proppant-System wurden mittels numerischer und analytischer Modellierungen untersucht. Charakteristisch für ein Partikelsystem aus Proppants und Quarzkörnern ist eine auffällig inhomogene Spannungsverteilung. Insbesondere treten unterhalb der Kontaktflächen von Proppants und Quarzkörnern ausgeprägte Zugspannungskonzentrationen bereits bei geringen Belastungen des Gesteins-Proppant-Systems auf. Diese Spannungskonzentrationen sind für die Zerstörungen am Gesteins-Proppant-Interface verantwortlich und können die beobachteten Rissmuster in Gesteins-Proppant-Systemen erklären.

Zur Untersuchung des Langzeitförderverhaltens sind Laborexperimente von bis zu 40 Tagen Dauer unter in-situ Reservoirbedingungen durchgeführt worden. Die Versuchsergebnisse zeigen, dass die Permeabilität der Gesteins-Proppant-Systeme von mechanischen ebenso wie von thermischen und elektro-chemischen Wechselwirkungen beeinträchtigt wird. Nach hinreichend langer Versuchszeit stellt sich eine konstante Permeabilität ein, die der *mechanisch induzierte FFS* marginal beeinflusst.

Zusammenfassend führt der *mechanisch induzierte FFS* zu relativ geringen, daher Produktivität und Langzeitförderverhalten von Reservoiren nicht schädigenden Effekten.

DOI: 10.2312/GFZ.b103-11098

Abstract

Reservoir formation damage is an issue that can affect the productivity of a reservoir during various phases of fluid recovery from the subsurface, including drilling, production, and workover operations. Hydraulic fracturing technology is one tool to overcome inflow impairments due to formation damage, as well as increase the productivity of reservoirs. To this end, fluid is pumped into the reservoir and a fracture propagates as long as the pressure at the fracture tip is sufficiently high. In general, the availability of the newly created fracture area is limited for production, if no *proppants* (sieved sand or ceramic spheres) are placed in the fracture to keep it open. Indeed, hydraulic fracturing operations can themselves be a source of reservoir formation damage. Permeability alterations adjacent to the newly created fracture face can impair the inflow into the fracture. Such impairment is commonly referred to as *fracture face skin* (FFS).

In context of this work, a new damage mechanism is proposed: the *mechanically induced fracture face skin*. This new mechanism results from mechanical interactions between the proppants and the reservoir rock, due to the increasing stress on the rock-proppant system during production. Proppant embedment into the fracture face and proppant crushing leads to fines production and can impair the fracture performance. In order to achieve sustainable, long-term productivity from a reservoir, it is indispensable to understand the hydraulic and mechanical interactions in the rock-proppant system.

In order to analyse the hydraulic and mechanical interactions, laboratory experiments using three different flow cells were conducted. These flow cells were used to localise and quantify the mechanical damage at the fracture face, as well as to investigate the long-term stability of a rock-proppant system under in-situ reservoir conditions.

The laboratory experiments identified a permeability reduction at the fracture face up to 90 %. The mechanical damage at the rock-proppant interface begins immediately with loading the rock-proppant system and for fracture closure stresses below 35 MPa, the damage is localised at the fracture face. Optical investigations identified quartz grain crushing, fines production and pore blocking at the fracture face, which are responsible for the observed *mechanically induced FFS*. For higher stresses, the damage moves into the proppant pack and can considerably affect the proppant pack permeability.

Numerical and analytical modelling of the rock-proppant system identified highly inhomogeneous stress distributions in the granular system of quartz grains and proppants. High tensile stress concentrations beneath the area of contact between quartz grains and proppants are observed even at small external stress applied to the rock-proppant system. These high stress concentrations are responsible for the early onset of damage at the fracture face and illustrate the types of proppant failure. The fracture patterns observed in the rock-proppant system were successfully matched with the stress pattern from the numerical and analytical models.

The modelling approaches highlight mitigation strategies to attenuate proppant embedment effects, to reduce fines production and to avoid a mechanically induced impairment of fracture performance. In particular, a coat of resin that covers the proppant will help to distribute the stresses at the contacts and suppress the high tensile stress concentrations.

The long-term stability of rock-proppant systems was investigated by means of long-term experiments up to 40 days at in-situ conditions. The experiments highlight that the permeability of rock-proppant systems is affected by electro-chemical and thermal interactions, as well as by mechanical effects. After a sufficient duration of experiment, the permeability stabilises at a constant level, which is minor influenced by the *mechanically induced FFS*.

In summary, the *mechanically induced FFS* exists and has an influence on the fracture inflow performance whereas the long-term productivity of a reservoir is not impaired

Table of Contents

Acknowledgment
Zusammenfassung
Abstract

1. Introduction 1
- 1.1 Enhanced Geothermal Systems: Geothermal Research Site Gross Schoenebeck 3

2 Fundamentals of Rock Mechanics, Fracturing Technology, and Formation Damage 5
- 2.1 Brittle Failure of Rocks 5
  - 2.1.1 Stress and Strain 5
  - 2.1.2 Deformation and Failure of Rocks 5
  - 2.1.3 Mohr-Coulomb Criterion 6
  - 2.1.4 Influence of Pore Pressure on Stress State 6
  - 2.1.5 Acoustic Emission 7
- 2.2 Stress distribution in loaded spheres 7
  - 2.2.1 Hertzian Contact Theory 7
  - 2.2.2 Diametral Compression of Spheres 8
- 2.3 Hydraulic Transport in Rocks 9
  - 2.3.1 Darcy’s Law 9
  - 2.3.2 Non-Darcy Flow 10
  - 2.3.3 Forchheimer Equation and Non-Darcy Flow Correction 11
- 2.4 Hydraulic Fracturing Technology 13
- 2.5 Propping Agents 17
- 2.6 Reservoir Formation Damage 18
  - 2.6.1 Fracture Face Skin 20
  - 2.6.2 Mechanically Induced Fracture Face Skin 21

3 Experimental Work 23
- 3.1 AEFC - Acoustic Emission Flow Cell 23
  - 3.1.1 AEFC - Axial Loading Frame and Confinement System 23
  - 3.1.2 AEFC - Pore Pressure System 24
  - 3.1.3 AEFC - Acoustic Emission Recording 24
- 3.2 BDFC - Bidirectional Flow Cell 25
  - 3.2.1 BDFC - Axial Loading Frame and Hoek Cell 25
  - 3.2.2 BDFC - Pore Pressure System 25
  - 3.2.3 BDFC - Design of Devices 26
- 3.3 AEFC & BDFC - Experimental Procedure 26
  - 3.3.1 AEFC & BDFC - Sample Preparation 28
  - 3.3.2 AEFC & BDFC - Saturation Process 30
- 3.4 AEFC & BDFC - Determination of FFS Permeability 30
  - 3.4.1 AEFC & BDFC - Rock Sample Length and Fracture Width Determination 31
  - 3.4.2 AEFC & BDFC - Differential Pressure Measurement 31
  - 3.4.3 AEFC & BDFC - Flow Velocities in the Setup 31
  - 3.4.4 AEFC & BDFC - Temperature Dependence of Fluid Viscosity 32
  - 3.4.5 AEFC & BDFC - Cumulative Error 32
- 3.5 LTFC - Long Term Flow Cell 32
  - 3.5.1 LTFC - Confining Pressure and Heating System 33
  - 3.5.2 LTFC - Pore Pressure System 33

DOI: 10.2312/GFZ.b103-11098

3.6 LTFC - Experimental Procedure 33
3.6.1 LTFC - Sample Preparation 33
3.6.2 LTFC - Saturation Process 33
3.6.3 LTFC - Electrical Conductivity Measurement 34
3.6.4 LTFC - Differential Pressure Measurement 35
3.6.5 LTFC – Temperature Dependence of Fluid Viscosity 35
3.6.6 LTFC – Cumulative error 35
3.7 Mercury Intrusion Porosimetry 36
3.8 2D Image Analysis 37
3.8.1 Procedure for Pore Space Investigation 37
3.8.2 Procedure for Grain Size Investigation 38

4 Characterisation of Sandstones and Proppants 39
4.1 Mineralogy of Bentheim and Flechtingen Sandstone 39
4.1.1 Bentheim Sandstone 39
4.1.2 Flechtingen Sandstone 39
4.2 Proppant Material 40
4.3 Microstructural Analysis 41
4.3.1 Pore and Grain Size Distribution of Bentheim and Flechtingen Sandstone 41

5 Experimental Results 45
5.1 Mechanical and Hydraulic Characterisation of Bentheim Sandstone and Flechtingen Sandstone 47
5.1.1 Compaction and Failure of Bentheim Sandstone: Acoustic Emission and Permeability Evolution 47
5.1.2 AE Hypocenter Locations 49
5.1.3 Spatial AE Distribution 50
5.1.4 Permeability of Gouge Layer 51
5.1.5 Influence of Compaction and Flow Rate on Hydraulic and Elastic Parameters 52
5.1.6 Evolution of Young’s Modulus 52
5.1.7 Evolution of Permeability 52
5.1.8 Influence of Pore Fluid Salinity on Permeability 54
5.2 Discussion of Mechanical and Hydraulic Characterisatioin of Bentheim and Flechtingen Sandstone 55
5.2.1 Brittle Failure of Bentheim Sandstone 55
5.2.2 Permeability Evolution during Brittle Failure 56
5.2.3 Permeability Evolution: Influences of Stress 57
5.2.4 Permeability Evolution: Influences of Flow Rate 57
5.2.5 Permeability Evolution: Influences of Fluid Salinity 58
5.2.6 Implications for RPI Experiments 58
5.3 Rock-Proppant Interaction Testing – AEFC 59
5.3.1 Bent 2.3: Bentheim Sandstone + Intermediate Strength Proppants 59
5.3.2 Bent 3.4: Bentheim Sandstone + Intermediate Strength Proppants 62
5.3.3 FB 1.6: Flechtinger Sandstone + High Strength Proppants 63
5.3.4 Microstructural Observations and Fracture Patterns 64
5.3.5 Permeability Damage Ratio 66
5.3.6 Spatial AE Activity Distribution 67
5.4 Rock-Proppant Interaction Testing – BDFC 69
5.4.1 Bentheimer Sandstone + Intermediate Strength & High Strength Proppants 69
5.4.2 Flechtingen Sandstone + Intermediate Strength & High Strength Proppants 71

5.4.3 Flechtingen Sandstone + Intermediate Strength Proppants / Continuous Stress Change 73
5.4.4 Fines Production and Fines Transport in the Proppant Pack 74
5.5 Rock-Proppant Interaction Testing - LTFC 76
5.5.1 FB 10.11: Flechtingen Sandstone 77
5.5.2 FB 10.12: Flechtinger sandstone + High Strength Proppants 77
5.5.3 FB 10.13: Flechtingen Sandstone + Intermediate Strength Proppants 79
5.5.4 Microstructural Observations 80

6 Stress Modelling 81
6.1. Analytical Approach: Diametral Compression 81
6.1.1. Contact Geometry 81
6.1.2. Stress Field at the Surface: Hertzian Contact 82
6.1.3. Stress Field in the Volume: Theory of Hiramatsu & Oka 83
6.1.4. Maximum Tensile Stress along the Axis of Loading 87
6.1.5. Maximum Tensile Stresses in Quartz Grains and Proppants 88
6.2. Numerical Approach: Idealised 2D-Contact Model of Quartz Grains and Proppants 90
6.2.1. Mechanical Modelling with Rockflow/Geosys 91
6.2.2. Results from 2D Mechanical Stress Modelling 91

7 Discussion 95
7.1 Diametral Loading of Spheres 95
7.2 Findings from Analysis of Acoustic Emission 95
7.2.1 Hypocenter Localisation 95
7.2.2 Source Type Analysis 96
7.2.3 Correlations between Source Types and Stress Distributions 97
7.3 Failure at the Rock-Proppant Interface 97
7.3.1 Initial Loading of Rock-Proppant Systems 98
7.3.2 Extent of the AE Cluster at the Rock-Proppant Interface 98
7.4 Failure within the Proppant Pack 99
7.5 Stress Pattern and Fracture Pattern 100
7.6 Influences on FFS permeability 101
7.6.1 Pore Structure of Sandstones 101
7.6.2 Macroscopic Tensile Fracture Generation via 3 Point Bending Test 101
7.6.3 Determination of Damage Penetration of FFS zone 101
7.7 Influence of Proppant Pack Permeability 102
7.8 Long-Term Influences on Permeability at Reservoir Conditions 104
7.8.1 Correlation Between Hydraulic and Electrical Flow in Rock-Proppant Systems 107
7.9 Implications for Hydraulic Stimulations 108
7.9.1 Impact of long-Term Testing at Reservoir Conditions 108
7.9.2 Implications for Propping Agents 109
7.9.3 Influence of Mechanically Induced Fracture Face Skin on Productivity 109
7.10 Field Observations of Fracture Face Skin 112

8. Conclusions and Outlook 113
8.1. Characterisation of Bentheim and Flechtingen Sandstone 113
8.2. Rock-Proppant Interaction Experiments 113
8.3. Long-Term Rock-Proppant Interaction Experiments 114
8.4. Modelling of Rock-Proppant Systems 114
8.5. Implications for Geothermal Research Site Gross Schoenebeck 114
8.6. Outlook 114

9. References 115
10. List of Figures 123
11. List of Tables 127
12. List of Symbols 129
Appendix 131
A1 Pressure and Flow Calibration 131
A2 Error Estimation 132
A2.1 AEFC & BDFC 132
A2.1.3 Influence of Temperature Measurement 132
A2.1.4 Rock Sample Length and Fracture Width Determination 132
A2.2 LTFC 133
A2.2.1 Influence of Temperature Measurement 133
A4 Stress-Strain Curves of RPI experiments 135
A5 Pore Pressure Curves 136
A6 From an Artificial Micrograph to a 2D-Mesh 138

1 Introduction

Hydraulic fracturing has been a standard technology used in the hydrocarbon industry for more than 40 years to overcome effects of formation damage and low rock permeability and to increase the productivity of a reservoir beyond its natural level [Economides & Nolte 2000]. Effects like drilling induced damage resulting from fines invasion into the formation or chemical incompatibilities of injected and reservoir fluid can alter the hydraulic properties of the wellbore surrounding rock. Additionally, economic considerations can demand a productivity increase of a well.

For hydraulic fracture generation, a reservoir is pressurised through the wellbore and if the fluid pressure exceeds fracture opening pressure, a fracture propagates into the reservoir normal to the minimum principle stress. Commonly, a propping agent (sieved sand or ceramic spheres) is added to the injected fluid to avoid complete fracture closure after pressure release. This propping agent settles in the fracture and after clean-up (flow back of the injected fracturing fluid), a highly permeable proppant pack remains (compare to figure 1.1). During production, the reservoir rock delivers fluid to the fracture and the proppant filled fracture transports this fluid to the wellbore, i.e. a reservoir is drained efficiently and economically with an appropriately designed hydraulic fracturing operation.

Design of an appropriate fracture geometry as well as placement of a sufficient proppant pack of the right proppant type is a key parameter to maintain long-term productivity. Proppant selection must consider hydraulic conductivity at in-situ stress conditions. Hydraulic conductivity is influenced by mechanical stress on proppant pack, leading to proppant crushing and embedment as well as to a reduction of fracture width and fines production. Understanding the hydraulic and mechanical interactions in the rock-proppant system is indispensable for achieving sustainable long-term productivity from a reservoir.

The productivity of a hydraulically fractured reservoir is often less than predicted from design considerations [Cramer 2005, Romero et al. 2003]. Treatment failure can be commonly attributed to fracture damage processes, such as: poor clean-up after the treatment, alterations due to infiltration processes and precipitation, and mechanical damages like proppant pack failure.

A wide range of laboratory, field, and theoretical studies cover the aspect of fracture damage mechanisms [Fredd et al. 2000; Wen et al. 2006, Behr et al. 2002, Nasr-El-Din 2003, Moghadasi et al. 2002, Lynn & Nasr-El-Din 1998]. Cinco-Ley & Samaniego V. [1977] introduced a formalism that describes the damage mechanism in terms of fracture length, reduced permeability and extent of damaged zone adjacent to the fracture (figure 1.1).

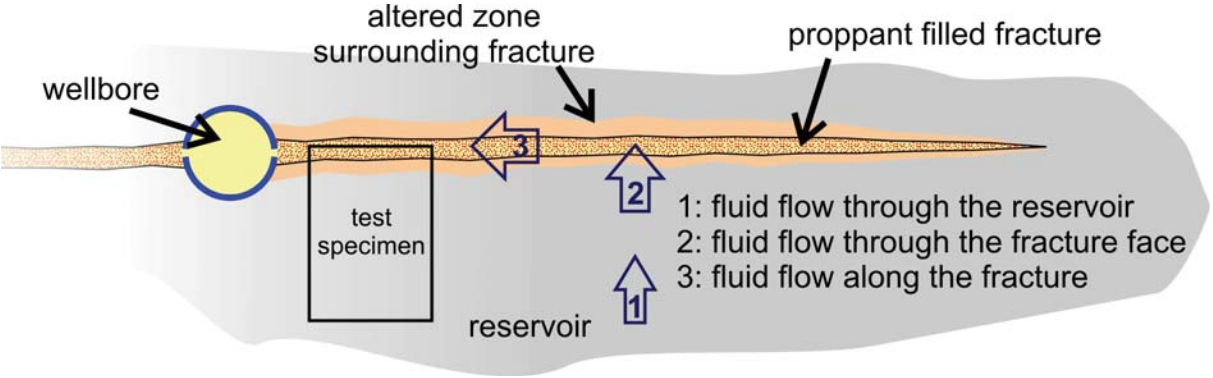
altered zone
surrounding fracture
proppant filled fracture
wellbore
3
2
test
specimen
1: fluid flow through the reservoir
2: fluid flow through the fracture face
3: fluid flow along the fracture
1
reservoir

Figure 1.1: *Flow directions in a reservoir with proppant filled fracture. Hydraulic fracture generation in a reservoir can alter the hydraulic properties in a zone surrounding the fracture. In particular, mechanical interactions between the fracture face and the proppants can create fines that block the pores of the rock matrix. If the well is produced, the fluid flow from the reservoir (1) that enters the fracture normal to the fracture face (2) is affected by this mechanically induced impairment. In order to investigate this flow impairment, specialised laboratory equipment is developed that model a cylindrical rock core with the adjacent proppant pack.*

They assumed a zone with a reduced permeability at the fracture face. A linear flow from the reservoir has to pass through this altered zone to enter the fracture. Hence, the fluid transport in a hydraulically fractured reservoir is affected by three different permeabilities: the reservoir rock permeability (1); the altered permeability at the fracture face (2), the proppant pack permeability in the fracture (3).

Flow impairment at the fracture face is commonly referred to as fracture face skin (FFS). A variety of numerical studies [Gdanski el al. 2005, Adegbola & Boney 2002, Behr et al. 2002], experimental work [Roodhart et al. 1988, Ahmed et al. 1979], as well as site investigations [Cramer 2005, Lynn & Nasr-El-Din 1998] treated the topic of FFS. A FFS can be caused by numerous effects like fluid-loss damage [Cinco-Ley & Samamiego V. 1981], filter cake build-up at the fracture face [Romero et al. 2003], relative gas-water permeability changes at the fracture face [Holditch 1979] as well as liquid condensates in gas condensate reservoirs [Wang et al. 2000].

Although the mentioned fracture face skin models exist, mechanical effects have not yet been taken into account. The hypothesis is that the mechanically induced FFS results from interaction between proppants and rock. With increasing differential stress on the rock-proppant interface, the proppant becomes embedded into the rock matrix. This leads to crushing of quartz grains and fines production at the fracture face. The produced fines block the pores of the rock resulting in an additional pressure drop normal to the fracture face. Legarth et al. [2005a] developed the conceptual model of the mechanically induced FFS explaining the origin of a mechanically damaged zone at the fracture face.

Up to now, no evidence has been given that the mechanical damage at the rock-proppant interface and the associated permeability reduction due to fines generation at the fracture face exist. Consequently, the aim of this work is the development of new laboratory equipment to locate the damaging effects and to quantify the mechanically induced FFS in terms of permeability reduction and penetration of the damaged zone.

To describe the impairment at the fracture face, three permeabilities of the rock-proppant system have to be taken into account: 1) rock permeability, 2) FFS permeability and 3) fracture (proppant pack) permeability (compare to figure 1.1). For that purpose, a cylindrical element of the fracture wall with the adjacent proppant pack is modelled experimentally as well as numerically.

The different aspects that influence the generation of a mechanical FFS, as well as its impact on the productivity of a reservoir are investigated by means of three different flow cells:

- Acoustic Emission Flow Cell (AEFC): The AEFC is employed for analysis and localisation of the crushing and damaging at the rock-proppant interface.
- BiDirectional Flow Cell (BDFC). The BDFC simulates the geometric flow conditions in reservoirs intersected by a proppant filled fracture and is used to quantify the permeability reduction at the fracture face as well as in the proppant pack.
- Long-Term Flow Cell (LTFC): The LTFC investigates rock-proppant interactions at in-situ conditions of a geothermal reservoir.

The empirical investigations are supported by numerical and analytical stress modelling of the rock-proppant interface. The analytical approach employs the theory of diametral point loading of a sphere and adopts this concept for the contacts at the rock-proppant interface. The numerical approach transfers the contact geometry from a thin-section to a finite element modelling software. The modelled stress pattern in a rock-proppant system are matched with the fracture pattern observed from experimental work

Subsequently, the impact of a mechanically induced FFS on the reservoir productivity, mitigation strategies and possible long-term effects, triggered by the mechanically induced FFS are discussed.

1.1 Enhanced Geothermal Systems: Geothermal Research Site Gross Schoenebeck

In the context of Enhanced Geothermal Systems (EGS) [Gérard et al. 2006; Calcagno & Sliaupa 2008] the hydraulic stimulation technologies are adopted from oil and gas industry to enlarge the access to the heat in the reservoir and to stimulate low permeable formations. The treatment concepts are highly developed in the hydrocarbon industry [Shaoul et al. 2007] as well as in the Hot Dry Rock (HDR) technology [Baria et al. 1999]. Indeed, the stimulation techniques require adjustment to apply them for hydrothermal reservoirs, since considerable higher amount of fluids are produced compared to hydrocarbon reservoirs [Zimmermann et al. 2008].

The geothermal research site Gross Schoenebeck is located in the North German Basin (NGB / figure 1.2a). A doublet system consisting of a production well (GtGrSk4/05) and an injection well (EGrSk3/90) [Zimmermann et al. 2007] was developed for geothermal power generation from the Lower Permian (Rotliegend formation) as an EGS [Huenges et al. 2007]. The designated pay zones are the Rotliegend sandstones as well as the tight volcanic rock (figure 1.2b), which provide fluid transport mainly due to inter-connected fractures. A detailed geological description is given by Norden & Förster [2006]. Both wells were hydraulically stimulated to overcome fluid impairments adjacent of the wellbore as well as to optimise the productivity.

The initial productivity of the well EGrSk3/90 was significantly lower than expected from core measurements. Inflow restrictions adjacent to the wellbore (commonly referred to as skin zone) were hypothesised as reason for the low productivity of EGrSk3/90 [Legarth et al. 2005b]. Two hydraulic fracturing open-hole treatments in the Rotliegend sandstones in 2002 were conducted to bypass the skin zone and to connect undamaged reservoir regions. Flow log measurements after stimulation ascertains the activation of the Rotliegend sandstones but the Fold Of Increase (FOI) lags behind expectations from modelling the stimulation campaign [Legarth et al. 2005b].

Missing the productivity goal in the first Groß Schönebeck well highlighted the importance of a well designed stimulation treatment in the second well GtGrSk4/05. The placement of a sufficient proppant pack of the right proppant type is a key parameter to maintain long-term productivity. Hence, the experimental program of this study has one focus on Rotliegend sandstone rock-proppant systems and the designated proppant types for hydraulic stimulation operation in the well GtGrSk4/05.

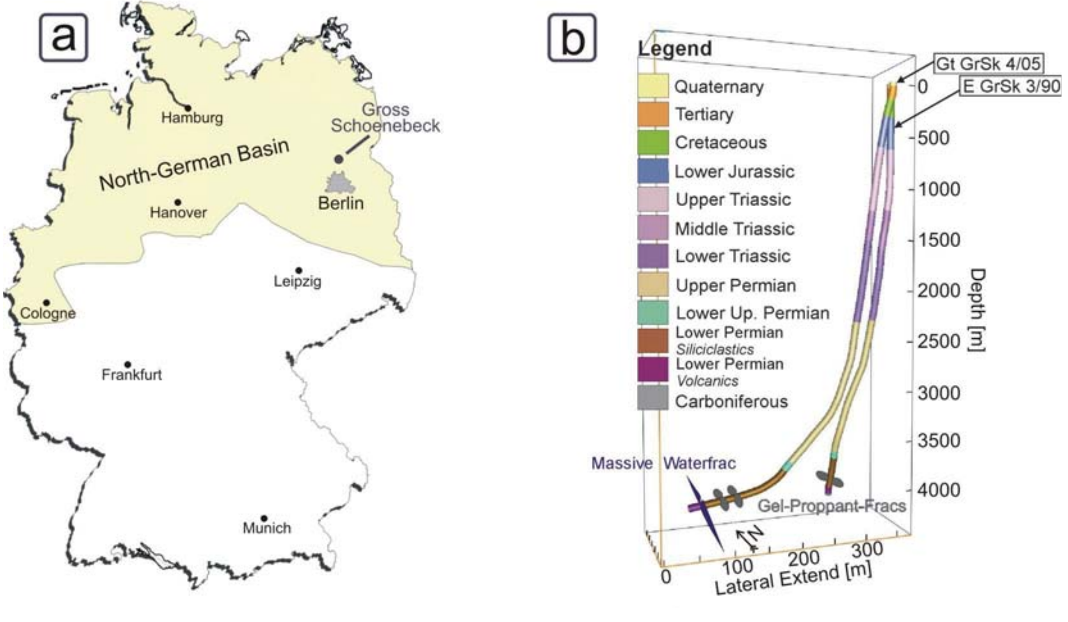
a
Hamburg
Gross Schoenebeck
North-German Basin
Hanover
Berlin
Leipzig
Cologne
Frankfurt
Munich
b
Legend
Quaternary
Tertiary
Cretaceous
Lower Jurassic
Upper Triassic
Middle Triassic
Lower Triassic
Upper Permian
Lower Up. Permian
Lower Permian Siliciclastics
Lower Permian Volcanics
Carboniferous
Gt GrSk 4/05
E GrSk 3/90
0
500
1000
1500
2000
2500
3000
3500
4000
Depth [m]
Massive Waterfrac
Gel-Proppant-Fracs
N
0
100
200
300
Lateral Extend [m]

***Figure 1.2:**.Location of the geothermal research site Gross Schoenebeck and well path of the doublet system [modified from Moeck et al.2008]. The geothermal research site Gross Schoenebeck is located 80km north from the capital Berlin in the North-German Basin (NGB). A doublet system consisting of a production well (GtGrSk4/05) and an injection well (EGrSk3/90) was developed for geothermal power generation from the Lower Permian (Rotliegend formation). The wells intersect typical a series of sediments from Cretaceous over Jurassic to Triassic known in the NGB.*

2 Fundamentals of Rock Mechanics, Fracturing Technology, and Formation Damage

2.1 Brittle Failure of Rocks

2.1.1 Stress and Strain

The illustration of fundamentals of stress and strain analysis follows Jaeger et al. [2007].

The traction vector **p** acting on a surface is expressed as the product of a second order tensor of nine stress components and a normal vector **n**:

$$\mathbf{p}(\mathbf{n}) = \begin{bmatrix} \sigma_{\mathbf{xx}} & \sigma_{\mathbf{xy}} & \sigma_{\mathbf{xz}} \\ \sigma_{\mathbf{yx}} & \sigma_{\mathbf{yy}} & \sigma_{\mathbf{yz}} \\ \sigma_{\mathbf{zx}} & \sigma_{\mathbf{zy}} & \sigma_{\mathbf{zz}} \end{bmatrix} \begin{bmatrix} n_x \\ n_y \\ n_z \end{bmatrix} = \sigma_{\mathbf{ij}} \cdot \mathbf{n} \qquad 2.1.$$

The stress acting on a face of a cube in direction of the normal vector is denoted with similar indices (e.g. σ_{xx}); it is called the normal stress. It is considered positive if the stress is compressive and negative if the stress is tensile. The in-plane stresses are shear stresses; they are acting perpendicular to the normal vectors of the plane and have dissimilar indices. In static equilibrium, the stress tensor is symmetrical with six independent components [Jaeger et al. 2007].

For a coordinate system with axis coinciding with the eigenvectors of the stress tensor, the tensor is reduced to the diagonal trace with the shear stresses equal zero. The remaining stress components are referred to as principal stresses σ_1, σ_2, and σ_3 [Hudson & Harrison 1997]. It is common to set $\sigma_1 > \sigma_2 > \sigma_3$. The principle stresses and their orientations are derived as Eigenvalues and Eigenvectors of the stress matrix.

In the following, the shear stresses will be denoted as τ_{xy} etc in addition. This notation has the advantage of a clear distinction between normal and shear stresses and is commonly used, e.g. by Timoshenko & Goodier [1970].

2.1.2 Deformation and Failure of Rocks

A cylindrical sample shortens along the direction of loading when a force F is applied to the endfaces. The axial stress applied on the sample is:

$$\sigma_1 = \frac{F}{\pi \cdot r^2} \qquad 2.2$$

where r is the radius of the sample. The axial strain ε_1 is the quotient of the displacement Δl and the sample length l:

$$\varepsilon_1 = \frac{\Delta l}{l} \qquad 2.3$$

In the classical theory of continuum mechanics, a linear relationship between stress and strain is assumed. For uniaxial stress, the coefficient of proportionality in this relationship – Hooke's Law - is the Young's modulus E:

$$\sigma_1 = E \cdot \varepsilon_1 \qquad 2.4$$

Hooke's Law is valid for an isotropic linear elastic solid, i.e. it is valid in a range of stresses and strains sufficiently far from failure of a rock.

The axial strain that occurs under axial loading of a specimen can be quantified by the Young's modulus. A specimen will not only deform in axial direction, it will deform in each of the two other perpendicular directions as well. A cylindrical specimen will get the shape of a cask. The quotient of lateral or radial strain ε_2 to axial strain ε_1 is called the Poisson ratio or Poisson number:

$$\nu=\frac{-\varepsilon_2}{\varepsilon_1} \qquad 2.5$$

For a linear elastic material ν varies between 0.0 – 0.5, whereas 0.5 is the Poisson number of an incompressible fluid. The volumetric strain $\Delta V/V$ is equal to the sum of the principle strains. For uniaxial compression of cylindrical samples the volumetric strain sums up to

$$\frac{\Delta V}{V}=\varepsilon_V=\varepsilon_1+2\cdot\varepsilon_2 \qquad 2.6$$

In terms of the principal coordinate system the three dimensional form of Hooke's law for isotropic elastic solids can be written as:

$$\begin{aligned}\sigma_1&=(\lambda+2\mu)\varepsilon_1+\lambda\varepsilon_2+\lambda\varepsilon_3\\ \sigma_2&=\lambda\varepsilon_1+(\lambda+2\mu)\varepsilon_2+\lambda\varepsilon_3\\ \sigma_3&=\lambda\varepsilon_1+\lambda\varepsilon_2+(\lambda+2\mu)\varepsilon_3\end{aligned} \qquad 2.7$$

The two elastic moduli appearing in equation 2.7 are the Lamé parameters: μ is the shear modulus and λ in combination with μ sums up to the bulk modulus K of a rock:

$$K=\left(\lambda+\frac{2}{3}\mu\right) \qquad 2.8$$

2.1.3 Mohr-Coulomb Criterion

The Coulomb criterion [Coulomb 1773] is widely used to characterise rock failure. The criterion is based on extensive empirical work and it predicts that failure of a rock or soil proceeds along a plane driven by shear stress τ. The motion is resisted by a normal force σ_n acting on the failure plane multiplied with a friction coefficient γ:

$$|\tau| = S_0+\gamma\cdot\sigma_n \qquad 2.9$$

The parameter S_0 is known as the cohesion of rock and γ is the coefficient of internal friction. A construction of Mohr's circles [Mohr 1900] in a (σ, τ) plane is adjuvant in order to determine γ and S_0. In this plane the angle between the Coulomb straight line and the σ_n-axis known as the angle of internal friction is defined as

$$\phi = \arctan(\gamma) \qquad 2.10$$

2.1.4 Influence of Pore Pressure on Stress State

Pore fluids can affect the fracture strength of rock through mechanical and chemical interactions with the matrix. The overall mechanical behaviour of a solid depends on the macroscopic stresses and on the pore pressure; this dependence is expressed by the effective stress law [Paterson & Wong 2005]:

$$\sigma_{ij\ eff} = \sigma_{ij}-P_P\cdot\delta_{ij} \qquad 2.11$$

where δ_{ij} is the Kronecker delta. Terzaghi [1923] proposed that the failure of a solid is controlled by the principal effective stress components of 2.12:

$$\sigma_{1\ eff} = \sigma_1-P_P \quad 2.12a \qquad \sigma_{2\ eff} = \sigma_2-P_P \quad 2.12b \qquad \sigma_{3\ eff} = \sigma_3-P_P \quad 2.12c$$

Experimental observations indicate that the effective stress law could be rewritten in the form:

$$\sigma_{ij\ eff} = \sigma_{ij} - \alpha P_P \cdot \delta_{ij} \qquad 2.13$$

The constant α is the so called Biot-Willis coefficient [Wang 2000]. This coefficient can vary between $\Phi \leq \alpha \leq 1$ [Fjaer et al. 1992], but most experiments on rocks support the conclusion that the Biot-Willis coefficient is unity [Jaeger et al. 2007].

Concerning the experiments presented in §5 three definitions for macroscopic stress acting on the specimens are of special interest:

1. Differential stress: $\sigma_{diff} = \sigma_1 - \sigma_3$ 2.14
2. Effective mean stress at triaxial conditions: $\sigma_{eff} = \frac{\sigma_1 + \sigma_2 + \sigma_3}{3} - P_P$ 2.15
3. At isostatic conditions equation 2.15 reduces to: $\sigma_{eff} = \sigma_3 - P_P$ 2.16

Equation 2.14 – 2.16 are valid under the condition: $\sigma_1 \geq \sigma_2 \geq \sigma_3$. The minimum principle stress σ_3 is equal to the confining stress P_C.

2.1.5 Acoustic Emission

Acoustic Emissions (AE) are transient elastic waves caused by sudden changes in stress state in solids under mechanical load [Pestman & van Munster 1996]. In rocks subjected to elevated stresses at low temperatures, the growth of microcracks is often associated with the radiation of AE. The frequency of the elastic waves scales with the source size. According to the range of grain size, the source area is about some square micrometers. As a result, the frequency spectrum ranges from 100 kHz to 2000 kHz in contrast to the recorded frequency of earthquakes, which have frequencies below some tenth of Hertz [Lockner 1993].

The analysis of acoustic emission provides information about the brittle failure mechanisms in solids. To locate an event at least 4 sensors recording the acoustic wave are necessary; in the present work, 10 to 12 piezoelectric P-wave transducers (PZT) are attached to the samples building a "small" seismic network. Homogenous low porosity specimens deformed under triaxial conditions show a relatively uniform distribution of AE events before reaching peak stress [Hirata et al. 1987]. During fracture nucleation phase, a localised and well organised AE pattern is formed in a specimen. This nucleation phase correlates with an increase of AE activity and the onset of dilatency [Stanchits et al. 2006].

Localisation of AE requires knowledge of the elastic wave velocities, which are affected by microcracks [Stanchits et al. 2006]. With regard to the orientation of these cracks, this can result in anisotropy of the elastic wave velocities [Schubnel et al. 2003]. Furthermore, it is not uncommon that anisotropy develops at high differential stress [Lockner 1993].

The appearance of acoustic emission far below the peak stress illustrate that deformation of a rock includes inelastic processes even at small loads. Elastic parameters of rock like Young's modulus, compressibility, bulk modulus and Lamés parameter will be influenced [Jaeger et al. 2007].

2.2 *Stress distribution in loaded spheres*

2.2.1 Hertzian Contact Theory

Hertz [1882] has developed a theory for contact of two spheres and the resulting maximum compressive and tensile stresses in the contact area for a hemispherical stress distribution. The theory includes contact of a sphere with a plate as a boundary case. Figure 2.1 illustrate the case of two compressed spheres with same diameter. The maximum compressive stress (σ_{c_max}) occurs in the centre of the contact circle and the maximum tensile stress (σ_{ra}) is observed at the outer boundary of the contact circle (red line in figure 2.1):

$$\sigma_{c\_max}=\frac{3F}{2\pi\cdot a^2} \qquad 2.17a \qquad\qquad \sigma_{ra}=-\frac{1-2\nu}{3}\sigma_{c\_max} \qquad 2.17b$$

where a is the radius of the contact circle.

$$a=\sqrt[3]{\frac{3\pi}{4}\frac{F\cdot R_1\cdot R_2}{E_{12}^*\left(R_1+R_2\right)}} \qquad 2.18$$

where R_1 and R_2 are the radii of the materials in contact.

In order to calculate a, the contact modulus E_{12}^* is needed:

$$\frac{1}{E_{12}^*}=\frac{1-\nu_1^2}{\pi\cdot E_1}+\frac{1-\nu_2^2}{\pi\cdot E_2} \qquad 2.19$$

where the indices 1 and 2 denote the materials in contact

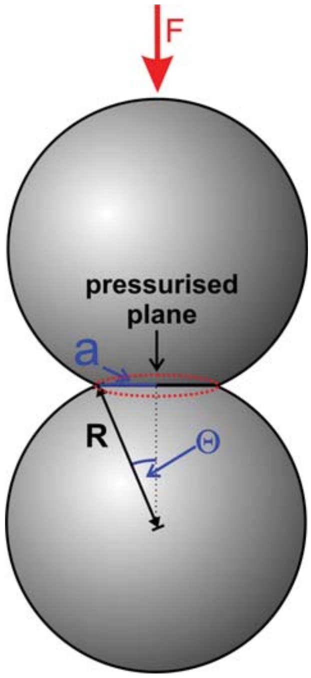

Figure 2.1: *Hertz contact model for two spherical bodies. F: force; R: radius of sphere; a: contact radius; Θ: contact angle*

2.2.2 Diametral Compression of Spheres

The problem of a uniaxial compressed sphere was treated by different researchers [Sternberg & Rosenthal 1952, Lurje 1963, Hiramatsu & Oka 1966]. Following Hiramatsu and Oka [1966], the particles in contact are approximated as isotropic elastic spheres. A spherical coordinate system with origin in the centre of the sphere and the variable radius r, polar angle θ, and azimuth φ is adopted (figure 2.2). For the diametral compression of spheres with radius R, the pair of point forces F is modelled by uniform radial stress p_H applied over two opposite spherical areas with an aperture angle of 2Θ. All other tractions are zero at the surface (r = R).

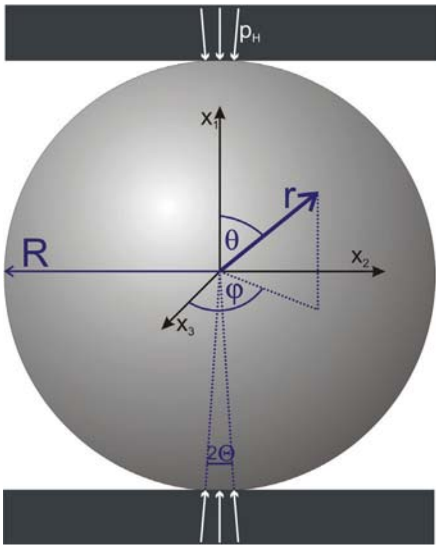

Figure 2.2: *Diametral compression of a sphere. A uniform radial stress (p_H) is applied over diametral spherical areas with the contact angle Θ.*

The uniform radial stress p_H can be expressed as:

$$p_H=\frac{F}{2\pi\cdot R^2\left(1-\cos\Theta\right)} \qquad 2.20$$

The solution is given in spherical coordinates [Hiramatsu & Oka 1966].

$$\sigma_{rr}=\sum_{n=0}^{m}P_{2n}\left(\cos\theta\right)\left\{\frac{\left(4n^2-2n-3\right)\lambda-2\left(2n+1\right)\left(n-1\right)\mu}{4n+3}A_{2n}r^{2n}+4n\left(2n-1\right)\mu C_{2n}r^{2n-2}\right\} \qquad 2.21$$

$$\sigma_{\theta\theta}=\sum_{n=0}^{m}P_{2n}\left(\cos\theta\right)\left\{\frac{\left(2n+3\right)\lambda\text{-}2\left(n\text{-}1\right)\mu}{4n+3}A_{2n}r^{2n}+4\mu nC_{2n}r^{2n-2}\right\}$$
$$+2\frac{\partial^2P_{2n}\left(\cos\theta\right)}{\partial\theta^2}\left\{\text{-}\frac{\left(2n+3\right)\lambda+\left(2n+5\right)\mu}{2\left(2n+1\right)\left(4n+3\right)}A_{2n}r^{2n}+\mu C_{2n}r^{2n-2}\right\} \qquad 2.22$$

$$\sigma_{jj}=\sum_{n=0}^{m}P_{2n}\left(\cos\theta\right)\left\{\frac{\left(2n+3\right)\lambda\text{-}2\left(n\text{-}1\right)\mu}{4n+3}A_{2n}r^{2n}+4\mu nC_{2n}r^{2n-2}\right\}$$
$$+2\cot\theta\frac{\partial P_{2n}\left(\cos\theta\right)}{\partial\theta}\left\{\text{-}\frac{\left(2n+3\right)\lambda+\left(2n+5\right)\mu}{2\left(2n+1\right)\left(4n+3\right)}A_{2n}r^{2n}+\mu C_{2n}r^{2n-2}\right\} \qquad 2.23$$

$$\sigma_{r\theta}=\sum_{n=0}^{m}\frac{\partial}{\partial\theta}P_{2n}\left(\cos\theta\right)\left\{\frac{4n\left(n+1\right)\lambda+\left(4n^2+4n\text{-}1\right)}{\left(2n+1\right)\left(4n+3\right)}A_{2n}r^{2n}+2\left(2n\text{-}1\right)\mu C_{2n}r^{2n-2}\right\} \qquad 2.24$$

All other shear stresses are zero. P_{2n} are the Legendre polynomials of order 2n. A_{2n} and C_{2n} are constants and λ and μ are the Lamé parameters, which can be expressed as:

$$\lambda=\frac{E\cdot\nu}{\left(1+\nu\right)\left(1\text{-}2\nu\right)} \qquad 2.25$$

$$\mu=\frac{E}{2\left(1+\nu\right)} \qquad 2.26$$

For the given boundary conditions, the constants A_{2n} and C_{2n} are:

$$A_{2n}=\text{-}\frac{\left(4n+3\right)\left(4n+1\right)\left\{\cos\Theta\,P_{2n}\left(\cos\Theta\right)\text{-}P_{2n-1}\left(\cos\Theta\right)\right\}}{\left\{\left(8n^2+8n+3\right)\lambda+2\left(4n^2+2n+1\right)\mu\right\}R^{2n}}p_H \qquad 2.27a$$

$$C_{2n}=\text{-}\frac{4n\left(n+1\right)\lambda+\left(4n^2+4n\text{-}1\right)\mu}{2\left(2n\text{-}1\right)\left(2n+1\right)\left(4n+3\right)\mu}R^2A_{2n} \qquad 2.27b$$

2.3 Hydraulic Transport in Rocks

2.3.1 Darcy's Law

The fluid transport properties of a rock depend on the interconnected void space in the rock. Deformation of the pore space, closure or creation of microcracks or deposition of particles will influence the transport properties. These effects can be studied by monitoring fluid permeability and electrical conductivity.

The permeability can be determined observing the transport of water as pore fluid through the void space of a rock sample. Three methods of measurement are used: 1. For a given flow rate, the pore pressure drop over the sample is measured at steady state conditions, i.e. constant flow velocity and constant differential pressure [Bear 1988]. 2. The transient pore pressure response of a rock to a sudden pore pressure change is analysed. 3. The pore pressure response of a rock to an oscillating pressure function is evaluated [Fischer 1992]. In the following, the steady state method, which is adopted for permeability determination in context of this work, will be explained.

Under triaxial compression, generally a positive correlation between changes in pore space and permeability is observed due to closure of microcracks or elastic deformation of pore space [Paterson & Wong 2005]. With onset of dilatancy, the trend reverses and permeability increase with the newly created pore space. The pore space creation correlates with an increase in AE activity. In porous rock, these correlations are not that well defined. Zhu & Wong [1997] presented data of porous sandstone samples showing a decreasing permeability with the onset of dilatancy. Heiland & Raab [2001] have shown that a well consolidated Flechtingen sandstone under triaxial testing conditions has a permeability decrease before and an increase after the yield point.

For low flow rates, the relation between the flow velocity vector **q** and the pore pressure P_P in the general anisotropic case is given by Darcy's law [Darcy 1856]:

$$\mathbf{q}=-\frac{\mathbf{k}}{\eta}\nabla\left(P_P-\rho_f\ \mathbf{g}\cdot\mathbf{x}\right) \qquad 2.28$$

where **k** is the permeability tensor of second order, η is the dynamic fluid viscosity and the term $\{\rho_f\,\mathbf{g}\,\mathbf{x}\}$ represents the gravitational force of the fluid; ρ_f denotes the fluid density [Bear 1988]. Assuming a principal coordinate system with $\mathbf{x}'=\{x',y',z'\}$ for the permeability tensor and neglecting the gravitational forces, Darcy's law can be rewritten in scalar form:

$$q_{x'}=-\frac{k_{x'x'}}{\eta}\frac{\delta P_P}{\delta x'} \quad 2.29a \qquad q_{y'}=-\frac{k_{y'y'}}{\eta}\frac{\delta P_P}{\delta y'} \quad 2.29b \qquad q_{z'}=-\frac{k_{z'z'}}{\eta}\frac{\delta P_P}{\delta z'} \quad 2.29c$$

Under the assumption that the flow velocity vector depends only on the pressure gradient in one direction, which is generally the case in laboratory experiments, Darcy's law can be employed for permeability calculation with this formula:

$$k=\eta\frac{Q}{A_S}\frac{\Delta l}{\Delta P_P} \qquad 2.30$$

where Q is the flow rate, A_S is the cross sectional area of the rock sample and the differential quotient of the pore pressure is replaced by difference quotient $\Delta P_P/\Delta l$. The permeability is expressed in m² in SI units, but very frequently the unit Darcy (D) is used, where 1 Darcy equals $0.987 \cdot 10^{-12}$ m². The following assumptions have to be met for validity of Darcy's Law:

1. Inertial forces can be neglected.
2. Steady state flow conditions are valid.
3. The medium is isotropic and fully saturated with a single phase fluid.
4. The fluid is homogeneous and contains only one phase.

In unfractured sedimentary rocks, two principal directions of permeability can lie in the bedding planes and the third one is perpendicular to the bedding planes. Typically, the permeability in the bedding planes is larger than that one normal to them. In fractured (hard) rocks the principal directions of the permeability tensor coincides with the direction of the fracture sets.

2.3.2 Non-Darcy Flow

According to Basak [1977], flow through porous media can be classified into three different flow zones, depending on local fluid velocity within the void space. The flow zones are known as: Pre-Darcy zone where the increase of flow velocity is disproportionally high compared to the increase of pressure gradient; the Darcy zone where the flow is laminar and Darcy's law is valid; and the Post-Darcy zone where flow velocity increase is less than proportional to the increase of pressure gradient (compare to figure 2.3). The transition between these flow zones is smooth.

These different flow zones may be characterised using Reynolds numbers [Bear 1988]:

$$Re=\frac{\rho_f v_0 d_0}{\eta} \qquad 2.31$$

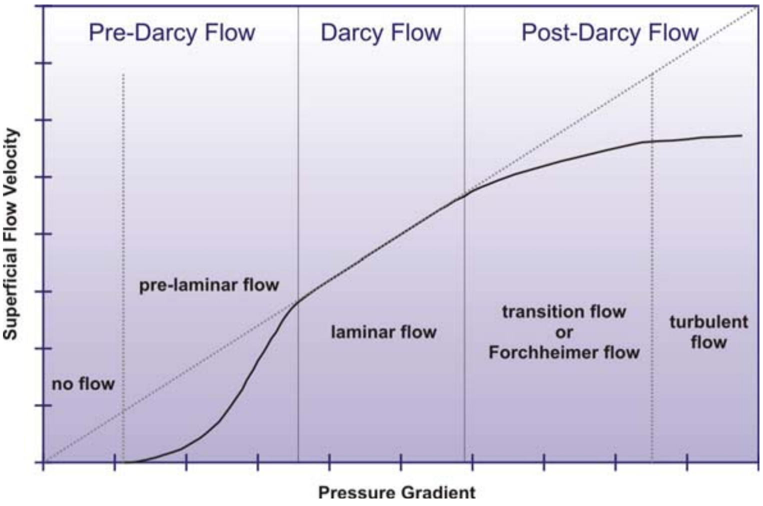

Figure 2.3: *Flow zones in porous media. Flow through porous media can be classified into three different flow zones, depending on local fluid velocity within the pore space [Basak 1977].*

where v_0 is the characteristic flow velocity and d_0 the mean free path. Typical values for the Reynolds number are given in table 2.1 [Fand et al. 1987].

A reasonable explanation why the flow does not follow Darcy's law for very small pressure gradient can be given by the boundary layer theory [Schlichting 1968]. Because of the strong liquid solid interactions, the viscous forces at the throats interfaces are much stronger than in the centre of the pore throats. With decreasing pressure gradient, the thickness of this boundary layer increases. The radii of pore throats e.g. in tight sandstones can be small with radii smaller than 100 nm. In the same rock, the largest pore throat radii can be ~ 10.000 nm. As a result, water may only flow through the 100-times larger pore throats as long as the small pore throats are blocked by the boundary layer [Wu et al. 2008]. With increasing pressure gradient (e.g. higher flow rate), the small pores start to take part in the flow transport leading to an increase of permeability. In the Post-Darcy zone (high flow rates), inertial forces begin to control the flow velocity and the flow field is not laminar.

Translated to the reservoir scale, the flow regimes can be found in the near field and the far field around the borehole and hydraulic fracture respectively. The flow regimes presented in figure 2.3 can have a considerable influence on the fluid transport in a reservoir. Near and within the wellbore, the fracture flow can be turbulent. In the surrounding of the wellbore or fracture, the pressure gradient meets Darcy's law. In sufficient distance from the borehole or fracture, the pressure gradient decreases potentially below the Pre-Darcy threshold and the permeability decreases as well.

zone	flow regime	Reynolds number
pre-Darcy	no flow	$Re<10^{-5}$
	pre laminar flow	
Darcy	laminar flow	$10^{-5}<Re<2.3$
post-Darcy	Forchheimer flow	$5<Re<80$
	turbulent flow	$120<Re$

Table 2.1: *Limits for flow regimes. Fand et al. [1987] define the flow regimes by upper and lower limits of Reynolds number.*

2.3.3 Forchheimer Equation and Non-Darcy Flow Correction

When flow velocity is too high and inertial effects begin to control the flow, Darcy's law is not longer applicable. Hence, Forchheimer [1901] added a non-Darcy term $\{\rho_f \mathbf{v}^2\}$ to Darcy's law enclosing the flow velocity **v**:

$$\nabla \mathbf{P}_P = \frac{\eta}{k}\mathbf{v} + \beta\rho_f \mathbf{v}^2 \qquad 2.32$$

where β is the Forchheimer number. With regard to laboratory setups, equation 2.32 is reformulated for the 1D case incorporating the superficial flow velocity of the fluid $v_D = Q/A_S$:

$$\frac{\Delta P_P}{\Delta l} = \frac{\eta}{k} v_D + \beta \rho_f v_D^2 \qquad 2.33$$

Forchheimer's equation can be used to correct the measured apparent permeabilities k_a in tests with high flow rates. Equation 2.33 is combined with equation 2.30, resulting in:

$$\frac{1}{k_a} = \frac{1}{k} + \beta \frac{\rho_f v_D}{\eta} \qquad 2.34$$

Bear [1988] or Whitaker [1996] state that the nonlinear interrelationship between flow velocity and pressure drop above the Darcy flow zone is not due to turbulence but due to inertial effects. Turbulence is initiated in the flow field not before a Re > 120. In this phase, the high flow velocity generates eddies, which take energy from the main flow field.

2.4 Hydraulic Fracturing Technology

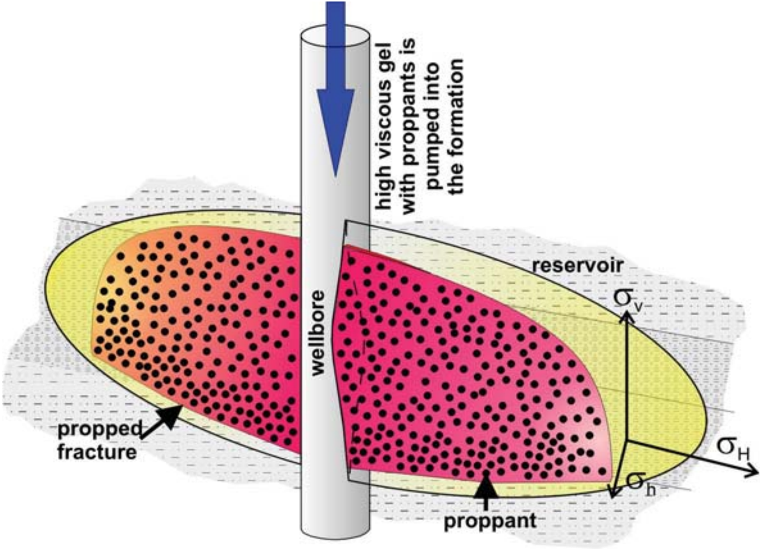

Figure 2.4: *Propped fracture in a reservoir. If fluid at high pressure is pumped into a reservoir, a fracture propagates perpendicular to the minimum principle stress. In the majority of reservoirs, the vertical stress (σ_V) is the largest, so that a vertical fracture propagates in direction of the maximum horizontal stress (σ_H) perpendicular to the minimum principle stress (σ_h). To avoid a rapid fracture closing after leak-off of the pumped fluid, usually a propping agent (sieved sand or ceramic spheres) is placed in the fracture.*

In order to create a hydraulic fracture in a reservoir, fluid is pumped through the wellbore into the formation and as a response, pressure arises (figure 2.4). If the pressure overcomes the fracture initiation pressure, the rock breaks perpendicular to the direction of minimum stress due to a tensile stress generated by the internal fluid pressure. If the vertical stress (σ_V) is the largest, a fracture propagates perpendicular to the minimum horizontal stress (σ_h) at which the fracture tip propagates in direction of the maximum horizontal stress (σ_H). This holds for the majority of reservoirs. In reality, the simple idea of splitting the rock incipient from the wellbore is more complex. There are a variety of parameters that influence the hydraulic fracturing process. In contrast to the classical model of pure tensile hydraulic fracturing, the increase in reservoir pressure can initiate the failure of pre-existing shear zones, rather than create new ones [Wallroth et al. 1996]. For instance, this type of hydraulic fracturing is reported from many geothermal test sites in hard rocks (e.g. granite) [Cornet & Julien 1989]. Coring through the zone surrounding a hydraulic fracture identifies numerous fracture branches along the fracture trace [Daneshy et al. 2004]. Daneshy et al. [2004] developed the concept of off-balance fracture growth. This concept states that the propagation of the main fracture is associated with numerous shear fractures and branches leading to a fracture network around the main fracture trace. On the laboratory scale, it has been demonstrated, that the fluid viscosity as well as the grain size has an influence on the fracturing process [Matsunaga et al. 1993]. A highly viscous fluid (oil) and smaller grain size promote tensile fracturing as the dominant process. In contrast, a fluid of low viscosity (water) and larger grain size reverse this trend. In addition, influence of bedding planes and rock properties can have a role in the process of fracture propagation, if the contrast between the principle stresses is small [Thiercelin & Roegiers 2000].

The rupturing of the rock and fracture growth expose new formation area to the injected fluid and the rate of fluid leaking off into the formation increases. As long as fluid is pumped at a rate higher than the fluid loss rate, the created fracture continues to grow into the formation. However, once pumping ceases and pressure drops below the fracture opening pressure, the fracture closes. As a result of the increasing fracture closure stress (e.g. during production), the remaining fracture can rapidly heal and the created fracture area will no longer be available for production. To avoid this, a propping agent (sand or ceramic spheres) is usually transported by the fluid into the fracture. Alternatively, in particular for carbonate rocks, the injected fluid can be an acid solution. The acid dissolves parts of the formation, leaving behind acid-etched channels extending into the reservoir. The fracture surface is altered and asperities on the surface prevent fracture closure.

Hydraulic fracture operations are performed on a well for two main reasons:

- Bypass a near-wellbore damage in order to return a well to its "natural" productivity: Near-wellbore damage can have several causes, such as drilling-induced damage resulting from fines invasion or chemical incompatibility between drilling fluids and the formation. The damage can also be affected by formation fines movement or scale deposition.
- Extending a conductive path to the formation and increasing productivity: Hydraulic fracturing operations extend a conductive channel deep into the reservoir and stimulate productivity beyond its "natural" level. This includes linking a network of natural fault zones to bring very tight reservoirs to production.

A key design parameter in well stimulation is the dimensionless fracture conductivity C_{fD}, which relates the capacity of the fracture to transmit fluids into the wellbore to the ability of the formation to deliver fluid into the fracture [Economides & Nolte 2000].

$$C_{fD} = \frac{k_f \cdot w_f}{x_f \cdot k} \qquad 2.35$$

k_f and w_f being fracture permeability and fracture width respectively; x_f is the fracture half length and k the formation permeability. For steady state conditions, the optimum C_{fD} is 1, but in reality C_{fD} should be around 10 or even higher to guarantee good drainage during transient flow periods [Economides & Nolte 2000]. To reach this goal, a fracture design with a strong contrast in conductivity between the fracture and the formation is necessary.

Three different concepts exist to stimulate a reservoir hydraulically depending on rock, formation and fluid properties: Hydraulic Proppant Fracturing, Water Fracturing, Hybrid Fracturing.

1.) Hydraulic Proppant Fracturing (HPF): Linear gels and cross-linked gels (highly viscous gels) with high proppant concentrations are used to create highly conductive, but short (compared to Waterfracs), fractures in a permeable reservoir with a porous matrix. The fracture creates a connection between the well and the reservoir and overcomes permeability impairments in the direct vicinity of the well (commonly referred to as skin [Dake 1978]), leading to an increase in productivity. After fracture generation and proppant pack placement, the well is shut-in for some time to allow the fluid to leak off. The fracture closes and fixes the proppant pack. The shut-in phase allows the temperature and chemical breakers to reduce the viscosity of the fracturing gel. Finally, the fracturing fluid is produced from the well (clean-up) and a propped fracture has been created. Table 2.2 shows an overview of the most relevant treatment parameters.

HPF treatments are the first choice for a formation of medium to high permeability. HPF permits good control over the stimulation parameters. The properties of the fracture can be predicted and optimised. With a special Tip Screen Out (TSO) [Economides & Nolte 2000], design widths of up to 25 mm are possible. For that purpose, a proppant pack is placed at the tip of the fracture. The additional drop in pressure at the proppant pack limits the length of fracture growth. If pumping is continued, the fracture widens. Thus, formations of varying permeability can be treated using this technology. Stimulation parameters could be optimised for certain reservoirs to achieve a sufficient C_{fD}.

HPF operations can cause problems in well performance: high proppant concentration can screen out in the near wellbore region due to pressure losses. The complex fluid chemistry can also show incompatibilities with reservoir fluids. Ineffective clean-up after fracturing treatment can result from gel residues (unbroken polymer chains) in the proppant pack. This is particularly problematic in reservoirs of moderate to high permeability [Aggour & Economides 1999]. In such reservoirs, high fracture conductivity is essential in order to achieve sufficient drainage of the reservoir ($C_{fD} >> 1$).

2.) Water Fracturing (WF), "self propped fracs" or "water fracs": Water in combination with a friction reducing chemical (slick water) without proppants or with a low proppant concentration (mainly sieved sand) are used to create long and small fractures. The aim of WF is to connect parts of the reservoir far from the borehole, to create a fracture network, to connect a natural joint network and to maximise the inflow area. In Hot Dry Rock applications [Baria et al. 1999], WF treatments are applied to connect two wells in a tight hard rock (e.g. granite). Table 2.2 gives an overview of the most relevant treatment parameters.

Mayerhofer & Meehan [1998] compared the performance of 50 waterfracturing treatments in the Cotton Valley with traditional hydraulic proppant fracturing treatments. The results show that in general waterfracs perform at least as well as standard fracs in fields with relatively low reservoir permeability. The advantage of WF compared to HPF and hybrid fracs is a considerable reduction in cost. Different studies have shown [Britt et al. 2006, Fredd et al. 2001, Mayerhofer & Meehan 1998] that the field of application is limited to reservoirs with a permeability < 1 mD. In such reservoirs it is important to maximise the inflow area, to facilitate the slow diffusion process of fluid through the tight rock matrix. Low formation permeability and high fracture half length allows the realisation of large dimensionless fracture conductivities despite width of the fracture is narrow.

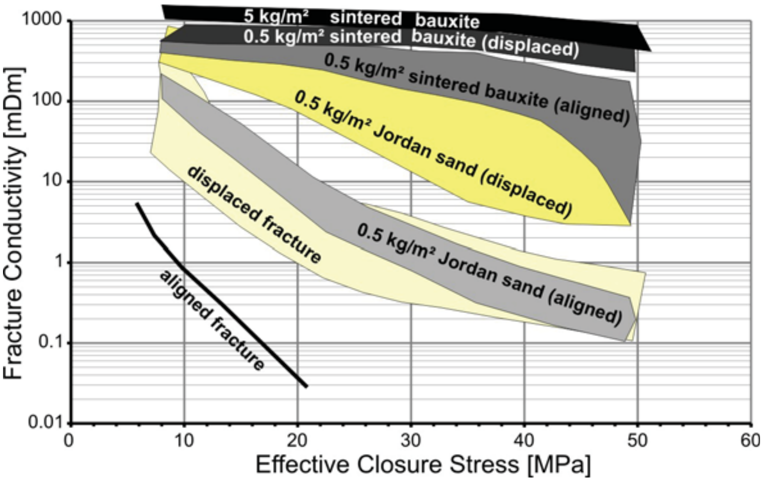

Figure 2.5: *Influence of proppants on fracture conductivity (modified from [Fredd et al. 2001]). Aligned fractures do not provide sufficient fracture conductivity at elevated effective stresses. Adding of propping agent (sand or sintered bauxite) overcomes the problem of rapid fracture closure. Highest fracture conductivity is achieved with large proppant pack (5 kg/m²) of sintered bauxite proppants. This conductivity range is computed from test with aligned and displaced fractures.*

The success of WF stimulation depends on the self-propping potential of the reservoir rock. This self-propping potential includes the ability of the rock to maintain "unpropped fracture conductivity". The unpropped fracture conductivity is a result of the residual fracture width, which is a function of the shear displacement of the fracture faces, the roughness (asperities) of fracture surface, and the strength of the rock [Rushing & Sullivan 2003]. Consequently, the alteration of fracture conductivity is dominated by the asperity and the self propping potential is based on parameters, which are difficult to measure or predict. The unpropped fracture conductivity may vary by at least two orders of magnitude [Sharma et al. 2004]. In general, the unpropped fracture conductivity at production conditions is too small to support production over a significant fracture length [Britt et al. 2006], and the created facture may heal rapidly as a result of creep and pressure solution processes at the asperities. Adding of propping agents (sieved sand or light weight proppants) to the frac fluid overcomes the problem of rapid fracture closure; a sufficient proppant concentration is necessary to create proppant dominated fracture conductivity. Fredd et al. [2000] found that a small concentration (~0.5 kg/m²) of sintered bauxite proppants (high strength proppant) as well as fracture face displacement is necessary to guarantee residual fracture conductivity at elevated fracture closure stresses (> 40 MPa). For smaller stresses it can be sufficient to use sand. Figure 2.5 shows an overview of the experimental results of Fredd et al. [2000]. 5 kg/m² of sintered bauxide proppants provide the maximum fracture conductivity. The narrow range of fracture conductivity shown in figure 2.5 was observed with various types of aligned and parallel fracture faces [Fredd et al. 2000].

The low viscosity of the fluids promotes proppant settling and can lead to insufficient proppant placement. The inability to carry proppants far away from the wellbore can limit the effective propped fracture length which is a key parameter for the production potential. At the end of treatment, the fracture can consist of a packed bed at the bottom (“dune”), an unpropped fracture at the top and a zone in between (“arch” zone) [Warpinski 2009].

3.) Hybrid Fracturing or “hybrid fracs”: The term “hybrid fracs” describes different types of fracture stimulations, which consist of various combinations of cross-linked gels, linear gels and slickwater fluid systems. The hybrid fracs offer the advantages of HPF and WF treatments by combining for instance an initial slick water phase to create the fracture geometry and a cross-linked gel, carrying the proppant load. The initial slickwater phase creates a fracture and the cross-linked gel with proppants follows this fracture (path of least resistance). The geometry of the created fracture differs from the geometry of a fracture generated with a conventional HPF stimulation design. The created fracture is considerably larger compared to HPF designs. In addition, the effective propped fracture length is higher [Coronado 2007]. The low viscosity of slickwater causes long fractures resulting in a maximised inflow area and an optimised drainage of low permeability reservoirs. In comparison to water fracs, this technology provides a more accurate estimation of the dimensions of the fracture created as well as the fracture conductivity.

Treatment Parameters	Hydraulic Proppant Fracs (HPF)	Water Fracs (WF)	Hybrid Fracs
frac fluid viscosity / η	≥ 100 cP	1-10 cP	~ 100 cP
proppant concentration	200 - 2000 g/l	0 – 200 g/l	200 - 500 g/l
fracture half length / x_f	≤ 150 m	up to 1000 m	≤ 250 m
fracture width / w_f	1 – 25 mm	≤ 1 mm	1 – 2 mm
fracture permeability / k_f	10 – 1000 D	10 – 1000 D	10 – 100 D
fracture conductivity / k_f*w_f	0.01 – 25 Dm	0.0001 – 1 Dm	0.01 – 1 Dm
reservoir permeability / k	1 – 1000 mD	≤ 0.1 mD	0.01 - 1 mD
Advantages	applies to intermediate to high permeability reservoirs good control of stimulation results special designs allow large fracture width good control of fluid leak-off	applies to low permeability reservoirs creates long fracture connects to natural joint networks reduced costs avoids fluid incompatibilities	applies to low permeability reservoirs good control of stimulation results increases effective propped fracture length compared to WF and HPF reduced chemical loading of fluids
Disadvantages	incompatibility of reservoir fluid with complex frac fluid chemistry ineffective clean-up (gel residues) screen-out of proppant in the wellbore due to high proppant loads	stimulations success is difficult to predict proppant placement problems screen-out due to weak proppant transport capabilities rapid fracture closure	incompatibility of reservoir fluid with frac fluid chemistry ineffective clean-up (gel residues) screen-out of proppant in the wellbore due to high proppant loads

Table 2.2: *Comparison of three different types of hydraulic fracture stimulations. Three different stimulation concepts exist depending on rock, formation and fluid properties. This table is compiled from Mayerhofer & Meehan [1998], Fredd et al. [2000], Economides & Nolte [2000], Rushing & Sullivan [2003], Britt et al. [2006], and Coronado [2007]*

The use of proppants makes it possible to predict the results of the fracture operation. Production data from a low permeability formation show that hybrid fracs can generate greater effective propped fracture lengths, than water fracs [Rushing & Sullivan 2003].

In comparison to HPF, the polymer loading in gels is reduced, which reduces the potential for polymer damage, and also lowers costs. Nevertheless, the chemistry of the cross-linked gel can lead to fluid incompatibilities and gel residues in the fracture. In addition, some slickwater systems show a potential for formation damage.

2.5 Propping Agents

Selecting the appropriate concentration and type of proppant for the fracture is a critical parameter for the success of a hydraulic fracturing treatment. Three different types of proppant are dominating the market: well-rounded quartz sands, intermediate strength proppants (ISP) and high strength proppants (HSP) (table 2.3). All types are available with resin coatings. The HSP type is manufactured from bauxite clays; the ISP type is made from fused ceramic or bauxite clays. The resin coating on some proppant (mainly sand) is cured during the manufacturing process; the main application of precured-resin-coated proppants is to increase the strength of sands at high stress. Curable coatings are also applied to sand or ceramic proppants. The main application of curable-resin-coated proppant, is to prevent proppant flow-back from the near wellbore region. Furthermore, glass beads, walnut shell, as well as metal and plastic materials were used or tested as propping agent.

The proppant microstructure, and therefore its physical properties, are a function of the material chemistry, as well as the manufacturing process [Cobb & Farrell 1986]. A typical chemical composition of ISP is 73 - 76 % Al_2O_3, 12 - 17 % SiO_2, 4 – 7 % Fe_2O_3, and 3 – 4 % TiO_2. The main phases after thermal processing of the raw material are: mullite (3 Al_2O_3 – 2 SiO_2) and corundum (Al_2O_3). Usually an amorphous phase (~ 15 %) is also present. The HSP type has higher alumina content; a typical chemical composition is 85 - 90 % Al_2O_3, 3 – 6 % SiO_2, 4 – 7 % Fe_2O_3, and 3 – 4 % TiO_2. The higher alumina to silica ratio results in a higher density and the main phase after thermal processing is crystalline corundum (α- Al_2O_3). The mullite phase and the amorphous phase are both small [Cobb & Farrell 1986].

The manufacturing process has a pronounced effect on the proppant integrity. In general, the raw material is grinded to a fine powder, pellets are processed from the powder and these pellets are sintered at 1500 °C. Difference in powder particle size distribution, as well as the packing procedure during pelletisation have an influence on the process. A finer grind will result in a more compact and stronger pellet. The formation of the crystal phase of a proppant is influenced by the time-temperature relation during the sintering process.

The strength of a proppant depends on the following parameters:

- proppant composition (mineral composition)
- manufacturing process (mineral phases, size of crystals, initial flaws and porosity)
- proppant size
- shape (roundness, surface asperities)

The proppant pack conductivity over lifetime of a well is affected by different mechanisms:

- Non-Darcy flow: velocity distribution in the fracture can affect the apparent fracture conductivity (Forchheimer flow and turbulent flow) (compare to §2.3.2)
- Multiphase flow: two or three phases in the reservoir have an influence on the relative permeabilities.
- Residual polymers (gel): incomplete clean-up process after fracture generation can lead to a considerable polymer concentration in the proppant pack (figure 2.6).
- Fines: creation, migration and deposit of fines in the fracture alters permeability

- First order changes in proppant pack width: the primary cause of fracture width changes are reorientation and packing of proppants as well as grain failure at contact points (figure 2.6).
- Second order changes in proppant pack width: embedment of proppants into the rock matrix leads to a reduction of fracture width, in particular in softer rocks (figure 2.6).

Further, fluid leak-off into the formation, as well as filter cake build-up at the fracture face, can influence the performance of a fracture (figure 2.6). Such a flow impairment at the fracture face is referred to as fracture face skin (FFS) and will be presented in detail in §2.6.1.

Proppants of larger size provide a more permeable pack. Larger grain sizes can be less effective in deep wells, because of greater stress sensitivity of these proppant packs. For larger proppants, a wider fracture is required and the particles settle more easily. Sand or other types of proppant can be coated in a curable resin. These proppant are mainly pumped in later stages of a hydraulic stimulation to bind the particles together in the fracture and reduce proppant flow back. In addition, Penny [1987] has shown that proppant embedment can be reduced due to proppant coating. The highly deformable coating causes larger contact area and reduce the contact stress. Proppant embedment is an effect of mechanical interaction between the proppant and the rock. HSP and ISP particularly cause destruction of the rock grains they come in contact with, resulting in small "craters" on the fracture face [Weaver et al. 2005].

proppant type	manufacturing process	field of application
frac sands	no	closure stresses < 40 MPa
intermediate strength proppants (ISP)	fused ceramic or sintered bauxide (rich in mullite)	30 MPa < closure stress < 65 MPa
high strength proppants (HSP)	sintered bauxide (rich in corundum)	closure stresses > 65 MPa

Table 2.3: *Categorisation of proppants based on maximum fracture closure stress.*

2.6 Reservoir Formation Damage

Reservoir formation damage describes various processes that cause operational and economical problems during production from a reservoir. Such damage processes can be affected by chemical, physical, biological and thermal interactions of formation and fluids. In addition, mechanical interactions of reservoir and hydraulic fractures under stress can influence the performance of a well. Formation damage is indicated by permeability impairment in the reservoir and loss in productivity. The following is a brief overview about formation damage processes, with the main focus on the fracture face skin. For a comprehensive study, see Civan [2000].

Formation damage is most commonly referred to [Bishop 1997]:

- fluid-fluid incompatibilities: chemicals in the drilling mud, fracturing fluid or reservoir fluid could precipitate out of the solution as a response to a change of the conditions (contact with another fluid, pT-conditions).
- rock-fluid incompatibilities: contact of swelling and dispersible clays with injected fluids can impair the permeability adjacent to a well.
- solid invasion: solids in the drilling mud could invade the formation. Internal filtering of these solids would lead to reduced permeability in the formation surrounding the borehole.
- phase trapping / water blocking: in a low permeability gas saturated matrix, the pore space has a low liquid saturation. If an aqueous phase were introduced into the formation, that would generate a high water saturation in the pore space. Due to the small pore space in rock of low permeability, a high amount of trapped water remains in the pores and the relative gas permeability is reduced.

- chemical adsorption / wettability alteration: the fluid flow in pores can be influenced by changes of the rock surface wettability, e.g. the reservoir rock, can change from oil wet to water wet during production.
- fines migration: fines in the produced fluid can bridge across the pore throats in the near-wellbore region or at the fracture face and reduce the well productivity. Migrating fines may consist of a variety of different materials, including clays and silts.
- biological activity: introduction of bacteria into the formation, resulting in the generation of slimes that reduce permeability.

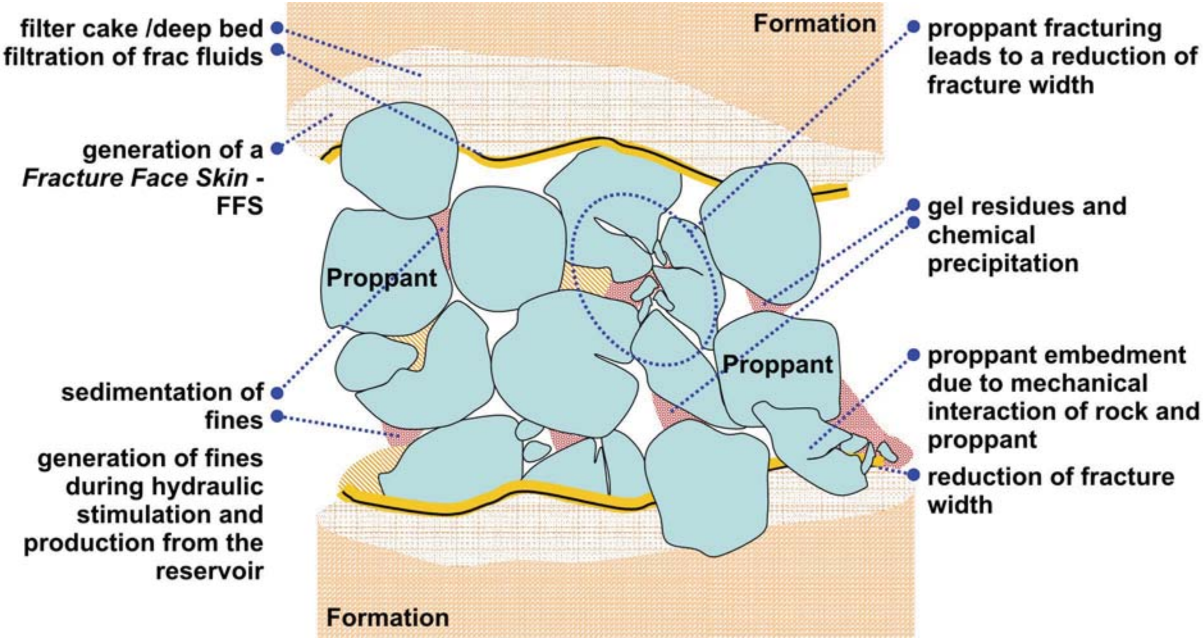
filter cake /deep bed filtration of frac fluids
generation of a *Fracture Face Skin* - FFS
sedimentation of fines
generation of fines during hydraulic stimulation and production from the reservoir
Formation
Proppant
Proppant
Formation
proppant fracturing leads to a reduction of fracture width
gel residues and chemical precipitation
proppant embedment due to mechanical interaction of rock and proppant
reduction of fracture width

Figure 2.6: *Mechanisms impairing proppant pack conductivity (modified from [Legarth et al. 2005a]). Different mechanism can influence the fracture performance. Gel residues, chemical precipitation, and sedimentation of fines can affect the proppant pack permeability. In high stress environments, proppant embedment and proppant crushing is an issue. A filter cake at the fracture face or filtration of frac fluid can impair the permeability adjacent to the fracture and generate a fracture face skin.*

Mainly two processes affect the permeability reduction in clay bearing rocks:

1. Clays can be released from the pore surface and migrate with the fluid through the pore space. At pore throats, the dispersed clay minerals can be deposited and impair the fluid flow.
2. Swelling clays first expand under favorable ionic conditions leading to a decreasing porosity and then disintegrate and migrate. At pore throats, deposition and bridging of the clay minerals can reduce the rock permeability.

Clay swelling can be controlled by adding a sufficient concentration of ions to the aqueous phase. The structure layers of clay always lack positive charges and interlayered cations are required to balance this charge deficiency. The distance between the layers is a function of the exchangeable cations and the composition of the solution. In particular, a high concentration of K^+ cations in the aqueous phase can prevent swelling and the subsequent formation damage. The small clay plates remain intact, because the small K^+ cations penetrate the interlayers and hold the small plates together [Mondshine 1973]. Larger cations like Na^+ or Mg^{2+} can disintegrate the small clay plates, because they do not fit into the interlayers gap. The edges of the clay plates will break off to form small fragments, and migrate with the fluid [Reed 1977].
To control permeability impairment due to clay alteration processes, a sufficiently high salt concentration, as well as a sufficiently small flow velocity, is indispensable. If the flow rate is too high, clay plates will disintegrate and migrate. This threshold is called the critical flow velocity [Rahman et al. 1995].

2.6.1 Fracture Face Skin

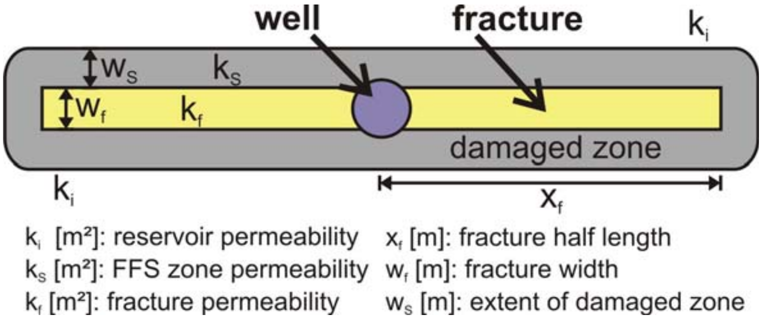
well
fracture
k_i
w_s
k_s
w_f
k_f
damaged zone
k_i
x_f
k_i [m²]: reservoir permeability
k_s [m²]: FFS zone permeability
k_f [m²]: fracture permeability
x_f [m]: fracture half length
w_f [m]: fracture width
w_s [m]: extent of damaged zone

Figure 2.7: *Conceptual model of a fracture face skin: The permeability adjacent to the fracture is reduced. This impairs fluid flow normal to the fracture face. [Cinco-Ley and Samaniego-V. 1977].*

The effect of flow impairments along the fracture on the transient behaviour of a finite conductivity fracture was investigated by Cinco-Ley and Samaniego V. [1977]. They presented a linear flow through two porous media, perpendicular to the fracture faces. One medium was the undamaged formation, the other the damaged reservoir rock directly next to the fracture (figure 2.7). This flow impairment is commonly referred to as a Fracture Face Skin (FFS) (figure 2.7). Cinco-Ley and Samamiego V. [1977] introduced the mathematical expression to quantify the FFS in terms of fracture half-length x_f, damage penetration zone w_s, and the ratio of unaffected reservoir permeability to reduced permeability k_i/k_s:

$$FFS=\frac{\pi \cdot w_s}{x_f}\left(\frac{k_i}{k_s}-1\right) \qquad 2.36$$

Several numerical studies have been conducted to analyse the influence of the FFS on well productivity. Cinco-Ley and Samamiego V. [1981] have shown that the transient well performance is mainly influenced during the formation linear flow period, i.e. at early times (figure 2.8). In this flow period, the pressure loss caused by flow in the fracture is negligible and the pressure transient behaviour of the well is governed by linear flow from the reservoir normal to the fracture plane. Figure 2.8 show that even a small FFS has a large influence on the dimensionless wellbore pressure. At late times, i.e. in the pseudo-radial flow regime, the influence of a FFS is small. The pseudo-radial flow period is characterised by a stabilised flow distribution in the fracture. The flow distribution in the reservoir is radial and no effects from of reservoir boundaries are observed. In this flow period, the pressure behaviour of a damaged reservoir approaches the curve for the undamaged case (FFS = 0) asymptotically (figure 2.8).

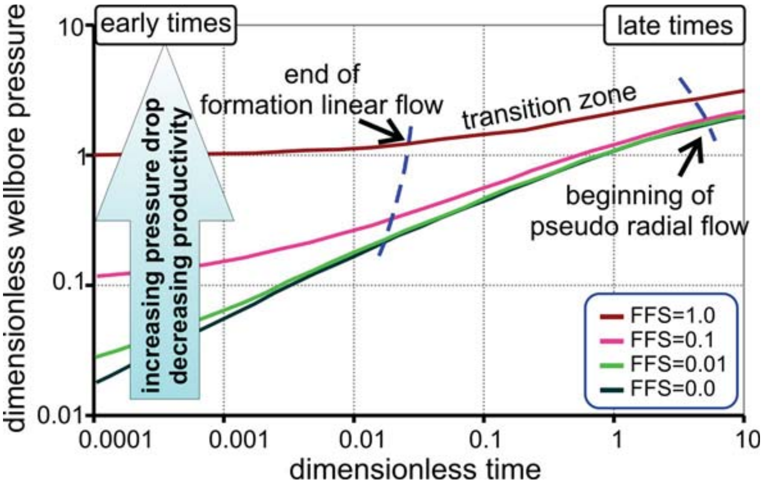

Figure 2.8: *Transient pressure behaviour of a well influenced by a fracture face skin (FFS). At early time (formation linear flow) a FFS has a large influence on the pressure behaviour of a well. In this flow period, the pressure behaviour of a well is controlled by a linear flow normal to the fracture face. In contrast, at late time the influence is negligible [Cinco-Ley and Samaniego-V. 1977]. In this flow period, the flow distribution in the fracture is stabilised and the flow distribution in the reservoir is radial.*

Romero et al. [2003] solved the problem of inflow impairments in the pseudo steady-state flow regime and introduced a variable FFS along the fracture. In this late time flow regime, the flow distribution in the reservoir is dominated by the reservoir boundaries.

Romero et al. [2003] describe the pseudo steady-state drawdown pressure ΔP_d in the reservoir with the influence function ψ:

$$\Delta P_d = \frac{\psi \, \mu \, B \, Q}{2\pi \, k \, h} \qquad 2.37$$

where h represents the effective reservoir thickness, μ the dynamic fluid viscosity, B the formation volume factor, and Q the flow rate. Equation 2.37 in combination with the dimensionless productivity index PI_D

$$PI_D \frac{2\pi \, k \, h}{B \, \mu} = \frac{Q}{\Delta P_d} = PI \qquad 2.38$$

can be used to determine the influence of a FFS on the productivity index:

$$PI_D = \frac{1}{\Psi + FFS} = \frac{1}{\frac{1}{PI_{D,s=0}} + FFS} \qquad 2.39$$

with $PI_{D,s=0}$ representing the dimensionless productivity index of the well with zero fracture face skin. Based on equation 2.39, a sensitivity analyses yields the productivity impairment caused by fracture face skin for different fracture half lengths and permeability reduction ratios. The calculation (figure 2.9) point out that a fracture with small fracture half length is more sensitive for a FFS damage. The extent of the damaged zone has to reach a sufficient thickness to impair productivity vastly. For instance at w_S = 1 m and k_i/k_S = 10 the productivity reduction in the pseudo steady state flow regime is 10 % to 20 %.

Adegbola & Boney [2002] ascertain that fluid loss in high permeability oil and gas wells can induce a high fracture face skin and lead to a significant productivity loss. Figure 2.6 illustrates the effect of fluid loss as well as the build up of a filter cake at the fracture face. Both mechanisms impair the permeability of the fracture face. In general, the effect of a FFS on productivity is small for long fractures in low permeable reservoirs but can be significant for short fractures in high permeable reservoirs [Economides & Nolte 2000]. Holdtich [1979] found that water blocking, i.e. relative permeability changes at the fracture face can impair low permeable gas reservoirs significantly.

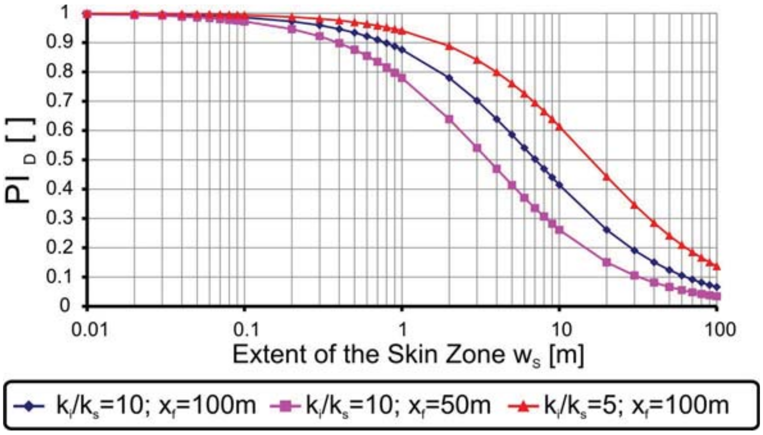

Figure 2.9: *Influence of a FFS on dimensionless productivity (PI_D) in the pseudo steady-state flow regime. The computation of PI_D highlights that the fracture face skin zone needs a sufficient extent (~ 1m) to affect the long-term productivity of a reservoir (reduction of 5 – 20 %).*

2.6.2 Mechanically Induced Fracture Face Skin

Several factors have been found to effect a FFS like fracturing fluid and polymer leak-off into the fracture face, gel residues, water blocking (relative permeability changes) and fines migration [Anderson et al. 1989, Adegbola & Boney 2002]. However, mechanical effects have not been taken into account.

The mechanically induced FFS results from interaction between proppants and rock which alters the rock-proppant interface [Legarth et al. 2005a]. With increasing effective stress on the rock-proppant interface, proppants get embedded into the rock matrix and grains get crushed. This leads to fines production and a compacted zone. The flow path becomes more tortuous and an additional pressure drop at the fracture face is evident. Figure 2.10 exemplifies the formation of the mechanically induced FFS.

Flow direction is important to investigate this mechanically induced permeability reduction. In standard flow cells like the 'API fracture conductivity test' unit [API 60 1989], the 'Split Core in Hassler Sleeve', or the 'Terra Tek Conductivity Test Unit' [API 60 1989, Anderson et al. 1989], flow is directed parallel to the fracture faces to analyse the permeability evolution of proppant packs. Specialised flow cells exist that allow flow normal the fracture face into the formation [Roodhard et al. 1988, Al-Abduwania et al. 2005] but the purpose of these studies was the quantification of permeability reduction due to internal filtration or fluid loss.

Legarth et al. [2005a] developed the conceptual model explaining the origin of a mechanical damaged zone at the fracture face and investigated proppant embedment via optical scanning methods. So far, no evidence is produced that mechanical destruction at the rock-proppant interface and associated permeability reduction due to fines generation exist.

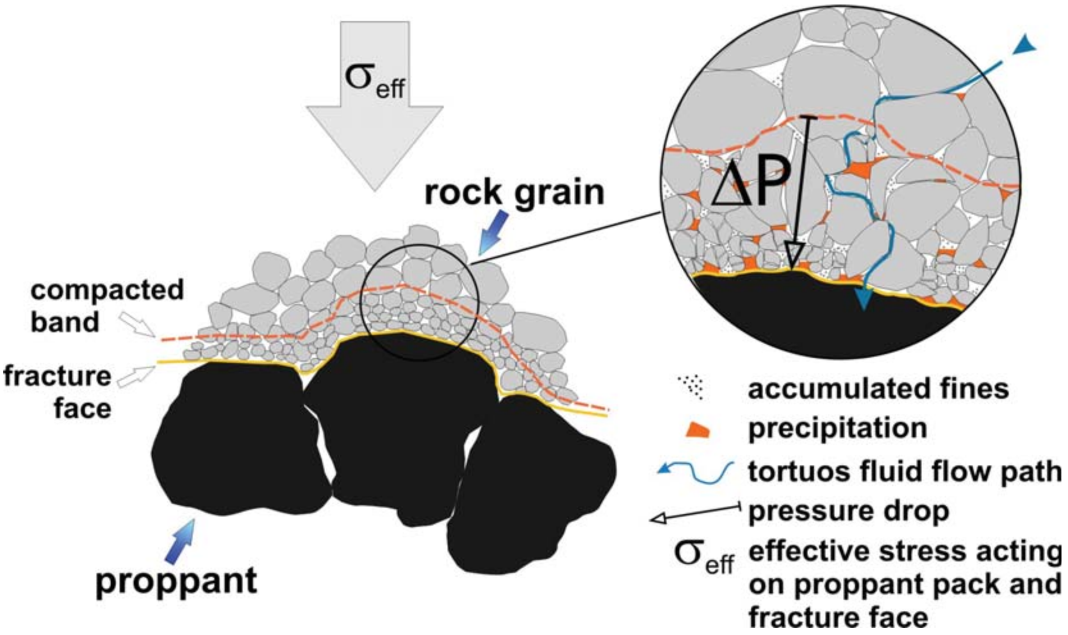
σ_{eff}
rock grain
ΔP
compacted band
fracture face
proppant
accumulated fines
precipitation
tortuos fluid flow path
pressure drop
σ_{eff} effective stress acting on proppant pack and fracture face

Figure 2.10: *Conceptual model of the mechanically induced FFS (modified from [Legarth et al. 2005a]). Increasing effective stress during production of a reservoir leads to proppant embedment into the fracture face. The grains at the rock-proppant interface get crushed and fines are produced. These fines at the interface block pores and as a consequence, an additional pressure drop is evident (∆P).*

3 Experimental Work – Testing Equipment and Techniques

3.1 AEFC - Acoustic Emission Flow Cell

In the context of rock-proppant interaction (RPI) testing, the Acoustic Emission Flow Cell (AEFC) is used to shed light on the microfracture processes at the contact of rock and proppant. Figure 3.1 shows a schematic view of a specimen sandwiching a proppant pack. The AEFC is also used to analyse the triaxial brittle failure of intact Bentheim sandstone cores.

3.1.1 AEFC - Axial Loading Frame and Confinement System

A servo-controlled Material Test Systems loading frame (MTS, Material Test Systems Corporation, Minneapolis MI, USA; model-no.: 815-315-03), including a pressure vessel (figure 3.7a), is used for these experiments. The maximum compressive force is 4600 kN. A high accuracy load cell with a range of 0-1000 kN and a sensitivity of ± 1 kN is utilised. The stiffness of the loading frame including the pressure vessel is $0.72 \cdot 10^{9}$ Nm^{-1}. The stiffness is determined for the dedicated loading range up to 300 kN by measuring stress-strain behaviour of different steel samples. The oil confining pressure system is servo-controlled. The maximum oil pressure is 200 MPa, the accuracy is about 0.1 MPa. The system and the data acquisition are run by the controlling software packages TestStarII and TestWare by MTS.

Two systems are used for strain measurement:

1. The axial displacement is measured by a linear variable displacement transducer (LVDT) mounted at the end of the piston, corrected for the effective stiffness of the loading frame. Strain uncertainty for LVDT measurement is about $5 \cdot 10^{-4}$.
2. For some experiments, lateral and horizontal as well as volumetric strain are estimated using two pairs of strain gages (FCB-6.350 from Tokyo Sokki Kenkyujo, Ltd.), which are glued directly onto the sample surface. The strain gages are oriented parallel to the sample axis and in a circumferential direction (figure 3.2). Each strain gage has a sensoring area of 6 mm x 2 mm. Strain uncertainty is about $1.6 \cdot 10^{-5}$. Volumetric strain ε_V is calculated as sum of axial strain plus two times the radial strain.

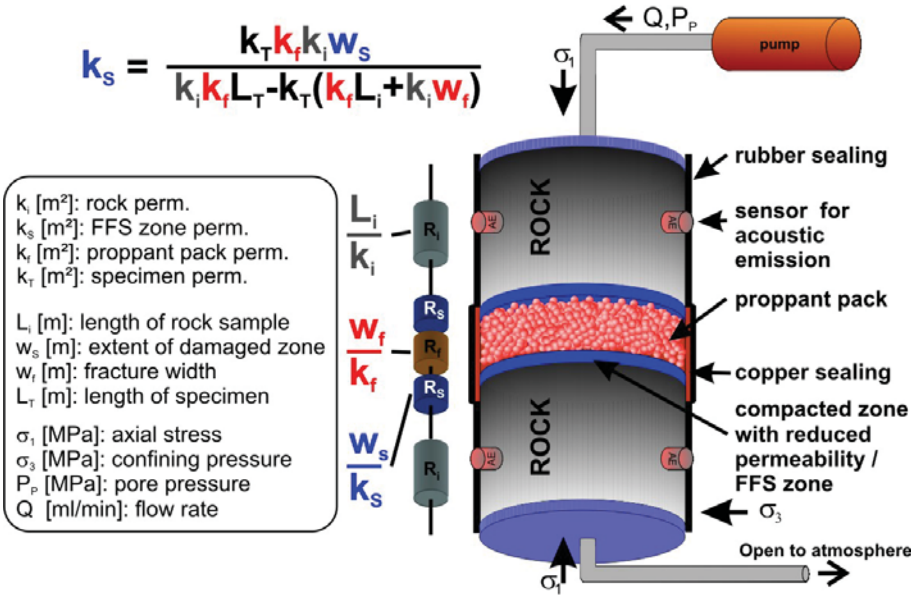
$k_S = \frac{k_T k_f k_i w_S}{k_i k_f L_T - k_T (k_f L_i + k_i w_f)}$
Q,P$_P$
pump
σ_1
rubber sealing
sensor for acoustic emission
proppant pack
copper sealing
compacted zone with reduced permeability / FFS zone
σ_3
Open to atmosphere
σ_1
ROCK
ROCK
AE
AE
AE
AE
k_i [m²]: rock perm.
k_S [m²]: FFS zone perm.
k_f [m²]: proppant pack perm.
k_T [m²]: specimen perm.
L_i [m]: length of rock sample
w_S [m]: extent of damaged zone
w_f [m]: fracture width
L_T [m]: length of specimen
σ_1 [MPa]: axial stress
σ_3 [MPa]: confining pressure
P_P [MPa]: pore pressure
Q [ml/min]: flow rate
$\frac{L_i}{k_i}$
$\frac{w_f}{k_f}$
$\frac{w_S}{k_S}$
R_i
R_S
R_f
R_S
R_i

Figure 3.1: *Schematic view of the Acoustic Emission Flow Cell (AEFC). The AEFC is designed to detect the microfracture processes at the rock-proppant interface and within the proppant pack. In order to determine the permeability of the FFS zone (blue), the setup is approximated as a series connection of hydraulic resistors ($R_i = R_i + R_S + R_f$).*

Constant displacement mode is applied in all experiments. The displacement rate is set to 1 µm/s; this corresponds to a strain rate of $1 \cdot 10^{-5}$ or $0.8 \cdot 10^{-5}$ s^{-1} depending on the sample length (100 mm and 125 mm, respectively).

3.1.2 AEFC - Pore Pressure System

Experiments are executed at room temperature under drained conditions. Fluid is delivered to the sample with a Quisix pore pressure pump. Flow direction is from the top to the bottom; the downstream side is open to the atmosphere. Pure (demineralised) water is used as pore fluid.

For the experiments Bent 1.1 – Bent 1.6 and Bent 2.2 - Bent 2.3, permeability is determined using a pressure transducer that is designed for a range of measurements of 0-1500 bar (Stellar Technologies GT1800-20000G-113). A pressure balance in the range of 0-5 bar was conducted. For short-term measurements with a careful control of zero level, a standard deviation of ~10 % is achieved. The results of this calibration are plotted in figure A1 in appendix A1.

In the experiments Bent 3.4 and Flecht 1.6, a high-resolution differential pressure transducer is used (Honeywell/Sensotec TJE BD121BN) with a pressure range of 3 bar and a full span error of 0.1 %.

The flow circle of the AEFC setup has an intrinsic pressure response. For accurate permeability determination, it is necessary to measure this pressure response of the entire experimental setup. For this purpose, the differential pore pressure of a 100 mm steel sample with a 1 mm capillary is measured (figure A2, appendix A1). The linear regression results in:

$$\Delta P_{AEFC} = 0.4743 \frac{mbar \cdot min}{ml} \bullet Q \qquad 3.1.$$

3.1.3 AEFC - Acoustic Emission Recording

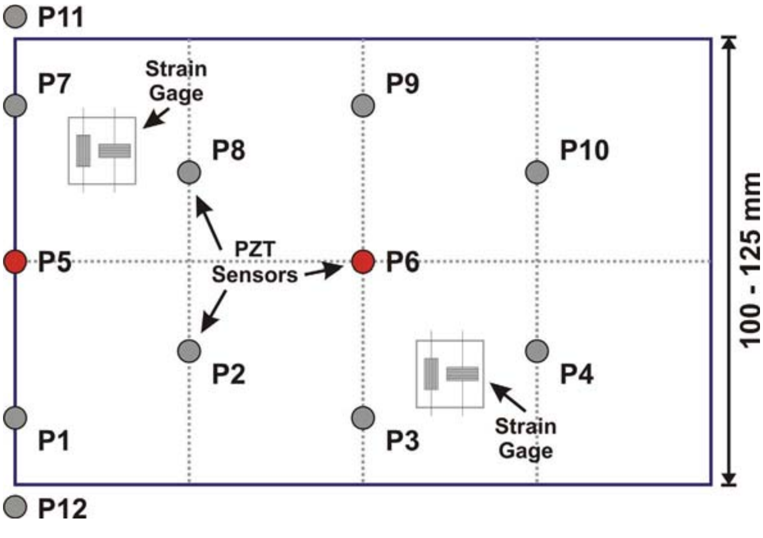

Figure 3.2: Placing of piezoelectric ultrasonic P-wave transducers (PZT) and strain gages. Unrolled mantle surface projection of the specimen.

10 to 12 piezoelectric ultrasonic P-wave transducers (PZT), each with a resonant frequency of 1 MHz, are either embedded in the pistons, or glued directly onto the sample surface and sealed in a neoprene jacket using two-component epoxy (compare to figure 3.1). The PZTs are used to localise the Acoustic Emission (AE) events, as well as to periodically measure P-wave velocities parallel (v_{p_vert}) and normal (v_{p_hor}) to the loading direction. Figure 3.2 shows the sample surface projected in a plane with 10 ultrasonic transducers and 2 bidirectional strain gauges. Two additional P-wave sensors are installed in end caps of the setup. The two PZTs highlighted in red are not attached to every sample. In particular, for proppant testing these PZTs are omitted.

After amplification to 40 dB, the full-waveform AE data and the ultrasonic signals for P-wave velocity measurements are recorded in a 12 channel transient recording system (DaxBox, Prökel GmbH, Germany) with a resolution of 16 bit at 10 MHz sampling rate. For periodic elastic wave velocity measurements, 5 P-sensors are used as emitters, applying 100 V pulses every 30 seconds. Software, developed by Dr. S. Stanchits (Helmholtz Centre Potsdam, Germany) is used for automatic selection using different criteria, including Akaike's information criterion [Leonhard & Kinnet 1999] for first motion amplitudes and for automated AE hypocenter location. First motion polarities are applied to distinguish AE source types as tensile, shear, and collapse (T-, S-, C-) events [Zang et al. 1998]. The hypocenter location algorithm is based on the downhill simplex algorithm [Nelder & Mead 1965], modified for anisotropic and inhomogeneous velocity fields. The AE hypocenter location error is estimated to about 2.5 mm.

3.2 BDFC - Bidirectional Flow Cell

Figure 3.3 shows a schematic view of the BDFC. The permeability evolution of the rock-proppant system and the proppant pack is tested separately in this setup; the differential pore pressure is measured in the axial and the horizontal direction (figure 3.3b).

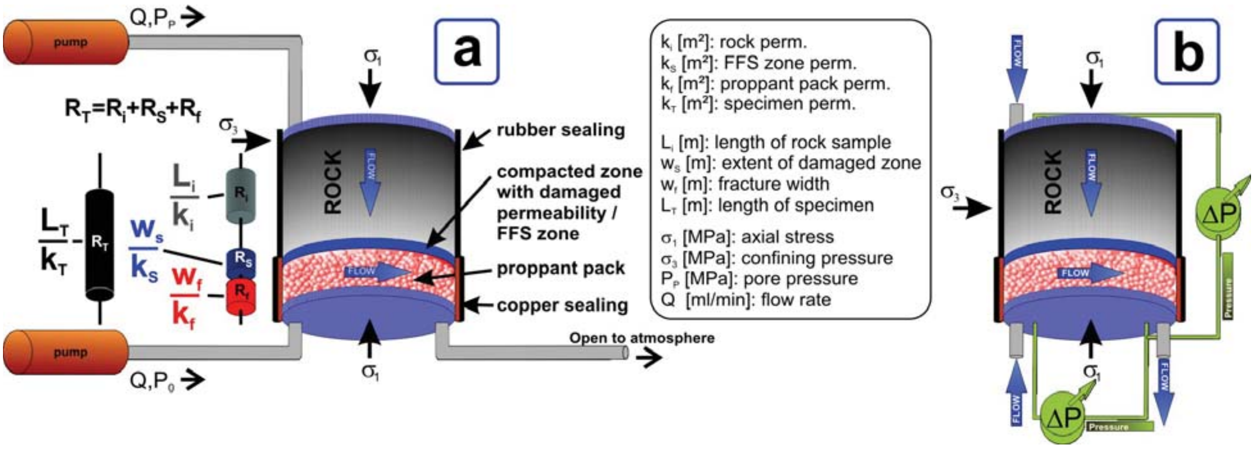
Q,P_P
pump
R_T=R_i+R_S+R_f
σ3
L_T / k_T
R_T
W_S / k_S
L_i / k_i
R_i
R_S
W_f / k_f
R_f
pump
Q,P_0
σ1
a
ROCK
FLOW
rubber sealing
compacted zone with damaged permeability / FFS zone
proppant pack
copper sealing
Open to atmosphere
σ1
k_i [m²]: rock perm.
k_S [m²]: FFS zone perm.
k_f [m²]: proppant pack perm.
k_T [m²]: specimen perm.
L_i [m]: length of rock sample
W_S [m]: extent of damaged zone
W_f [m]: fracture width
L_T [m]: length of specimen
σ1 [MPa]: axial stress
σ3 [MPa]: confining pressure
P_P [MPa]: pore pressure
Q [ml/min]: flow rate
b
FLOW
σ1
σ3
ROCK
FLOW
ΔP
Pressure
FLOW
FLOW
σ1
FLOW
ΔP
Pressure

Figure 3.3: *Schematic view of the Bidirectional Flow Cell (BDFC). The BDFC is designed to analyse the permeability alteration of the proppant pack and the rock-proppant system simultaneously.*

3.2.1 BDFC - Axial Loading Frame and Hoek Cell

The MTS loading frame is used to apply the axial stress to the BDFC, therefore only the differences between the two flow cells are presented here.

The stiffness of the loading frame, including the BDFC, is $0.70 \cdot 10^9$ Nm^{-1}. The Hoek Cell confining pressure system is manually driven. Confining pressure of the manually driven pump drops slightly, but remains stable for several hours. The accuracy is about 1 MPa. A minimum confining pressure of 5 MPa is necessary to completely seal the sample against bypass flow.

Constant axial displacement mode is applied for all experiments. The displacement rate is set to 1 µm/s. This corresponds to a strain rate of $1.5 \cdot 10^{-5}$ to $0.8 \cdot 10^{-5}$ s^{-1}, depending on the sample length, which can vary between 65 and 120 mm.

3.2.2 BDFC - Pore Pressure System

Experiments are conducted at room temperature and under drained conditions. Flow direction is downwards; the downstream side is open to the atmosphere. Pure water and 2 % KCl brine is used as pore fluid.

The permeability is determined with a high resolution differential pressure transducer by Honeywell/Sensotec (TJE BD121BN) with a pressure range of 3 bar and a full span error of 0.1 %. The intrinsic pressure response ΔP_{BDFC} of the flow system is nearly linear (figure A3 / appendix A1); the linear regression results in:

$$\Delta P_{BDFC} = 0.0366 \frac{\mathrm{mbar} \cdot \mathrm{min}}{\mathrm{ml}} \bullet Q \qquad 3.2$$

Darcy's law implies parallel flow lines for permeability measurement. This rule is violated during axial permeability measurement of rock-proppant systems using the BDFC. One of the flow distribution circle segments (figure 3.4) is used as downstream flow port. The permeability of the proppant pack is so high, that this influence can be neglected compared to rock and FFS permeability. This is demonstrated by the calculation in §3.4. The proppant pack permeability has to be reduced by a factor of 50 compared to the rock permeability before the permeability measurement of the rock-proppant system is influenced. In practice, this means that plenty of fines must be deposited in the proppant pack before its influence becomes important.

3.2.3 BDFC - Design of Devices

The BDFC (figure 3.4) is designed to work with a conventional Hoek Cell [Hoek & Franklin 1968] for confining pressure. All parts are made of working steel LA 550 (RM 1000 N/mm², E 196 GPa). Flow and pressure ports are separated to make the pressure measurement independent of any permeability changes in the flow paths, e.g. blocking. Both pistons have a groove along their outer diameter to hold an o-ring in place. This o-ring in combination with the Hoek Cell gasket seals the specimen and avoids any bypass flow.

The top plug cylinder ($\varnothing$ = 50 mm) is attached to a support plate. Flexible tubes made from stainless steel connect the flow and pressure ports (figure 3.5); the maximum line pressure is 10 MPa. Fluid is delivered to the sample from top to bottom.

The bottom plug cylinder ($\varnothing$ = 50 mm) for proppant testing (bottom plug 1 / figure 3.6) has two pressure and two flow ports. The two flow ports are connected to flow distribution circle segments to the left and right of the PEEK plate (Polyetheretherketon) (figure 3.6). The differential pressure is measured between the two small slots in the centre of the PEEK plate. The pressure measurement slots are 25 mm apart and 0.4 mm wide. Hence, proppants (20/40 mesh / 0.4 - 0.8 mm) cannot enter the small slots. Fluid channels for pressure measurement are caped with a filter disk made from sintered copper. The filters prevent blocking by mobilised fines

A PEEK plate is used as support for the proppant pack. PEEK has a Young’s modulus of 3.7 GPa and a tensile strength of 90 MPa. The synthetic material PEEK is stiff enough to support the load, but the Young’s modulus is low enough to avoid proppant crushing on contact with the PEEK. Plastic deformation of the PEEK will embed proppants. The confining pressure forces a copper foil into a small groove below the PEEK plate and seals the proppant pack.

A second bottom plug (bottom plug 2/ figure 3.6) is used for mechanical and hydraulic testing of intact rock samples (without proppants). The second bottom plug is manufactured similarly to the top plug, and is interchangeable with the proppant testing bottom plug (plug 1). It has only one flow and one pressure port and the fluid is distributed via a network of grooves. Specimen length can vary from 60 mm to 125 mm.

The BDFC is mounted onto a metal plate that provides the fluid connectors for the bottom piston (figure 3.5). This plate holds the differential pressure sensor, the safety valve and two toggles to switch flow directions, i.e. between horizontal (proppant) flow and axial flow through the specimen. The plate assures a centred positioning below the MTS piston, which is spherically seated.

3.3 AEFC & BDFC - Experimental Procedure

A rock-proppant interaction (PRI) experiment is performed in three steps. The hydraulic and mechanical characterisation of the sandstones presented in §5.1 is similar to step 1. The images in figures 3.7 and 3.8 illustrate the different steps of an RPI experiment.

1. The initial permeability of the sandstone sample k_i, the poroelastic permeability dependence at defined stress levels, and the Young’s modulus E_R are determined. Three loading cycles up to the level of 65 MPa differential stress are applied to assure a preloading of the samples and avoid irreversible permeability changes as a result of closure of microcracks. The differential stress is calculated according to equation 2.14. The permeability of the rock (k_i) is measured during the 4th loading cycle at defined stress levels.

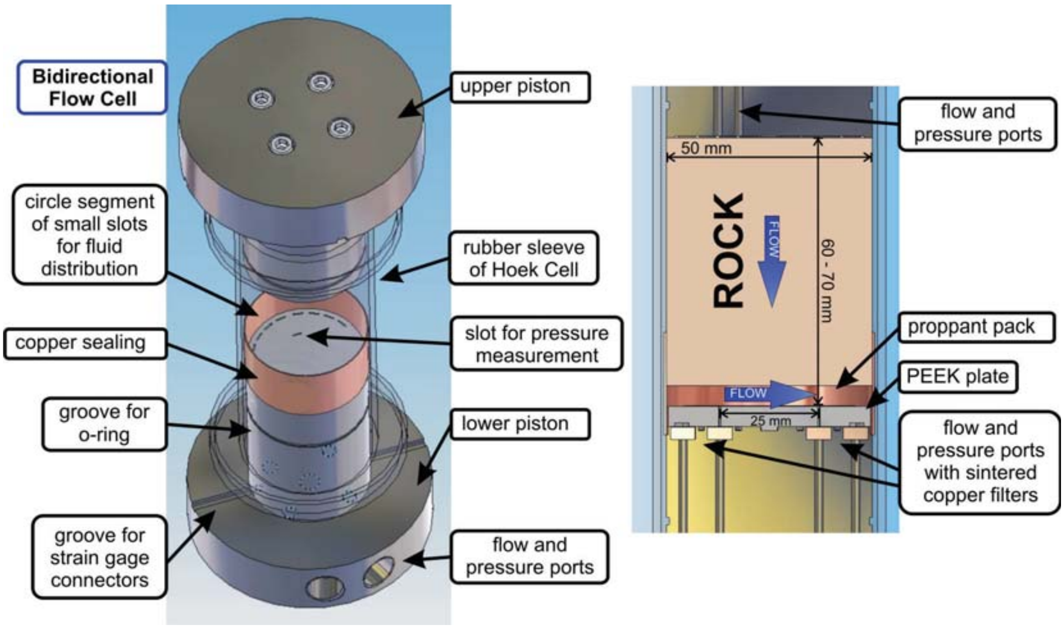
Bidirectional Flow Cell
upper piston
circle segment of small slots for fluid distribution
rubber sleeve of Hoek Cell
copper sealing
slot for pressure measurement
groove for o-ring
lower piston
groove for strain gage connectors
flow and pressure ports
flow and pressure ports
50 mm
ROCK
FLOW
60 - 70 mm
proppant pack
PEEK plate
FLOW
25 mm
flow and pressure ports with sintered copper filters

Figure 3.4: *The Bidirectional Flow Cell (BDFC). The BDFC simulates the flow conditions in a reservoir intersected by a propped fracture. The proppant pack is placed on the PEEK plate and the rock cylinder is aligned on top. Two o-rings in combination with the rubber sleeve of the Hoek Cell seal the specimen. Bottom plug 1 is shown.*

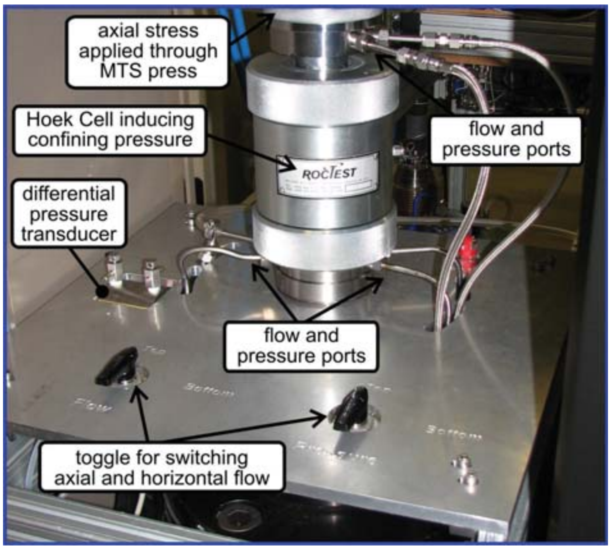
axial stress applied through MTS press
Hoek Cell inducing confining pressure
ROCTEST
flow and pressure ports
differential pressure transducer
flow and pressure ports
toggle for switching axial and horizontal flow

Figure 3.5: *BDFC mounted on its carriage in MTS press. The BDFC is designed to work with a Hoek Cell applying the confining pressure. Flow and pressure ports for axial and horizontal permeability measurements are separated in order to make the pressure measurement independent of pressure changes in the flow paths.*

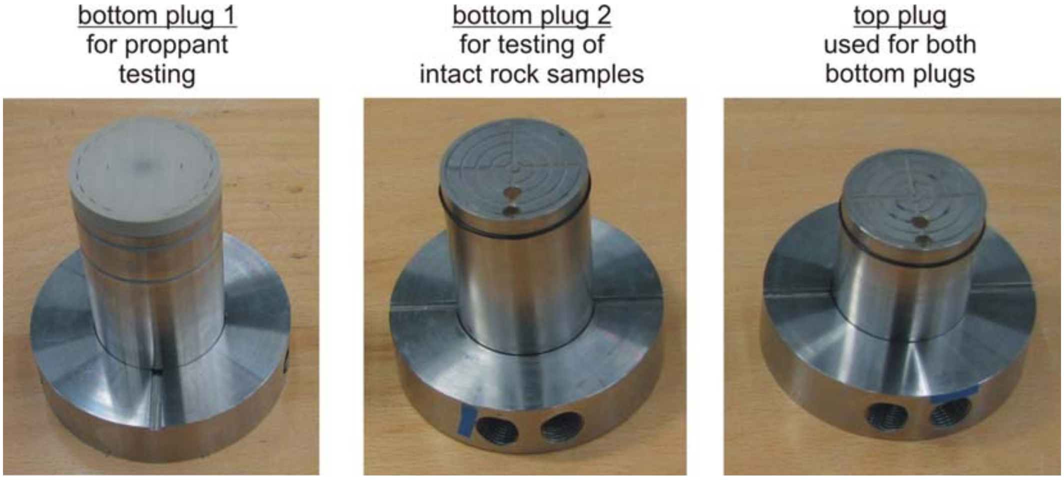
bottom plug 1
for proppant testing
bottom plug 2
for testing of intact rock samples
top plug
used for both bottom plugs

Figure 3.6: *Bottom and top plugs of BDFC used for proppant testing (plug 1) and rock testing (plug 2).*

2. A tensile fracture comparable to an idealised hydraulic fracture generation is created in a 3-Point Bending test [Sun & Ouchterlony 1986] (figure 3.7b). To initiate the tensile fracture, a straight notch (30 mm long and 2 mm deep) is carved into the specimen. To distinguish between permeability reduction due to tensile fracture generation and due to rock-proppant interactions, the permeability of the specimen with tensile fracture k_{tf} is also determined for the Bentheim sandstone samples. For Flechtingen sandstone samples, this extra measurement was disregarded, because the permeability of the Flechtingen rock is so low (~ 1 mD) that the influence of few fines in the fracture face can be neglected. To preserve the tensile fracture in its primary conditions (e.g. alignment, contacts, amount of produced fines), the fracture was not propagated through the complete sample, but a narrow connection keeps the two halves in place.
3. The images in figures 3.7 and 3.8 give an impression of the experimental procedure for step 3. The PEEK plate of the BDFC is fitted on top of the flow and pressure ports (figure 3.8b). A copper foil seal is fitted around the bottom piston (figure 3.8c and 3.9b). A proppant pack is placed (3.7c and 3.8c). Plane-parallel alignment of the rock specimen to the lower piston of BDFC is achieved by vibrating the setup. Alignment parallel to the piston axis is verified with a water level (figure 3.8d) in two measurements at right angles to each other.

   To fit the AEFC specimens, the copper foil is applied around the lower half of the rock sample. A proppant pack is placed and the second half of the rock is fitted on top (figure 3.7c). The above alignment procedure is conducted. The specimen is seated in a neoprene jacket and the brass housings are glued through the jacket directly on the rock surface (figure 3.7d).

   Exact alignment is crucial for a successful experiment. If the rock sample is tilted relative to the piston axis, the specimen will not be uniformly loaded, the fracture does not close uniformly. A perfect alignment is not possible with a water level, but it is exact within ± 5°. Hence, the maximum shear loading of rock sample and proppant pack would be within a range of 8 % of the axial load.

   The o-rings and the pistons of the BDFC are lubricated using a film of silicon to provide a good seal and mobility in the rubber sleeve of the Hoek Cell. After assembling the AEFC or BDFC, the setup is moved into the MTS press and loaded axially with σ_1 = 2.5 MPa. A confining pressure of σ_3 = 10 MPa is applied to avoid fluid by-pass.

   During execution of the experiment, the specimen is axially loaded to simulate fracture closure under production conditions. Loading is stopped in constant displacement mode at defined stress levels (σ_{diff} = 5, 20, 35, 50 MPa) and permeability of the rock-proppant system is measured according to Darcy's law (§2.3.1). The permeability in axial direction is determined with both flow cells at each stress level; the proppant pack permeability is measured with the BDFC exclusively.

3.3.1 AEFC & BDFC - Sample Preparation

For the AEFC and BDFC experiment, sandstone cores with a length of 100 to 120 mm and a diameter of 50 mm are cored from blocks parallel to the bedding planes.

The end surfaces of all rock cylinders are ground plane-parallel and perpendicular to the cylinder axis. The samples are cleaned of dust in an ultrasonic bath and dried in a vacuum at 45 °C. The Bentheim sandstone is very homogenous; bedding planes are difficult to locate. The layering of Flechtingen sandstone is pronounced and the grain radius can differ considerably from layer to layer. For all experiments, homogenous blocks of Flechtingen sandstone are given preference.

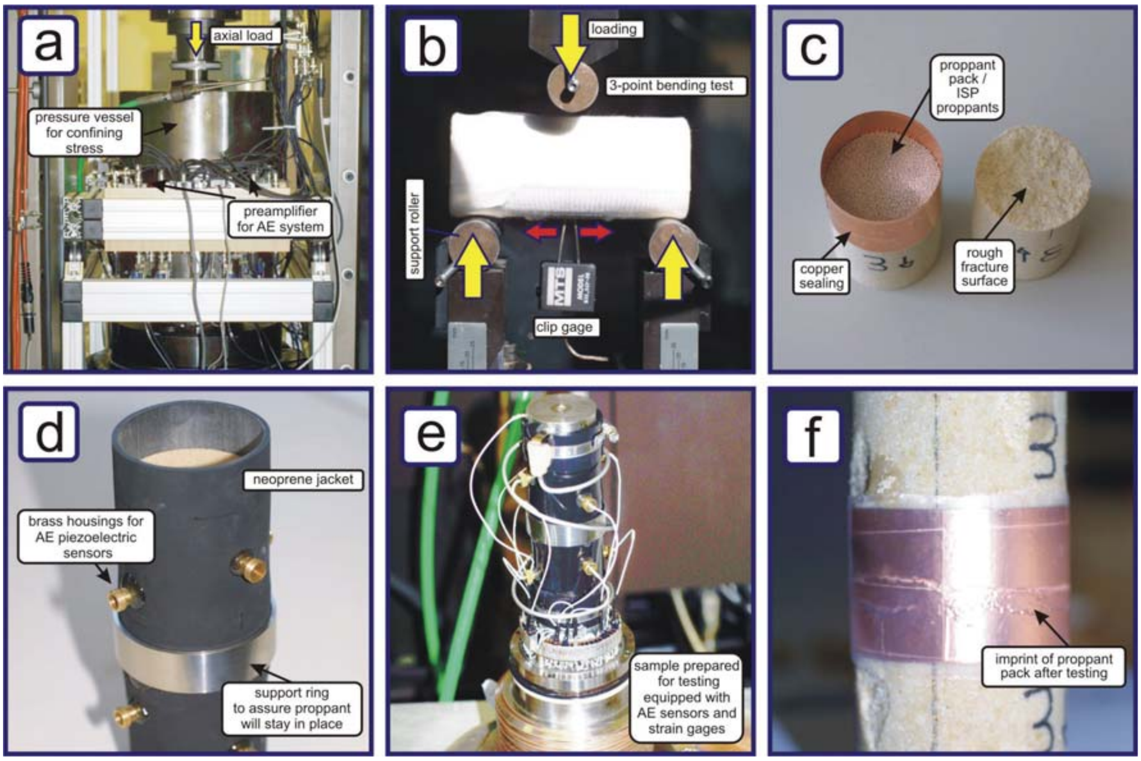
a
axial load
pressure vessel for confining stress
preamplifier for AE system
b
loading
3-point bending test
support roller
clip gage
c
proppant pack / ISP proppants
copper sealing
rough fracture surface
d
neoprene jacket
brass housings for AE piezoelectric sensors
support ring to assure proppant will stay in place
e
sample prepared for testing equipped with AE sensors and strain gages
f
imprint of proppant pack after testing

Figure 3.7: *Photo collection of preparation and execution of a rock-proppant interaction test with the AEFC. a) pressure vessel of the AEFC in the MTS loading frame; b) a 3-point bending test creating a macroscopic tensile fracture; c) specimen preparation with a Bentheim sandstone and ISP; d) specimen equipped with brass housings for AE transducers; e) fully mounted specimen with electrical connections; f) Bentheim sandstone specimen after testing*

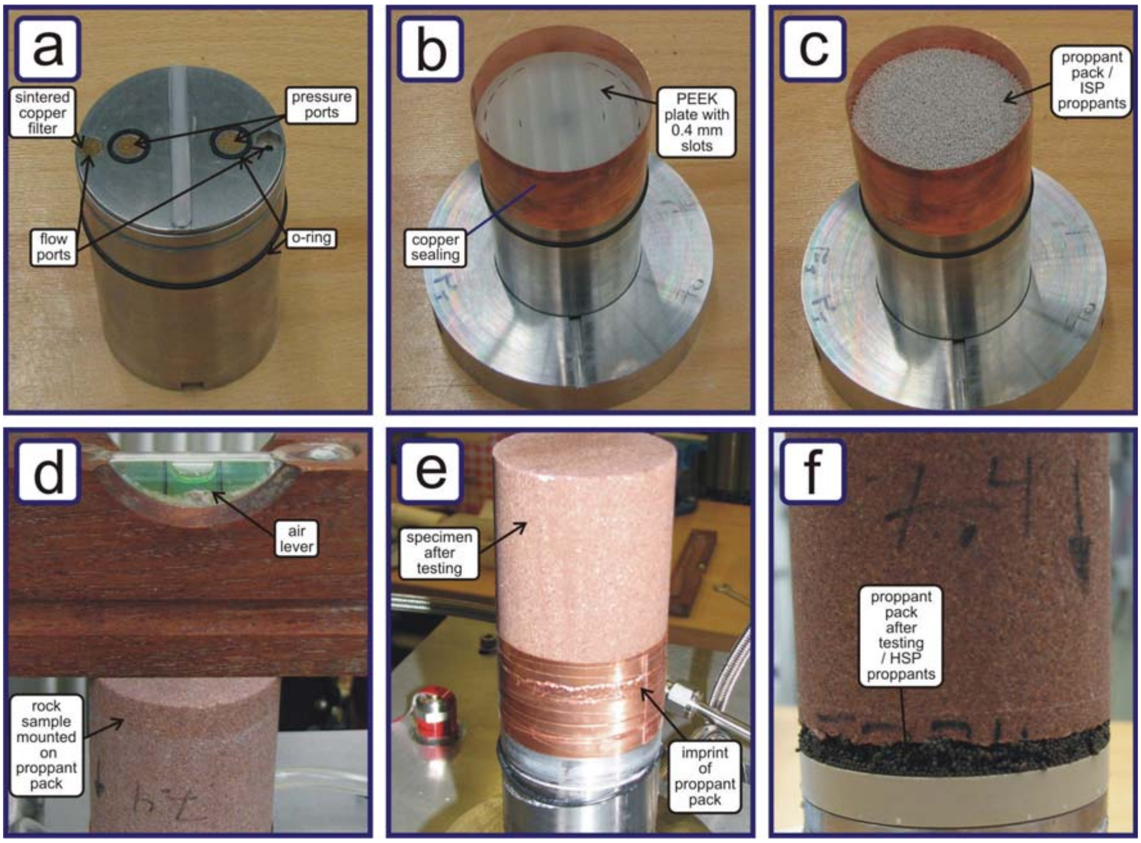
a
sintered copper filter
pressure ports
flow ports
o-ring
b
PEEK plate with 0.4 mm slots
copper sealing
c
proppant pack / ISP proppants
d
air lever
rock sample mounted on proppant pack
e
specimen after testing
imprint of proppant pack
f
proppant pack after testing / HSP proppants

Figure 3.8: *Photo collection of preparation and execution of a rock-proppant interaction test with the BDFC. a) bottom plug with pressure and flow ports; b) mounted PEEK plate for proppant support; c) placing of proppant pack on PEEK plate; d) mounting and levelling of rock core; e) specimen after testing; f) HSP pack and Flechtingen sandstone*

3.3.2 AEFC & BDFC - Saturation Process

For a reliable permeability measurement, the saturation process is a critical parameter. Remaining air bubbles in the pores would lead to an erroneous permeability measurement. In particular, trapping of gas can block small pores in the tight Flechtingen sandstone.

A vacuum pump evacuates the setup down to 0.5 kPa. Then the specimen is saturated with pure water or a 2 % KCl brine. Fluid is delivered to the specimen with an amount 3 times the pore volume (approximately 120 ml for Bentheim sandstone and 40 ml for Flechtingen sandstone).

The saturation procedures for the two rock types are the same, but the time required is different for each: a Bentheim sandstone specimen is evacuated within 1 hour and saturated within a few minutes by applying a constant flow rate of 10 ml/min. In contrast, the tight Flechtingen sandstone has to be evacuated over night (at least for 10 hours), and saturated for a whole day

3.4 AEFC & BDFC - Determination of FFS Permeability

Figures 3.1 and 3.3 show a schematic view of a sample for rock-proppant interaction (RPI) testing. The proppant pack is placed between two rock halves. In order to calculate the permeability of the FFS zone, the setup is approximated as a connection of hydraulic resistors R_i, R_S and R_f in series (figure 3.1 and figure 3.3a). Each resistor is the quotient of length (L) of the segment and the appropriated permeability (k). This results in following equations for the hydraulic resistance of the rock-proppant system (L_T/k_T) and the FFS permeability k_S:

$$\frac{L_T}{k_T}=\frac{L_i}{k_i}+\frac{w_f}{k_f}+\frac{w_S}{k_S} \qquad 3.3a$$

$$k_S=\frac{k_T k_f k_i w_S}{k_i k_f L_T - k_T\left(k_f L_i + k_i w_f\right)} \qquad 3.3b$$

The notation of the symbols is given in table 3.1

k_T	specimen permeability	L_T	length of specimen
k_i	rock permeability	L_i	length of rock sample
k_f	proppant pack permeability	w_f	fracture width
k_S	FFS zone permeability	w_S	extent of FFS zone / damage penetration

Table 3.1: *Quantities defining the hydraulic properties of rock-proppant systems.*

Equation 3.3b requires the permeability of the proppant pack as an input parameter, which cannot be measured with the AEFC. In order to determine the FFS permeability, the hydraulic resistance of the proppant pack in equation 3.3b is ignored, leading to:

$$k_S=\frac{k_T k_i w_S}{k_i L_T - k_T L_i} \qquad 3.4$$

This simplification is acceptable, because the impact of k_f on k_S is small compared to that of k_i and k_T, as long as the contrast between k_i/k_f is large. This can be shown if k_f is expressed as a factor f multiplied with k_i:

$$k_S=\frac{k_T k_i w_S}{k_i L_T - k_T L_i - \frac{k_T w_f}{f}} \qquad 3.5$$

As long as $f \geq 50$, the term $\{k_T w_f / f\}$ is small compared to the term $\{k_i l_T - k_T l_i\}$, and can thus be neglected. This is obviously true for the proppants used for the experiments. They provide permeability above 100 D, even at high differential stresses.

3.4.1 AEFC & BDFC - Rock Sample Length and Fracture Width Determination

The length of the rock-proppant system L_T is calculated from displacement u:

$$L_T = L_{Ri} - u \tag{3.6}$$

including L_{Ri}, the initial length of the rock specimen. This is only valid, if the zero level of the recording system for the LVDT of the MTS remains unchanged during the three-step procedure of a RPI experiment. The fracture width is given as:

$$w_f = L_T - L_{Ri} - \frac{\sigma_{diff}}{E_R} L_{Ri} \tag{3.7}$$

where E_R is the Young’s modulus of the rock.

For experiments with the BDFC, L_{Ri} has to be measured using a caliper gauge. This results in greater inaccuracy of length determination compared to the AEFC. The face of the fracture is not smooth, therefore the length is determined 6 times at an angle of ~ 60° against the exterior. The standard deviation of this measurement ΔL_{Ri} is ± 0.2 mm. This uncertainty is in accordance with an average value of height differences of 0.26 mm, calculated by Backers et al. [2003] from 2D fracture face laser scans.

3.4.2 AEFC & BDFC - Differential Pressure Measurement

For the two rock types and the proppant pack, different measurement procedures and flow rates are applied to determine the differential pore pressure ΔP_P under steady state conditions, whereupon the average of the differential pore pressures $\overline{\Delta P}_P$ is calculated.

Table 3.2 gives a summary of the procedures conducted for proppant pack and rock permeability determination.

	Bentheim sandstone	Flechtingen sandstone
evacuation	$P_P \geq 500$ Pa; t =1 h	$P_P \geq 500$ Pa; t ≥ 10 h
saturation	Q = 10 ml/min; t = 10 min	Q = 0.05 - 0.2 ml/min; t = 24 - 36 h
k_T, k_i determination	Q = 1 - 60 ml/min $\overline{\Delta P}_P$ averaged from 30 s	Q = 0.05 - 0.2 ml/min; $\overline{\Delta P}_P$ averaged from 60 s
k_f determination	Q = 20 - 60 ml/min; $\overline{\Delta P}_P$ averaged from 20 s	Q = 20 - 80 ml/min; $\overline{\Delta P}_P$ averaged from 20 s

Table 3.2: *Procedures for evacuation, saturation and differential pore pressure measurements. P_P: pore pressure, $\overline{\Delta P}_P$ mean of differential pore pressure, Q: flow rate, t: time*

3.4.3 AEFC & BDFC - Flow Velocities in the Setup

At the Gross Schoenebeck geothermal research site, a flow rate of Q = 100 m³/h is required for sustainable electric power production [Zimmermann et al. 2008]. For the following calculation it is assumed that the whole inflow is attributed to one penny shaped fracture with x_f = 50 m radius. The Darcy flow velocity at the fracture face is:

$$v_D = \frac{Q}{2\pi \cdot x_f^2} = 4.4 \cdot 10^{-7} \frac{m}{s} \tag{3.8}$$

In relation to specimen radius r_S = 25 mm, this is equivalent to a flow rate of 0.05 ml/min for the RPI experiments. Hence, the flow rates used in Flechtingen sandstone experiments are realistic (table 3.2).

For the proppant pack in the penny shaped fracture, this calculation results in a Darcy flow velocity at the wellbore entry of:

$$v_D = \frac{Q}{2 \cdot x_f \bullet w_f} = 2.8 \cdot 10^{-2} \frac{m}{s} \qquad 3.9$$

where w_f is assumed to 5 mm. This Darcy flow velocity is equivalent to a flow rate of 420 ml/min in the BDFC. It is clear that non-Darcy flow effects will lead to a highly reduced apparent permeability at the wellbore entry [Dacun & Engler 2001]. The flow rates used in the experiments are too small to simulate those effects.

3.4.4 AEFC & BDFC - Temperature Dependence of Fluid Viscosity

The viscosity η of water has a strong temperature dependence at lower temperatures (0°C - 100°C). An exponential function is used to determine the viscosity of water [µPas]:

$$\eta(T) = 1634 \cdot e^{-0.0232 \cdot T} \quad \forall\, 5°C \le T \le 45°C \qquad 3.10$$

The viscosity data are taken from NIST (National Institute of Standards and Technology / www.nist.gov).

3.4.5 AEFC & BDFC - Cumulative Error

Summation of the relative errors influencing the measurement results in the errors for k_i, k_f and k_T. Typical values are given in table 3.3.

The error for the FFS permeability (k_S) results from adding the relative cumulative errors of single permeability determinations:

$$\frac{\Delta k_S}{k_S} = \frac{\Delta k_i}{k_i} + \frac{\Delta k_T}{k_T} \qquad 3.11$$

The effect of Δk_f is disregarded. This error is large, the influence on k_S is small (see above). A detailed error estimation is given in appendix A2.

	Bentheim sandstone AEFC	Bentheim sandstone BDFC	Flechtingen sandstone ADFC&BDFC	Proppant pack BDFC
standard deviation of differential pressure measurement	≤ 5.0 %	≤ 0.7 %	≤ 0.03 %	≤ 20 %
zero level drift	≤ 2.5 %	≤ 2.0 %	–	≤ 5 %
systematic error of differential pressure transducer	- / -	- / -	~ 0.1 %	- / -
temperature influence	~ 2.3 %	~ 2.3 %	~ 2.3 %	~ 2.3 %
error of rock sample length determination	- / -	- / -	- / -	~ 5.0 %
cumulative relative errors $\frac{\Delta k_i}{k_i} / \frac{\Delta k_T}{k_T} / \frac{\Delta k_f}{k_f}$	~ 10 %	~ 5 %	~ 2.5 %	~ 30 %

Table 3.3: *Influence of different measurement and systematic errors on the permeability determination using the AEFC and BDFC.*

3.5 LTFC – Long-Term Flow Cell

The permeability experiments are performed with High-Pressure-Temperature permeameter (figure 3.9), that allows the continuous measurement of various petrophysical parameters. Milsch et al. [2007] give a detailed description.

3.5.1 LTFC - Confining Pressure and Heating System

A stainless steel pressure vessel (figure 3.10f) with a maximum isostatic oil pressure of 140 MPa and a maximum oil temperature of 200 °C is used for long-term experiments. No differential stress can be applied to the specimen. The servo-controlled confining pressure system keeps the isostatic pressure constant within ± 0.05 MPa, the pressure transducer has a noise of ± 0.002 MPa. The confining oil is heated by a resistance-heating element maintaining a constant temperature within ± 0.5 °C. The oil temperature is measured with thermocouples (PT-100 RTD) placed into the pressure vessel and attached to an Agilent 34970A multimeter via feed-troughs. The oil heats the pore fluid to the temperature of the oil as it flows through a spiral pipe suspended in it.

3.5.2 LTFC - Pore Pressure System

The four pore fluid pumps (type: Isco 260D; figure 3.9) provide a continuous fluid flow through the sample from the bottom to the top. The maximum line pressure is 52 MPa. During the experiment, the downstream pump keeps the sample pressurised, whereas the upstream pump provides the fluid flow. The flow rate can be varied from 0.01 to 107 ml/min. Pore fluid is a 0.1 mol (0.3 %) NaCl brine. The differential pore pressure for the specimen is determined by opening a bypass valve between the up- and downstream side and measuring a reference pressure. Hence, differential pressure ΔP_P is independent of drifting behaviour of the sensor.

3.6 LTFC - Experimental Procedure

The images in Figure 3.10 show an overview of the preparatory steps necessary for a LTFC experiment. A specimen is placed between two stainless steel plugs. Only Flechtingen sandstone is investigated using this setup. For the electrical conductivity measurement, horizontal silver rims are painted onto the rock surface. Brine is used as the pore fluid to enable an electrical conductivity measurement parallel to the permeability determination. The effective stress is calculated according to equation 2.16.

The electrical conductivity is very sensitive to alterations in the paths taken by the fluid. The distance between the rims is 25 mm for an intact sample, but it varies depending no the proppant pack used. The specimen is jacketed in heat shrinkable tube. Two of these tubes are used. The inner tube is preformatted and passes through some silver foil, which connects the silver rims (figure 3.10d). The outer tube seals the perforation by squeezing silicon glue into the space between both tubs. For RPI experiments a third shrinkable tube is utilised to place a proppant pack in a cut rock core (figure 3.10a&b).

3.6.1 LTFC - Sample Preparation

For the LTFC experiments, sandstone cores with a length up to 45 mm in length and 30 mm in diameter are cored from Flechtingen sandstone blocks, parallel to the bedding planes. The further preparation process is similar to the procedure used for AEFC and BDFC (§3.3.1).

3.6.2 LTFC - Saturation Process

The specimen is saturated for 24 hours with 0.1 mol NaCl solution in a vacuum cabinet. All pipes of the LTFC are pre-filled with brine to avoid the intrusion of air into the pore pressure system. After mounting the specimen into the pressure vessel, a confining pressure of 5 bar is applied and fluid is delivered to the specimen from bottom to top of the sample. The confining pressure and temperature is increased to defined levels, and the long-term permeability measurement begins.

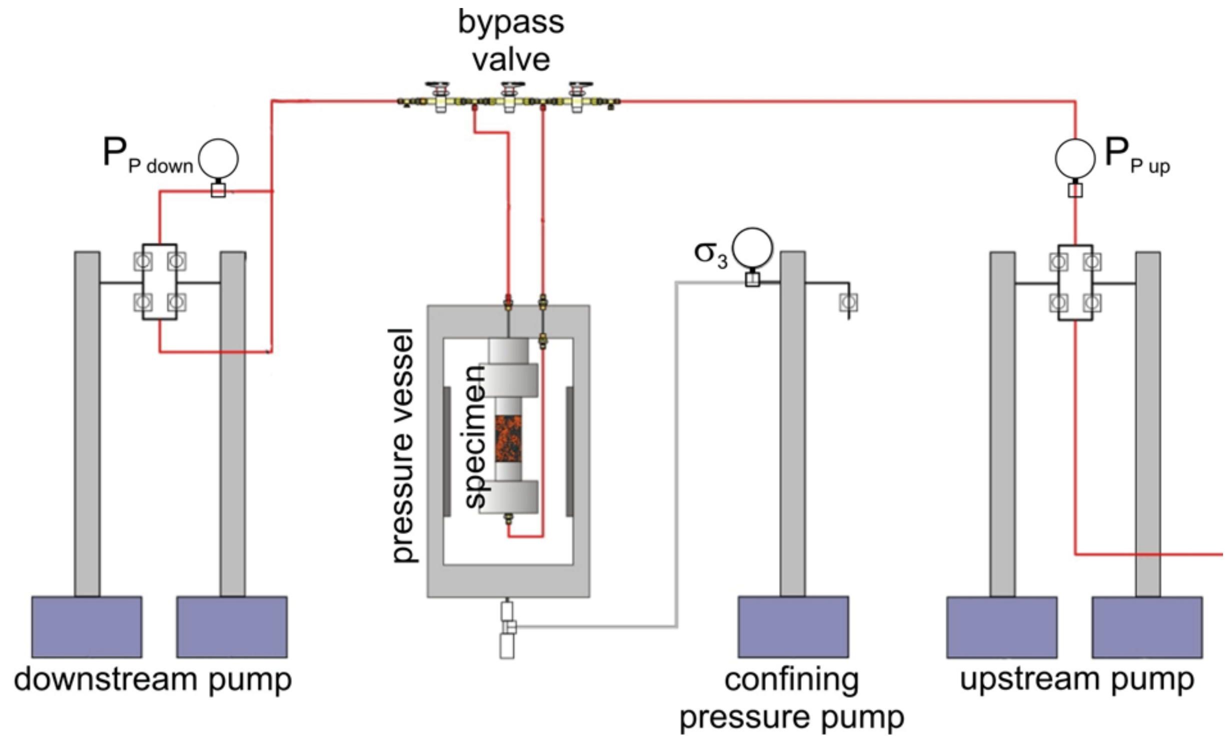

Figure 3.9: *Schematic view of flow cycle and confining pressure system of the Long-Term Flow Cell (LTFC) (modified from [Milsch et al. 2007]). Two upstream pumps deliver fluid to the specimen; two downstream pumps keep the pore pressure constant. For permeability measurement the bypass valve between the up- and downstream side is opened and a reference zero level pore pressure is measured.*

3.6.3 LTFC - Electrical Conductivity Measurement

At temperatures below some hundred degrees Celsius, the electrical transport in a porous medium is predominantly determined by the conduction through the pore fluid. Hence, the electrical conductivity is affected by changes of the pore structure comparable to the permeability [Walsh & Brace 1984]. The change of electrical conductivity correlates to the changes in permeability due to deformation of the void space before and during dilatancy [Gómez et al. 1997]. The hydraulic and the electrical transport properties of a fluid saturated rock can be interrelated via microstructural properties [Schön 2004, Milsch et al. 2008 and references therein] using the formation factor FF [Archie 1942], which is the ratio of fluid conductivity κ_f to rock conductivity κ_R at a given temperature:

$$FF = \frac{\kappa_f}{\kappa_R} = \frac{c}{\Phi^m} \qquad 3.12$$

The formation factor is related empirically to the porosity of a rock Φ, whereby the exponent m is about 1.3 for unconsolidated sandstone and between 1.8 and 2.0 for consolidated sandstones [Trautwein 2005]. The value c is a conformation factor. Equation 3.12 is only valid if the rock conductivity is based on the fluid conductivity in the interconnected pore space exclusively. In clay rich rocks, the surface conductivity has to be taken into account.

A function generator (Agilent 33220A) provides a voltage signal for the electrical conductivity measurements. Typically, the signal is an AC-sine wave with 1.0 V peak-to-peak amplitude and a frequency of 13Hz. A four-electrode configuration is used for measuring electrical conductivity. The specific electrical conductivity κ_R is given by [Milsch et al. 2007]:

$$\kappa_R = \frac{d_r}{R_S \cdot A_S} = \frac{U_{shunt} \cdot d_r}{U_{Ag} \cdot R_{shunt} \cdot A_S} \qquad 3.13$$

where R_S is the sample resistance, d_r is the distance between the silver lines, A_S is the cross sectional area of the sample, U_{shunt} is the voltage across the shunt, U_{Ag} is the voltage between the silver rims and R_{shunt} is the shunt resistance. The shunt resistance is set to 1 kΩ. From κ_R, the formation factor is calculated according to equation 3.12.

The electrical conductivity is measured continuously. The temperature dependence of fluid conductivity for formation factor calculation is determined by:

$$\kappa_f(T)=\kappa_f\big|_{25°C}\cdot\left(1+\alpha_f\cdot\left(T\text{-}25°C\right)\right) \qquad 3.14$$

The conductivity of NaCl brine at 25 °C is 10.8 mS/cm; α_f is determined empirically and amounts to 0.0125 C^{-1}.

3.6.4 LTFC - Differential Pressure Measurement

In order to minimise the error in the pressure measurements caused by drift and offset, a special technique using only one sensor for differential pressure measurement is applied. For each measurement a bypass valve between the upstream and downstream sides is opened, resulting in an instantaneous pressure balance. The differential pressure ΔP_P can be calculated from the two pressure values before and after opening the valve. Permeability is taken at constant flow rate Q = 0.05 – 0.1 ml/min, if P_P is constant for at least 10 min.

	Flechtingen sandstone
saturation	Q = 0.0; t = 24 h, vacuum cabinet
k_T, k_i determination	Q = 0.05 - 0.1 ml/min; ΔP_P from bypass opening pressure differences
κ_R determination	Q = 0.0 ml/min; during bypass opening phase

Table 3.4: *Parameters for permeability and electrical conductivity measurement using the long-term flow cell.*

The noise of the pressure transducers is about ± 0.01 bar. Parameters for saturation, as well as permeability and electrical conductivity measurement procedures are summarised in table 3.4.

3.6.5 LTFC – Temperature Dependence of Fluid Viscosity

The viscosity η of water is only slightly temperature dependent in the ranging from 140 to 160 °C. A power law fit is used to determine the viscosity of water (µPas):

$$\eta(T)=35155\cdot T^{-1.0418} \quad \forall\, 70°C\leq T\leq 160°C \qquad 3.15$$

The viscosity data are taken from NIST (National Institute of Standards and Technology / www.nist.gov).

3.6.6 LTFC – Cumulative error

The accuracy in determining k_i and k_T is influenced by the noise of the pressure transducer and the stability in temperature of the oil heating the pore fluid The differential pressure error $\Delta\overline{\Delta P_P}$ is estimated from standard deviation of upstream and downstream pressure, as it is calculated from the difference between them. The standard deviation is about 0.03 bar, which is equivalent to 1 % relative error. The errors for k_i and k_T are given in table 3.5.

	Flechtingen sandstone / LTFC
standard deviation of pressure measurement	≤ 1.0 %
temperature influence	~ 2.0 %
cumulative relative errors $\frac{\Delta k_i}{k_i}/\frac{\Delta k_T}{k_T}$	~ 3.0 %

Table 3.5: *Errors influencing the permeability determination using the LTFC.*

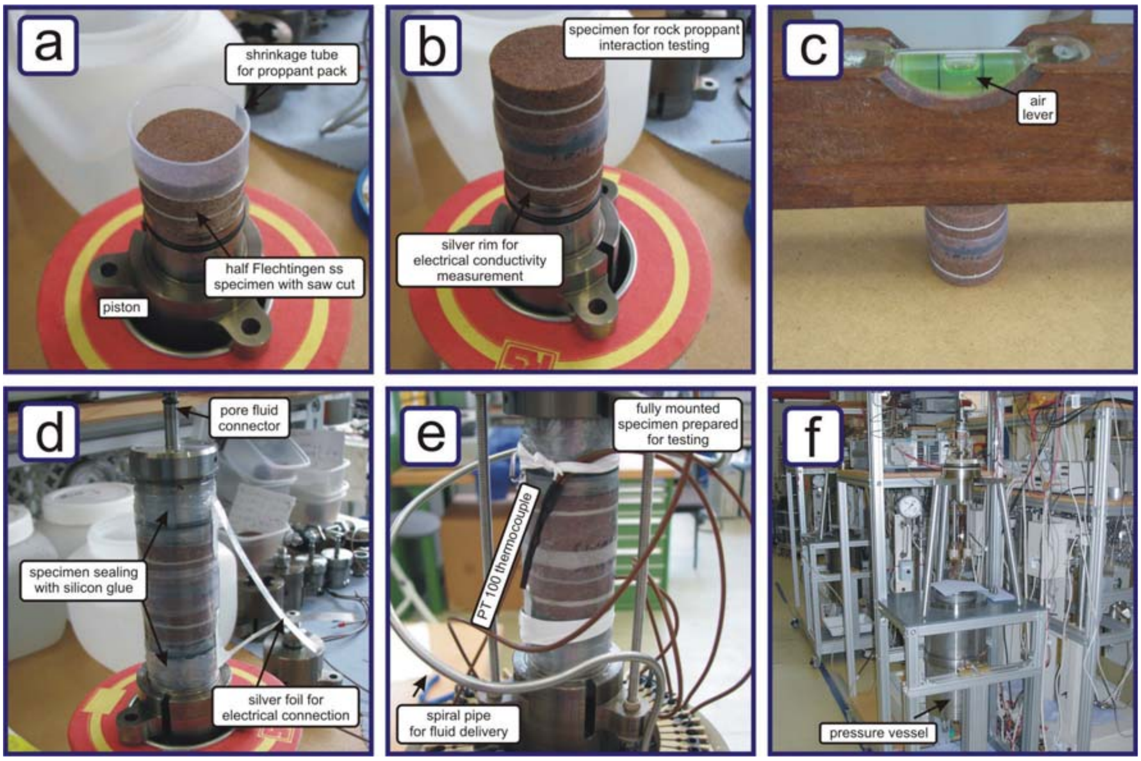
a
shrinkage tube for proppant pack
half Flechtingen ss specimen with saw cut
piston
b
specimen for rock proppant interaction testing
silver rim for electrical conductivity measurement
c
air lever
d
pore fluid connector
specimen sealing with silicon glue
silver foil for electrical connection
e
fully mounted specimen prepared for testing
PT 100 thermocouple
spiral pipe for fluid delivery
f
pressure vessel

Figure 3.10: *Photo collection of preparation and execution of a rock-proppant interaction test with the LTFC. a) the fracture in the Flechtingen core is idealised by a sawed cut; b) the specimen with silver rims and HSP pack; c) levelling of the specimen; d) mounting of top and bottom plug, the specimen is sealed with shrinkage tube and silicon glue; e) a spiral pipe in a oil bath delivers the fluid to the specimen; f) pressure vessel of long-term flow cell.*

3.7 Mercury Intrusion Porosimetry

For mercury intrusion porosimetry experiments, a sample (3-6 g weight) dried in a vacuum oven, is placed in a container (dilatometer), mounted in the Fisons Macropores Unit 120 apparatus and evacuated for at least 15 minutes. Mercury is delivered to the dilatometer to a defined level. Gas pressure is applied stepwise to the mercury column in the capillary and the drop of mercury column is registered. The Macropores Unit is designed for pressures up to 2 bars, the used dilatometer allows an identification of pores < 50 µm. After pressure release the dilatometer is dismounted, weighted and placed in the pressure vessel of Fisons Porosimeter 2000WS. This apparatus applies stepwise an oil pressure up to 2000 bars and measures the volume of displaced mercury automatically. The volume of mercury that intrudes into the pore space due to a pressure increase from P_i to P_{i+1} is equal to the pore volume in the associated size range r_i to r_{i+1}. Pore radii as function of applied pressure are determined by Washburn's equation [Washburn 1921]:

$$r_{p\_HG} = -\frac{2 \cdot \gamma_{HG} \cdot \cos\vartheta_{HG}}{P} \qquad 3.16$$

where γ_{HG} is the surface tension of mercury and ϑ_{HG} is the wetting angle of mercury. The manufacturer gives default values for $\vartheta \cdot_{HG}$ (141.3 °) and γ_{HG} (480 mN/m). Washburn's equation is based on a tube model for pore space. The given pressure range (0 – 2000 bar) yields a tube radii range from 360 µm to 0.004 µm. The design of the utilised dilatometer allows measurements of pore radii to 50 µm.

Beside the radii distribution, the bulk (ρ_{bulk}) and grain density (ρ_g) as well as the interconnected porosity (Φ_{HG}) can be estimated. Derivation of these physical parameters and more about mercury intrusion porosimetry can be found in [Webb 2001].

3.8 2D Image Analysis

2D image analysis of a sandstone thin-section allows a direct determination of total porosity, pore size distribution, pore shape factors and number of pores. Additionally, grain size distributions and grain shape factors can be gained from specially prepared thin section pictures. The digital image analysis is based on the stereological methods extrapolating 3D structures from 2D, fundamentals are given by Underwood [1970]. Two different software packages are adopted: 1. KSRun from Zeiss for pore space analysis and 2. ImageJ [Igathinathane et al. 2008] for grain size determination. The stepwise, semi automatic procedures are explained in detail in the following.

The equivalent pore radius r_{p_opt} is calculated from the pore area A_p:

$$r_{p\_opt}=\sqrt{\frac{A_p}{\pi}} \qquad 3.17$$

Different geometry factors can be achieved from perimeter length. For this investigation, the circularity C is chosen. It is defined as the quotient of two radii, the equivalence radius calculated from area r_{p_opt} and the equivalence radius calculated from perimeter $r_{perimeter}$. This is expressed as a ratio of measured pore area A_P to the area of a circle with the same perimeter l_p.

$$C=\frac{r_{p\_opt}}{r_{perimeter}}=4\pi\frac{A_P}{l_P^2} \qquad 3.18$$

For a perfect circle C is 1, $\pi/4$ for a square, and 0 for a line. The circularity is roughly anti reciprocal to the axis ratio F_E of an ellipse with the same area and the same perimeter as the investigated pore, respectively. For calculation of F_E the equation for area A_E and perimeter P_E of an ellipse are taken into account:

$$A_E=\pi\cdot a\cdot b \qquad 3.19a, \qquad P_E=\sqrt{\pi\cdot a\cdot b} \qquad 3.19b$$

where a and b are the main axis of the ellipse. This leads to the relation between C and F_E:

$$F_E=\frac{1}{C}+\sqrt{1-\frac{1}{C}} \qquad 3.20$$

Additionally, quantities of the pore density D_p and the optical porosity (Φ_{opt}) can be achieved from 2D image analysis. The grain size determination delivers an equivalent grain radius r_{g_opt} calculated from the grain area A_g:

$$r_{g\_opt}=\sqrt{\frac{A_g}{\pi}} \qquad 3.21$$

To correct the grain size as well as the pore size for the statistical unlikelihood of intercepting a grain / pore across its full diameter [Underwood 1970], a correction factor is applied of 3/2 and 2/3, respectively.

3.8.1 Procedure for Pore Space Investigation

A thin section (~30 µm) with blue epoxy is prepared and placed in the Zeiss Axioplan microscope. The blue epoxy guarantees a good contrast between the geo material and the pore space. This microscope is equipped with a digital camera providing a resolution of 1300 x 1030 dots. The software KSrun (Zeiss / Germany) is used for semiautomatic image analysis. A two-step procedure is conducted to tune the KS400 software for an automated image analysis.

- A micrograph from the thin section is taken and a representative area in an epoxy-filled pore is picked. The picking procedure defines hue, light, and saturation (HLS) bands within the spectrum of the micrograph.
- Once the software is tuned, the automated detection procedure analyses the pore space picture by picture. It is important that pores are not analysed twice. The software refuses pores at the image section borders. The detection limit is 31 pixels/pore; resulting in a lower detection limit for the pore area in dependence on the adopted focus. An Excel macro file is programmed to calculate geometric parameters of the pores from the KSRun data.

3.8.2 Procedure for Grain Size Investigation

The grain size determination is conducted with the software package ImageJ [Igathinathane et al. 2008] comparable to the two-step procedure for pore space investigation. The software ImageJ allows a quick and accurate particle size analysis from any picture. Several micrographs from a thin section are created and the grains are manually separated along the grain boundaries with image processing software. Binary pictures are created by reducing the colour depth from RGB to black-and-white. A reasonable threshold between black and white has to be chosen.

- The dimensions of a micrograph are defined in ImageJ. The automated analysis creates a data file with geometric parameters of the grains (area, perimeter, minimum and maximum feret). The procedure is repeated for all micrographs. The lower detection limit is set to 4 pixels.
- The data files are imported into an Excel sheet and a macro is used to estimate geometric parameters of the grains.

4 Characterisation of Sandstones and Proppants

4.1 *Mineralogy of Bentheim and Flechtingen Sandstone*

4.1.1 Bentheim Sandstone

The Bentheim sandstone (Gildehaus quarry, Germany) is a Lower Cretaceous, homogeneous, yellow sandstone containing 94 % quartz, 5 % feldspar, and about 1 % mica (figure 4.1). The mineralogical composition is determined by point counting the minerals in a thin section using a microscope. 300 points are evaluated. For each mineral identification, the thin section is shifted by an equidistant step, assuring that no grain is counted twice. Quartz grains were found to be subrounded to subangular (figure 4.2a).

The mineralogical composition is in accordance with the mineralogy given by Klein & Reuschlè [2003]. Their Bentheim sandstone specimens contain 95 % quartz, 3 % feldspar, and 2 % kaolinite. In the current thin section analysis, no kaolinite is found although macroscopic kaolinite lenses are present in the samples. This is caused by three reasons:

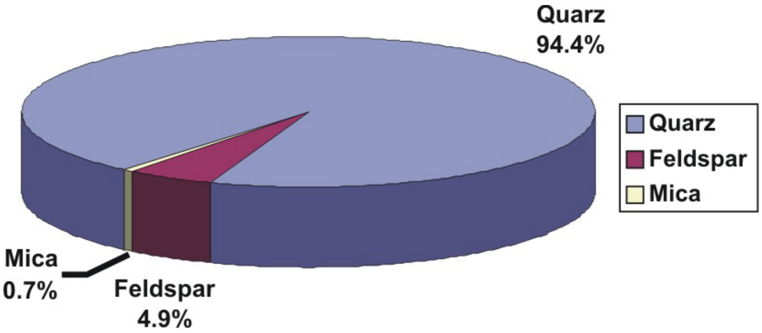

Figure 4.1: *Mineral composition of Bentheim sandstone as determined by point counting*

1. The composition of Bentheim sandstone likely varies between different sampling locations.
2. During thin section preparation including drilling, cleaning, cutting, and saturating with epoxy kaolinite minerals get mobilised and are rinsed out.
3. The accuracy of this statistical counting method is strongly dependent on the sample size. 300 points might be too few and a small mineral phase is missed.

4.1.2 Flechtingen Sandstone

The Flechtingen Bausandstein (Sventesius quarry, Germany) is a lower Permian (Rotliegend), well consolidated, well sorted, cross bedded, and fine grained sandstone with a permeability in the range of µD to mD. Grains were found to be rounded to subrounded (compare to figure 4.2c). The sample contains 59 % quartz, 8 % feldspar, 6 % kaolinite, 5 % rock fragments, and about 20 % of cement (figure 4.3). The rock fragments consist of quartz, siltstone, and mudstone. A detailed cement composition is not specified in this study, but quartzeus, kaolinic, argillaceous, and ferritic cement is detected.

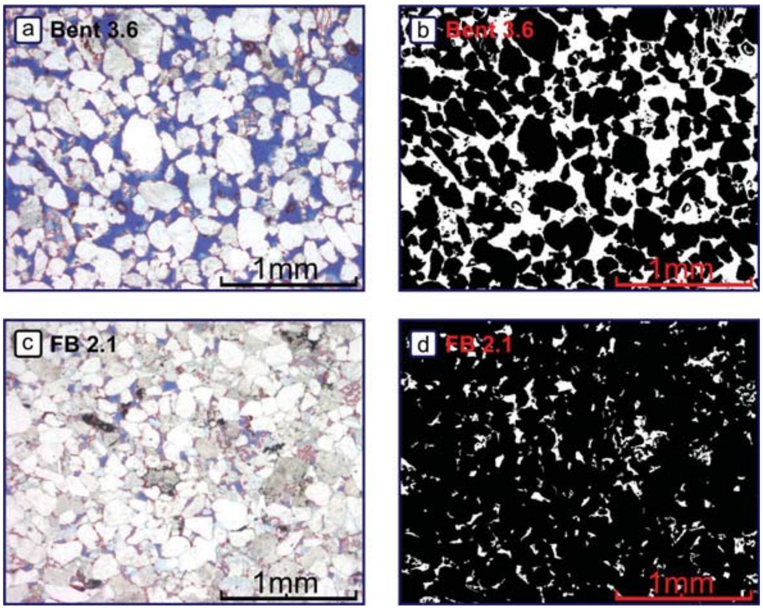

Figure 4.2: *Micrographs and binary pictures of Bentheim and Flechtingen sandstone*

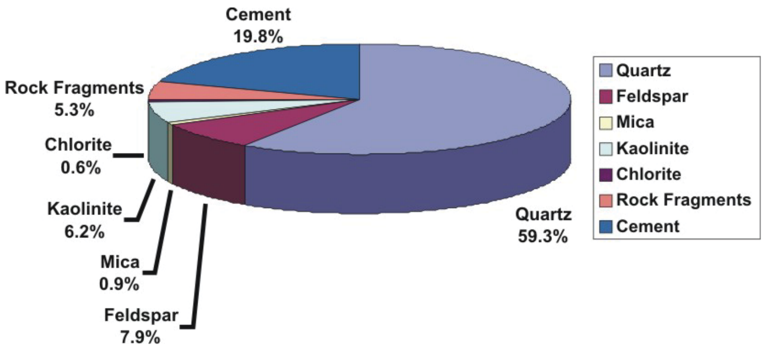

Figure 4.3: *Mineral composition of Flechtingen sandstone as determined by point counting*

Trautwein [2005] has analysed Rotliegend sandstones cores taken from the geothermal research well Groß Schönebeck EGrSk3/90. In the study of Trautwein, quartz, feldspar, carbonate, illit, and ferric oxide are identified as the main minerals in the cement composition. The argillaceous-ferritic oxide crusts are coating the grains and giving the typical red colour of that rock. The cement contains about 9 %illite. The results of Trautwein [2005] cannot be compared directly with the investigation of this work, because the Flechtingen Bausandstein is taken from a different location. In addition, the mineral composition may differ due to mineral alterations.

4.2 Proppant Material

Two kinds of proppants are used in this study: 1) intermediate strength proppants (ISP) made from fused ceramics with 20/40 mesh size (proppant particle diameter: 0.4 – 0.8 mm), bulk density is 1570 kg/m³, d_{50} is about 760 µm. 2) High strength proppants (HSP) composed of sintered bauxite with 20/40 mesh, bulk density is 2000 kg/m³, d_{50} is about 700 µm. The permeabilities of both proppant types as function of the fracture closing stress in a proppant flow cell are given in figure 4.4a. Data in figure 4.4a are adopted from manufacturer's data sheet. The fracture closure stress describes the effective stress acting on the fracture faces. Both proppants types are well rounded; figure 4.4b shows exemplarily a micrograph of an unloaded ISP pack.

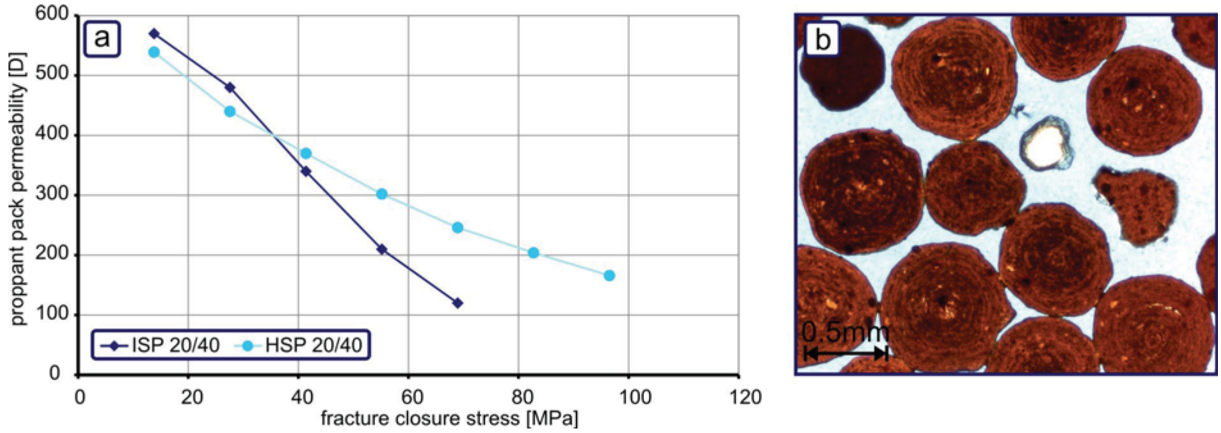

Figure 4.4: *a) Fracture closure stress dependence of proppant permeability. ISP: intermediate strength proppant; HSP: high strength proppants. 20/40 mesh size corresponds to a diameter of 0.4 – 0.8 mm. b) Micrograph of an ISP pack*

proppant type	**HSP**		**ISP**	
	compounds	[weight %]	compounds	[weight %]
chemistry	Al_2O_3	83	Al_2O_3	51
	SiO_2	5	SiO_2	45
	TiO_2	3.5	TiO_2	2
	Fe_2O_3	7	Fe_2O_3	1
	Other	1.5	Other	1

Table 4.1: *Chemical compounds of HSP and ISP (taken from manufacturer's data sheet).*

4.3 Microstructural Analysis

Two different methods are applied to the Bentheim and Flechtingen sandstone sample in order to determine the pore and grain size distribution: Mercury intrusion porosimetry and 2D Image analysis (compare to §3.7 and §3.8). Mercury intrusion porosimetry method enables an identification of geometric properties of the connected 3D pore space. With image analysis, a 2D cut of the 3D system of the pore space is investigated. With this method, the interconnected pore space and the trapped pore space are identified in addition.

4.3.1 Pore and Grain Size Distribution of Bentheim and Flechtingen Sandstone

Thin sections of Bentheim and Flechingen sandstone samples are investigated for pore and grain size distribution as well as circularity of pores. In addition, the results from mercury injection methods are given in the same plots. As an example, a Bentheim and a Flechtingen sandstone are presented in figure 4.5. For pore and grain size characterization, intervals of different parameters are listed in table 4.2. The grain size analysis is conducted for the Bentheim sandstone exclusively; it was tried for Flechtingen sandstone, but cementation is too high to separate grains from pores effectively.

The 2D image analysis is a statistical method and the accuracy is strongly dependent on size of the random sample. Table 4.2 gives an overview over minimum and maximum number of pores and grains per thin section, which have been investigated in the study at hand.

	Bentheim sandstone	Bentheim sandstone	Flechtingen sandstone
	pores	grains	pores
number of pores / grains	8267 - 17987	6660 - 7561	12410 - 37496
number of micrographs	81 - 132	41	58 - 81
lower detection limit (circular pores)	5.3 µm / 31 pixels	0.58 µm / 4 pixels	1.4 µm / 31 pixels

Table 4.2: *number of pores, micrographs and lower detection limits for 2D optical grain and pore size investigation.*

Figure 4.5 shows the pore and grain size determined by 2D scanning method (blue and pink curve) and the pore size distribution gained from mercury porosity (red curve). The Bentheim sandstone has a total optical porosity of about 20 – 22 %. The total porosity of Flechtingen sandstone ranges from 8 – 11 %. The difference to the mercury method is 1 – 3 %.

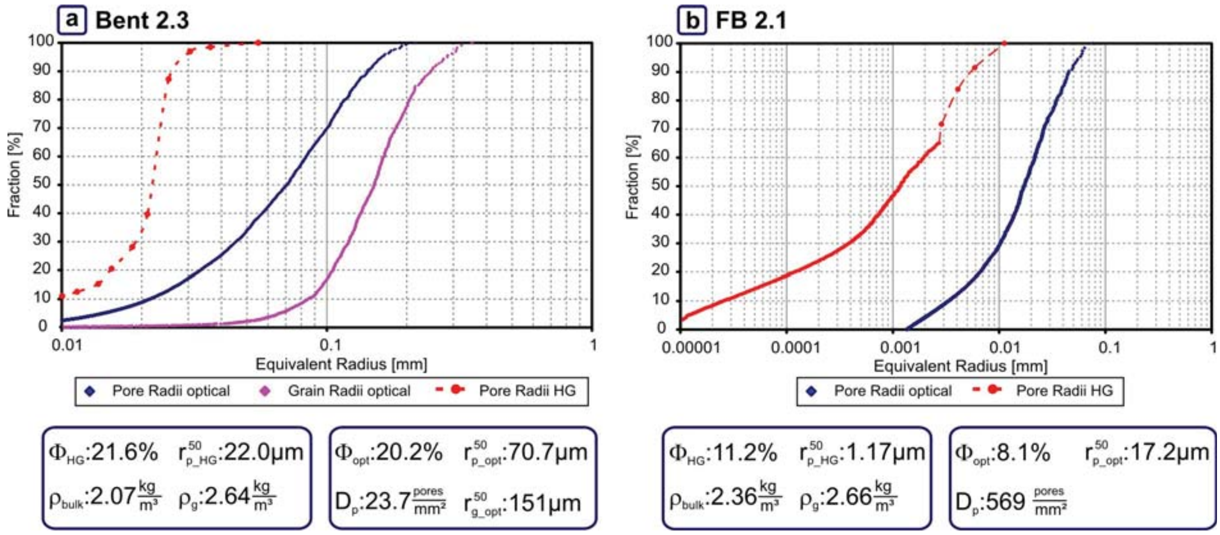

Figure 4.5*: Pore and grain size distributions of Bentheim and Flechtingen sandstone determined with 2D optical scanning method (opt) and mercury intrusion porosimetry (HG). The pore size distribution determined with 2D optical scanning method (dark blue curve) and mercury intrusion porosity (red curve) differ significantly. The distribution of the latter one is shifted to smaller radii. The Flechtingen rock has a smaller porosity and a smaller mean pore size compared to Bentheim rock. Refer to table 4.3 for description of the symbols.*

Concerning the pore size distribution, an obvious difference between optical and mercury investigation is observed. The discrepancy is in the order of one magnitude for Bentheim sandstone and up to two orders of magnitude for Flechtingen sandstone. The Bentheim sandstone has optically determined pore sizes from 5 – 300 µm (figure 4.5a). The mercury intrusion method delivers a range from 0.02 – 50 µm. The values from lower detection boundaries of both methods are not shown in figure 4.5.

The optical pore size distribution from Flechtingen sandstone varies from 1.5 – 110 µm whereas the mercury method gives a range from 0.004 –14 µm. These differences are reflected in the average pore radii, which are determined at 50 % of pore size distribution. The average optical pore size $r^{50}_{p\_opt}$ is ~ 100 µm for Bentheim rock and ~ 20 µm for Flechtingen rock. The mercury method delivers an average value of 24 µm for Bentheim sandstone and 0.8 µm for Flechtingen sandstone. These large differences between the both detection methods can be found by other authors as well [Blöcher et al. 2007]. This discrepancy can be explained by two effects based on the resolution (1) and the pore shape (2).

1. The 2D image analysis has an upper and lower detection boundary. The lower boundary is given by the size of a pixel or a cluster of pixels, which is defined as smallest pore. The upper boundary is the size of one micrograph or the area of all pixels in one micrograph, respectively. Hence, the resolution of 2D image analysis is limited to a bandwidth of two orders of magnitude if the magnification is fixed. Very small pores are ignored usually leading to a shift of the pore size distribution to larger radii.

   The Flechtingen sandstone has a large amount of small pores as well as some large pores; both pore sizes are neglected in the 2D analysis. Hence, the optical pore size distributions in figure 4.5b do not show the classical s-shape; the curves are cut at lower and upper boundaries. The Bentheim specimen (figure 4.5a) possesses a small amount of small pores; therefore, the classical s-shape is better resolved. The upper boundary of pores size distributions are cut as well.

   The mercury intrusion porosimetry provides a detection range of 5 nm and 50 µm – four decades. The lower boundary is given by the maximum pressure of the testing machine and the upper boundary is defined by the minimum mercury column above the sample at ambient pressure. Hence, the small pores are enclosed in this investigation and the large pores are neglected. Due to the large detection range, the typical s-shape can be recognized in the red curves (figure 4.5b). The Bentheim curves consist of the low pressure part of the Macropores Unit only, since this rock contains very small amount of pores < 10 µm. The typical s-shape is reproduced well. The Flechtingen curve is composed of Macropores Unit data and Porosimeter 2000WS data. In the transition zone, the curves exhibit unsteady behaviour.

2. The shape of pores has a large influence on the mercury intrusion method, since the analysis is based on a tube model for pore space. In sandstone, the interconnected pore space is composed of tube-like, sheet-like and nodal pores [Bernabe 1991]. Reverberi et al. [1966] described these sandstone pores as inkwells. An inkwell pore is filled with mercury when the pressure overcomes the small diameter of the opening. Hence, mercury intrusion porosimetry shifts the pore radii distribution to smaller diameters. The shift is dependent on the ratio between throat radii to pore cavity radii; a larger ratio leads to a larger shift.

In addition, grain radii distributions are determined from Bentheim rock micrographs (pink curve in figure 4.5a). The grain radii extend from 30 – 300 µm. The radii distributions have the classical s-shape; hence, the majority of grains are covered with this analysis. The average optical grain radii $r^{50}_{r\_opt}$ vary from 150 – 200 µm (determined at 50 % of grain radii distribution). Schutjens et al. [1995] identified grain sizes in the same range for Bentheim sandstone.

method	parameter	symbol	unit	Bentheim sandstone	Flechtingen sandstone
mercury intrusion porosimetry	porosity	Φ_{HG}	%	21.3 -22.6	9.3 – 11.2
	mean pore radii	$r^{50}_{p\_HG}$	µm	17 - 22	0. 46 – 1.17
	bulk density	ρ_{bulk}	kg/m³	2.06	2.26 – 2.42
	grain density	ρ_g	kg/m³	2.65	2.66
2D image analysis	porosity	Φ_{opt}	%	20.2 – 22.7	8.1 – 10.9
	mean pore radii	$r^{50}_{p\_opt}$	µm	70 - 126	17 - 36
	mean grain radii	$r^{50}_{g\_opt}$	µm	151 - 197	- / -
	pore density	D_P	pores/mm²	17.8 – 23.7	570 - 1230

Table 4.3: *Parameters for characterisation of Bentheim and Flechtingen rock. The Bentheim rock has a higher porosity and a larger mean pore size compared to Flechtingen rock. In contrast, the Flechtingen rock has significantly more pores per mm². The two methods – mercury intrusion porosimetry and 2D image analysis – show a large difference in mean pore radii. This difference reflects the ratio between pore throat radius and pore cavity radius.*

With regard to the micrographs shown in figure 4.2a-d, it is obvious that the 2D optical scanning method delivers more accurate results for the two sandstone types. Visually one can approximate that the blue epoxy filled pores of the Bentheim sample (figure 4.2a) have diameters in the range of 10 – 300 µm. Figure 4.2b illustrates the pore space in this rock as a binary picture. The Flechtingen sandstone in figure 4.5b shows pores in the range 1 – 100 µm. The average pore sizes measured with mercury injection is 5 (Bentheim sandstone) to 30 (Flechtingen sandstone) times smaller than the average pore sizes determined with 2D image analysis. The tube pore model employed by the Washburn's equation [Washburn 1921, Webb 2001] is an inappropriate simplification for these sandstone types. The mercury intrusion porosimetry delivers the distribution of pore throats, which expose the fluid transport properties of a rock. The factors of 5 (Bentheim sandstone) and 30 (Flechtingen sandstone) between the two methods lead to the conclusion that the ratio between pore throat radii to pore cavity radii [Reverberi et al. 1966] is larger for Flechtingen sandstone. The mercury injection method emphasises the pore throats that control the fluid transport. Hence, the factors between both methods indicate the pore network of Bentheim sandstone is better connected compared to the Flechtingen sandstone; the Flechtingen sandstone shows a poorer connectivity. Trautwein & Huenges [2003] analysed Rotliegend sandstone cores from the geothermal research well EGrSk3/90 and found similar large shifts between optical and mercury method.

Both methods highlight that the Flechtingen rock has a wider pore size range. This finding is pronounced in the mercury intrusion porosimetry observations where the Flechtingen samples exhibit a range over 4 decades. Hence, the Flechtingen sandstone pores show a more heterogeneous distribution compared to Bentheim sandstone pores.

Another parameter, which highlights large differences between both rock types, is the 2D pore density D_p. For Bentheim sandstone the pore density correlates clearly with the average pore radius. With decreasing pore radii an increase of D_p is observed. The Bentheim sandstone has 18 – 24 pores/mm². Klein & Reuschlé [2003] detected 21 pores/mm² analysing Bentheim rock thin sections.

In contrast, the Flechtingen sandstone shows the large amount of 570 – 1230 pores/mm² and the correlation with the pore radius is less significant.

The pore geometry of both sandstone types is compared in figure 4.6a&b. The circularity C as well as the axis ratio of an ellipse F_E is plotted as a function of equivalent radius. Since the F_E is nearly the reciprocal of C both values are displayed in the same figure; the axis for F_E is plotted in reverse order.

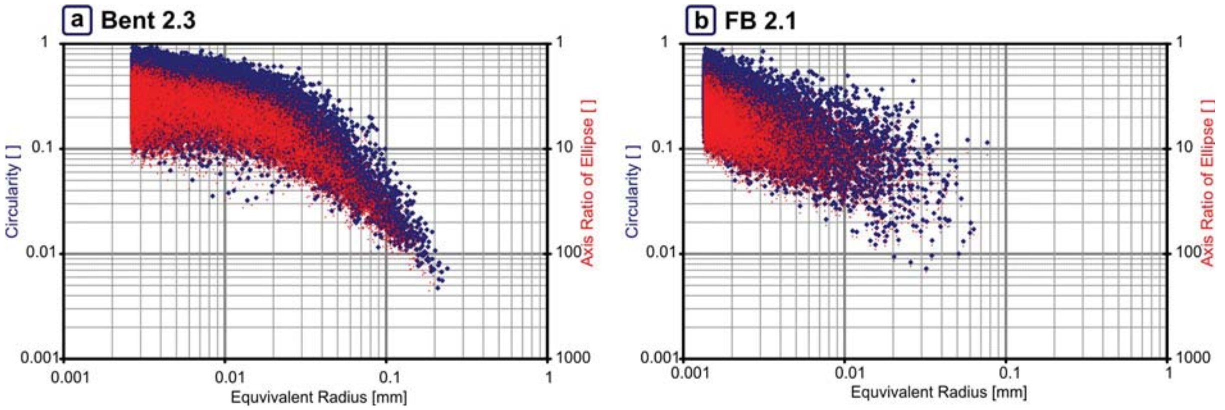

Figure 4.6*: Circularity ratio and axis ratio of ellipse for Bentheim and Flechtingen sandstone calculated from 2D image analysis. In contrast to the Flechtingen rock, the circularity ratio of Bentheim rock is split in two parts: 1) A large amount of small pores is distributed over a circularity range 0.1 - 1. 2) A fraction of pores with large radii exists that shows a drastic decrease of circularity. A circularity of one describes a perfect spherical pore. The axis ratio, calculated from an elliptical pore model, mirrors this trend. The circularity of Flechtingen pores decreases uniformly with the radius.*

For radii smaller than 30 µm no significant differences between Bentheim and Flechtingen sandstone can be observed. The circularity varies between 1 and 0.05. The axis ratio is given within the limits of 3 and 50. With increasing pore radius, the circularity of both rock types decreases. For pores larger than 30 µm the Bentheim specimen shows a trend to more irregular shape. In contrast to the Flechtingen samples, the pore space distribution is split in two parts: smaller pores are well rounded and larger pores show a significant decrease of circularity with size. The axis ratio feature the same trend, the Bentheim rock has large pores with a high aspect ratio from 10 to 100.

The differences between Bentheim and Flechtingen pore shape are highlighted in figure 4.7 where the fraction of pore space is plotted as function of the circularity. For this purpose, the pore area from 2D analysis is sorted by its circularity and a cumulative curve of pore space is computed. Data from three Bentheim specimens (green curves) and three Flechtingen specimens (blue curves) are shown. For instance, at fraction of 50 % the Bentheim circularities are in the range of 0.015 – 0.042 whereas the Flechtingen samples have circularities in the range of 0.046 – 0.084. For the same fraction of pore area the Bentheim sandstone features pores with up to 6 times larger perimeters compared to the Flechtingen sandstone.

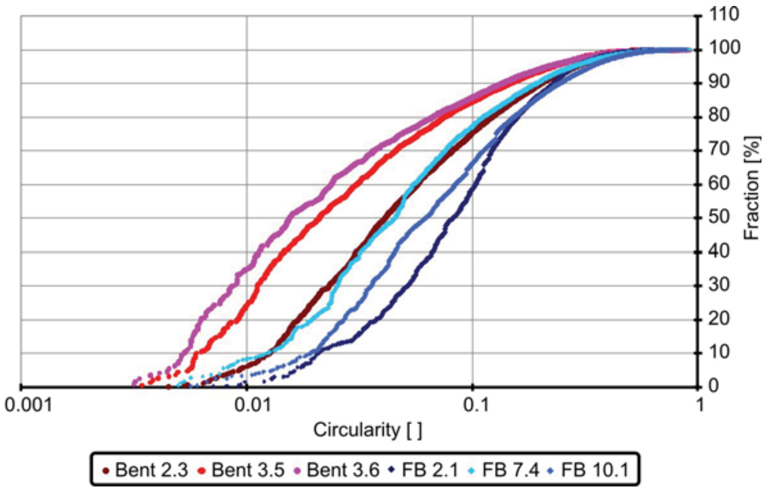

Figure 4.7: *Cumulative pore space of Bentheim and Flechtingen sandstone as function of circularity. The Bentheim pores (red colours) show a smaller circularity at the same fraction of pore space compared to the Flechtingen pores (blue colours). Hence, the Bentheim pores are less spherical.*

In summary, the Flechtingen sandstone has a larger amount of small pores with a less irregular shape and with larger circularities compared to the Bentheim sandstone. The pore shape distribution of Bentheim rock is split in two parts; a fraction of large pores with highly irregular shape exists.

5 Experimental Results

The following chapter presents the results and discussion of experiments conducted for the rock-proppant interaction (RPI) analyses. This chapter is subdivided into five sections:

§5.1: Mechanical and Hydraulic Characterisation of Bentheim and Flechtingen sandstone. The sandstones are characterised by means of permeability, pressure dependence of permeability, Young's modulus and Mohr-Coulomb type brittle failure. Understanding the stress induced alterations of rock structure and permeability is crucial for the subsequent RPI experiments with these rock types.

§5.2: Discussion of Mechanical and Hydraulic Characterisation of Bentheim and Flechtingen sandstone

§5.3: Rock-Proppant Interaction Testing: Acoustic Emission Flow Cell. The AEFC is used to identify and localise the damage at the rock-proppant interface and in the proppant pack in-situ during test execution.

§5.4: Rock-Proppant Interaction Testing: Bidirectional Flow Cell. The BDFC was developed to simulate the geometric flow conditions in a reservoir intersected by a fracture (compare to figure 1.1). Experiments with the BDFC are conducted to quantify the permeability alteration due to mechanical interaction of rock and proppants at the fracture face and within the proppant pack.

§5.5: Rock-Proppant Interaction Testing: Long-term Flow Cell. The goal of long-term investigations of rock-proppant systems is to analyse physical effects of long-term production from a geothermal reservoir. Experiments at realistic in-situ conditions are indispensable. This includes the continuous transport of fluid through the rock and the rock-proppant interface, at reservoir temperature and pressure.

The type of experiment presented in the following sections and the used flow cells are listed in table 5.1.

specimen name	type of experiment	flow cell	specimen name	type of experiment	flow cell
Bent 1.1	shear	AEFC	Bent 3.4	RPI	BDFC
Bent 1.2	shear	AEFC	Bent 3.5	RPI	BDFC
Bent 1.3	shear	AEFC	Bent 3.6	k/E	BDFC
Bent 1.4	k/E	AEFC	Bent 4.14	UCS	- / -
Bent 1.5	k/E	AEFC	Bent 4.17	UCS	- / -
Bent 1.6	k/E	AEFC	FB 1.5	k/E	BDFC
Bent S1	shear	AEFC	FB 1.6	RPI	AEFC
Bent S2	shear	AEFC	FB 2.1	RPI	BDFC
Bent S3	shear	AEFC	FB 7.4	RPI	BDFC
Bent 2.2	RPI	AEFC	FB 10.1	k	LTFC
Bent 2.3	RPI	AEFC	FB 10.2	RPI	LTFC
Bent 3.1	RPI	BDFC	FB 10.3	RPI	LTFC

Table 5.1: *List of all experiments of the present study conducted with Bentheim and Flechtingen sandstone. k/E: determination of permeability and/or Young's modulus; UCS: uniaxial compression experiment; shear: triaxial shear experiment; RPI: rock-proppant interaction experiment*

The experiments are conducted with three pore fluids (KCl brine, NaCl brine, pure water) for the following reasons.

- KCL brine is a standard that is used in a variety of permeability studies, in particular in oil industry related research [Civan 2000]. The KCl brine can stabilise the clay minerals to avoid a permeability alteration. The stabilisation is dependent on the salt content [Rahman et al. 1995] and can be up to 10 % for clay sensitive formations [Lynn & Nasr-El-Din 1998]. KCl brine is corrosive and if traces of oxygen are present in the fluid, the setup can corrode and the fines from corrosion can influence the permeability measurement.
- NaCl brine is used in the LTFC. The concentration is about 0.5 % (0.1 molar). Electrical conductivity measurements of the fluid saturated rock are conducted with this setup. In order to exclude effects of the electrical surface conductivity and to determine the electrical properties of the pore space, a small salinity of the fluid is necessary [Milsch et al. 2008].
- The advantage of pure (demineralised) water is that this fluid shows no corrosion effects in the setup. However, it has a significant influence on the permeability of clay bearing rocks. The permeability decreases due to chemical fluid-rock interactions. In general, the permeability stabilises on a defined level after a sufficient time.

  Fluids with very low mineral content like the demineralised water used for permeability testing can induce permeability reductions due to the electrochemical interactions between the negative charges at the rock surface and the ions and water dipoles. Three effects play a role: steaming potential, Stern potential, and the surface conductivity. Preiss [2000] investigated the influence of these effects on the permeability of sandstones numerically and experimentally. Sandstones with a permeability range of 100 µD – 8 D were tested with different pore fluids with salinities of 10^{-1} – 10^{-5} mol/l. The numerical studies show that a combination of the three electrochemical effects reveals a maximum permeability reduction of 5 % within a pore radius interval typical for sandstones. This predicted reduction was not measurable in the conducted laboratory experiments; the fluid salinity reduction results in no influence on permeability. The influence of electrochemical effects is limited to small pore radii; these small pores make only a minor contribution to the overall flow. The fluid follows the way of least resistance through the rock pore space, i.e. the fluid is transported predominantly though the large pore radii with high permeability. Hence, the influence of electrochemical interactions between the demineralised water and the rock are negligible for the rock-proppant interaction experiments.

5.1 Mechanical and Hydraulic Characterisation of Bentheim Sandstone and Flechtingen Sandstone

5.1.1 Compaction and Failure of Bentheim Sandstone: Acoustic Emission and Permeability Evolution

Three triaxial deformation experiments with Bentheim sandstone samples equipped with 12 PZTs are conducted in the AEFC. Vertical and horizontal strain is measured with strain gages. The p-wave velocity is measured in vertical (v_{p_vert}) and in horizontal (v_{p_hor}) directions. Loading is stopped in displacement mode at defined stress levels, and the permeability is determined. In experiment Bent 1.3, the stress was cycled in order to analyse the influence of ongoing microstructural changes on the mechanical behaviour of Bentheim rock. After rock failure, permeability measurement is continued in order to analyse the influence of the produced fines in a shear band. The testing parameters are listed in table 5.2. A malfunction of the AE system in experiment Bent 1.1 incurs the loss of AE data.

	Bent 1.1	**Bent 1.2**	**Bent 1.3**
specimen length	100 mm	100 mm	100 mm
strain rate	10.0 10^{-6} s^{-1}	10.0 10^{-6} s^{-1}	10.0 10^{-6} s^{-1}
diff. stress	0 - 109 MPa	0 - 103 MPa	0 - 142 MPa
conf. pressure	10 MPa	20 MPa	10 MPa
flow rate	35 ml/min	- / -	60 ml/min
mean pore pressure	0.13 – 0.23 MPa	- / -	0.15 – 0.22 MPa

Table 5.2.: *Testing parameters for triaxial compression experiment with Bentheim sandstone.*

Figure 5.1 shows the stress-strain behaviour of specimen Bent 1.1, Bent 1.2 and Bent 1.3. In addition, the Young’s modulus is plotted. The different stages of a triaxial deformation experiment can be seen in these curves: Under increasing differential stress, rocks first exhibit elastic deformation, as indicated by the linear portion of the axial strain curve. The onset of dilatancy (yield point) is defined as the point of inflexion to decreasing volumetric strain. The yield point is marked by large red dots in figure 5.1 and is taking place between 75% and 90% of peak strength. During this phase, the axial stress-strain curve of experiment Bent 1.1 and Bent 1.2 is still linear (indicating elastic deformation), although the dilatant volumetric strain curve indicates stable crack growth. A sharp decrease of differential stress in the post-peak region indicates the failure of the rock accompanied by a development of a shear band.

A significant permeability reduction after rock failure is recorded. Comparing the pre-peak to post-peak permeability, experiment Bent 1.1 shows a permeability reduction by a factor of 10 and experiment Bent 1.3 by a factor of 1.5, respectively (figure 5.2). A reactivation of the shear zone leads to a further permeability reduction. During permeability measurement at constant displacement, stress relaxation is observed due to ongoing microstructural changes within the sample (figure 5.1).

Prior to the yield point, the Young’s modulus (E) shows only minor variations (figure5.1a-c). A slight increase of E can be observed between first and second loading step. E of Bentheim sandstone is about 22 GPa. Above the yield point, a considerable decrease of E is observed. The decrease is accompanied by a decrease of vertical and horizontal p-wave velocity (figure5.3a&b). Blue dashed lines in figure 5.3 indicate the pre-failure, post-failure, and reactivation stage of experiment Bent 1.2 and Bent 1.3. The stress cycling during experiment Bent 1.3 above the yield point shows that the ongoing inelastic rock deformation has no influence on the Young’s modulus of the reloading stage (figure 5.1b).

The p-wave velocities (v_{p_vert} and v_{p_hor}) increase during isostatic loading of Bentheim sandstone (13 % for Bent 1.2 and 4 % for Bent 1.3). The initial p-wave velocity (figure 5.3) is 3.75 km/s for Bent 1.3 and 3.74 km/s for Bent 1.2, respectively.

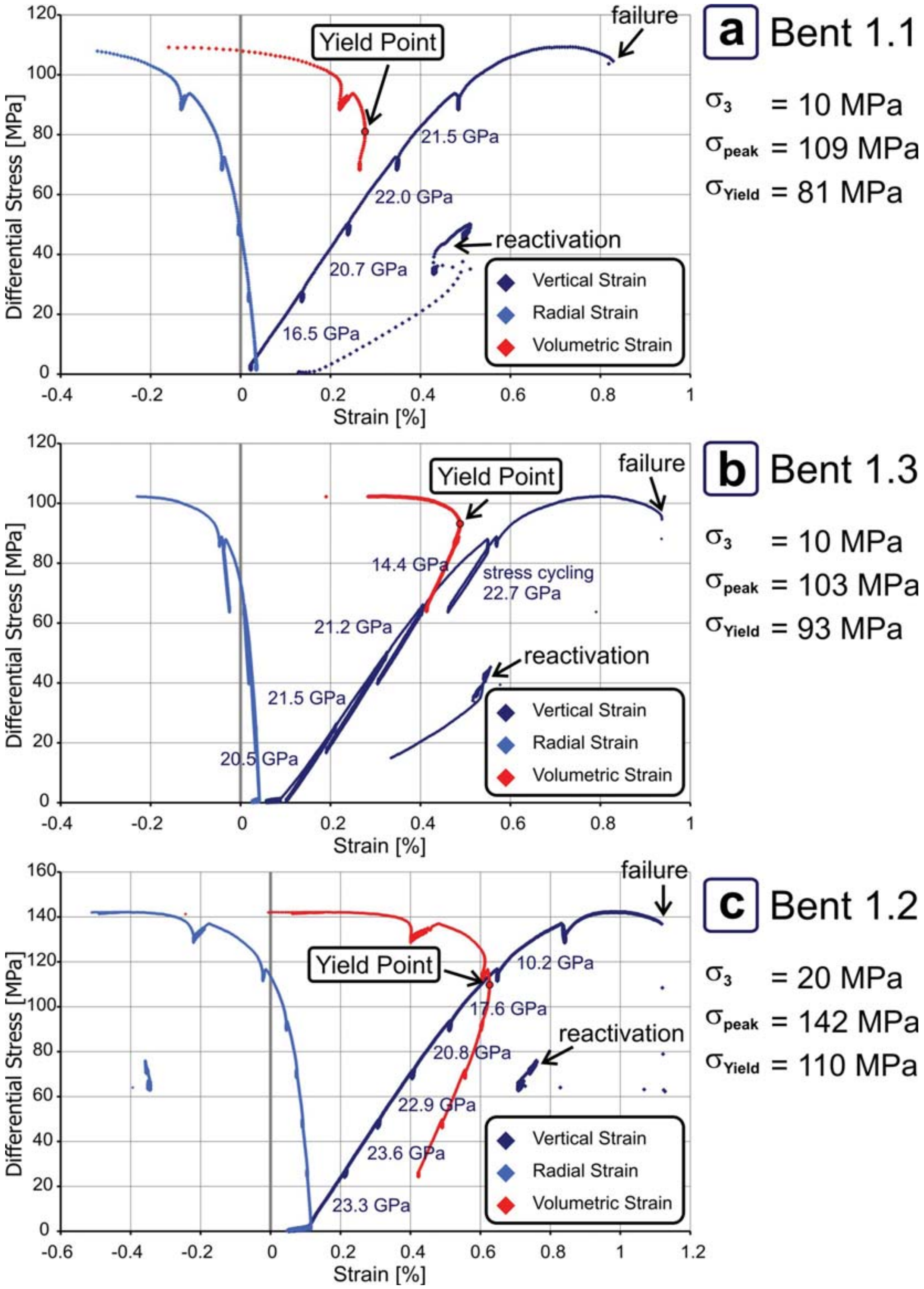

***Figure 5.1**: Stress-strain behaviour of triaxially loaded Bentheim sandstone. Three Bentheim sandstone samples were traixially loaded with confining pressure (σ_3) of 10 MPa and 20 MPa. The differential stress reaches a maximum followed by macroscopic failure of the rock specimen. Peak stress (σ_{peak}) increases with increasing σ_3. Hence, the Bentheim sandstone shows a Mohr-Coulomb type of failure. The onset of dilatancy (yield point, σ_{Yield}) is marked with large red dots. The yield stress is reached at 75 % - 90 % of σ_{peak}. The Young's modulus (dark blue numbers) shows minor variation below the yield point and decreases above the yield point. Near to failure, the volumetric strain crosses the zero line.*

Prior to failure, no change in v_{p_vert} is detected (figure 5.3) for Bent 1.3. In contrast, v_{p_hor} mirrors every loading and unloading cycle of this experiment. During compaction of Bent 1.2, an increase of v_{p_vert} in the first two loading cycles is observed (about 3 %). Already the forth loading cycle up to σ_{diff} = 90 MPa leads to a decrease of 0.5 %, which correlates with a reduction of E. A further reduction of v_{p_hor} (4.5 %) is observed at 60 % of the peak stress.

The horizontal and vertical p-wave velocities of both experiments are significantly reduced during failure. The reduction is about 5 % for v_{p_vert} and 23 – 30 % for v_{p_hor}.

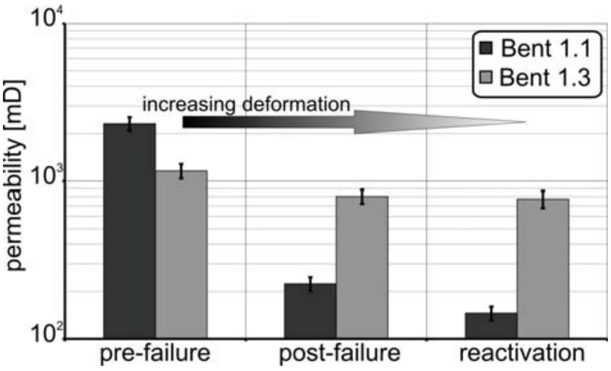

***Figure 5.2**: Permeability reduction during triaxial compaction of Bentheim sandstone.*

5.1.2 AE Hypocenter Locations

The hypocenters of AE events from Bent 1.3 are plotted in figure 5.4a, separated into three loading stages. Up to 70 % of peak stress, only a few randomly distributed AE events are located in the specimen. In general, the total number of events (258) before failure is small. In contrast, the nucleation of the shear zone leads to a change in the AE pattern from randomly distributed to a more organised and localised pattern. The AE activity is reduced near the ends of the specimen due to lower stress caused by lateral support of the steel plugs [Lockner 1993].

The shear zone AE pattern has an extent in the zx-plane of 12 mm (figure 5.4). The shear angle is 28° from σ_1-axis. The reactivation of the shear zone leads to abundant highly localised events along the shear plane. The number of T-type events increases, and the S-type events decrease.

Figure 5.4b shows the three stages of Bent 1.2 experiment. The distribution of AE event hypocenters is comparable to Bent 1.3, in general. Up to almost 80 % of the peak stress, no nucleation zone is visible. The hypocenters are oriented at the specimen end faces and around the brass housings of the PZT. Obviously, these events are generated artificially by the setup. The grooves for fluid distribution embedded in the pistons lead to stress concentration at the end faces of the specimen. The accumulation of AE events around the brass housing might be an effect of compaction of some remaining air bubbles in the glue, which is used to fix the housings. Edge cracking at the brass housings on the rock surface is another possible explanation for this observation. Most events are of C-type (green dots).

With increasing stress, a nucleation of AE locations adjacent to the shear zone takes place, but the number of events is small compared to experiment Bent 1.3, and no clear localisation of the shear zone is possible in the failure stage pf experiment Bent 1.2. A change in first motion polarities from C-type to S- and T-type is observed. The shear angle is 31°. In contrast to the nucleation phase, the shear fracture reactivation is accompanied by a localised AE pattern.

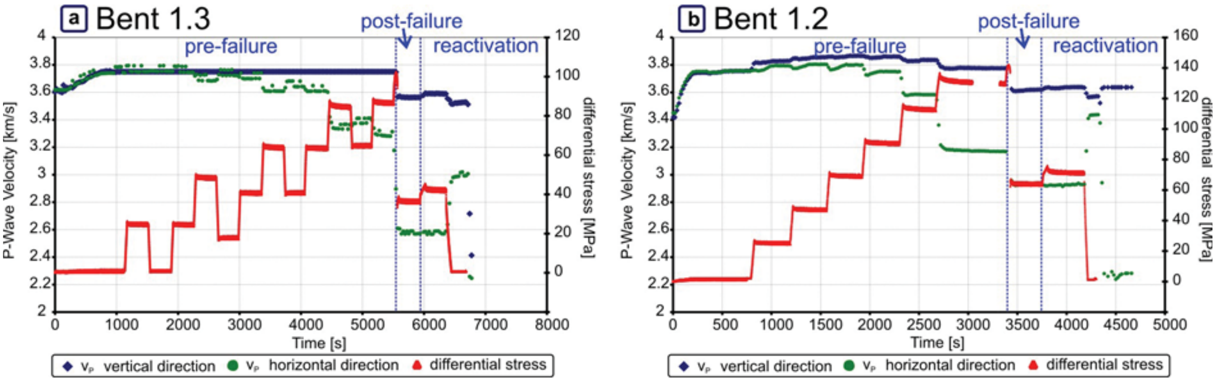

***Figure 5.3**: Vertical and horizontal p-wave velocity as function of time and differential stress. The blue dashed lines indicate the three stages of the experiments: pre-failure, post-failure and reactivation of the shear zone. A malfunction of the AE system in experiment Bent 1.1 incurs the loss of ultrasonic transmission data. The onset of dilatency is accompanied by a clear reduction of horizontal p-wave velocity (green curve). This is an indication for an increase of crack density in the loaded specimen. The loading was cycled (figure a / red curve) in experiment Bent 1.3 in order to identify alteration of Young's modulus due to inelastic compaction of Bentheim rock. At defined stress levels, the loading was stopped in displacement mode for permeability determination.*

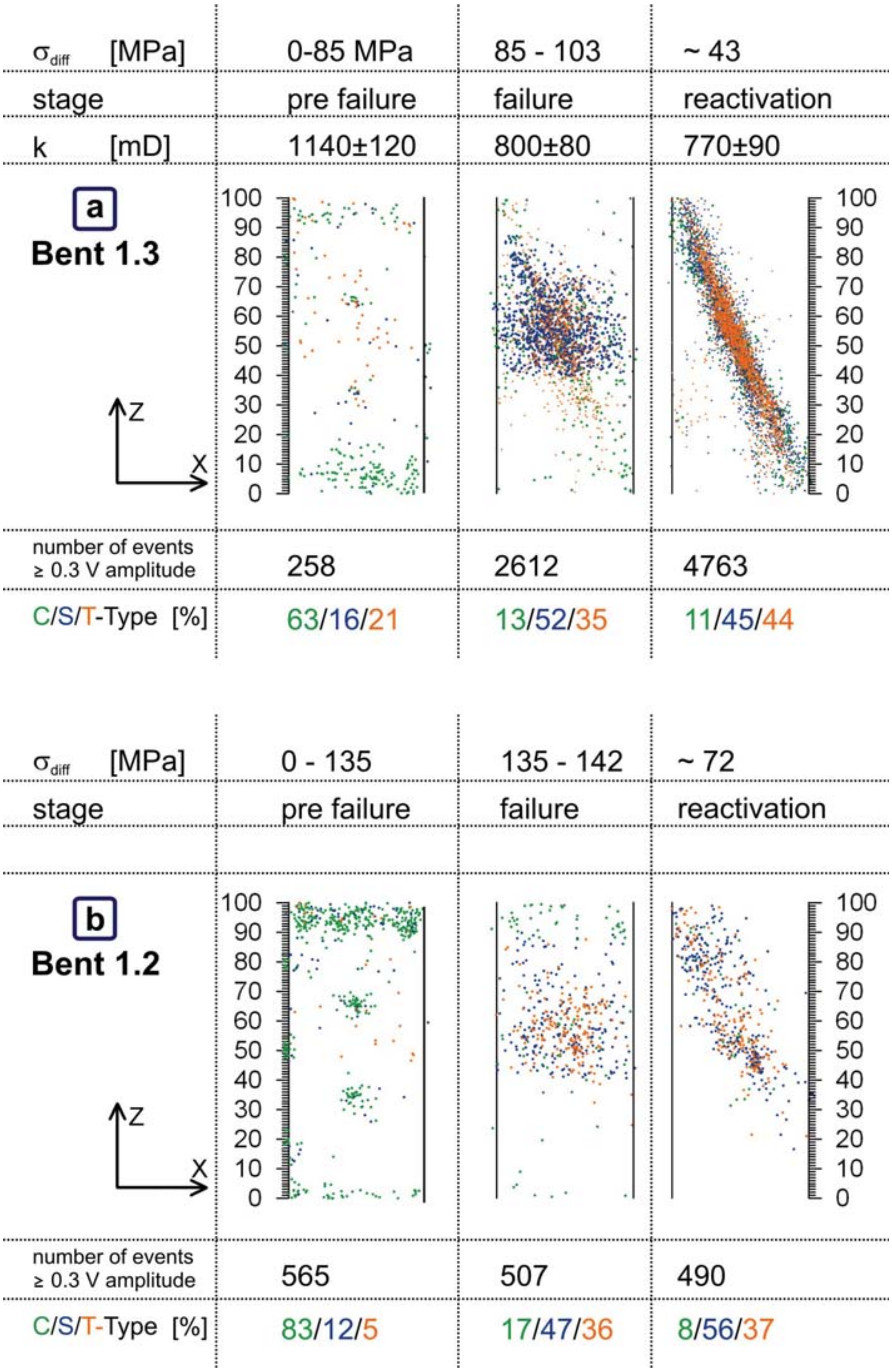

Figure 5.4: *AE hypocenter localisation of experiment Bent 1.2 and Bent 1.3. Before failure, the number of events is small. The events are located at the end-faces and around the AE sensor housings. During failure, a nucleation surrounding the shear zone is visible. The reactivation leads to a highly localised shear band in experiment Bent 1.3. With increasing differential stress, a shift from C-type to S-and T-type events is observed. The permeability of Bent 1.3 is reduced by a factor of 1.5 after shear failure. The reactivation leads to a further reduction. During experiment Bent 1.2, the pore pressure system was partly blocked; no permeability data are determined.*

5.1.3 Spatial AE Distribution

The spatial AE distribution normal to the fracture faces of experiment Bent 1.3 is analysed for the failure and the reactivation loading stage. For that purpose, the AE-events adjacent to the fracture trace are counted and plotted (figure 5.5) with a spacing of 1 mm. The events are localised adjacent to the fracture plane (figure 5.5a); the AE activity has a maximum in the fracture centre (distance = 0). The reactivation of the shear fracture focuses the AE hypocenters around the fracture trace; abundant events are detected from the centre.

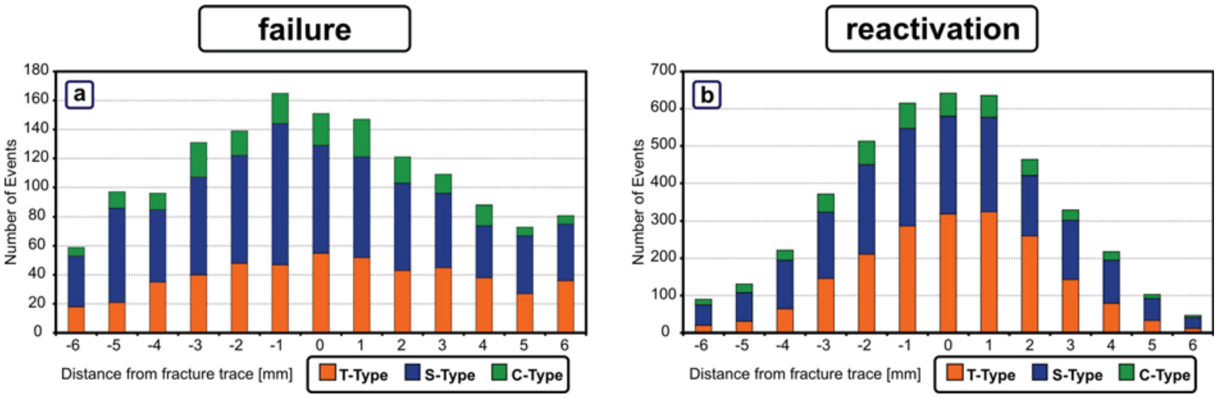

***Figure 5.5**: Spatial AE distribution of experiment Bent 1.3. A spatial AE distribution normal to the shear fracture trace is computed from the discrimination of AE hypocenters into C-, S-, T-type (collapse, shear, tensile). The reactivation focuses the events along the fracture trace. In the fracture centre, an increase of T-type events and a decrease of S-type events are observed.*

In general, the process of nucleation and fracture propagation is dominated by S-type events (~ 50 %), but abundant T-type events (~ 30 %) are observed as well. The reactivation of the shear fracture reverses this trend. An increase of T-type events (~ 50 %) and in decrease of S-type events (~ 40 %) in the fracture centre are observed.

5.1.4 Permeability of Gouge Layer

Examination of a micrograph of Bent 1.1 (figure 5.6) shows the produced fines at the fracture face responsible for the permeability reduction during shearing (highlighted in yellow). From the micrograph, the mean thickness of the gouge zone (w_G) is estimated at 0.2 mm. In order to determine w_G, the area of the gouge zone at both fracture faces in the 2D micrograph is measured over the entire length of the shear zone, and an equivalent thickness of the gouge layer related to the fracture length is calculated.

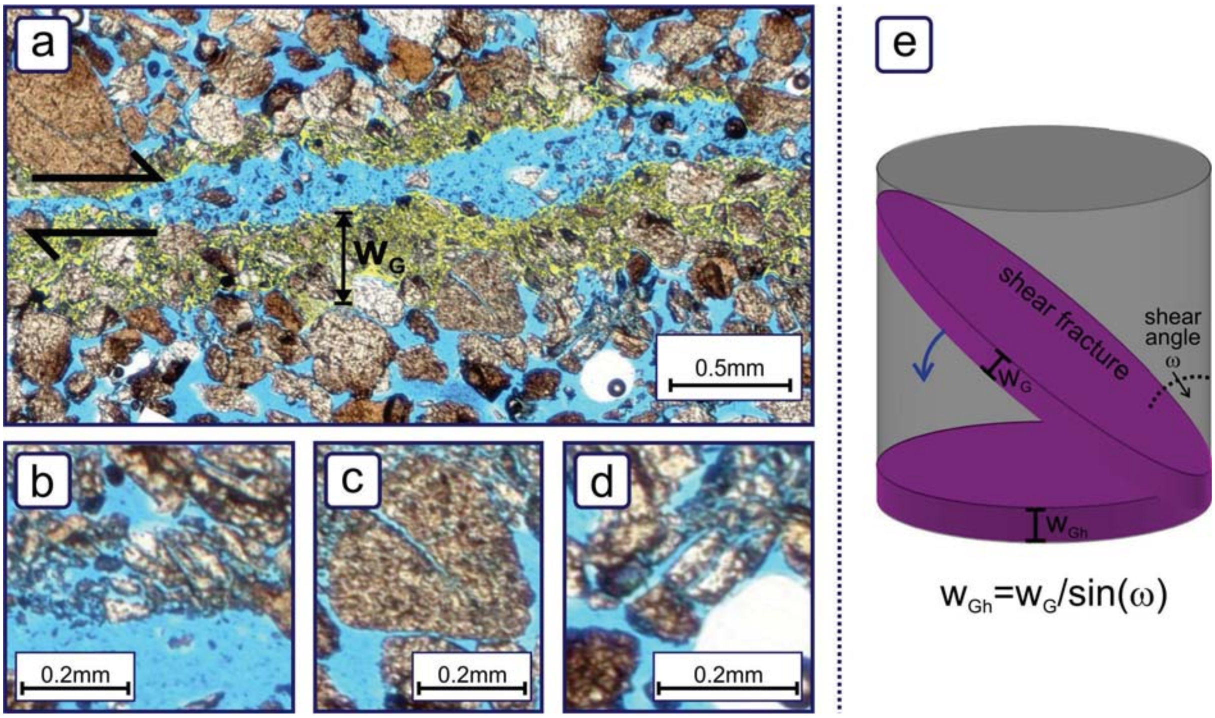

***Figure 5.6**: Micrographs from the shear zone (Bent 1.1). The thickness of the gouge layer (w_G) in the shear fracture is determined from micrographs (yellow zone, figure a). The magnifications (figure b-c) show that a macroscopic shear fracture involves microscopic tensile fracturing of grains. In order to determine the permeability of the gouge layer, the layer with the thickness w_G is rotated into horizontal direction and an equivalent thickness (w_{Gh}) is calculated (figure e).*

The permeability of the gouge zone (k_G) is computed with equation 3.4. For this purpose, it is necessary to rotate w_G into horizontal direction (figure 5.6e). This results in an equivalent thickness of gouge layer w_{Gh} of 0.42 mm. The change of permeability after failure is attributed to the gouge layer exclusively. The initial permeability (k_i) of equation 3.4 is the Bentheim rock permeability before failure and w_{Gh} is adopted for the extent of the FFS zone (w_S) in equation 3.4.

This calculation leads to $k_G = 1.4 \pm 0.3$ mD. The initial permeability of Bent 1.1 (2200 mD) is reduced by a factor of about 1700. The same calculation for experiment Bent 1.3 delivers a permeability of the gouge zone of 7.7 ± 1.8 mD, i.e. a reduction by a factor of 180.

5.1.5 Influence of Compaction and Flow Rate on Hydraulic and Elastic Parameters

In the following section, the influence of compaction within the elastic stress interval for Bentheim and Flechtingen sandstone will be presented. With regard to the RPI experiments, it is important to determine the number of necessary loading cycles to assure elastic behaviour of Young's modulus and permeability. The flow rate dependence of permeability of Bentheim sandstone is investigated in order to define an optimum flow rate for the RPI experiments. This data compilation contains experiments conducted with the AEFC and BDFC.

The BDFC is equipped with plug 2 (compare to §3.2). 100 – 120 mm Bentheim sandstone and 120 mm Flechtingen sandstone specimens are tested in triaxial compression. Specimen diameter is 50 mm. Testing parameters are listed in table 5.3.

	Bent 1.4	**Bent 1.6**	**Bent 3.3**	**Bent 3.5**
specimen length	100 mm	100 mm	120 mm	120 mm
strain rate	$10.0\ 10^{-6}\ s^{-1}$	$10.0\ 10^{-6}\ s^{-1}$	$8.3\ 10^{-6}\ s^{-1}$	$8.3\ 10^{-6}\ s^{-1}$
diff. stress	0 - 50 MPa	0 - 50 MPa	0 - 67 MPa	0 - 67 MPa
conf. pressure	10 MPa	10 MPa	10 MPa	10 MPa
flow rate	50 ml/min	50 ml/min	1-10 ml/min	1-10 ml/min
mean pore pressure	0.10-0.14 MPa	0.10-0.15 MPa	0.10-0.12 MPa	0.10-0.11 MPa
	FB 1.5	**FB 1.6**	**FB 7.4**	**FB 2.1**
specimen length	120 mm	120 mm	120 mm	120 mm
strain rate	$8.3\ 10^{-6}\ s^{-1}$	$8.3\ 10^{-6}\ s^{-1}$	$8.3\ 10^{-6}\ s^{-1}$	$4\ 10^{-6}\ s^{-1}$
diff. stress	0 - 65 MPa	0 - 65 MPa	0 - 65 MPa	0 - 65 MPa
conf. pressure	10 MPa	10 MPa	10 MPa	10 MPa
flow rate	0.02 ml/min	0.02 ml/min	0.05 ml/min	0.1 ml/min
mean pore pressure	0.18-0.24 MPa	0.18-0.25 MPa	0.13-0.22 MPa	0.17-0.20 MPa

Table 5.3: *Parameters of different experiments for Young's modulus and permeability determination within the elastic stress interval.*

5.1.6 Evolution of Young's Modulus

The experiments in the previous section point out that the Young's modulus (E) is affected by closure of microcracks during initial loading of a specimen. In order to assure linear elastic behaviour, Bentheim and Flechtingen sandstone specimens are cyclic loaded up to σ_{diff} = 65 MPa (figure 5.7). 65 MPa is equal to 65 % of maximum peak load for Bentheim rock at σ_3 = 10 MPa.

The first loading causes a stiffening of Bentheim rock and Flechtingen; E increases by 15 %. After the first cycle, further loading cycles have minor impact on E. In contrast to the Bentheim sandstone, the modulus of Flechtingen rock shows fluctuations about ± 0.3 GPa.

5.1.7 Evolution of Permeability

The Bentheim sandstone (Bent 1.6) shows a slight decrease of permeability k_i due to loading cycles; the permeability at maximum σ_{diff} (65 MPa) is about 1 – 4 % smaller than k_i of the unloaded sample (figure 5.8a). Five loading cycles affect a maximum permeability reduction of 5 %. Compressive stress has only a minor influence on permeability.

With regard to the measurement error (~ 10 %), no significant changes of permeability can be ascertained. The same conclusion is drawn from experiment Bent 3.5 presented in figure 5.8b. The permeability is plotted as a function of the flow rate (Q) and σ_{diff}. The initial and last values of σ_{diff} in experiment Bent 3.5 are negative (~ -8 MPa). These values correspond to σ_1 = 2 MPa and σ_3 = 10 MPa. This test was conducted with the BDFC, which allows an independent control of the confinement and the axial stress. The specimen Bent 3.5 had already been pre-loaded 3 times.

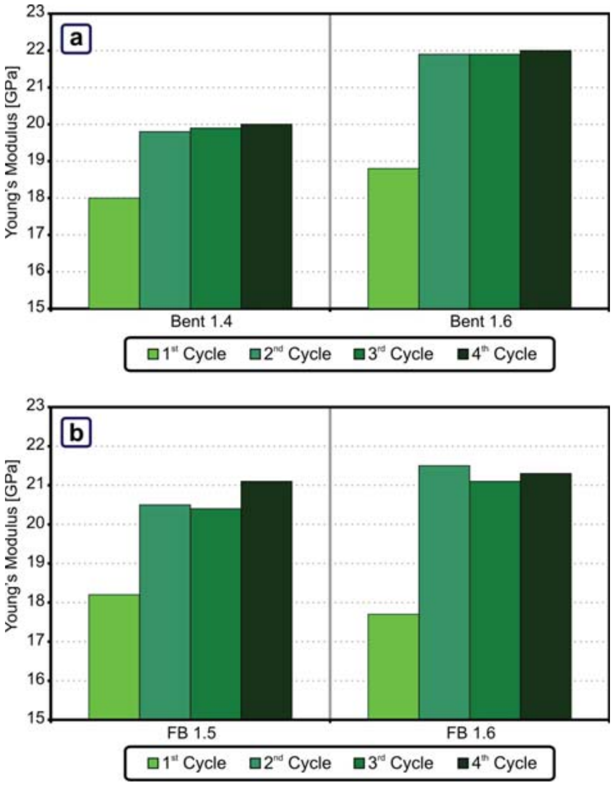

Figure 5.7: *Evolution of Young's modulus due to cyclic loading. Between 1st and 2nd loading cycles the Bentheim (a) and Flechtingen (b) sandstone shows clear stiffening; in the subsequent loading cycles minor variations are determined.*

At small flow rates (Q = 1 ml/min) the permeability (k_i) seems to decrease (~ 10 %) with increasing σ_{diff} comparable to experiment Bent 1.6. With increasing flow rate, the permeability of Bent 3.5 is almost constant. A slight increase of k_i is observed with increasing Q. With regard to the measurement error, both findings are not significant.

In contrast, the FB 1.5 specimen (figure 5.8c) loaded up to σ_{diff} = 65 MPa shows a clear stress dependent permeability. Three loading cycles are required to guarantee a poroelastic behaviour (figure 5.8c). The permeability reduction caused by the three cycles is about 50 %. Poroelastic permeability behaviour is characterised by a k_i decrease of 12 - 15 % within the applied loading range. A power law fit [Ghabezloo et al. in press] matches the variation of the permeability with differential stress (figure 5.8d).

This investigation is performed for four specimens: FB 1.5, FB 1.6, FB 2.1, and FB 7.4. The latter two are not shown here. The permeability differential stress coefficient of these three experiments is between -0.07 and -0.09. The permeability functions are listed in table 5.4. A list of permeabilities and Young's moduli for Bentheim and Flechtingen rock specimens investigated in the study at hand are given in appendix A3. In general, the permeability of consolidated Bentheim sandstone specimens varies between 1300 und 2500 mD; the permeability of consolidated Flechtingen rock specimens is in the range of 86 to 546 µD.

specimen	poroelastic permeability behaviour
FB 1.5	$k_i = 85.6\ \sigma_{diff}^{-0.0916}$
FB 1.6	$k_i = 100.7\ \sigma_{diff}^{-0.0739}$
FB 2.1	$k_i = 546\ \sigma_{diff}^{-0.0944}$
FB 7.4	$k_i = 193.8\ \sigma_{diff}^{-0.0932}$

Table 5.4*: Differential stress functions of Flechtingen sandstone. A power law fit is used to match the poroelastic stress dependence of Flechtingen rock in the differential stress interval 0 – 65 MPa.*

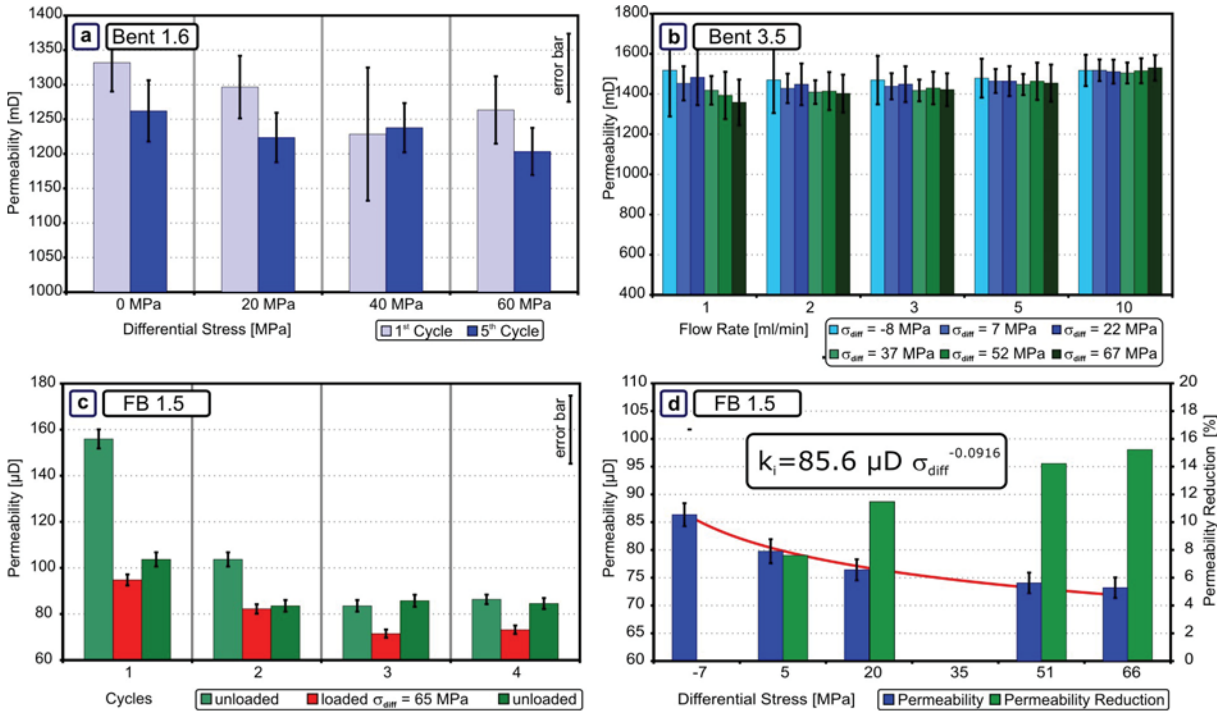

Figure 5.8: *Permeability of Bentheim and Flechtingen sandstone as a function of loading cycles, stress and flow rate. The Bentheim sandstone shows only minor variations of permeability due to cyclic loading (figure a) and flow rate (figure b). Both experiments show a small stress dependence of permeability (Bent 1.6: ~ 5 %; Bent 3.5 ~ 10 % at flow rate = 1 ml/min). With regard to the measurement error, this dependence cannot be ascertained. Four loading cycles are necessary to assure pure poroelastic permeability behaviour of Flechtingen rock (figure c). Within the differential stress interval 0 -65 MPa, the permeability (k_i) decreases by 15 %. The stress dependence is exponentially fitted (figure d).*

5.1.8 Influence of Pore Fluid Salinity on Permeability

The influence of pore fluid salinity on permeability will be demonstrated in this section. It is well known that mobilisation and swelling of clay minerals due to different pore fluids impair permeability of a rock on laboratory scale as well as on reservoir scale [Civan 2000, Byrne & Patey 2003, Rahman et al. 1995]. In order to deal with this problem, the two rock types are exposed to different brines (2 % KCl and 0.1 mol NaCl) and pure water. NaCl brine is used for the LTFC exclusively. No clear distinction between consolidation, temperature effects, and chemical fluid-rock interactions on k_i is made with this flow cell. Hence, in this section only the tests with KCl and pure water are compared. Figure 5.9 plots the relative permeability changes of Bentheim and Flechtingen rock after a defined fluid exposure time up to 24 hours. A constant flow rate and a constant confining pressure are applied for these experiments with no differential stress (see table 5.3). The two Bentheim sandstone experiments show no dependence on fluid salinity and exposure time. With regard to the error, no alteration of permeability can be determined. In contrast, the Flechtingen rock shows a reduction of k_i with both

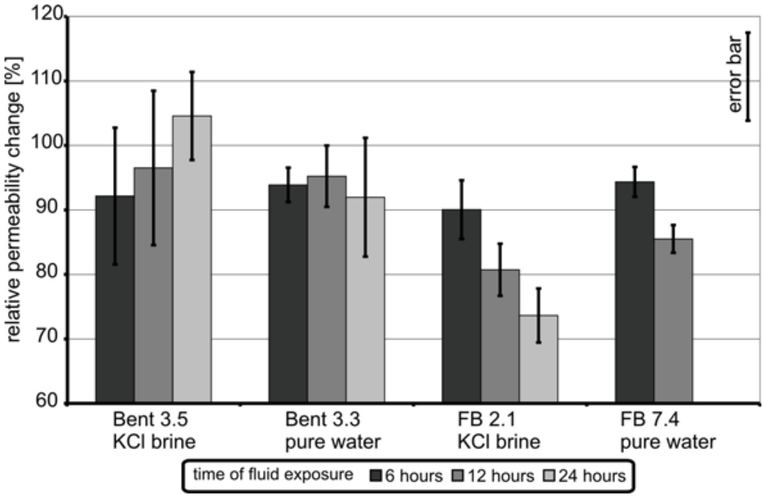

***Figure 5.9**: Relative permeability changes due to fluid-rock interactions. Within the error margin, the Bentheim sandstone shows no permeability alteration due to fluid exposure. In contrast, the Flechtingen sandstone permeability is significantly reduced with KCL brine, as well as with pure water as pore fluid.*

fluids; no significant differences between pure water and 2 % KCL brine can be drawn. The permeability of specimen FB 2.1 is reduced to 80 % after 12 hours of delivering fluid to the specimen; with pure water a reduction to 85 % is observed.

5.2 Discussion of Mechanical and Hydraulic Characterisatioin of Bentheim and Flechtingen Sandstone

5.2.1 Brittle Failure of Bentheim Sandstone

Under triaxial loading conditions with a confining pressure up to 20 MPa, the Bentheim sandstone deforms in the brittle regime and shows shear localisation. This is in accordance with the work of Klein et al. [2001] and Klein & Reuschle [2003]. The failure of Bentheim sandstone is characterised by a Mohr-Coulomb failure mode [Paterson & Wong 2005]. The differential stress shows a peak, beyond which strain softening occurs. The peak stress (σ_{peak}) increases with increasing confinement (σ_3). Visual inspection of the samples confirmed that each has failed by shear localisation along an inclined zone cutting across the sample.

Peak strength, yield point and Young's modulus of the three AE experiment are listed in table 5.5. In addition, values from other Bentheim sandstone experiment at σ_3 = 0.1 and 5 MPa are given. The unconfined experiments (uniaxial compression) start to dilate at 90 % of the peak load, whereas the yield point of confined experiments is at 75 % of peak stress. The volumentric strain of experiment Bent 1.3 (σ_3 = 10 MPa) show the yield point at 90% of the peak stress (figure 5.1b); this measure is obviously erroneous. The change of stress-axial strain behaviour (figure 5.1b) as well as the significant decrease of horizontal p-wave velocity above 70 MPa differential stress (figure 5.3a) indicate microstructural changes already at ~70 % of the peak strength. The mean values from table 5.5 are used to construct a Mohr-Coulomb diagram [Jaeger et al. 2007] and determine the cohesion (S_0 = 11 MPa) and coefficient of internal friction (γ = 1.02). The coefficient of internal friction corresponds to an internal friction angle of 45.7°. The construction diagram is shown in figure A4 in appendix A3.

Elastic properties of the Bentheim sandstone are affected by two mechanisms. The Young's modulus increases with confinement (0.1 – 20 MPa) and increases with differential stress prior to the yield point from 18.7 to 22.8 GPa (figure 5.1 & table 5.5). Presumably, closure of microcracks as well as elastic grain contact deformation lead to this increase of moduli. This is consistent with the increasing (vertical) p-wave velocity prior to the yield point and the high percentage of C-type events. Such behaviour has been observed in triaxial experiments compacting a porous assembly of glass spheres [Domenico 1977], as well as in triaxial experiments of soft rocks [Yoshinaka et al. 1996]. Compaction above the yield point seems to accompany an increase of crack density and leads to a reduction in p-wave velocity and Young's modulus. This observation is in good agreement with investigations performed by Scott et al. [1993] on Berea sandstone and Fortin et al. [2005] on Bleurswiller sandstone.

specimen	confining pressure σ_3	onset of dilatancy σ_{Yield}	peak stress σ_{peak}	Young's modulus E
	MPa	MPa (% of σ_{peak})	MPa	GPa
Bent 4.17	0.1	40.4 (89.5)	45.1	18.8
Bent 4.14	0.1	41.0 (90.3)	45.4	18.7
Bent S1	5	- / -	76.8	- / -
Bent S2	10	- / -	99.9	- / -
Bent S3	10	- / -	99.0	- / -
Bent 1.1	10	81.0 (74.1)	109.3	21.9
Bent 1.3	20	93.2 (90.4)	103.0	22.8
Bent 1.2	10	109.8 (76.9)	142.8	21.1

Table 5.5: *Peak stress, onset of dilatancy, and Young's modulus of Bentheim sandstone experiments.*

The shear band has an optical width of ~ 1000 µm (see figure 5.6). For Bentheim sandstone with a mean grain diameter of 300 – 400 µm (see §4.3.1), this corresponds to a 2.5-fold of the grain diameter, wide optical fracture process zone (FPZ).

In contrast, the "acoustic" FPZ is about 35 grain diameters (12 mm). Both limits are arbitrary in some sense; both depend on the resolution of the applied method. Zang et al. [2000] found in granite specimens a visible and an acoustic FPZ of 2 and 9 grain diameters, respectively. The average width of the acoustic FPZ in their study was about 12 mm wide, comparable to the Bentheim sandstone.

It is important to note that from first motion analysis, no interpretation of relative movement of the fracture planes of a microfracture is possible. The first motion polarities can give an indication about the involved fracture mechanism. The analysis highlights that S-type and T-type events are involved in the nucleation and propagation of a shear band. On the contrary, the closure of microcracks before dilatancy is almost pure C-type. The shear fracture reactivation is T-type dominated. Optical inspection identifies grains split by tensile cracking along the fracture plane (figure 5.6b-d).

Stanchits et al. [2006] identified a decrease in T-type events close to failure during triaxial loading of granite and basalt samples (σ_3 = 20 MPa). They concluded that shear cracks connect the previously formed tensile cracks. During nucleation and failure of porous Bentheim sandstone, a large increase of S-type events is observed (up to 60 %) as well. In contrast, in a porous rock point loading at grain-grain contacts can also lead to failure in tensile mode. Zhang et al. [1990] explained grain crushing in sandstones by a Hertzian contact stress model [Hertz 1882], which predicts tensile fracturing by indentation. During loading, cracks and grain boundaries sufficiently aligned to the macroscopic principal stresses can be activated in shear and tensile mode. Backers et al. [2003] and Stanchits et al. [2003] reported that the growth of a macroscopic tensile fracture in pure Mode I loading involves T-type and S-type events on the microscale. Hence, the stresses and stress distributions on the micro-level differ significantly from the stresses on the macro-level i.e. from externally applied stress.

The reactivation of the shear zone in experiment Bent 1.3 shows that the events along the fracture trace have a high amount of T-type (~ 50 %) and S-type events (~ 40 %). This can be explained by sliding, rolling, and diametral loading of grains on the fracture face during reactivation. The sliding process leads to S-type events. During this sliding, grains are diametrally loaded between the fracture faces and split in tensile mode. This hypothesis might be investigated in further studies.

5.2.2 Permeability Evolution during Brittle Failure

The interrelation between permeability and porosity depends on many factors including porosity, pore size, pore throats, connectivity and tortuosity. Fortin et al. [2005] observed a permeability evolution consistent with inelastic compaction of rock. Permeability was reduced by an order of magnitude comparable to experiment Bent 1.1. A factor of 6-600 between initial permeability and permeability in the compacted zone was estimated by Fortin et al. [2005] for triaxially deformed sandstone. For this estimation, they used a statistical, physical approach that takes into account different models for the pore shape. The reduction ratio of Bent 1.1 is 1700 and 3 times higher. In contrast, the reduction ratio of Bent 1.3 is 180 and is in accordance with the reduction factor found by Fortin et al. [2005]. It is important to note that the shear fracture of experiment Bent 1.1 has not connected the end faces of the specimen. Hence, flow transport crosses the damaged fracture faces and does not proceed from the top to bottom plug along the fracture trace. This is not guaranteed for experiment Bent 1.3 and can explain the large difference between both.

The differences of permeability reduction factor between the presented study and Fortin et al. [2005] may be attributed to the employed methods. They estimated the reduction factor indirectly from relations between permeabilities, porosity, and estimated crack density. In the present study, the calculation of permeability contrast is determined from direct permeability measurement of the gouge layer.

5.2.3 Permeability Evolution: Influences of Stress

Keaney et al. [1998] identified five phases that a rock experiences in triaxial deformation experiments and linked these phases to the evolution of permeability. They stated that in the first phase compaction of existing cracks and deformation of grain boundaries leads to a decrease of permeability by a factor of two – comparable to the result of this study. Blöcher et al. [2007] investigated the Flechtingen rock and identified the same initial decrease in permeability by a factor of two due to consolidation effects in isostatic loading experiments up to 70 MPa. The Flechtingen sandstone has a smaller permeability (up to a factor of 100) than the Rotliegend reservoir sandstone of Gross Schoenebeck tested by Trautwein & Huenges [2005]. The poroelastic permeability reduction of ~ 15 % (permeability differential stress exponent about -0.09) over a differential stress range of 50 MPa is similar. With regard to the poroelastic behaviour, the Flechtingen rock can be used as an outcrop equivalent of the Rotliegend sandstone of the Gross Schoenebeck site. The Bentheim rock does not show a stress dependent permeability up to a differential stress of 65 MPa.

5.2.4 Permeability Evolution: Influences of Flow Rate

Soni et al. [1978] reported a series of tests of flow through unconsolidated sand with the result that the Darcy flow zone (compare to §2.3.2) is in the pressure gradient range of 0.45 bar/m - 2.3 bar/m. Wu et al. [2008] presented data from tight rocks with permeabilities between 0.2 – 5 mD from two different rock types with different clay content. The two rock types show a threshold pressure gradient between pre-laminar and laminar flow of 1.5 bar/m and 30 bar/m, respectively. Transferred to the highly permeable Bentheim and low permeable Flechtingen rock specimen (length 0.1 – 0.12 m) used in the present study, lower limits for pressure gradient can be estimated. The differential pore pressure should be at least 0.045 bar for high permeable sandstones and 0.15 bar for low permeable sandstone to assure Darcy flow conditions.

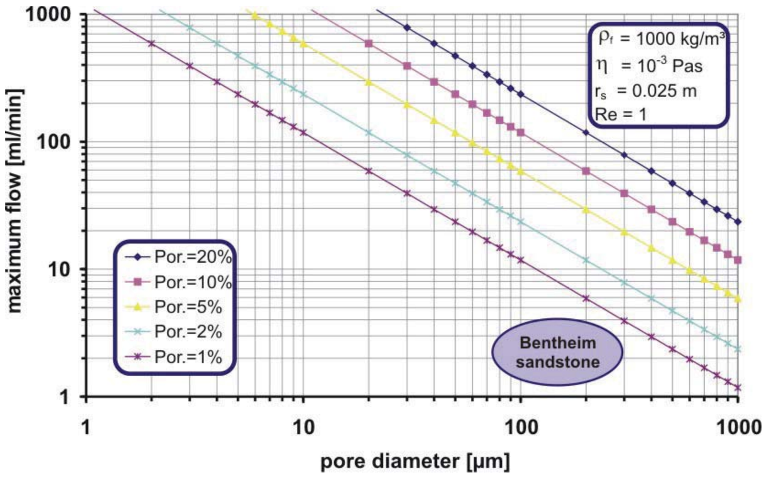

Figure 5.10: *Estimation of flow rate interval for Bentheim sandstone permeability measurements. A tube-like pore model is assumed to estimate maximum flow rates within the laminar flow regime.*

Concerning the Flechtingen rock, the pressure gradients are ~ 30 bar/m (Q = 0.02 – 0.1 ml/min). With regard to the study of Wu et al. [2008], Darcy conditions are ascertained. In general, the flow rate dependence of Bentheim sandstone permeability is negligible in the investigated flow rate interval. With regard to Soni et al. [1978], the minimum flow rate should be about 1 ml/min, which corresponds to a pressure gradient of 0.06 bar/m.

The permeability of Bentheim sandstone shows no stress dependence in the linear-elastic regime. A tube-like pore model for this highly permeable rock can be assumed [Gueguen & Dienes 1989]. A calculation of maximum flow velocities at laminar conditions (Re = 1) can be derived from the Reynolds number (Re) [Bear 1988]:

$$Q=\frac{Re\cdot\pi\cdot r_s^2\cdot\eta\cdot\Phi}{\rho_f\cdot d_0} \tag{5.1}$$

where r_s is the sample radius, η is the dynamic viscosity, Φ is the porosity, and ρ_f the fluid density. The result is plotted in figure 5.10 as function of d_0, i.e. as function of the pore diameter. The figure highlights that even at high flow rates of 50 ml/min Darcy's law should not be violated (blue line, Φ = 20 %).

In contrast to the majority of experiments conducted for the present study, a less sensitive pore pressure sensor is used for experiments Bent 1.1 – Bent 1.6 and Bent 2.2 - Bent 2.3, and flow rates up to 50 ml/min are applied. The calculation shows that Darcy's law is still valid at this high flow rate. This is in accordance with Soni et al. [1978]. At a high flow rate of 50 ml/min the threshold for Darcy flow conditions is only slightly exceeded. The consequences for the rock-proppant interaction experiments with Bentheim sandstone are:

Permeability of intact Bentheim rock specimens can be measured with flow rates up to 50 ml/min. If the hydraulic properties are altered due to mechanical interaction of rock and proppants, a Forchheimer correction of permeability [Forchheimer 1901, Gidely 1981] is necessary. If applicable, a small flow rate (e.g. Q = 5 ml/min) should be used for RPI experiments. With regard to the characterisation of pore space of Bentheim rock (§4.3.1), it is obvious that the pore space is not tube-like. A factor of 5 between pore radii and throat radii was estimated. However, the mercury intrusion porosimetry, which identifies mainly the distribution of pore throats, determined that the amount of small pore throats (< 10 µm) is small (~ 10 %).

5.2.5 Permeability Evolution: Influences of Fluid Salinity

Permeability impairment due to clay alteration processes can be controlled with a sufficiently high salt concentration. The permeability reduction of Flechtingen rock after 12 hours of fluid exposure is 20 % for KCl brine and 15 % for pure water, respectively. The Flechtingen sandstone contains about 6 % kaolinite and 9 % illite [Stammnitz 1992]. The salt concentration is not high enough to stabilise the clay minerals. Rahman et al. [1995] demonstrated that permeability reduction of illite (4 %) bearing sandstone can be prevented using KCl brine or NaCl brine with concentrations of 4 % and 4.5 %, respectively However, the permeability stabilises on a defined level after ~ 24 hours. Hence, before the initial permeability of a Flechtingen sandstone is measured, fluid must be delivered to the specimen at least for 24 hours.

Bentheim sandstone with a clay content of 2 % kaolinite shows no significant decrease of permeability due to flow of different fluids. Optical examinations of the specimens after experiment execution identifies that kaolinite lenses are washed out. The grain size of kaolinite is in the range of 0.2 – 1 µm. Compared to the majority of pore throat radii of Bentheim sandstone (10 – 100 µm), it is obvious that the dispersed kaolinite is transported through the pore space, and only a minor fraction will be deposited.

5.2.6 Implications for RPI Experiments

Within the differential stress interval 0 – 65 MPa, the permeability of Bentheim sandstone shows no dependence of stress and stress cycling. In contrast, the Flechtingen sandstone has a clear dependence of both. At least three stress cycles are necessary to assure poroelastic behaviour. The Young's modulus is considerably influenced by closure of microcracks during initial loading of both sandstones; one preloading cycle yields a linear elastic behaviour. The permeability of Flechtingen sandstone is affected by clay alteration and transport even at a small flow rates; the permeability stabilises on a defined level. Taking into account a sufficient fluid exposure time (≥ 24 hours), RPI experiments can be conducted with the Flechtingen rock and pure water as pore fluid.

The maximum differential stress of RPI experiments is 50 MPa at 10 MPa confining pressure. This is sufficiently below the yield point of Bentheim sandstone to avoid any influence on the RPI experiments. The Flechtingen rock is not tested in triaxial brittle deformation in the present study. The Flechtingen rock was the subject of different investigations [Zang 1997, Heiland 2003]. Heiland [2003] found a peak stress of σ_1 ~ 90 MPa at a σ_3 = 10 MPa. Hence, the designated maximum σ_{diff} = 50 MPa for the RPI testing is below the onset of dilatancy.

5.3 Rock-Proppant Interaction Testing – AEFC

The Acoustic Emission Flow Cell (AEFC) is used to locate and analyse the microfracture processes at the rock-proppant interface and within the proppant pack. Four experiments are conducted; three with Bentheim sandstone and one with Flechtingen sandstone. The AE emission system is employed for three experiments only: Bent 2.3, Bent 3.4, and FB 1.6. Experiment Bent 2.2 is conducted in order to verify permeability data from experiment Bent 2.3. Table 5.6 shows the testing parameters of the four experiments. Exemplarily, stress-strain and differential pore pressure plots of PRI experiments are shown in appendix A4 and A5.

rock testing				
	Bent 2.2	**Bent 2.3**	**Bent 3.4**	**FB 1.6**
specimen length	100 mm	100 mm	120 mm	120 mm
Young's modulus	21.4 GPa	20.7 GPa	22.8 GPa	21.3 GPa
permeability	2170 mD	1630 mD	2120 mD	100 µD
strain rate	$10.0\ 10^{-6}\ s^{-1}$	$10.0\ 10^{-6}\ s^{-1}$	$8.30\ 10^{-6}\ s^{-1}$	$8.30\ 10^{-6}\ s^{-1}$
diff. stress	0-50 MPa	0-50 MPa	0-68 MPa	0-66 MPa
conf. pressure	10 MPa	10 MPa	10 MPa	10 MPa
mean pore pressure	0.1–0.12 MPa	0.1–0.15 MPa	0.1–0.11 MPa	0.1–0.23 MPa

rock-proppant interaction testing				
	Bent 2.2	**Bent 2.3**	**Bent 3.4**	**FB 1.6**
specimen length	105.0 mm	105.2 mm	122.3 mm	123.5 mm
fracture width	4.97 mm	5.16 mm	2.32 mm	3.46 mm
proppant type	ISP	ISP	ISP	HSP
strain rate	$8.00\ 10^{-6}\ s^{-1}$	$8.00\ 10^{-6}\ s^{-1}$	$8.17\ 10^{-6}\ s^{-1}$	$8.10\ 10^{-6}\ s^{-1}$
diff. stress	0-20 MPa	0-51 MPa	0-52 MPa	0-53 MPa
conf. pressure	10 MPa	10 MPa	10 MPa	2 & 10 MPa
mean pore pressure	0.1–0.13 MPa	0.1–0.21 MPa	0.1–0.12 MPa	0.1–0.19 MPa

***Table 5.6**: Testing parameters of rock-proppant interaction (RPI) experiments with the Acoustic Emission Flow Cell (AEFC).*

5.3.1 Bent 2.3: Bentheim Sandstone + Intermediate Strength Proppants

Permeability change and location of AE events during loading of a Bentheim sandstone specimen with 2 lb/ft² (~ 10 kg/m^2 / w_f ~ 5 mm) of intermediate strength proppants (ISP) are shown in figure 5.11a-f. The AE hypocenters are projected normal to the z-, y-, x-axes of five loading steps. Over 42,000 AE events are located. About 12,000 events have amplitudes > 2 Volts. In figure 5.11 events with amplitudes > 5 Volts are plotted only, in total 6067 hypocenters. The 5 Volt threshold is chosen to reduce the location errors and highlight strong events. The amplitude of an AE signal is related to the magnitude of the microfracture event. Since the energy transfer between the housings and the sensors is not quantified, no calculation of magnitudes from signal amplitudes is possible.

Only the inner part of the specimen is plotted from 40 mm ≤ z ≤ 80 mm. The AE events are separated in T-, S-, and C-type. Fracture width (w_f) is calculated from equation 3.7 and the permeability of the FFS zone (k_S) from equation 3.4. Fracture width is plotted in figure 5.11 in order to visualise its location (black lines). In the first loading step (figure 5.11a) the confining pressure (σ_3 = 10 MPa) is applied.

High flow rate of 60 ml/min is applied during rock-proppant interaction (RPI) testing with the AEFC. At these high flow rates, Darcy conditions cannot be guaranteed, particularly for the low porosity FFS zone. Hence, a β-factor correction based on the Forchheimer equation (§2.3.3) is performed [Gidley 1991].

σ_{diff} [MPa]	**0** (isostatic)	**5**	**20**	**35**	**50**
k_i [mD]	1630±160	1640±80	1600±90	1700±200	1540±80
k_T [mD]	374±5	386±8	346±3	330±5	300±5
k_s [mD]					
w_f [mm]	5.169±0.002	4.945±0.002	4.558±0.003	4.258±0.003	3.955±0.003

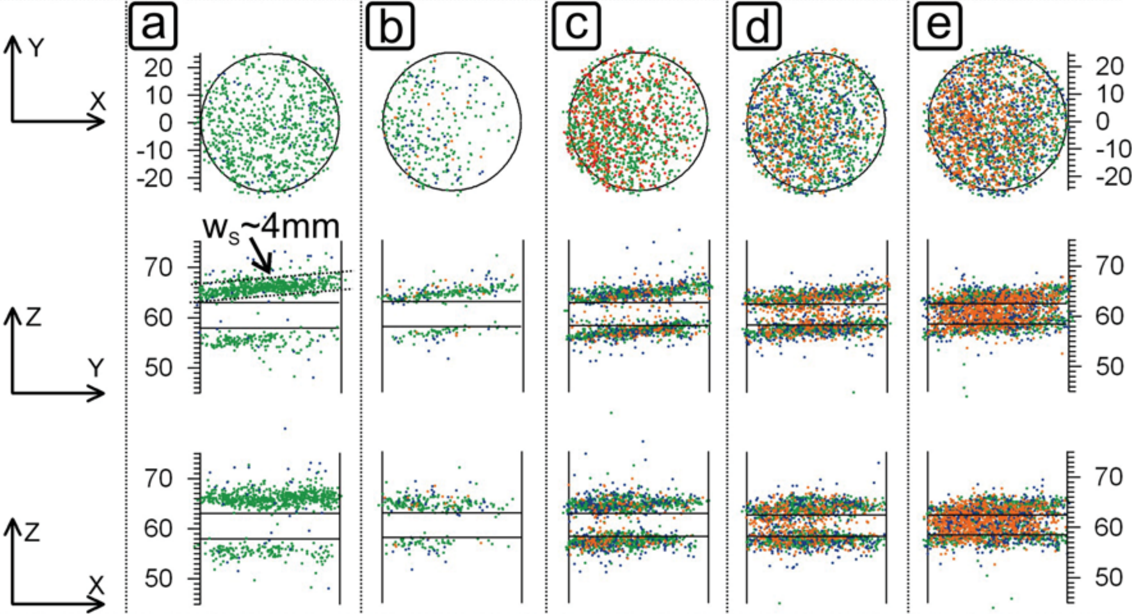

number of events > 5 V amplitude	894	305	1630	1844	2394
C/S/T-Type [%]	95/4/1	78/16/6	69/19/12	56/22/22	42/26/32

Figure 5.11: *Permeability evolution and AE hypocenters of experiment Bent 2.3. Permeability alteration and location of AE events during loading of a Bentheim sandstone specimen with 10 kg/m^2 of intermediate strength proppants (ISP) is shown. All AE events with amplitudes > 5 V are displayed; the fracture faces are indicated with solid horizontal lines. Grain crushing starts at low differential stress (σ_{diff}) at the rock-proppant interface, indicated by the clustering of AE hypocenters (figure a) at the fracture face. With increasing σ_{diff} (figure b-d) the AE activity moves into the proppant pack. The initial permeability (k_i) at σ_{diff} = 0 MPa (isostatic loading; σ_3 = 10 MPa) is about 1600 mD. After applying σ_3, the permeability of rock-proppant system (k_T) is reduced by factor of four. With increasing σ_{diff} an ongoing reduction of k_T is observed. Damage penetration w_S is estimated from the thickness of the AE cluster (figure a / dashed lines); it is about 4 mm. With increasing σ_{diff} the relation between tensile (T- type), shear (S- type), and collapse (C-type) events is shifted. The amount of T- and S-type events increases at the expense of C-type events.*

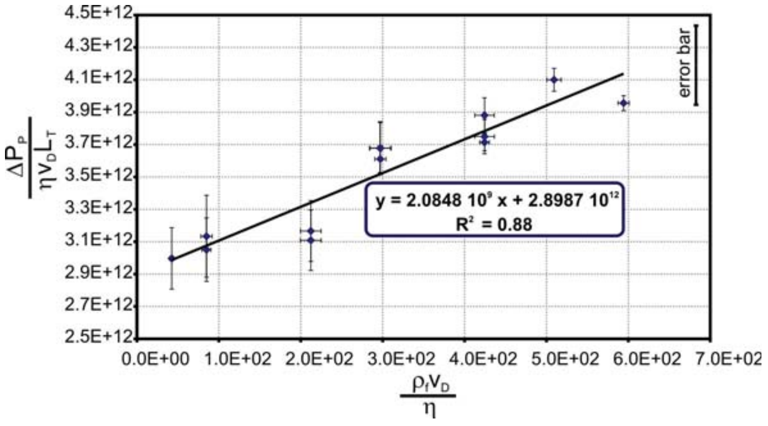

Figure 5.12: *Determination of β-factor. Due to high flow rates, Darcy flow conditions (laminar flow) are violated during rock-proppant interaction test of experiment Bent 2.3. Hence, a β-factor correction based on the Forchheimer equation is performed [Gidley 1991]. A β-factor (slope) of 2.1 10^9 1/m is determined.*

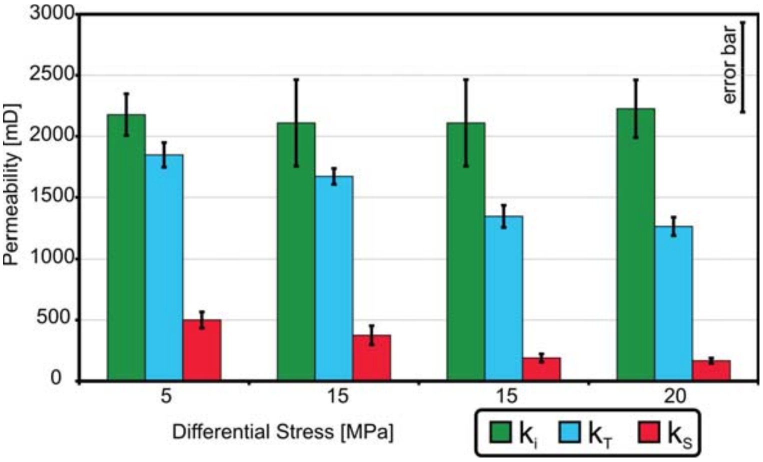

***Figure 5.13**: Permeability evolution of Bent 2.2 specimen. Rock-proppant interaction experiment Bent 2.3 was repeated with specimen Bent 2.2 because the reduction of the rock-proppant specimen permeability (k_T) was conspicuously high. The initial rock permeability (k_i / green bars) of specimen Bent 2.2 is 2170 ± 170 mD. At σ_{diff} = 5 MPa the k_T is reduced by 15 %; a further reduction to 1260 ± 80 mD (blue bars) is observed. FFS permeability k_S yields a reduction from 500 ± 70 mD to 170 ± 20 mD (red bars). With respect to k_i, permeability is reduced by a factor of 4 to 13.*

A step rate test from 5 to 70 ml/min flow rate is executed before differential loading of the sample. Figure 5.12 illustrates the influence of Darcy flow velocity on the apparent permeability. A β-factor (slope) of 2.1 10^9 1/m. is determined. With this β-factor the permeability measurements of RPI experiment Bent 2.3 is corrected for non-Darcy flow effects.

The initial permeability of specimen Bent 2.3 (k_i) at σ_{diff} = 0 MPa (isostatic loading of σ_3 = 10 MPa) is about 1630 ± 130 mD and shows no variation up to 50 MPa with regard to the error. The permeability of the specimen Bent 2.3 after creating a tensile fracture (k_{tf}) via a 3-point bending test is measured (compare to §3.3); it is 1540 ± 80 mD. With regard to the measurement error, no change of permeability is determined due to creation of a macroscopic tensile fracture in the Bentheim sandstone specimen.

After isostatic loading of the specimen with proppant pack, k_T is reduced by a factor of 4 (374 ± 5 mD) compared to k_i; up to σ_{diff} = 50 MPa a further reduction to 300 ± 5 mD is observed. The damage penetration (w_S) is estimated from the thickness of the AE cluster, indicated as a dashed line in figure 5.11a; it is about 4 mm.

The clustering of AE hypocenters in figure 5.11a indicates that grain crushing and proppant embedment starts at both fracture faces instantaneously with applying σ_3. Initially, no events within the proppant pack are observed. With increasing σ_{diff} (figure 5.11b-d) the AE activity moves from the fracture face into the proppant pack. At the last loading stage, high AE activity within the proppant pack is detected. In figure 5.11b and 5.11c clustering of AE events in the left part of the specimen (-25 mm ≤ x ≤ 0 mm) is observed. This is an indicator for a small asymmetry in loading. This leads to a stress concentration in the left part of the fracture faces. The solid horizontal lines in figure 5.11a-e show the fracture width calculated from displacement data (see §3.4.1).

Majority of AE events (95 %) during initial isostatic loading are C-type (figure 5.11a). With increasing σ_{diff}, the relation between T-, S-, and C-type events shifts, whereby the amount of S-type events increases from 16 % to 26 %. The amount of T-type events is 6 % initially and increases to 32 %. This finding correlates with the observed movement of AE activity into the proppant pack.

The 4-times permeability reduction (k_T = 374 mD) after isostatic loading (σ_{diff} = 0 MPa) is very high. Further tests will reveal that the initial isostatic loading with confining pressure does not affect a 4-fold reduction. Hence, this measurement is erroneous and will not be used for further investigations.

Consequently, permeability data were taken from experiment Bent 2.2, which features almost identical experimental conditions except two modifications: 1) Maximum load is σ_{diff} = 20 MPa to exclude any permeability alteration due to proppant crushing. (Crushing events are recorded from proppant pack at 35 MPa (see figure 5.11d)). 2) Technical problems demanded a 24 hour stop of the experiment at σ_{diff} = 15 MPa. Due to a malfunction, no AE data were recorded during experiment Bent 2.2. The testing parameters are listed in table 5.6; the results are displayed in figure 5.13.

In comparison, k_i = 2170 ± 170 in experiment Bent 2.2 shows no permeability variation up to σ_{diff} = 20 MPa. At σ_{diff} = 5 MPa the permeability of rock-proppant system (k_T) is reduced by 15 % to 1850 ± 100 mD, up to a σ_{diff} = 20 MPa a further reduction to 1260 ± 80 mD is observed (figure 5.13). The stop due to technical reasons has affected a reduction of k_T from 1670 mD to 1340 mD within 24 hours of constant load. The calculation of FFS permeability k_S yields a reduction from 500 ± 70 mD to 170 ± 20 mD. With respect to k_i, the permeability at the fracture face is reduced by a factor of 4 and 13, respectively. The fracture width is reduced by 12 % at σ_{diff} = 20 MPa. Experiment Bent 2.3 shows the same reduction of width at this differential stress.

5.3.2 Bent 3.4: Bentheim Sandstone + Intermediate Strength Proppants

Experiment Bent 3.4 is conducted with ISP. A smaller proppant concentration of 1.0 lb/ft^2 (~5 kg/m^2 / w_f ~ 2.3 mm) is used. This leads to two to three layers of proppants. Testing conditions were otherwise identical to experiment Bent 2.3. Due to smaller proppant concentration, a perfect alignment of rock halves with respect to the specimen axis was not feasible, causing a non-uniform loading and a non-uniform fracture closure, respectively. Proppant concentrations of 1.0 lb/ft^2 and smaller are realistic assessments for a multiplicity of stimulated reservoirs. In particular, in low permeable reservoirs, where fracture length is important in order to increase productivity, proppant concentrations can be low. A non-uniform fracture closure and inhomogeneous loading of the proppant pack is promoted in fractures with small proppant concentrations.

Figure 5.14a-e shows the hypocenters of the AE events and the calculated permeabilities of the five loading steps. Over 44,000 AE events are located; about 11,200 have amplitudes above 2 V. 4,117 hypocenters with amplitude > 5 Volts are plotted in figure 5.14. Comparable to experiment Bent 2.3, the damage starts at the rock-proppant interface. Due to a small fracture width of about 2 mm, the separation of upper and lower fracture faces is only visible in figure 5.14a and 5.14b. The fracture closes non-uniformly leading to a non-uniform stress distribution at the fracture face. The AE events are clustered at the left side of figure 5.14b-c (-25 mm ≤ x ≤ 5 mm). With increasing load the AE cluster moves slightly from left to right side.

After axial loading up to σ_{diff} = 50 MPa, only 75 % of the fracture face is affected by damage; the other 25 % (indicated in grey in figure 5.14e) remain unaffected. The initial permeability (k_i) of this Bentheim sandstone specimen at σ_{diff} = 0 MPa (σ_3 = 10 MPa, isostatic loading) is about 2280 ± 10 mD, with a poroelastic permeability decrease of 5 % within the applied loading range. The permeability is measured with a flow rate of 5 ml/min. Permeability of the specimen with macroscopic tensile fracture (k_{tf}) is 1710 ± 15 mD. A permeability reduction due to 3-point bending tensile fracture generation is observed.

The specimen with the proppant pack has a k_T = 1600 ± 90 mD at σ_{diff} = 0 MPa (σ_3 = 10 MPa, isostatic loading). This first k_T value correlates with the specimen permeability with macroscopic tensile fracture (k_{tf}). With increasing σ_{diff}, permeability is reduced to 980 ± 40 mD. The permeability of the FFS zone (k_S) varies from 300 ± 20 mD for σ_{diff} = 0 MPa to 115 ± 5 mD at a σ_{diff} = 50 MPa. For k_S determination, a w_S of 4 mm is set, following experiment Bent 2.3. The fracture width is reduced by 54 % at σ_{diff} = 50 MPa. In this context, it is important to note that the non-uniform loading results in a stress concentration of the proppant pack and in a pronounced damage on the left side of the sample.

During the experiment, the amount of C-type events (~ 90 %) as well as of S-type events (~ 10 %) is almost constant. The number of T-type events is very small (1 – 2%).

σ_{diff} [MPa]	**0** (isostatic)	**5**	**20**	**35**	**50**
k_i [mD]	2280±10	2230±6	2200±14	2180±8	2150±13
k_T [mD]	1600±90	1400±50	1280±80	1130±40	980±40
k_s [mD]	300±20	220±7	184±12	145±5	115±5
w_f [mm]	2.324±0.004	2.284±0.006	1.711±0.007	1.349±0.004	1.100±0.007

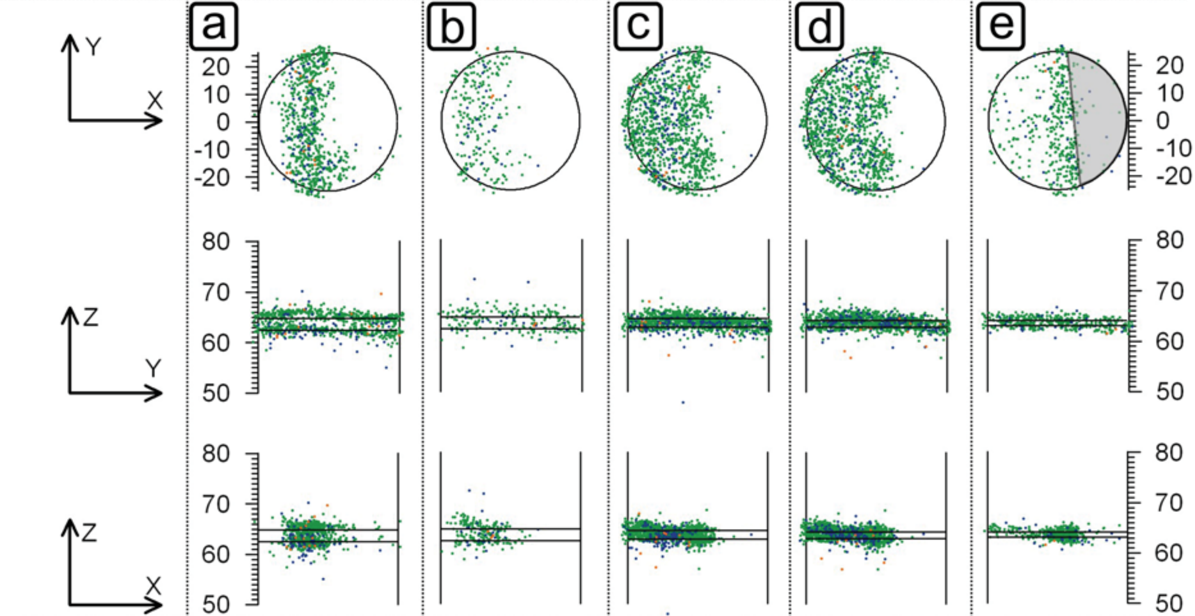

number of events > 5 V amplitude	780	236	1546	1147	408
C/S/T-Type [%]	88/10/2	87/11/2	91/8/1	88/11/1	91/8/1

Figure 5.14*: Permeability evolution and AE hypocenters of experiment Bent 3.4. Experiment Bent 3.4 is conducted with a concentration of 5 kg/m^2 of intermediate strength proppants (ISP). Comparable to experiment Bent 2.3, the damage starts at the rock-proppant interface. The small fracture width (w_f ~ 2 mm) inhibits a clear separation of AE event clusters from the upper and lower fracture face. The fracture closes non-uniformly, indicated by the non-uniform AE hypocenter distribution. At maximum σ_{diff}, 25 % of the fracture face is unaffected (grey area / figure e). The initial permeability (k_i) of this Bentheim sandstone is about 2280 mD. The permeability of the FFS zone (k_S) is reduced due to rock-proppant interactions by a factor of 19 at σ_{diff} = 50 MPa. With increasing σ_{diff} the relation between tensile (T- type), shear (S- type), and collapse (C-type) events remains constant. The amount of T- and S-type is small compared to C-type.*

5.3.3 FB 1.6: Flechtingen Sandstone + High Strength Proppants

FB 1.6 is run with low permeable Flechtingen sandstone and high strength proppants (HSP) with a concentration of 2 lbs/ft² (~ 10kg/m² / w_f ~ 3.5 mm). Figure 5.15a-e presents the hypocenters, as well as the permeabilities. In total 16,700 events are registered, whereas 1,800 hypocenters are calculated from signals with onset amplitudes > 2 V. The initial permeability (k_i) is 94 ± 2 μD with poroelastic permeability decrease of 10 % within the applied loading range. Permeability is determined with a flow rate of 0.02 ml/min. In figure 5.15a initial permeability and AE locations at σ_3 = 2 MPa is shown.

The small confining pressure was chosen in order to minimise damage at the fracture face and to determine the initial permeability of the rock-proppant system. At this small confining pressure (isostatic stress conditions), k_T is 7 μD higher than k_i. This results in a permeability of the FFS zone (k_S) of 230 μD. At σ_{diff} = 5 MPa, k_T is reduced to 72 ± 2 μD resulting in a k_S of 19.0 ± 0.9 μD. At maximum differential stress, k_T amounts to 63 ± 2 μD, resulting in a further decrease of k_S to 12.8 ± 0.6 μD.

σ_{diff} [MPa]	**0** (isostatic)	**5**	**20**	**35**	**50**
k_i [µD]	94±2	87±2	86±2	85±2	84±2
k_T [µD]	101±3	72±2	64±2	62±2	63±2
k_s [µD]	230±11	19.0±0.9	12.7±0.6	11.8±6	12.8±0.6
w_f [mm]	3.33±0.07	3.14±0.02	2.944±0.011	2.838±0.007	2.747±0.006

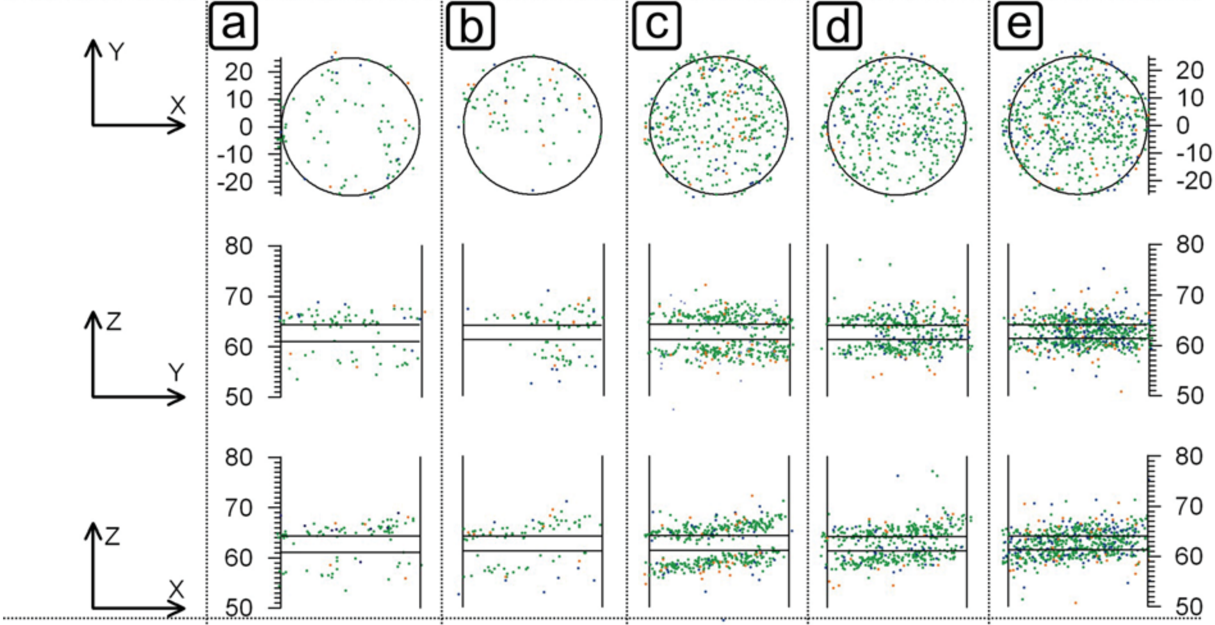

number of events > 2 V amplitude	86	86	440	440	631
C/S/T-Type [%]	85/9/6	80/11/9	84/9/7	87/9/4	77/17/6

Figure 5.15*: Permeability evolution and AE hypocenters of experiment FB 1.6. Tight Flechtingen sandstone is tested with 10 kg/m² of high strength proppants (HSP). The initial permeability (k_i) is 94 ± 2 µD with a poroelastic permeability decrease of 10 % within the applied stress interval. The permeability of the FFS zone (k_S) varies between 19 mD at 5 MPa differential stress (σ_{diff}) and 12 mD at maximum σ_{diff}. Comparable to the Bentheim sandstone experiments, the AE activity is located at the fracture faces and moves into the proppant pack with increasing stress. In contrast to the Bentheim sandstone experiments, the total number of events is smaller. The main activity is C-type. With increasing σ_{diff} a small increase of S-type events can be observed.*

In the first three loading steps, the AE events are located at the fracture face (figure 5.15) comparable to experiment Bent 2.3 and 3.4. Above 20 MPa differential stress, AE activity from the proppant pack is observed. During the experiment, S-type events increase slightly (9 – 17 %) and C-type events decrease (85 – 77 %). The number of T-type events is almost constant; it varies from 6 – 9 %. The fracture width is reduced by 18 % at σ_{diff} = 50 MPa.

5.3.4 Microstructural Observations and Fracture Patterns

Figure 5.16a-e shows a micrograph (thickness of thin section is 40 µm) of the proppant pack and adjacent rock of experiments Bent 3.4 and FB 1.6. At the fracture face, the rock grains in contact with a proppant are completely disintegrated and a lot of fines are produced (figure 5.16a,d,e). The fracture face is compacted, and the pore space decreases. The created fines stay in place and block the neighbouring pores, as well as the flow paths. Damage of proppants can be observed as well; they are cleaved mainly into bigger parts (figure 5.16a,d).

Fines production from ISP crushing is relatively small, but some proppants are fractured. No cleavage fractures in HSP can be found in figure 5.16c, but some fragments are visible in the micrograph. Most fractures within proppants are developed as curved fractures from contact to contact point (figure 5.16d). In general, embedding of HSP and crushing of Flechtingen sandstone grains is small compared to ISP in contact with Bentheim sandstone.

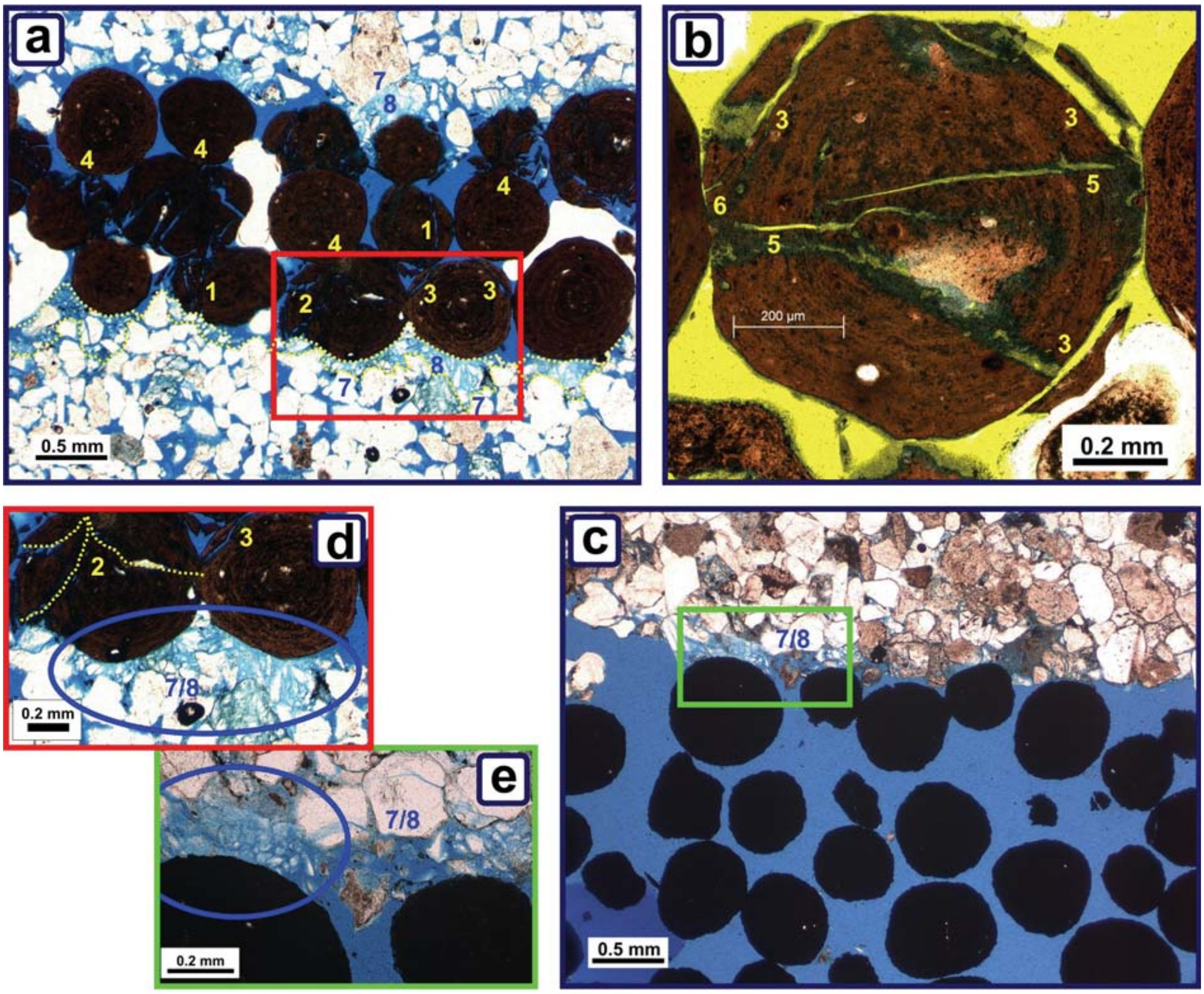

1: Cleavage fractures of proppants in axial direction
2: Curved fractures between contact points
3: Chipping near contact regions
4: Proppant fracturing starts mainly at proppant proppant contact
5: Fractures starting near the contact region
6: Crushing at the contact region of proppants
7: Embedment of proppants into the rock matrix
8: Total disintegration of quartz grains and fines production at the fracture face

Figure 5.16*: Micrograph of loaded rock-proppant systems in Bentheim and Flechtingen sandstone / Classification of fracture pattern. The figure shows micrographs from thinsections (thickness 40 µm) manufactured from rock-proppant contacts. At the fracture face, the Bentheim rock grains (mainly quartz) in contact with proppants are completely disintegrated, and abundant fines are produced (figure a,d,e). Damage of ISP (figure a,b,d) can be observed as well; proppants are mainly cleaved into bigger parts. In contrast, almost no fragments from HSP are visible (figure c). The Flechtingen rock grains are fractured and disintegrated at the rock-proppant contact (figure e). In general, the damage of Flechtingen rock is small compared to Bentheim rock. The observed fracture patterns are classified (compare to the listing).*

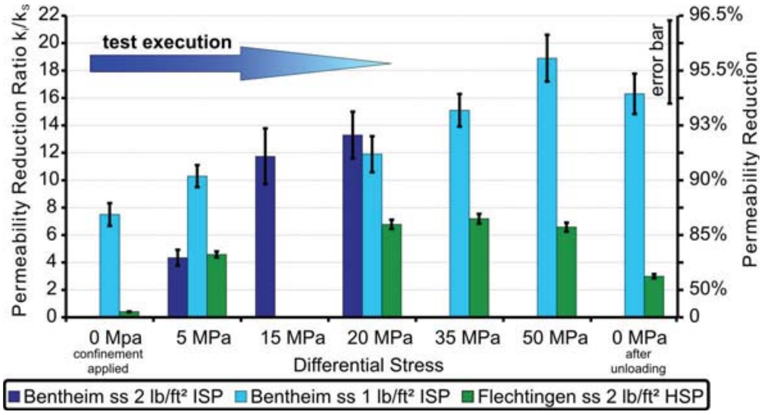

Figure 5.17*: Permeability reduction and permeability reduction ratio of experiments Bent 2.2, Bent 3.4, and FB 1.6. After isostatic loading (σ_{diff} = 0 MPa) the permeability at the fracture face is reduced by a factor of 7 in experiment Bent 3.4 and a further reduction up to 19 (reduction: 95 %) is determined for maximum differential stress. The evolution of permeability ratio of Bent 2.2 parallels with the evolution of Bent 3.4. At σ_{diff} = 20 MPa both experiments feature the same k_i/k_S value of ~ 13. The Flechtingen rock features a smaller reduction ratio compared to Bentheim rock; it is about 7 (reduction: 85 %) for maximum differential stress.*

Grain crushing and blocking of pore space are rarely observed (figure 5.16c&e) at the fracture face of Flechtingen sandstone

The fracture patterns are classified in figure 5.16a&b:

1) Proppant cleavage fractures in direction of the maximum principal external stress
2) Curved proppant fractures connecting contact points
3) Fractures developing from proppant-proppant contact lead to chipping
4) Proppant fractures start mainly from proppant-proppant contacts
5) Fracture initiation is located near the contact region; the fracture propagates from contact region towards the proppant centre
6) In direct vicinity of the contact area, a zone with dense fracture pattern develops
7) Proppants are embedded into the rock matrix
8) Total disintegration of quartz grains and extensive fines production

In §7.5 the observed fracture patterns will be matched with the stress patterns gained from 2D rock-proppant interaction stress modelling.

5.3.5 Permeability Reduction Ratio

From experiments Bent 2.2, Bent 3.4 and FB 1.6 the permeability reduction and the permeability reduction ratios k_i/k_S (compare to equation 2.36) are plotted in figure 5.17. The calculation of the permeability reduction ratio of experiment Bent 2.3 is excluded since the measured k_T values are erroneous.

The isostatic loading (σ_3 = 10 MPa) leads to a permeability reduction ratio of ~ 7 in experiment Bent 3.4, and a further reduction up to a factor of 19 is determined for maximum differential stress. That means the permeability at the fracture face is reduced by 85 % - 95 %. After unloading, a residual permeability reduction ratio of 16 is observed. The evolution of permeability reduction ratio of Bent 2.2 is comparable to the evolution of Bent 3.4: Initial permeability reduction ratio is smaller but at σ_{diff} = 20 MPa both experiments feature the same k_i/k_S value of ~ 13. It is important to note that at 20 MPa differential stress almost no proppant crushing will affect permeability.

Hence, this ratio is purely caused by mechanical rock-proppant interaction. In contrast to Bentheim specimens, the Flechtingen sandstone shows an increase of k_T at small σ_3 = 2 MPa; therefore the reduction ratio is 0.4. At σ_{diff} = 50 MPa the maximum permeability reduction of 7 is achieved, i.e. the permeability at the fracture face is reduced by 85 %. After unloading, a ratio of 3 remains.

For k_S calculation, w_S is estimated from the AE cluster width (see figure 5.11a). Because the AE locations have an uncertainty of 2.5 mm, w_S determined from AE cluster represents an upper limit for the extent of the mechanically induced FFS. An alternative method is the estimation of w_S from micrographs. This method was used in §5.1.4 for estimation of the gauge zone width of a shear fracture.

For a micrograph based w_S estimation, the mean damage penetration is calculated adopting the method from §5.1.4. All pixels that are part of the fracture face skin in a micrograph are counted (yellow dashed lines in figure 5.16a). With respect to the specimen diameter (50 mm), a thickness of 0.15 mm is computed for the FFS zone.

specimen	diff. stress MPa	permeability of FFS zone / k_S mD	reduction ratio / k_i/k_S from micrograph w_S	reduction ratio / k_i/k_S from AE w_S
Bent 2.2	20	6.3 ± 0.8	350 ± 50	13.3 ± 1.7
Bent 3.4	50	5.3 ± 0.5	430 ± 40	18.9 ± 1.7

Table 5.7: *Permeabilities and permeability reduction ratio computed from damage penetrations (w_S) determined from micrographs, as well as from acoustic emission hypocenter locations.*

This w_S yields a k_i/k_S ratio that is 27 times larger for Bent 2.2 and 3.4; the results are given in table 5.7. The discrepancy between both methods will be discussed in §7.6.3 in detail

5.3.6 Spatial AE Activity Distribution

In experiment Bent 2.3 indications are given that the onset of proppant crushing at σ_{diff} = 35 MPa correlates with the increase of tensile events. This will be analysed by computing a spatial distribution of T-, S-, and C-type events for the two last loading steps of all three AE experiments. For that purpose, the AE-events are classified in 1mm thick layers adjacent to the fracture trace. (figure 5.18a-f). The position of the fracture faces in indicated in figure 5.18.

The main AE activity in experiment Bent 2.3 at σ_{diff} = 35 MPa is observed near the fracture faces. About 60 % of the events are C-type, whereas S- and T-type are about 20 %. The activity from the proppant pack is about five times smaller compared to the fracture faces. About 50 % of the activity in the proppant pack is T-type, 30 % S-type and 20 % C-type.

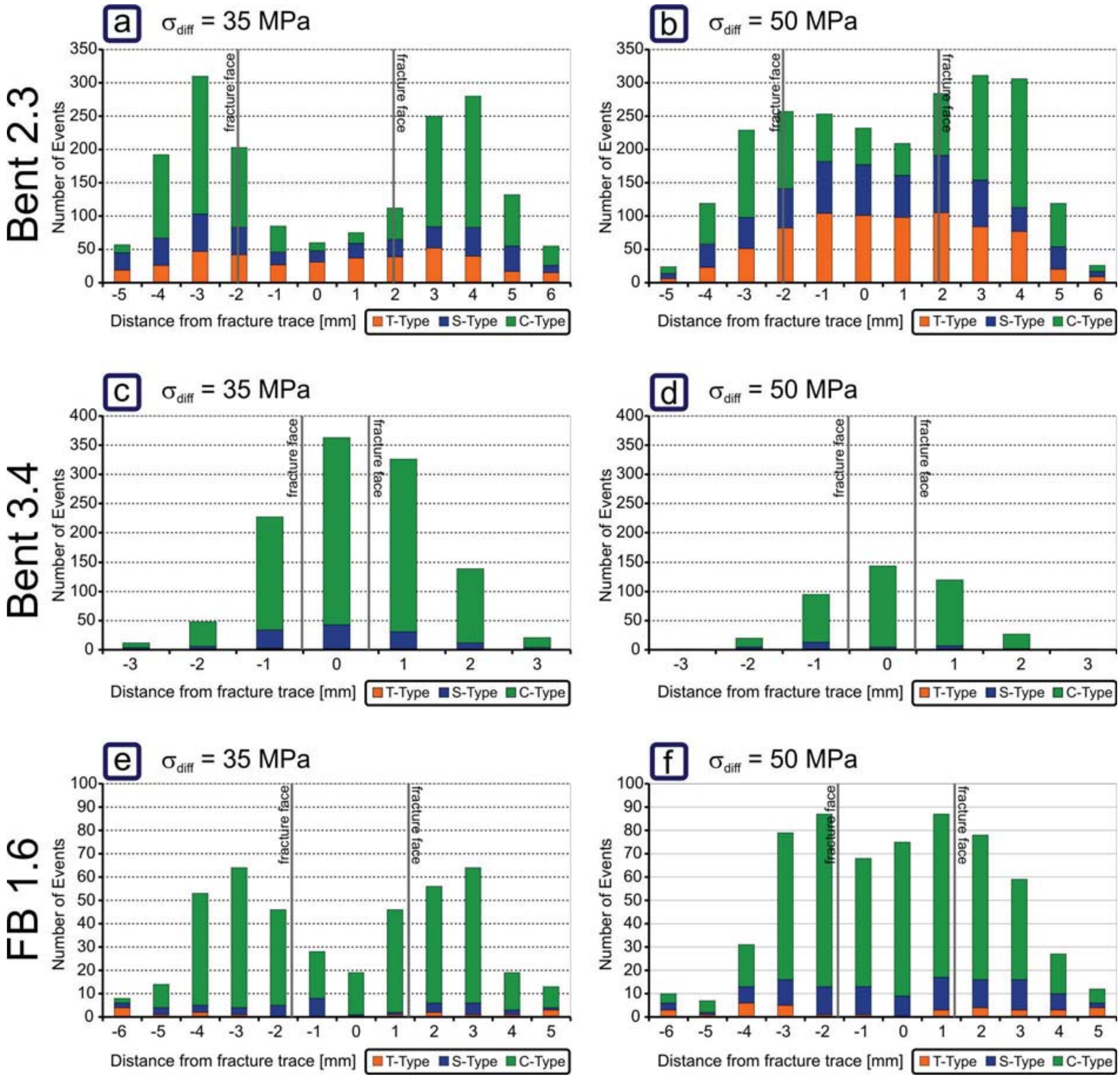

***Figure 5.18**: Spatial AE distribution for Bentheim and Flechtingen RPI experiments. The main AE activity is located at the fracture faces in experiment Bent 2.3 (figure a,b). At maximum differential stress, high AE activity from the proppant pack is recorded (figure b). The damage at the rock-proppant interface is C-type dominated (collapse-type / green), whereas the damage in the proppant pack is T-type dominated (tensile-type / orange) (figure a,b). In RPI experiment FB 1.6 (figure e,f) and Bent 3.4 (figure c,d), the majority of events at the fracture face is C-type. In contrast to experiment Bent 2.3, a domination of C-type is observed within the proppant pack. About 10 % S-type (shear / blue) and almost no T-type is observed in these experiments.*

This percentage distribution of AE events does not change for σ_{diff} = 50 MPa (figure 5.18b), but the number of events detected from the proppant pack increases. In comparison to figure 5.18a, a small increase of T- and S-type at the expense of C-type events can be observed

Figure 5.18c&d displays the AE distribution for experiment Bent 3.4. The fracture width of specimen Bent 3.4 is too small to separate the events from fracture face and proppant pack clearly. At σ_{diff} = 35 MPa the AE events are highly localised around the trace of the fracture. The main activity is observed from the centre (proppant pack), but the adjacent classes show a high activity at the same order of magnitude. Almost no T-type events are recorded (~ 1 %), 88 % of the events are C-type and 11 % are S-type. At σ_{diff} = 50 MPa, about 90 % of the activity is C-type, no increase of T- and S-type events is observed. In contrast to experiments Bent 2.3 and FB 1.6, the total number of events is reduced in the last loading step.

In experiment FB 1.6, considerably fewer events are recorded compared to experiments Bent 2.3 and Bent 3.4, but a separation between fracture face and proppant pack is visible (figure 5.18e). At σ_{diff} = 35 MPa, about 90 % of the AE activity at the fracture face is C-type, some S-type (~ 9 %) and some T-type events (~ 4 %) are observed. Comparable to experiment Bent 2.3, an increase of T- and S-type at the expense of C-type is recorded in the last loading step. Within the proppant pack the activity increases, almost no T-type event is recorded, the main activity is C-type.

5.4 Rock-Proppant Interaction Testing – BDFC

5.4.1 Bentheim Sandstone + Intermediate Strength & High Strength Proppants

Results of the rock-proppant interaction (RPI) experiments Bent 3.1 and Bent 3.5 are summarised in figure 5.19a-f as a function of differential stress (σ_{diff}). A confining pressure (σ_3) of 10 MPa is applied with a Hoek-Cell [Sun & Ouchterlony 1986]. The setup is downstream open to atmosphere; the mean pore pressure is about 1 bar. Flow rate for testing the rock and the rock-proppant system is 5 ml/min; for testing the proppant pack the flow rate is 60 ml/min. Initially a confining pressure of 10 MPa is applied to the specimen in order to seal the specimen against bypass flow. Only a small axial load is applied in order to measure the initial permeability of a rock-proppant system. Hence, σ_{diff} is negative at the beginning of an experiment because the confining pressure is higher than the axial stress. The experiments with intermediate strength (ISP) and high strength proppants (HSP) are conducted with two different Bentheim sandstone cores. The two cores are from the same sandstone block, and they have almost the same permeability. Testing parameters are listed in table 5.8.

rock testing			rock-proppant interaction testing		
	Bent 3.5	**Bent 3.1**		**Bent 3.5**	**Bent 3.1**
specimen length	120 mm	120 mm	specimen length	64.0 mm	65.2 mm
Young's modulus	21.9 GPa	21.3 GPa	fracture width	4.6 mm	3.9 mm
permeability	1480 mD	1460 mD	proppant type	ISP	HSP
strain rate	$8.30\ 10^{-6}\ s^{-1}$	$8.30\ 10^{-6}\ s^{-1}$	strain rate	$1.56\ 10^{-6}\ s^{-1}$	$1.53\ 10^{-6}\ s^{-1}$
diff. stress	0-67 MPa	0-67 MPa	diff. stress	0-52 MPa	0-53 MPa
conf. pressure	10 MPa	10 MPa	conf. pressure	10 MPa	10 MPa
mean pore pressure	0.10-0.11 MPa	0.10-0.11 MPa	mean pore pressure	0.10-0.11 MPa	0.10-0.11 MPa

Table 5.8*: Parameters for rock-proppant interaction testing of ISP and HSP with Bentheim sandstone.*

The initial permeability (k_i) of both Bentheim sandstones specimens is about 1470 mD with no poroelastic permeability change within the loading range (figure 5.19a). Already at σ_{diff} = -8 MPa (corresponding to an axial stress of 2 MPa), the permeability of the rock-proppant system (k_T) shows a clear reduction compared to k_i. Both specimens (ISP and HSP) have almost the same initial permeability reduction The specimen with ISP has a k_T of 1210 ± 60 mD and the specimen with HSP has a k_T of 1180 ± 40 mD. A further reduction at maximum σ_{diff} to 950 ± 40 mD and 890 ± 30 mD, respectively, can be observed. After unloading the sample (last value in figure 5.19a), the permeability is reduced permanently and no permeability recovery can be detected.

The permeabilities of the FFS zone (k_S) are calculated using equation 3.3b. The results are displayed in figure 5.19b. The ISP and the HSP specimen have a k_S = 260 ± 30 mD initially. At σ_{diff} = 50 MPa the specimens show a reduced permeability of 141 ± 11 mD and 125 ± 8 mD, respectively. The permeability reduction ratio (k_i/k_S) varies between 11 and 6 (figure 5.19c). That means compared to k_i the permeability at the fracture face is reduced by 80 % - 90 %.

Figure 5.19d plots the permeability of the proppant pack (k_f). The errors of these measurements are high (up to 40 %) due to resolution limit of the used differential pressure transducer. The ISP has an initial k_f of 480 ± 200 D, for the HSP k_f is 450 ± 130 D. The ISP permeability is clearly reduced to k_f = 180 ± 30 D for maximum σ_{diff}. The HSP permeability reduction is moderate; k_f is 320 ± 30 D at maximum differential stress. After unloading and opening the fracture, damage and a lot of fines are observed in both proppant packs. Crushed proppants as well as fines from quartz grains are visible (figure 5.22).

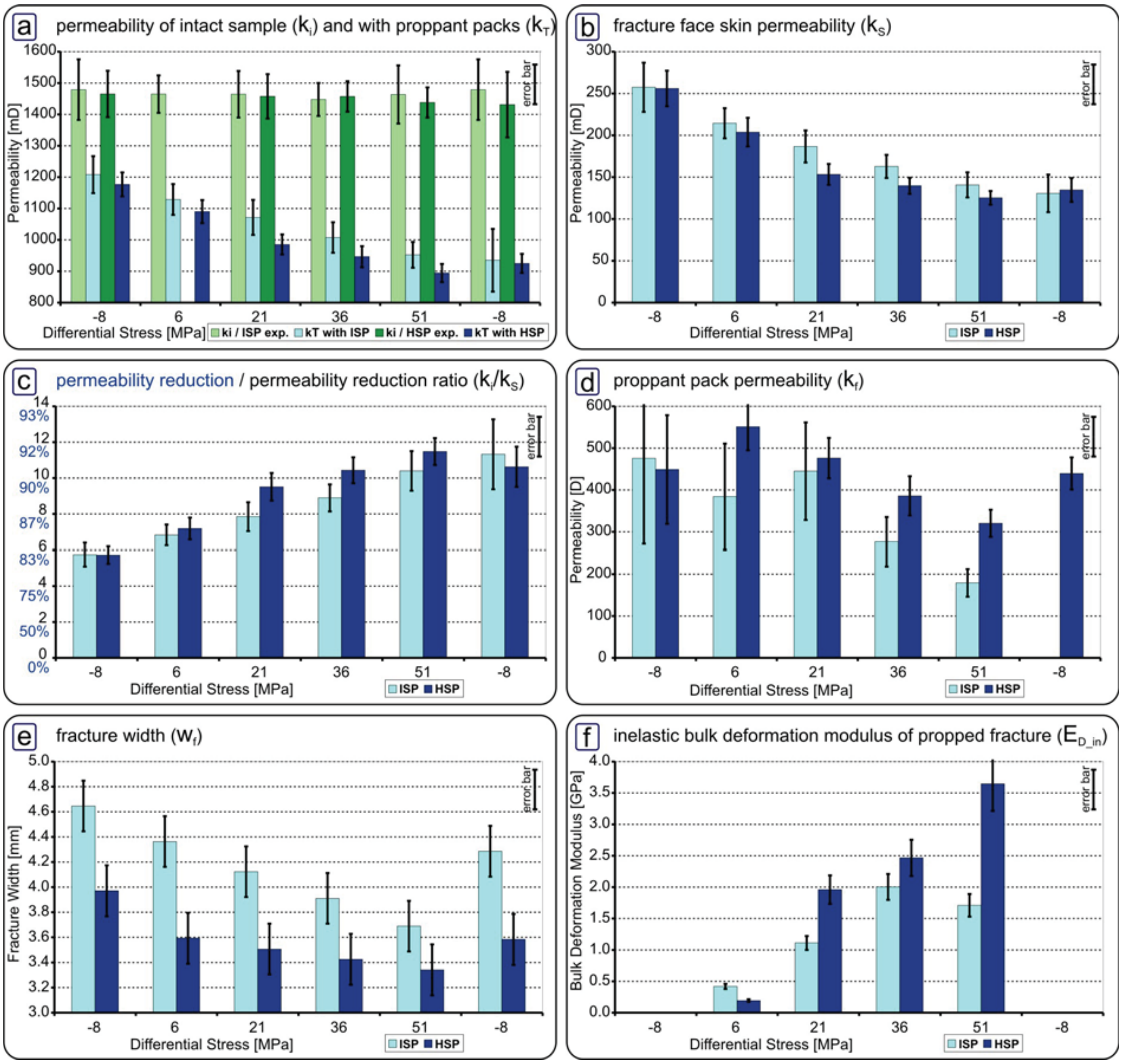

Figure 5.19: *Results from rock-proppant interaction testing of ISP and HSP with Bentheim sandstone. Figure a, b, and d show the permeability evolution during of the intact Bentheim rock specimen (k_i), rock-proppant system (k_T), fracture face skin zone (k_S), and proppant pack (k_f). The permeability of Bentheim sandstone is not stress dependent within the applied stress interval (0 – 50 MPa), whereas the rock-proppant system features a significant permeability reduction with increasing differential stress. This leads to a reduction ratio (figure c) between 6 and 11 compared to k_i. , i.e. the permeability is reduced by 80 % - 90 %. The proppant pack permeability (k_f) of both proppant types is reduced by factor of 2 within the applied stress interval (figure d). The HSP pack has a smaller initial fracture width compared to the ISP pack (figure e); the reduction of fracture width (w_f) is about 12 % for both proppant types. From the change in fracture width, the inelastic bulk deformation modulus (E_{D_in}) of the rock-proppant system is extracted (figure f). A small modulus reflects a high amount of inelastic deformation. The modulus is small at initial loading of the rock-proppant systems and increases with differential stress. A difference between both proppant types becomes obvious at maximum differential stress (50 MPa). The ISP shows a decrease indicating an increase of inelastic deformation, whereas the HSP shows an opposing trend.*

The measurements of proppant pack permeability were difficult. Fines from crushed quartz grains block the small flow and pressure ports (width 0.4 mm) of the setup during the experiments. The determined permeability values are in the range of the values from the manufacturer data sheet (compare to §4.2). The manufacturer specifies for the ISP a permeability range of 550 D - 250 D within the applied stress interval and for the HSP 550 D - 350 D, respectively.

The ISP pack has an initial fracture width of 4.6 mm which is reduced by 20 % at σ_{diff} = 50 MPa. The HSP has a smaller initial width of 4.0 mm due to higher density of that proppant material. Reduction of width is 16 %; it is smaller since this proppant type is tougher and less damage of the proppant pack can be expected. From stress change ($\Delta\sigma_{diff}$) and reduction in fracture width (Δw_f), a bulk deformation modulus E_D is determined:

$$E_D = \frac{\Delta\sigma_{diff}}{\Delta w_f} \cdot w_{fi} \qquad 5.2$$

where w_{fi} is the initial fracture width prior to axial loading. The bulk deformation modulus comprises elastic and inelastic components from compacting the proppant pack and the rock-proppant interface. The deformation of the proppant pack is caused by reorganisation and damage of proppants, as well as elastic deformation. The damage of quartz grains at rock-proppant contact is inelastic. Additionally, elastic deformation of quartz grains occurs at the rock-proppant interface. During unloading (last values in figure 5.19f) the deformation is controlled by elastic component exclusively. Hence, E_D from unloading (E_{D_el}) can be used in order to extract the bulk deformation modulus that reflects the inelastic components (E_{D_in}):

$$E_{D\_in} = \frac{E_{D\_el} \cdot E_D}{E_{D\_el} - E_D} \qquad 5.3$$

A small E_{D_in} accompanies large inelastic deformation. E_{D_in} quantifies the mechanical damage in the rock-proppant system. Figure 5.19f shows the E_{D_in} values for the two Bentheim RPI experiments. The initial differential loading (σ_{diff} = 6 MPa) leads to a small E_{D_in} = 0.4 GPa for ISP and 0.2 GPa for HSP. With increasing differential stress, the bulk deformation modulus increases as well. In general, the modulus of ISP is smaller than the modulus of HSP. This difference becomes obvious at σ_{diff} = 50 MPa, where HSP shows a significant increase of E_{D_in} accompanied with a reduction of inelastic deformation. In contrast, ISP shows a decrease of E_{D_in} accompanied with an increase of inelastic deformation. Besides damage, the inelastic deformation is characterised by reorganisation and compaction of the proppant pack, particularly during the first loading step.

5.4.2 Flechtingen Sandstone + Intermediate Strength & High Strength Proppants

Results of RPI experiment FB 7.4 are shown in figure 5.20a-f as a function of the differential stress (σ_{diff}). Loading conditions are identical to the Bentheim sandstone experiments. The mean pore pressure is about 2-3 bars. Flow rate for testing the rock and the rock-proppant system is 0.05 ml/min; for testing the proppant pack, flow rate is 60 ml/min. Testing parameters for these experiments are listed in table 5.9.

The initial permeability of this Flechtingen sandstone (k_i) is about 200 µD with a poroelastic permeability change of 15 % (figure 5.20a) within the applied loading range. At σ_{diff} = -7 MPa, which corresponds to an axial stress of 3 MPa, k_T shows a clear reduction.

rock testing		**rock-proppant interaction testing**		
	FB 7.4		**FB 7.4**	**FB 7.4**
specimen length	120 mm	specimen length	65.3 mm	63.3 mm
Young's modulus	19.1 GPa	fracture width	4.8 mm	3.9 mm
permeability	196 µD	proppant type	ISP	HSP
strain rate	$8.30\ 10^{-6}\ s^{-1}$	strain rate	$1.53\ 10^{-6}\ s^{-1}$	$1.57\ 10^{-6}\ s^{-1}$
diff. stress	0-65 MPa	diff. stress	0-53.7 MPa	0-53.8 MPa
conf. pressure	10 MPa	conf. pressure	10 MPa	10 MPa
mean pore pressure	0.13-0.22 MPa	mean pore pressure	0.10-0.20 MPa	0.10-0.22 MPa

***Table 5.9**: Parameters for rock-proppant interaction testing of ISP and HSP with Flechingen sandstone*.

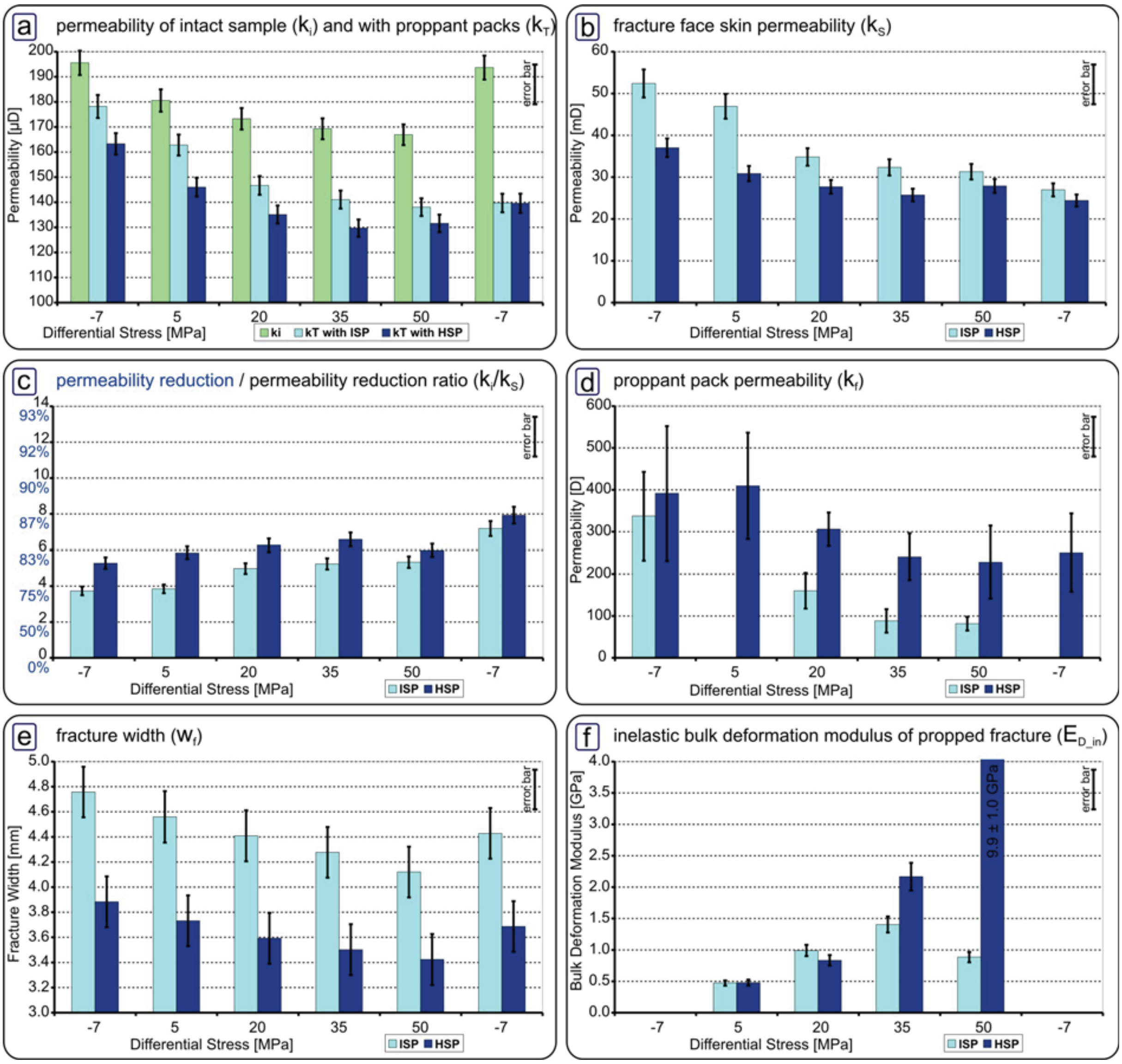

Figure 5.20: *Results from rock-proppant interaction testing of ISP and HSP with Flechtingen sandstone. Figures a, b, and d show the permeability evolution during experiment execution of the intact Flechtingen rock specimen (k_i), rock-proppant system (k_T), fracture face skin zone (k_S), and proppant pack (k_f). The permeability of Flechtingen sandstone shows a poroelastic permeability reduction of 15 % within the applied stress interval (0 – 50 MPa). The rock-proppant system features a significant higher permeability reduction with increasing differential stress; at maximum differential stress, the permeability is reduced about 25 %. This decrease is caused by the permeability reduction at the rock-proppant interface. This leads to a permeability reduction ratio (figure c) between 4 and 8, i.e. the permeability of the FFS zone is reduced by 75 % - 87.5 %. The proppant pack permeability (k_f) of both proppant types decreases with increasing stress (figure d). The ISP and HSP are reduced by a factor of 4 and 2, respectively. The HSP pack has a smaller initial fracture width compared to the ISP pack (figure e); the reduction of fracture width (w_f) is about 12 % for both proppant types. From the change in fracture width, the inelastic bulk deformation modulus (E_{D_in}) of the rock-proppant system is extracted (figure f). A small modulus reflects a high amount of inelastic deformation. Both proppant types have the same, small E_{D_in} at initial loading of the sample. With increasing differential stress, an increase of modulus is observed.*

The permeability of the rock-proppant system (ISP) is reduced to k_T = 180 ± 5 µD, the HSP rock-proppant system has a reduced permeability of k_T = 163 ± 4 µD. At maximum σ_{diff} a further reduction to 138 ± 4 µD and 131 ± 4 µD, respectively, is observed. After unloading the sample, a residual permeability reduction remains.

The permeabilities of the FFS zone are displayed in figure 5.20b. The ISP specimen shows initially a permeability reduction by a factor of 4 (k_S = 52 ± 3 µD); the HSP sample has a reduction by a factor of 5 (k_S = 37 ± 2 µD). At σ_{diff} = 50 MPa both specimens have a k_S value of about 31 µD. The permeability reduction ratio increases from 4 to 8 (compare figure 5.20c), whereby the HSP has a slightly higher damage potential. This means compared to initial value k_i, the permeability at the fracture face is reduced by 75 % - 88 %.

Figure 5.20d shows the permeability of the proppant pack (k_f). The ISP has an initial k_f = 338 ± 105 D and the HSP has k_f = 390 ± 160 D. The ISP is reduced drastically to k_f = 81 ± 16 D at maximum σ_{diff}. The HSP permeability decreases to 228 ± 90 D The HSP permeabilities are within the range of manufacturer's data (550 D - 350 D), whereas the ISP permeabilities show a significant discrepancy to the manufacturer's data (550 D – 250 D). Technical problems inhibit the permeability measurement at σ_{diff} of 5 MPa and -7 MPa for the ISP type.

In figure 5.20e fracture width as function of differential stress is plotted. The ISP pack has an initial width about 4.7 mm, which decreases by 13 % at σ_{diff} = 50 MPa. The HSP has a smaller initial width of 3.9 mm, but the reduction is slightly smaller at 12%. The initial modulus of inelastic bulk deformation (E_{D_in}) is 0.5 GPa for both proppant types (figure 5.20f). With increasing σ_{diff} the modulus increases as well. Comparable to the Bentheim sandstone experiments (previous section), the modulus of ISP shows a decrease at maximum differential stress, whereas the modulus of HSP shows a strong increase (E_{D_in} = 10 GPa).

5.4.3 Flechtingen Sandstone + Intermediate Strength Proppants Continuous Stress Change

In order to compare the continuous permeability changes of Flechtingen sandstone with the permeability alteration of a rock-proppant system under increasing differential stress, an experiment (FB 2.1) with a small strain rate about 7.5 10^{-6} s^{-1} and continuous stress change was conducted. This experiment is not adopted for k_T calculation, because the strain rate was still too high to guarantee steady-state pressure conditions (Darcy conditions are violated). The experiment illustrates the additional permeability reduction observed in the rock-proppant system. Flow rate for testing the rock as well as the rock-proppant system is 0.1 ml/min; the pore fluid is 2 % KCl brine. Testing parameters for this experiment are listed in table 5.10.

rock testing		**rock-proppant interaction testing**	
	FB 2.1		**FB 2.1**
specimen length	120 mm	specimen length	66.2 mm
Young's modulus	13 GPa	fracture width	4.7 mm
permeability	546 µD	proppant type	ISP
strain rate	4.2 10^{-6} s^{-1}	strain rate	7.6 10^{-6} s^{-1}
diff. stress	0-67 MPa	diff. stress	0-53 MPa
conf. pressure	10 MPa	conf. pressure	10 MPa
mean pore pressure	0.17-0.20 MPa	mean pore pressure	0.10-0.17 MPa

***Table 5.10**: Testing parameters of rock-proppant interaction experiment with continuous stress change.*

Two curves are plotted in figure 5.21. The green curve shows the poroelastic permeability change of the intact Flechtingen rock. At maximum differential stress (50 MPa) the permeability is reduced by 15 %. The blue curve reflects the continuous permeability change of the rock-proppant system (Flechtingen sandstone with ISP). The discontinuities in the blue permeability curve are caused by intermittent loading to measure proppant pack permeability.

For direct comparison of the relative permeability change, the curves are normalised with their initial values (k_i = 535 µD and k_T = 415 µD, respectively). It is obvious that the permeability reduction of rock-proppant system (k_T) is larger than the poroelastic permeability change. The permeability of the rock-proppant system is reduced by 25% and unloading does not recover the permeability completely. The comparison of the curve shapes point out that the majority of permeability reduction due to rock-proppant interactions occurs within the differential stress interval 0 – 20 MPa. In this interval the blue curve has a significantly steeper slope compared to the green curve, whereas the slopes in the interval 20 – 50 MPa are almost identical.

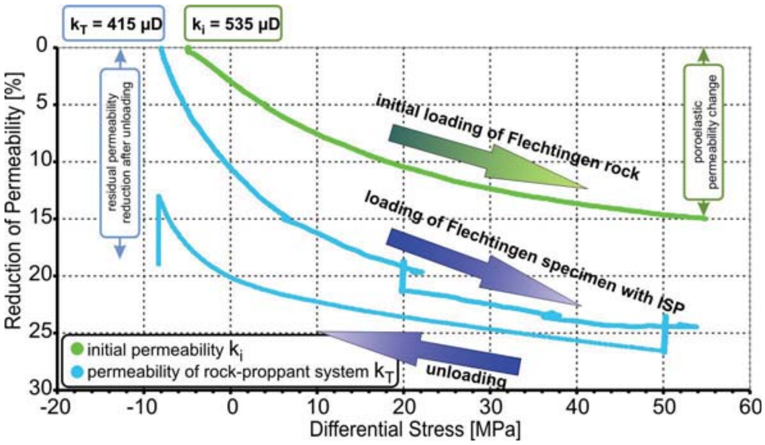

Figure 5.21*: Continuous permeability change of a Flechtingen sandstone (FB 2.1) with ISP pack. The comparison shows that the permeability reduction of the rock-proppant system (k_T / blue curve) is significantly larger than the poroelastic permeability reduction of the Flechtingen sandstone (k_i / green curve). In particular, within the differential stress interval 0 – 20 MPa the blue curve features a steeper slope compared to the green curve. After unloading the specimen, a residual permeability reduction of 19 % is observed.*

After unloading the specimen completely, a further reduction of permeability is observed. This reduction is an effect of non steady-state pressure conditions during unloading the specimen; a strain rate of $3\ 10^{-5}$ 1/s was used for unloading. After unloading, the experiment is continued until steady-state conditions are reached. The permeability is reduced permanently by 19 %.

5.4.4 Fines Production and Fines Transport in the Proppant Pack

After opening the fracture, photos are taken from the proppant pack and the fracture face with a reflected-light microscope (figure 5.22a-f). Figures 5.22a&b show micrographs of the proppant pack of RPI experiment FB 7.4 with ISP. The proppant pack permeability was dramatically reduced during this experiment (compare to figure 5.20d / light blue bars). The optical inspection of the proppant pack identifies a large amount of fines from crushed proppants. Figures 5.22c&d illustrate the proppant imprints (proppant embedment) into the fracture face. The grains below the contact are completely disintegrated, indicated by the white spots on the red Flechtingen or grey-pink Bentheim sandstone.

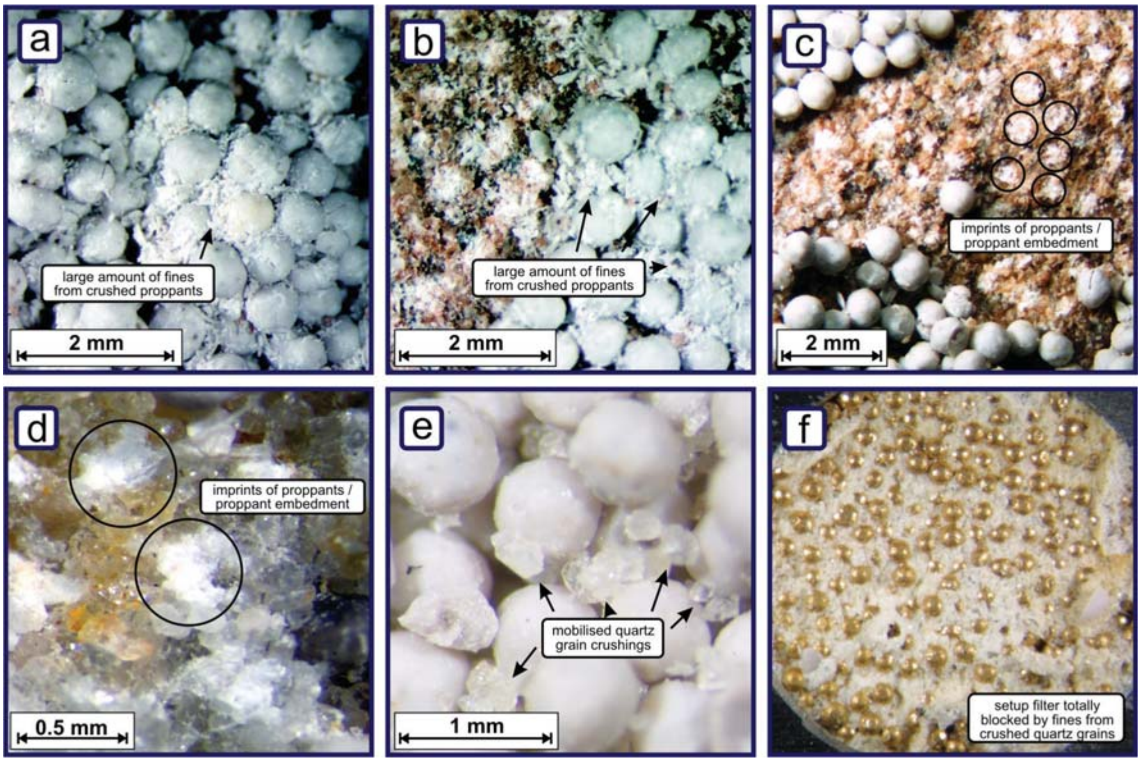
a
large amount of fines from crushed proppants
2 mm
b
large amount of fines from crushed proppants
2 mm
c
imprints of proppants / proppant embedment
2 mm
d
imprints of proppants / proppant embedment
0.5 mm
e
mobilised quartz grain crushings
1 mm
f
setup filter totally blocked by fines from crushed quartz grains

Figure 5.22*: Photo collection of proppant packs and fracture faces after testing with the BDFC. The photos show fines produced from crushed proppants (figures a and b), as well as from quartz grains (figures e and f). Figures c and d illustrate the imprint of proppants (embedment) into the rock matrix.*

These micrographs show that not the entire fracture face is affected by mechanical damage. The damage is limited to the direct contact area between grains and proppants, about 2/3 of the fracture face remains unaffected. The thin sections in §5.3.4 give the same impression of proppant embedment (compare to figure 5.16). Figures 5.22e&f illustrate the fines transported from the fracture face into the proppant pack. In figure 5.22e, some crushings from quartz grains accumulate in the pore space of the proppant pack. If these crushings are small enough, they are transported through the pore space and deposit in the filter of the setup. Fines from quartz grains have completely blocked the downstream filter of the BDFC (figure 5.22f). In order to avoid any influence on the permeability measurements, this downstream filter was removed from the setup after the first tests.

5.5 Rock-Proppant Interaction Testing - LTFC

Experimental results of three long-term experiments are presented in this section: FB 10.11, FB 10.12, FB 10.13. An effective stress (σ_{eff}) of 10 MPa is applied to the specimens in the long-term flow cell (LTFC). This σ_{eff} corresponds to the expected maximum effective pressure (σ_{eff_max}) acting on the proppant pack at designed drawdown conditions in the Gross Schoenebeck production well GtGrSk4/05 [Zimmermann et al. 2008]. To simulate drawdown conditions during a gas lift test in the Gross Schoenebeck injection well EGrSk3/90, σ_{eff} is increased up to 27 MPa. The maximum effective stress (σ_{eff_max}) on the proppant pack normal to the fracture face is:

$$\sigma_{eff\_max}=\sigma_h-P_P+\Delta P_{dd} \qquad 5.4$$

where σ_h is the minimum horizontal stress in the reservoir, P_P is the pore pressure and ΔP_{dd} is the differential drawdown pressure during production. The main pay zone of the geothermal reservoir is the Lower Dethlingen formation (σ_h = 52 MPa) [Legarth et al. 2005b, Zimmermann et al. 2008]. A second, less permeable pay zone is the Upper Dethlingen (σ_h = 59 MPa). The reservoir pore pressure at equilibrium conditions is P_P = 44 MPa, and the designed long-term draw down of the reservoir is about 100 m fluid column, corresponding to ΔP_{dd} = 1 MPa. During testing operations (nitrogen lift test), pore pressure was lowered by ~ 12 MPa. This leads to a maximum effective stress (σ_{eff_max}) on proppant pack in the Upper Dethlingen of 27 MPa and in the Lower Dethlingen of 20 MPa. During long-term production, the stress on proppant pack is about 10 MPa.

In order to simulate reservoir conditions, a maximum isostatic pressure of 50 MPa is applied to the rock specimens and the temperature is increased up to 150 °C. Pore fluid is 0.1 molar NaCl brine. Milsch et al. [2007] have ascertained that effects of electrical surface conductivity can be neglected if 0.1 molar NaCl-brine is used as pore fluid. Table 5.11 lists all relevant reservoir parameters.

reservoir parameters / Gross Schoenebeck			
		Upper Dethlingen	**Lower Dethlingen**
reservoir depth	z	4080 m TVD	4120 m TVD
bottom hole temperature	T	150 °C	150 °C
min. horizontal stress	σ_h	59 MPa	52 MPa
reservoir pore pressure	P_P	44 MPa	44 MPa
long-term drawdown	ΔP_{dd}	1 MPa	1 MPa
max. drawdown	ΔP_{dd}	12 MPa	12 MPa
resulting effective stresses for long-term rock-proppant interaction testing			
long-term effective stress	σ_{eff}	16 MPa	9 MPa
max. effective stress	σ_{eff}	27 MPa	20

Table 5.11: *Reservoir parameters of Gross Schoenebeck pay zones and resulting effective stresses for long-term testing of Flechtingen sandstone and rock-proppant systems.*

The complex mounting and sealing procedure of the specimens in the LTFC inhibits the direct comparison of the initial rock permeability (k_i) with the permeability of the rock-proppant system (k_T) measured with the same rock specimen. In particular, during dismounting of the core holder, the decreasing confining pressure leads to tension cracks in the silicon glue, and small amounts of confining oil can penetrate the specimen. These oil traces alter the permeability of the sandstone, and mounting the same specimen twice (comparable to the RPI experiments in §5.3 and §5.4) would lead to erroneous results. In order to compare permeabilities of the Flechtingen sandstone (k_i) and the rock-proppant systems (k_T), cores from a homogeneous Flechtingen sandstone block are drilled with small offset between the individual drill cores.

FB 10.11 is an intact sample, used to test the hydraulic long-term behaviour of the Flechtingen sandstone at reservoir conditions. FB 10.12 and FB 10.13 contain a 2 lb/ft² (~ 10 kg/m²) proppant layer of ISP and HSP, respectively. Table 5.12 specifies the relevant testing parameters. Figure 5.23a-c presents the permeability (blue dots) and formation factor (green dots), confining pressure (black line), pore pressure (black line), and temperature (red line) as function of time. The effective stress is characterised by the area between the confining pressure graph and pore pressure graph.

		rock testing	**rock-proppant interaction testing**	
		FB 10.11	**FB 10.12**	**FB 10.13**
specimen length	L	40 mm	42.2 mm	43.8 mm
distance of rims	d_r	25 mm	32.2 mm	33.8 mm
confining pressure	σ_3	15–50 MPa	15–50 MPa	3–50 MPa
pore pressure	P_P	5–40 MPa	5–40 MPa	0.5–40 MPa
temperature	T	40–150 °C	40–150 °C	40–150 °C
proppant type		- / -	HSP	ISP
flow rate	Q	0.05–0.1 ml/min	0.05–0.1 ml/min	0.05–0.1 ml/min

***Table 5.12**: Testing parameters for LTFC investigations.*

5.5.1 FB 10.11: Flechtingen Sandstone

Specimen FB 10.11 was subjected to a continuous flow for 16 days. During the first day, P_P is 5 MPa, σ_3 is 15 MPa and the temperature is increased from room temperature to reservoir temperature of 150 °C (compare to black, grey and red graphs in figure 5.23a).

A significant reduction of permeability from 0.86 mD to 0.18 mD after 5.5 hours (0.2 days) can be observed (table 5.13). No distinction between a temperature, fluid or stress driven effect is possible. The reduction can be caused by temperature increase, by irreversible consolidation processes or by chemical interaction of the clay minerals with the pore fluid. This problem will be discussed in detail in §7.8.

After the initial phase of experiment FB 10.11, k_i decreases slightly over 7 days to 0.12 mD and then keeps constant for the remaining time of the experiment. The change in pressure conditions from σ_3 = 50 MPa to 15 MPa with σ_{eff} = constant (day 9), shows that k_i is only influenced by changes in effective pressure. After 15 days of testing, temperature decreases to 30 °C, whereby k_i shows a small increase to 0.13 mD. This increase can be an artefact due to a non-perfect viscosity adjustment. At ambient conditions, the fluid viscosity shows large temperature dependence. Small errors in temperature determination have a strong effect on permeability (compare to §3.4.4). The long-term permeability (k_i = 0.120 ± 0.007 mD) at reservoir conditions of this Flechtingen rock sample is determined in the time interval 8 d – 15 d.

The decrease of k_i within the first five days is accompanied by a decrease of formation factor FF (green squares in figure 5.23a). During the high confining pressure stage of the experiment (time interval 1 d – 9 d), FF is about 38. In contrast to permeability, FF reacts more sensitively to the changes in pressure conditions (day 9). The decrease of σ_3 to 15 MPa at σ_{eff} = constant leads to an increase of FF to 44. This corresponds to a decrease of electrical conductivity (κ_R) of the specimen.

5.5.2 FB 10.12: Flechtingen sandstone + High Strength Proppants

Experiment FB 10.12 is conducted with a Flechtingen sandstone core and a high strength proppant (HSP) pack of 2 lb/ft² (~ 10 kg/m^2). The testing procedure is identical to experiment FB 10.11. A delay of 1 day between increasing σ_{eff} and increasing T enables the possibility to differentiate between temperature and stress effects on the permeability. The initial permeability of the rock-proppant system (k_T) is about 0.76 mD (measured after 0.1 days of fluid flow / table 5.13). At time 0.8 d, the permeability is reduced to 0.128 mD – comparable to the permeability reduction in experiment FB 10.11. Increasing the temperature to 150 °C, leads to a further reduction of k_T. The permeability of the rock-proppant system stabilises at 0.1 mD after two days.

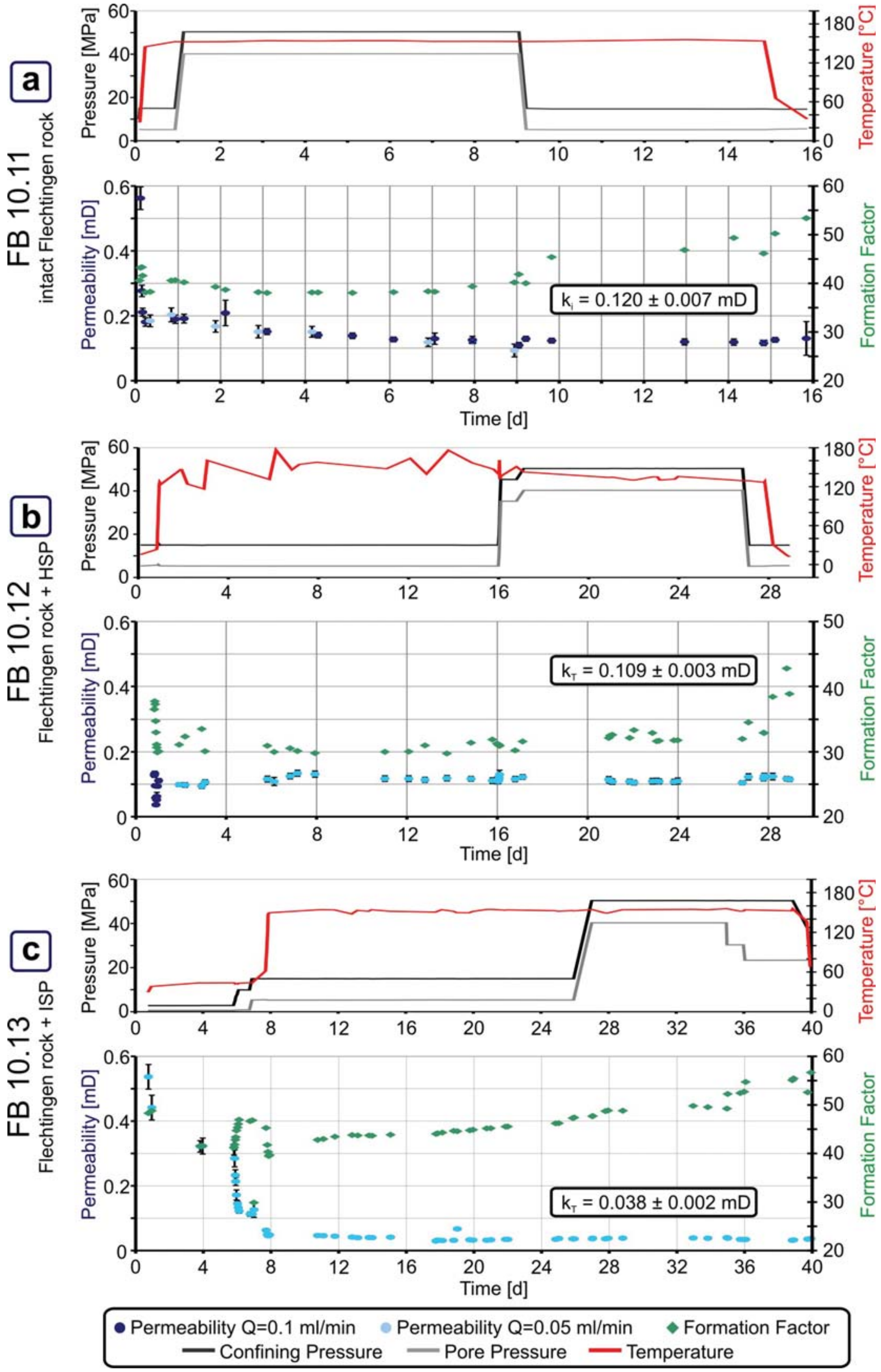

Figure 5.23: *Permeability and formation factor from testing Flechtingen sandstone with ISP and HSP packs in the LTFC. Figure a-c shows the permeability (k_i, k_T) and the formation factor FF, effective stress, and temperature as function of time. The effective stress is characterised by the area between the graphs of confining pressure (black line) and pore pressure (gray line). Obviously, the permeability (blue dots) undergoes a reduction due to pressure and temperature changes, as well as time of fluid exposure. After sufficient time, the permeability reaches a constant level. A permeability decrease is accompanied by an increase of the formation factor (green squares). Hence, the impairment of fluid pathways is accompanied by a reduction of electrical rock conductivity.*

experiment FB 10.11 / intact specimen					
time [d]	eff. stress [MPa]	temp. [°C]	permeability [mD]	permeability reduction [%]	formation factor [ ]
0.08	5	28	0.86 ± 0.04	- / -	41
0.2	10	150	0.18 ± 0.01	~ 80	38
8 - 15	10	150	0.120 ± 0.007	~ 85	44
experiment FB 10.12 / HSP					
time [d]	eff. stress [MPa]	temp. [°C]	permeability [mD]	permeability reduction [%]	formation factor [ ]
0.1	10	35	0.76 ± 0.05	- / -	11
0.8	10	48	0.133 ± 0.007	~ 80	37
2.2	10	150	0.098 ± 0.007	~ 87	30
21 - 27	10	150	0.109 ± 0.003	~ 85	32
experiment FB 10.13 / ISP					
time [d]	eff. stress [MPa]	temp. [°C]	permeability [mD]	permeability reduction [%]	formation factor [ ]
0.75	2.2	30	0.54 ± 0.04	- / -	48
5	2.2	44	0.322 ± 0.02	~ 44	41
7	10	45	0.172 ± 0.02	~ 70	47
8	10	150	0.048 ± 0.002	~ 92	40
25 - 35	10	150	0.038 ± 0.002	~ 93	50
35	20	150	0.034 ± 0.002	~ 94	53
36	27	150	0.032 ± 0.002	~ 95	56

Table 5.13*: Evolution of permeability and formation factor of three long-term experiments conducted with Flechtingen sandstone, high strength (HSP) and intermediate strength proppants (ISP).*

During the experiment of 29 days, permeability shows only minor variations. A mean value of k_T = 0.109 ± 0.003 mD is calculated within the time interval 21 d - 27 d. Increasing and decreasing of σ_3 (day 16 and day 27 / σ_{eff} = constant), induces a very small alteration of permeability. The formation factor (FF) shows a small increase in the high confining pressure stage from 30 to 32.

5.5.3 FB 10.13: Flechtingen Sandstone + Intermediate Strength Proppants

Experiment FB 10.13 (figure 5.23c) is conducted with an intermediate strength proppant (ISP) pack of 2 lb/ft² (~ 10 kg/m^2). In order to differentiate between fluid interaction effects, temperature effects and stress effects on permeability, delay times between changing these parameters are inserted in the experimental schedule. At the end of the experiment (day 35), P_P is decreased to 30 MPa and 23 MPa, respectively, while σ_3 is constant at 50 MPa. This increase of σ_{eff} simulates drawdown conditions during the nitrogen lift test conducted in Gross Schoenebeck well EGrSk3/90.

Initially, P_P is 0.5 MPa, σ_3 is 3 MPa, and T is 40 °C (table 5.13). At these stress and temperature conditions, fluid flow is delivered to the sample for 6 days. The initial permeability (k_T) is about 0.54 mD after 0.5 days (table 5.13). After 4 days, k_T has decreased to 0.32 mD. Increasing σ_{eff} to 10 MPa (day 6) leads to a reduction of k_T to 0.17 mD. The temperature increase to 150 °C at day 8 has a large influence on permeability; k_T is further reduced to 0.048 mD (table 5.13). In general, the formation factor mirrors the k_T behaviour. The increase of σ_{eff} at day 6 results in an increase of FF from 41 to 47.

Within the time interval 10 – 18 d, k_T reaches a final value of 0.038 ± 0.002 mD. The change in stress conditions (σ_{eff} = const.) at day 26 does not affect the permeability. The increase of σ_{eff} to 20 MPa and 27 MPa (day 35) leads to an alteration of permeability and formation factor. FF increases from 48 to 53 and 56, respectively. This corresponds to a decrease of electrical rock conductivity of 6 % and 11 %. Similarly, k_T shows a reduction to 0.034 mD (σ_{eff} = 20 MPa) and

0.032 mD (σ_{eff} = 27 MPa). The permeability is reduced about 10 % and 15 %, respectively. These reduction values are calculated with respect to the long-term values of FF and k_T.

5.5.4 Microstructural Observations

Microscopic observations of thin sections from experiments FB 10.12 and FB 10.13 (figure 5.24) point out that almost no damage of rock or proppant can be found in the proppant pack or at the rock-proppant interface. Proppant embedment is small or non-existent. The fracture face is flat since the fracture was sawed for the RPI experiments with the LTFC. At a few rock-proppant contacts, damaged grains are observed (figure 5.24a&c). At the contact, the grains are fractured and disintegrated. The produced fines are transported into the adjacent pore space. In contrast to the Bentheim sandstone RPI experiments (compare to §5.3.4), the proppant embedment and fines production at the fracture face is small.

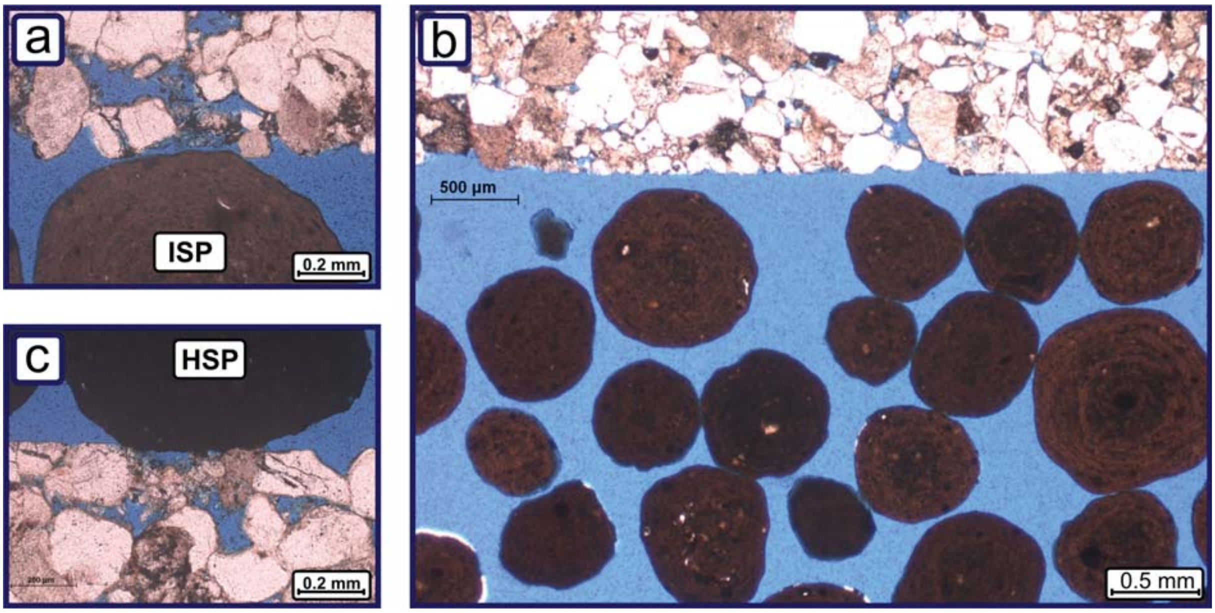

Figure 5.24: *Micrographs from long-term experiments with Flechtingen sandstone and ISP / HSP. The amount of damage observed at the rock-proppant interface is small. Some quartz grains are crushed at the interface; the proppants do not show fracturing.*

6. Stress Modelling

The aim of the following chapter is to understand the stress distribution arising in the proppant pack and quartz grains and to explain the damage at the fracture face and within the proppant pack. Two approaches are employed for stress calculation: 1) an analytical approach based on the theory of Hiramatsu & Oka [1966] for diametral loading of spheres; and 2) a numerical approach based on the software package Rockflow/Genesys [Wang & Kolditz 2005]. Experimental loading conditions are simulated on a 2D model of a proppant-filled fracture in a Bentheim sandstone.

6.1. Analytical Approach: Diametral Compression

In this section, a detailed stress analysis of proppant and quartz grains in contact is presented. For that purpose, the loading of proppants and quartz grains is treated as diametral loaded spheres. The complete stress field in a stressed sphere cannot be described with one single theory. Two different approaches are used: One for the stress field within the sphere and another one for the contact regions. The stress field and deformation at the contact is calculated with the Hertzian contact theory [Hertz 1882] (compare to §2.2.1). The stresses in the proppant or quartz grain volume are computed with the theory of Hiramatsu & Oka [1966] (compare to §2.2.2). The different theories are adopted for an analysis of the mechanical interaction of rock and proppant and possible failure scenarios.

6.1.1. Contact Geometry

Figure 6.1 shows the idealised contact geometry at the proppant-quartz grain boundary. The proppant pack and the quartz grains matrix are approximated as a simple cubic packing of spheres; the spheres in contact are isotropic and elastic. The proppants are loaded in the direction of the maximum external stress, which corresponds to the axis of compression in figure 6.1. All stress vectors that deviate from the direction of maximum external stress are neglected. The coordinate system is located in the centre of the proppant. Two different geometries for the rock-proppant contact are considered for the stress calculations:

- a single contact in the direction of the maximum external stress, comparable to a proppant-proppant contact, denoted as 1Q-geometry
- a proppant in contact with three quartz grains (compare to figure 6.1), denoted as 3Q-geometry

The latter geometry is more realistic for a compacted granular media. Indices are used in the following to differentiate the stress calculations as well as the resulting tensile stresses (σ_t) in proppants and quartz grains:

- proppant-proppant contact:	PP	σ_{tPP}
- proppant-quartz contact:	PQ	σ_{tPQ}
- quartz-proppant contact:	QP	σ_{tQP}

The discrimination between the latter two is made, since the stress calculation at the proppant-quartz contact results in different stresses for both.

The load on a single PP-contact as well as on the 1Q PQ-contact as a function of the externally applied differential stress (σ_{diff}) is:

$$F_{PP} = F_{PQ} = \frac{\sigma_{diff}\, A_S}{N_{PL}} \qquad 6.1,$$

where A_S is the cross sectional area of the specimen and N_{PL} is the number of proppants per layer within the proppant pack. N_{PL} is derived by weighting 1000 proppants at first and dividing the weight of the proppant pack by the weight of a single proppant.

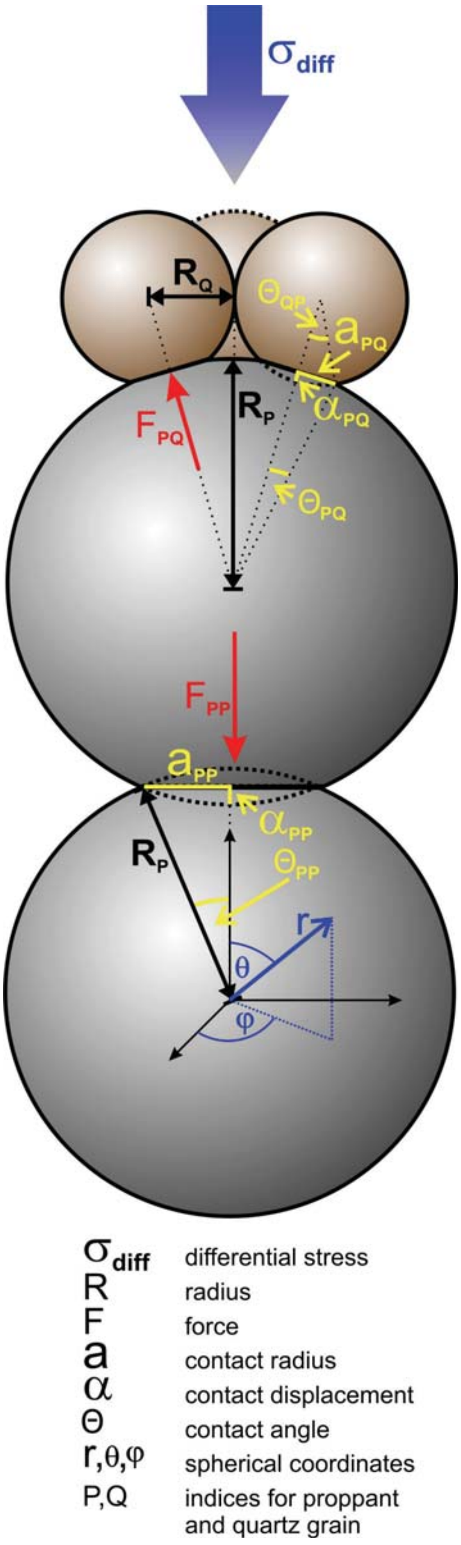

Figure 6.1: *Idealised load geometry at the rock-proppant interface (true relative scale). In order to model the stresses at the rock-proppant interface and in the proppant pack, an idealised load geometry is designed. The quartz grain matrix and the proppant pack is approximated as simple cubic packing. A proppant is in contact with three quartz grains (3Q-geometry).*

In the 3Q-geometry, the force F_{PQ} is a function of the proppant and quartz radii R_P and R_Q and the contact displacement α_{PQ}.

$$F_{PQ}=\sqrt{1-\frac{R_Q^2}{\left(R_Q+R_P-2\alpha_{PQ}\right)^2}}\,\frac{F_{PP}}{3} \qquad 6.2.$$

Since $\alpha_{PQ} / R_P \ll 1$ and $\alpha_{PQ} / R_Q \ll 1$ for stiff bodies, α_{PQ} is neglected in this equation.

The contact radii a_{PP} and a_{PQ} are derived from the Hertzian contact theory [Hertz 1882, Timoshenko & Goodier 1970]. From a, the contact angle (Θ) between two spheres is computed:

$$\Theta_{PP} = \arcsin\left(\frac{a_{PP}}{R_P}\right) \qquad 6.3a$$

$$\Theta_{PQ} = \arcsin\left(\frac{a_{PQ}}{R_P}\right) \qquad 6.3b$$

$$\Theta_{QP} = \arcsin\left(\frac{a_{PQ}}{R_Q}\right) \qquad 6.3c$$

Three different contact angles exist: Θ_{PP}, Θ_{PQ}, and Θ_{QP}. These angles and the forces F_{PP} and F_{PQ} are input parameters for the stress analysis following Hiramatsu & Oka [1966]. A spherical coordinate system with origin in the centre of the sphere as well as the variable radius r, polar angle θ, and azimuth φ are adopted (compare to figure 6.1). For the diametral compression of spheres with radius R, the pair of forces F is modelled by uniform radial stress p_H applied over two opposite spherical areas with an aperture angle of 2Θ.

6.1.2. Stress Field at the Surface: Hertzian Contact

The theory of Hertz [1882] is employed for the calculation of maximum tensile stresses at the surface (equation 2.18b). The maximum tensile stress is observed at the outer boundary of the contact circle (compare to §2.2.1):

$$\sigma_{ra}=-\frac{1-2\nu}{3}\sigma_{c\_max} \qquad 6.4$$

where σ_{c_max} is the maximum compressive stress in the centre of the contact circle. The material parameters for the calculation are listed in table 6.1. These parameters are taken from literature [Shackelford & Alexander 2000, Landolt & Börnstein 1987]. For reason of simplicity, pure corundum is assumed for the proppant material. HSP is manufactured mainly from pure corundum (~ 80 %).

	quartz grain	proppant / corundum
diameter	300 µm	760 µm
Young’s modulus	80 GPa	380 GPa
Poisson ratio	0.17	0.23
tensile strength	40 - 80 MPa	~ 250 MPa

Table 6.1: *Parameters of quartz grains and proppants (corundum) for Hertzian contact stress calculation. Material parameters are taken from Shackelford & Alexander [2000] and Landolt & Börnstein [1987].*

ISP has a quartz content up to 50 % and therefore contains, besides corundum, a fraction of mullite. The tensile strength of mullite is about 1/3 the tensile strength of corundum.

The tensile stresses for the three contact geometries (PP, PQ, and QP) calculated for 4 loading steps (σ_{diff} = 5, 20, 35, 50 MPa) of the RPI experiments are displayed in figure 6.2. The 3Q-geometry of figure 6.1 is used to approximate the contact loads F.

Already at small external differential stress (5 MPa), the calculated tensile stresses at the surface (1.2 – 1.7 GPa) significantly exceed the tensile strength of proppants and quartz grains. Hence, the initiation of cracks at the contact circle can be expected at this small external stresses. The observation from acoustic emission experiments shows that these initial cracks do not affect failure of proppants. No proppant crushing is observed at small loads from rock-proppant systems tested in the AEFC (compare to §5.3). The high tensile stresses are limited to a very small volume and decrease strongly with increasing distance. The stress gradient is high and the crack will probably not propagate through the sphere and split the proppant. Schönert [2004] found that ring cracks caused by high tensile stress perpendicular to the contact circle occur but these cracks did not disintegrate the spheres.

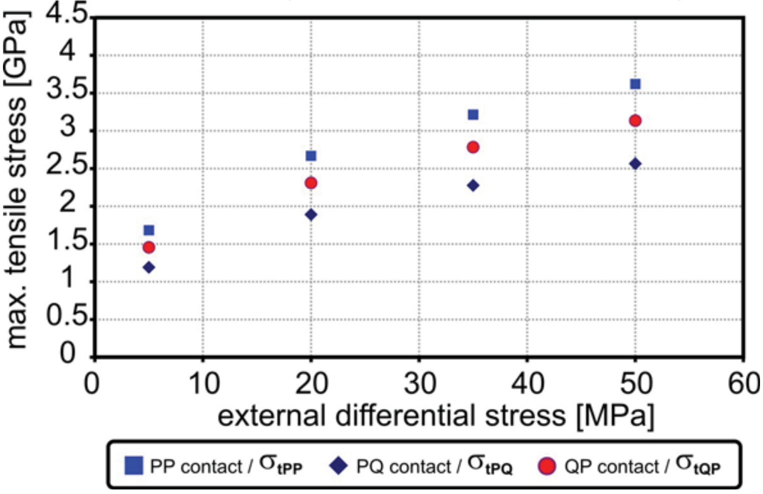

Figure 6.2: *Maximum tensile stresses at the outer boundary of the contact circle. Hertzian contact theory [Hertz 1882] is adopted for maximum tensile stress calculation at the contact of proppants (P) and quartz grains (Q). The resulting tensile stress maxima in PP-contacts (σ_{tPP}) and at PQ-contacts proppants (σ_{tPQ}, σ_{tQP}) are high (1.1 – 3.6 GPa). Initiation of cracks can be expected at the outer boundary of the contact circle at small external stresses.*

To understand the failure of proppants and quartz grains, the induced stresses in the volume of the loaded sphere have to be considered.

6.1.3. Stress Field in the Volume: Theory of Hiramatsu & Oka

In order to discuss the stresses and potential failure mechanisms in a diametral loaded sphere, the theory of Hiramatsu & Oka [1966] is used. Equations 2.21 – 2.24 (compare to §2.2.2) are computed for a standard set of geometric and material parameters (table 6.2). The solution is independent from Young’s modulus. The problem is symmetric; therefore, for one quadrant of the sphere the stress severity (S) is calculated for 100 x 100 equidistant points. The stress severity describes the local stress in a sphere as a factor of the medium stress applied to the cross-sectional area of the sphere:

$$S=\frac{\sigma}{F/\left(\pi\cdot R^2\right)} \qquad 6.5$$

radius of sphere	R	1
contact angle	Θ	1°
Poisson ratio	ν	0.23
loading force	F	1

Table 6.2: *Parameter for stress calculation of diametral compressed spheres with the theory of Hiramatsu & Oka [1966].*

where F and R are the force acting on a sphere and the sphere radius, respectively. For a convergence of the solution, the summations in equation 2.21 – 2.24 are computed to the order (m) of 100 using the software package Mathematica. It was determined that the stress severity shows negligible variations for m ≥ 60. The principle stresses (σ_1, σ_2, σ_3) as well as the shear stress in the xy-direction (σ_{xy}) are plotted in figure 6.3. The principal stresses σ_1 and σ_3 are within the xy-plane while σ_2 is the principal stress normal to this plane. Compressive stresses are plotted as positive and tensile stresses are plotted as negative here, following the usual sign conventions of rock mechanics.

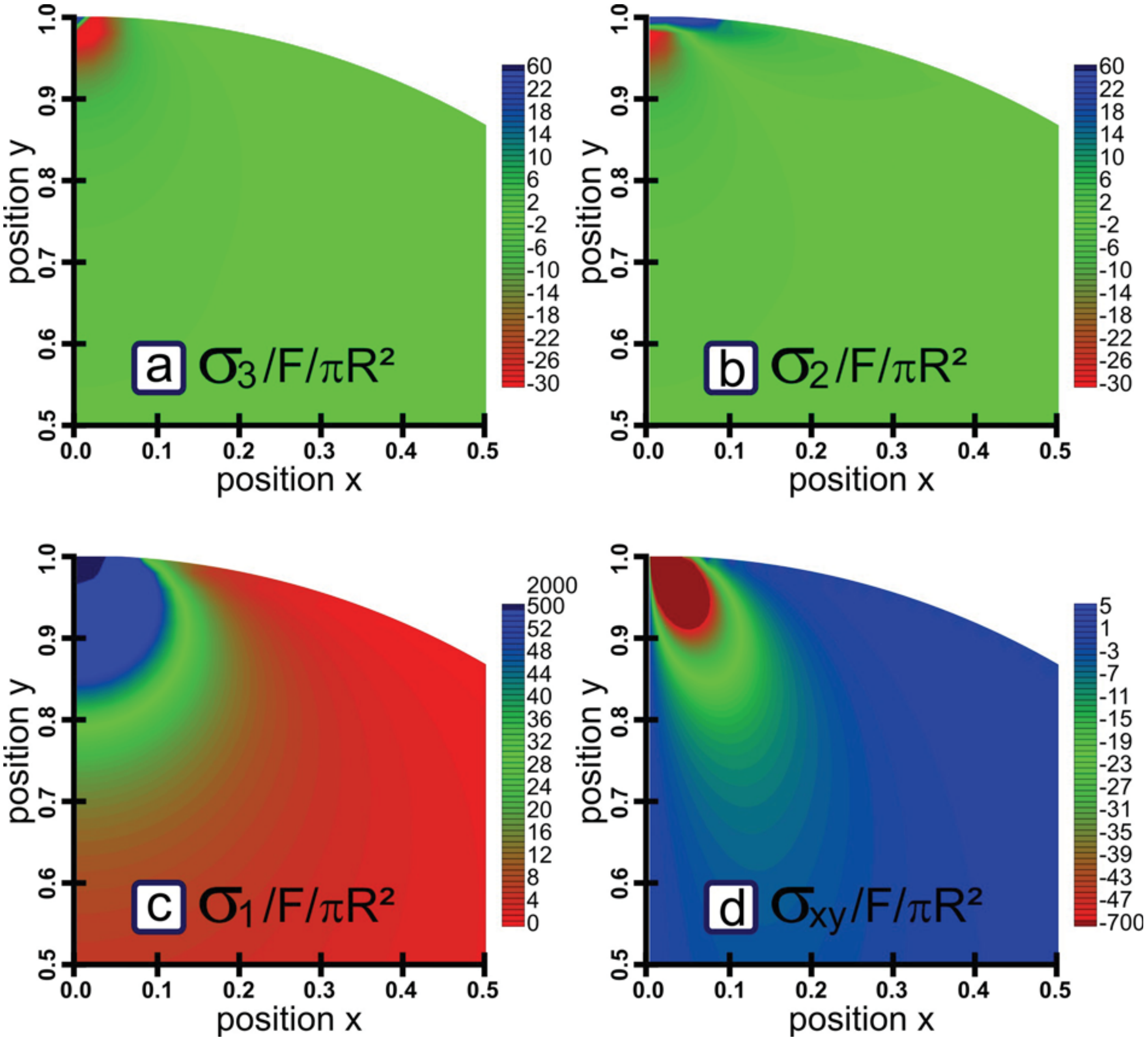

Figure 6.3: *Stress severity of principal stresses (σ_1, σ_2, σ_3) as well as shear stress σ_{xy} of a diametral loaded sphere. The stresses in a diametral loaded sphere are expressed as stress severity (S). S normalises σ_1, σ_2, σ_3 and σ_{xy} with medium stress applied to the cross-sectional area of the sphere ($F/\pi R^2$). Compressive stresses are positive and tensile stresses are negative; algebraic sign for shear stresses denote the direction of deformation. A tensile stress concentration beneath the surface is obvious in figure a and b with extremes at about -37. The maximum principle stress is everywhere compressive; the maximum is about 2000 (figure c). The shear stress shows maximum values of about -700 (figure d).*

Cracks propagate if the local stress in the vicinity of a material failure is high enough to meet the fracture criterion. In isotropic materials, cleavage cracks propagate perpendicular to the maximum tensile stress and shear cracks parallel to the maximum shear stress. Hence, the considerations here about breakage and fracture propagation are based on the stress field.

If a local maximum of tensile stress exists, a cleavage crack can propagate from this initiation point. The stress analysis shows a possible crack pattern in the spheres as long as the cracks do not modify the stress field. Indeed, a crack modifies the stress field by definition.

Figures 6.3a-c shows that all principle stresses along the axis of loading are compressive beneath the contact area. In a small volume below the contact ($0.9 < y < 1.0$/ figure 6.3c), the maximum principle stress (σ_1) reaches a stress severity value between 100 and 2000. The intermediate (σ_2) and minimum principle stresses (σ_3) show both a localised minimum of stress severity ($-37 < S < -5$) near the contact region ($0.9 < y < 1.0$/ figure 6.3a&b). Additionally, the plot of shear stress severity (figure 6.3d) identifies a pronounced minimum with values up to -700 (table 6.3).

	extremes of stress severity		**type of stress**
contact angle	**1 °**	**5 °**	
σ_1	2000	130	max. compressive stress
σ_2 / σ_3	-37	-1.7	max. tensile stress
σ_{xy}	-700	-100	max. shear stress

Table 6.3: *Extremes of stress severity for two contact angles and resulting stress types in diametral loaded sphere.*

From these observations, different potential failure types can be derived:

1. The tensile stress along the loading axis is not uniformly distributed; a high degree of stress anisotropy exists. This anisotropy will be analysed below in detail. At both contacts, the tensile stress concentrations (figure 6.3a&b) initiate a fracture beneath the contact, if the tensile stress overcomes the tensile strength. The arising fractures propagate along a meridional plane through the sphere and strikes in the centre of the sphere. Because the stress distribution is rotationally symmetric, a sphere can fail in fragments shaped like orange slices. This tensile cleavage crack is illustrated in figure 6.4.
2. The high Hertzian tensile stress at the contact circle may initiate a fracture at the contact circle. The high Hertzian tensile stress concentration is limited to a very small volume. For this reason, it is not visible in figure 6.3. Comparable to failure type 1, this type of fracture would propagates along a meridional plane through the sphere. A differentiation between type 1 and 2 is possible from identification of initiation point. The possible fracture initiation points are indicated with red dots in figure 6.4.
3. In the direct vicinity of the contact region, a special type of crack can be observed: the cone crack. This cone crack is initiated at a ring crack at the surface, where the tensile stress perpendicular to the contact circle shows a maximum. These ring cracks are known from indenter experiments [Geandier et al. 2003, Warren 1995]. The driving force of this ring crack is the very high Hertzian tensile stress at the surface. The ring crack propagates only a little into the sphere. Then, the cone crack starts from the contact circle and propagates towards the axis of loading. This leads to a shallow fragment below the contact area (figure 6.4). From high stress energy density (tensile and compressive stresses) in that area, a dense crack pattern and a large amount of fine fragments can be produced.
4. The shear stress in the loaded sphere can propagate a shear fracture if the stress exceeds the shear strength along a possible shear plane. The maximum shear stress occurs in the direction of the loading axis (not shown in figure 6.3). Obviously, no shear displacement is possible in this direction. Beneath the contact, the shear stress severity

is very high along the xy-direction. Hence, the propagation of a fracture along the shear stress trajectories is likely. A shear probability study is necessary to clarify if shear fracturing is relevant for disintegration of diametral loaded spheres. This study is beyond the scope of this work and might be investigated in future.

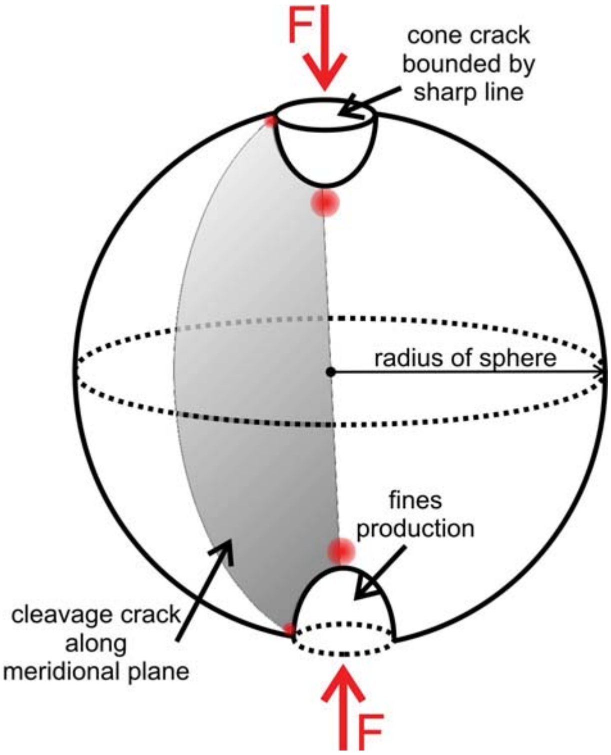
F
cone crack bounded by sharp line
radius of sphere
fines production
cleavage crack along meridional plane
F

Figure 6.4: *Possible fracture pattern in a diametral loaded sphere. The consideration about stress field in diametral loaded spheres leads to two possible fracture types: the cone crack at the contact and the cleavage crack. The red dots indicate points of fracture initiation.*

Table 6.3 lists the extremes of stress severity for a contact angle of 1 ° and 5 °. This comparison highlights that an increasing contact angle results in a significant reduction of stress severity and stresses. Hence, the radius of contact circle has a major impact on the stability of a sphere or a proppant, respectively.

The magnifications of two proppants observed in proppant packs (figure 6.5) illustrate fracture patterns. Figure 6.5a is a picture from ISP after loading with the BDFC up to σ_{diff} = 50 MPa. The proppant is cleaved into orange slices and the cone crack area in the middle is highly fragmented (fracture type 3). The sharp line is driven by the maximum tensile stress at the boundary of the contact circle. The micrograph in figure 6.5b identifies two fractures in a proppant. Both fractures are initiated beneath the contact area and propagate towards the centre (fracture type 1). The observed crack pattern correlates with the crack pattern described from theoretical considerations illustrated in figure 6.4.

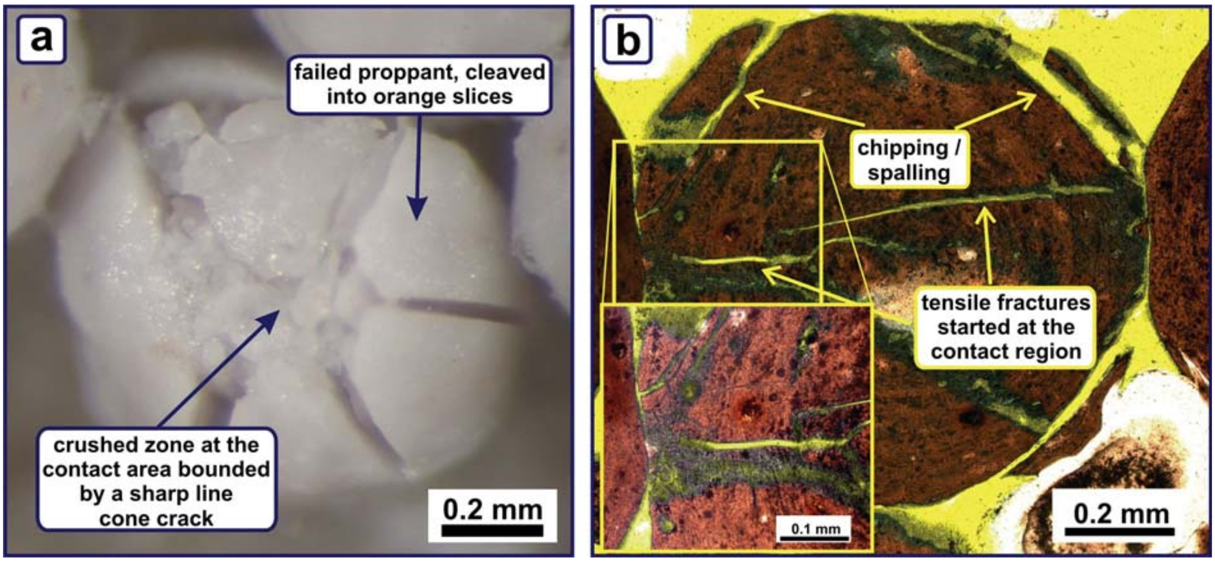
a
failed proppant, cleaved into orange slices
crushed zone at the contact area bounded by a sharp line cone crack
0.2 mm
b
chipping / spalling
tensile fractures started at the contact region
0.1 mm
0.2 mm

Figure 6.5: *Fractures in proppants. Photos of two intermediate strength proppants after loading the proppant pack to a differential stress of 50 MPa are presented in figure a and b. The proppant in figure a is cleaved into orange slices, and the cone crack area is visible. The contact area is highly fragmented, and abundant fines are produced. Figure b identifies two fractures starting from the contact regions and propagating towards the centre. The observed crack patterns are in accordance with the crack patterns described from theoretical considerations about diametral loaded spheres (figure 6.4).*

Both fractures in the proppant (figure 6.5b) have there maximum aperture beneath the contact (see magnification) and do not propagate towards the surface where the stress becomes compressive. Hence, these fractures potentially initiated from the high tensile stress concentration along the axis of loading (fracture type 1). Beside these cleavage fractures, chipping of proppant fragments is visible in figure 6.5. The observations made from the principle stresses in a loaded sphere cannot explain this chipping at the surface. A hypothesis is that this fracture type initiates due to high tensile stress in the contact circle and propagates to the surface driven by high shear stresses.

6.1.4. Maximum Tensile Stress along the Axis of Loading

The investigation in the last section demonstrates that loaded proppants fail in tensile mode. Hence, studying of tensile stress fields and their inhomogeneity along the axis of compression (θ = 0) will deliver insights on the location and onset of crack initiation.

Stress calculation within proppant and quartz spheres due to increasing diametral load F is a non-linear problem. With increasing F, the contact angle (Θ) increases in dependence of Young's modulus (E), Poisson ratio (ν), and F. The change of Θ influences the stress field in the loaded sphere.

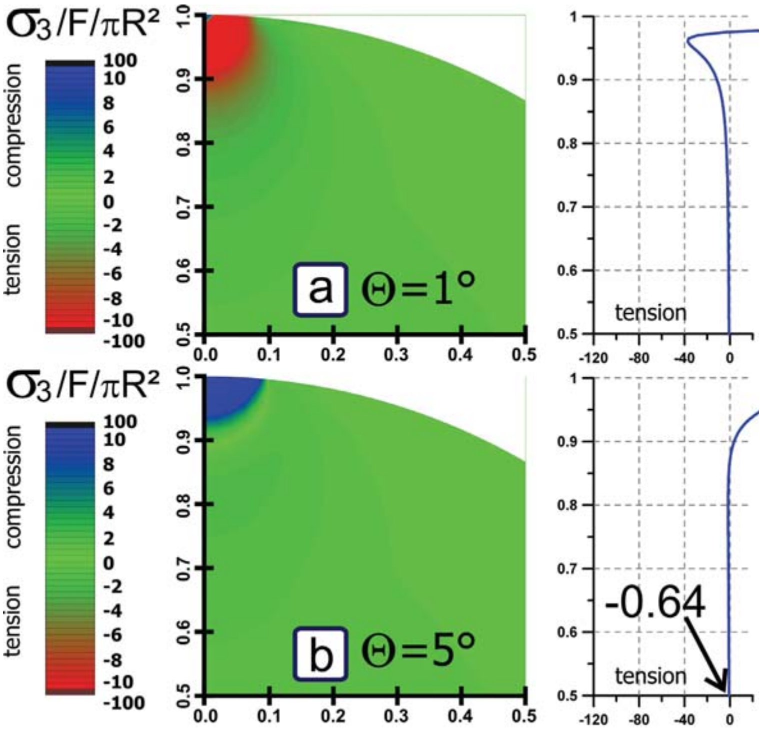

Figure 6.6: *Stress severity of σ_3 for two contact angles. The stress severity (S) plotted for two contact angles shows that an increasing contact angle suppresses the tensile stress concentration beneath the surface. For Θ = 5 the severity is evenly distributed over the inner 90 % of the sphere.*

Figure 6.6 shows the stress severity of the minimum principle stress ($S_{\sigma3}$) for Θ = 1 ° and Θ = 5 °. In figure 6.6a the red tensile stress concentration beneath the contact is obvious. The graph in figure 6.6a plots $S_{\sigma3}$ along the axis of loading. $S_{\sigma3}$ is uniformly distributed over the inner part of the proppant and amounts to -0.64 in the centre. Approximately, at position 0.95 a minimum stress severity is observed. For a large contact angle (Θ = 5), the stress severity extreme decreases, and $S_{\sigma3}$ becomes uniformly distributed over the inner 90 % of the sphere. A plateau region with $S_{\sigma3}$ = -0.64 exists from the centre to y = 0.9. Above this position, the stresses become compressive. For a small contact angle (Θ = 1), a 60-fold tensile stress concentration compared to the Θ = 5 case is present.

The minima of $S_{\sigma3}$ are dependent on Θ as well as on the Poisson ratio (ν) (compare to §2.2.2). In order to analyse the maximum tensile stress concentration as a function of Θ and ν, a sensitivity analysis is conducted (figure 6.7) within limits of: $1 \leq \Theta \leq 10$ and $0.1 \leq \nu \leq 0.4$

A dual-fit algorithm is employed to approximate the maximum tensile stress severity (S_{t_max}) as a function of contact radii and Poisson ratio. In the first step, the evolution of maximum severity is power law fitted and in the second step, the resulting factors and exponents are matched with a quadratic function.

$$S_{t\_max} = \left(682 \cdot v^2 - 583 \cdot v + 128\right) \Theta^{(9.22 \cdot v^2 - 1.33 \cdot v - 1.89)} \quad \forall\, 1° \leq \Theta \leq 10° \qquad 6.6$$

S_{t_max} shows an increase with decreasing Θ and decreasing ν. For large Θ and ν, S_{t_max} converge against ~ -0.6, the value of the severity plateau. The overall error of this approximation of the stress severities is about 11 %, whereas the deflection is high (up to 30 %) for small contact angles (~ 1 °) and large Poisson ratios (~ 0.4).

The point where the crack growth initiates probably coincides with the maximum induced tensile stress, if microcracks are evenly distributed. For the given geometry, two fracture initiation scenarios can be derived:

1) If the contact angle is large enough (Θ > 5°) and the tensile stress is homogeneously distributed over the inner 90 % of the sphere, the fracture propagates at load F_1 from the centre towards the boundary along the axis of loading.
2) If the contact angle is small, the fracture will propagate from a point near the surface at smaller load F_2 compared to case 1. The ratio F_1/F_2 is defined by S_{t_max}. The high stress gradient in the contact region causes an explosive breakage and leads to abundant fine fragments.

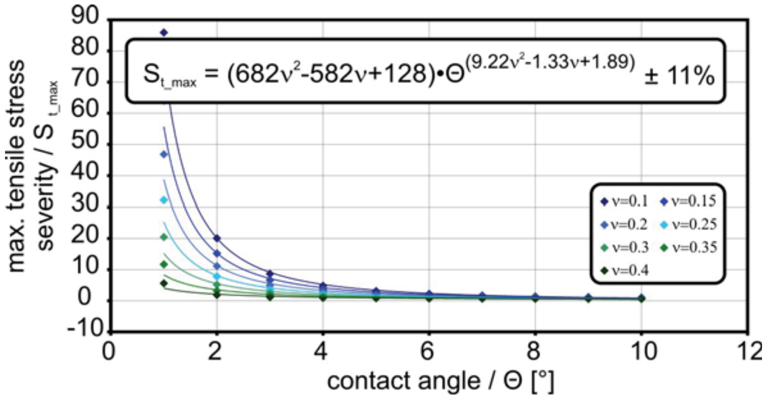

Figure 6.7: *Tensile stress severity as function of contact angle (Θ) and Poisson ratio (ν). The extremes of stress severity are fitted with the function S_{t_max}. S_{t_max} can be used to calculate the maximum tensile stresses in a loaded sphere along the axis of loading.*

6.1.5. Maximum Tensile Stresses in Quartz Grains and Proppants

Equation 6.6 is employed for the calculation of maximum tensile stress in the volume of diametral loaded quartz grains and proppants. The input parameters are listed in table 6.4. The calculation is conducted for the intermediate strength proppants (ISP) and the high strength proppants (HSP) in contact with a quartz grain.

Maximum compressive loads of ISP and HSP, determined by means of a single proppant testing in a specialised load cell [Legarth et al 2005a], are used to calculate the tensile strength of both proppant types. The proppants were loaded in a diametral load geometry of two PCBN-anvils (Polycrystalline Cubic Boron Nitride) (figure 6.8). The theory of Hiramatsu & Oka [1966] is adopted to determine the tensile strength from maximum compressive loads. A mean value and a minimum tensile strength for both proppant types is given in table 6.4. The calculations correlate with literature values for pure corundum ceramics (~ 250 MPa) and pure mullite (~ 110 MPa) [Shackelford & Alexander 2000].The Young's moduli, Poisson ratios, and the tensile strength of quartz in table 6.4 are taken from literature [Shackelford & Alexander 2000, Landolt & Börnstein 1987].

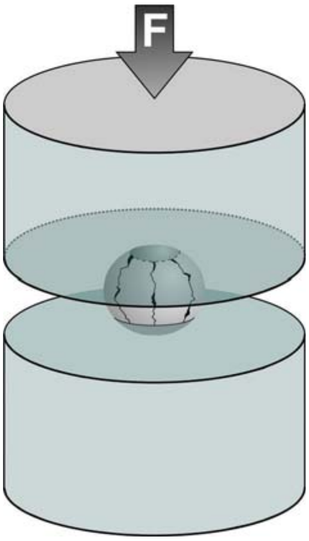

Figure 6.8: *Schematic view of single proppant testing load cell. The proppants are transported automatically between two PCBN pistons (Polycrystalline Cubic Boron Nitride) and the peak force (F) before failure is recorded.*

	quartz grain	**ISP**	**HSP**
Young's modulus [GPa]	80	110	380
Poisson ratio [ ]	0.17	0.23	0.23
diameter [µm]	300	760	700
mean tensile strength [MPa]	40 - 80	160 ± 30	270 ± 80
minimum tensile strength [MPa]	- / -	~ 95	~ 150

Table 6.4: *Parameters for the calculation of maximum tensile stresses in quartz grains and proppants. Material parameters and well as tensile strength of quartz are taken from Shackelford & Alexander [2000] and Landolt & Börnstein [1987]. Tensile strength of ISP and HSP is determined from single proppant testing*

Both contact geometries (1Q and 3Q) are taken into account (compare to §6.1). The contact forces and the associated contact angles are calculated for four loading steps (σ_{diff} = 5, 20, 35, 50 MPa). S_{t_max} is used to calculate a maximum tensile stress according to the loading steps of the experiment. Figure 6.9 shows the maximum tensile stress in a proppant at PP contact σ_{tPP}, in a proppant at PQ σ_{tPQ} contact, and in a quartz grain at QP contact σ_{tQP}.

Even at small loads (5 MPa), the tensile strength of quartz (blue area) is exceeded in the 1Q-geometry and in the 3Q-geometry for both proppant types (figure 6.9a). Hence, in both geometries failure of quartz grains can be expected at small external stresses. In contrast, stresses in ISP and HSP at quartz-proppant contacts are significantly smaller than the tensile strength of these proppant types. For comparison, the tensile strength of ISP is indicated (green area) in figure 6.9b. Initiation of proppant fracturing at the rock-proppant interface is unlikely. The last figure shows the stresses in ISP and HSP caused by proppant-proppant loading in the proppant pack. In the last loading stage, σ_{tPP} is ~ 95 MPa for ISP and ~ 165 MPa for HSP. The arising tensile stresses are smaller than the tensile strength of ISP (green area) and HSP (not shown in figure 6.9c).

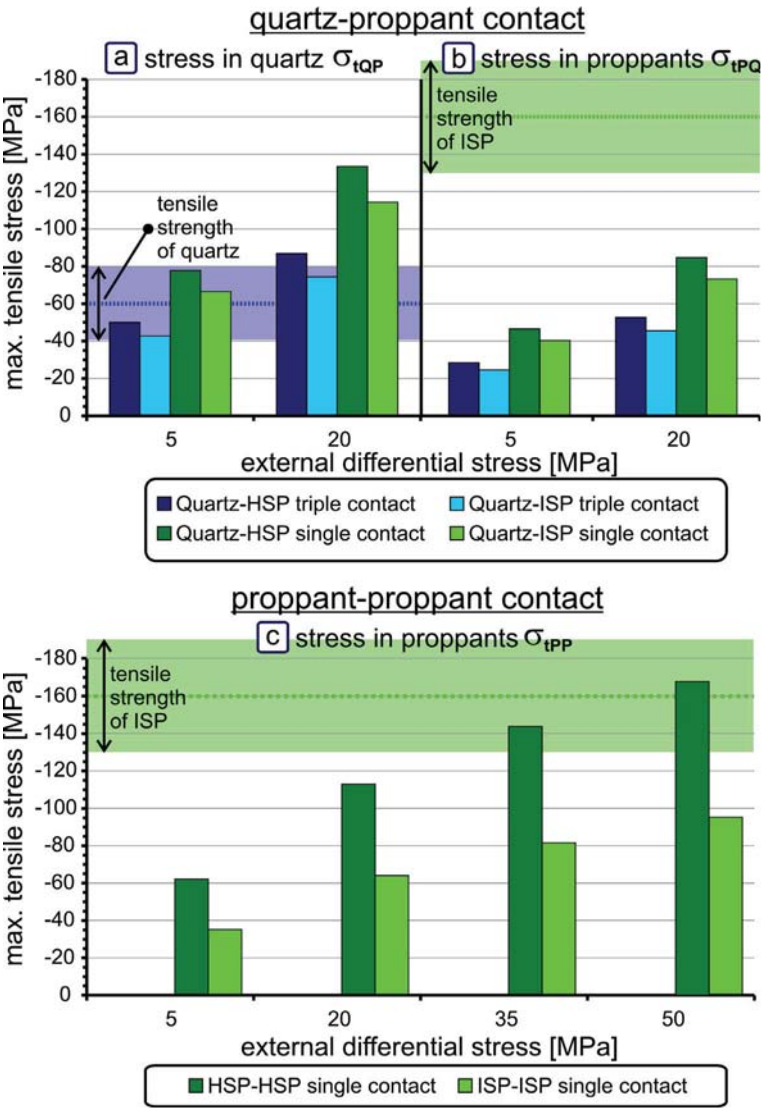

Figure 6.9: *Maximum tensile stresses in quartz grains and proppant as a function of the external differential stress. Figure a shows that even at small external differential stresses (5 MPa) the maximum internal tensile stress in quartz (σ_{tQP}) exceeds the tensile strength of quartz (blue area). This holds for both geometries: the single and the triple quartz-proppant contact. In contrast, the tensile stresses in proppant at the rock-proppant interface (σ_{tPQ}) are too small to initiate failure (figure b). Even at maximum differential stress, the developing tensile stresses at proppant-proppant contact are smaller than the tensile strength of ISP (green area) and HSP (270 ± 80 MPa / not shown in figure c).*

6.2. Numerical Approach: Idealised 2D-Contact Model of Quartz Grains and Proppants

The aim of this pure mechanical elastic modelling approach with the software package Rockflow/Geosys [Wang & Kolditz 2005] is the identification of stress pattern and stress concentrations, which explain the observed fracture pattern in the proppant pack. For this purpose, an idealised 2D-contact model of the rock-proppant interface is generated and loaded with input boundary conditions of AEFC and BDFC experiments.

In the previous section, the contact stress problem between quartz grains and proppants was calculated by means of simplified diametral load geometry. In fact, a proppant will have more contacts, at least three fixed in place, but more contacts are possible. In a hexagonal or cubic closest packing each proppant would have 12 neighbours. The reality will lie between these two extremes.

It is not possible to take a micrograph of a proppant-filled fracture for this modelling approach. In a 2D cut through a 3D packed bed of spheres, the spheres will show very few contact points. For instance, in figure 5.16c some proppants seem to levitate in a matrix of blue epoxy. In order to rebuild the grain structure as well as the shape of proppants precisely, an idealized 2D contact model is designed from micrographs of Bentheim rock and ISP. Figure 6.10 is composed of a micrograph from a fracture face of a tensile fracture and micrographs from proppants. The contacts between proppants and fracture face in three dimensions (3D) are projected into two dimensions (2D). The number of contacts and contact radii is arranged for each proppant or quartz grain.

Different contact geometries comparable to possible contact scenarios in a propped fracture are assembled. An embedded proppant (B), a three-point load geometry (C & D), a very small contact area between quartz grain and proppant (C & D), and a proppant surrounded by six neighbours (F & I) are assembled in figure 6.10.

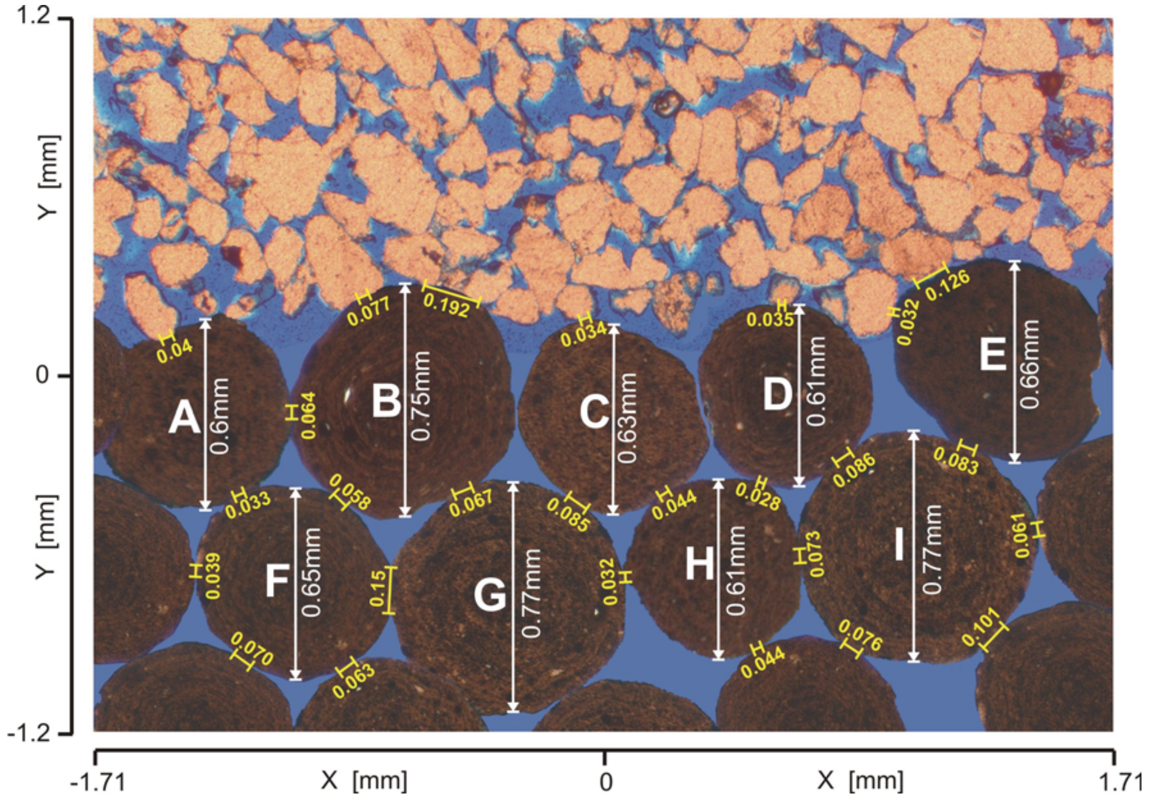

__Figure 6.10:__ Artificial 2D-contact model of a rock-proppant system. In order to model the mechanical interaction at the rock-proppant interface, a rock-proppant system is assembled from micrographs of proppants and Bentheim sandstone. The contact diameters (yellow numbers) and the proppant diameters are given in mm.

contact type	min. contact angle [°]	max. contact angle [°]
PP	2.0	4.0
PQ	2.4	15.0
QP	2.5	8.0

Table 6.5: *Contact angle interval used for the idealised 2D-contact model. PP: proppant-proppant contact; PQ: proppant-quartz contact; QP: quartz-proppant contact*

The latter geometry corresponds to a 2D view of cubic closest packing.

The modelling software Rockflow/Geosys is executed with a non-deformable mesh. The Hertzian contact theory [Hertz 1882] delivers the contact radii in the 2D-model for proppant-proppant (PP) contacts. The differential stress varies from 5 – 50 MPa for the calculation. The contact radii are fixed and will not deform due to loading the 2D-model. In order to cover the differences of possible contact radii at the rock-proppant interface, the radii for proppant-quartz (PQ) and quartz-proppant (QP) contacts are varied in a wide range (table 6.5). That means contact radii smaller and larger than calculated with the Hertz theory are defined. For instance, an embedded proppant has a very large contact angle, whereas a subangular quartz grain has a very small contact angle. In figure 6.10, the diameter of each proppant and each contact is given in mm. A detailed description of the conversion process necessary to generate a 2D-mesh from the artificial micrograph is given in appendix A6.

6.2.1. Mechanical Modelling with Rockflow/Geosys

The simulation software Geosys/Rockflow [Korsawe et al. 2003, Wang & Kolditz 2005] combines four processes that control transport in porous media (chemical, thermal, hydraulic and mechanical). With regard to this study, the mechanical modelling tool is employed to model the stresses in the rock-proppant system. Material and boundary parameters have to be defined for the FE-simulation.

The mesh is fixed and not deformable; no extra mesh fixation is necessary to keep it in place. Four lines at the outer boundary are created. These lines apply constant stress to the model borders (first order boundary condition). For time discretisation, 11 steps of 360 seconds are chosen. In the first time step, all four lines apply a confining pressure of 10 MPa to the model borders. This stress remains constant for the vertical boarders for the complete simulation time. The two horizontal lines apply an increasing stress at the horizontal model borders from time step 2 - 11. At each time step, the stress in the vertical direction (y-direction) is increased by 5 MPa, resulting in a maximum vertical stress (σ_{YY}) of 60 MPa and a horizontal stress (σ_{XX}) of 10 MPa. The mechanical properties of the two materials are defined by Young's modulus and Poisson ratio. The values from the literature [Shackelford & Alexander 2000] are chosen in accordance to the analytical modelling approach (§6.1). Pure corundum is assumed for proppant composition. Table 6.6 lists the dimensions of the investigated area and the material parameters. The output parameters are the xx- and yy-normal stress and strain as well as the xy-stress and strain.

material	Young's modulus	Poisson ratio	area of investigation	stress in xx-direction	stress in xy-direction
quartz	80 GPa	0.17	2.4 x 3.42 mm²	10 MPa	10-60 MPa
corundum (proppant)	380 GPa	0.23			

Table 6.6: *Parameters for mechanical modelling of the 2D-contact model.*

6.2.2. Results from 2D Mechanical Stress Modelling

The modelling results are plotted with the software package Tecplot. Figure 6.11a-f shows the maximum principle stress (σ_1), the minimum principle stress (σ_2), and the xy-shear stress (σ_{xy}) for two loading stages of σ_{diff} = 5 MPa and σ_{diff} = 50 MPa. An inner section of the complete modelling area is selected in order to exclude effects from the borders. Initiation of fractures in quartz grains and proppants is expected at local tensile stress concentrations. In addition, the shear stress distribution can provide information about the initiation of shear fractures in the rock-proppant system. Table 6.7 shows the maximum stresses for σ_{diff} = 50 MPa observed in the vicinity of the contacts. Discrimination between two types of maxima is made: the maximum values for the stress detected in single nodes of the mesh and the stress maxima distributed over a small area (> 10 notes).

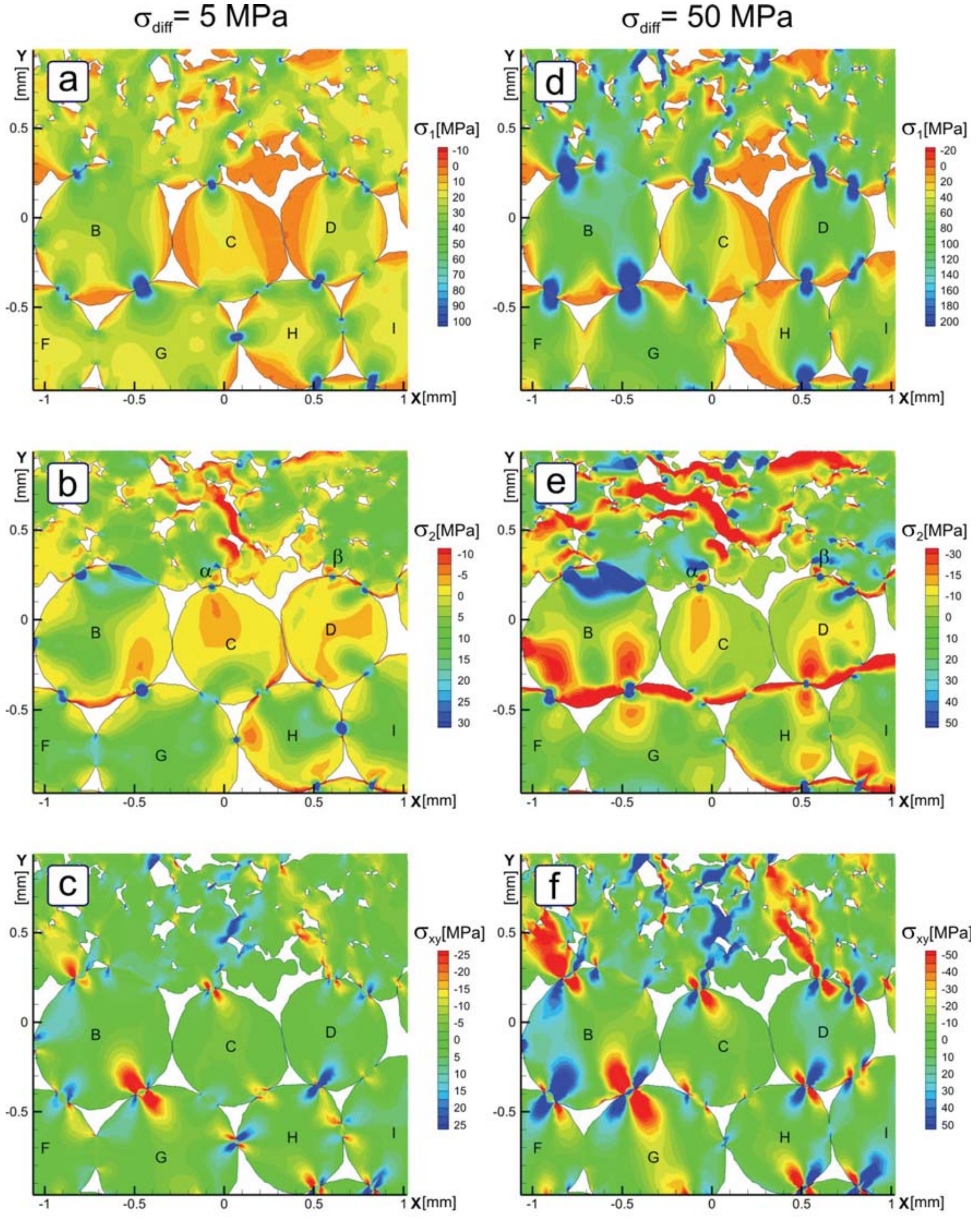

Figure 6.11: *Stress distribution in a loaded rock-proppant system. Maximum principle stress (σ_1), minimum principle stress (σ_2), and xy-shear stress (σ_{xy}) for two loading stages of σ_{diff} = 5 MPa and σ_{diff} = 50 MPa are plotted. An inner section of the complete modelling area is selected. Highly localised tensile stress concentrations at contacts are identified in quartz grains (region α and β) and in proppants. In addition, tensile stress distributions are observed that tend from the contacts towards the surface or connect proppant contacts. Magnitudes of compressive and shear stresses can be very high in the contact region.*

The stress distribution in figure 6.11a-c represents the initial differential loading phase of a rock-proppant interaction (RPI) experiment. At the contacts, σ_1 is compressive (figure 6.11a); maximum compressive stresses are ~ 200 MPa. Curved tensile stress distributions are observed between contacts. Tensile stress concentrations in the quartz grains beneath the QP-contact area are visible. They are denoted with α and β in figure 6.11b. The local tensile stress in the quartz grains is about -6 MPa. The maximum shear stress at the rock-proppant interface is about 70 MPa (figure 6.11c). The positive and negative values of σ_{XY} characterise the direction of displacement.

At σ_{diff} = 50 MPa, the tensile stress extremes in the quartz grains are intensified (figure 6.11e). Tensile stress extremes up to -40 MPa are observed. In contrast, the neighbouring proppants feature significantly smaller tensile stress concentrations (~ -20 MPa) beneath the contact area.

At proppant-proppant contacts, maximum tensile stresses up to -40 MPa are determined. These maxima exist at small contact areas exclusively (proppant G-B and H-D). If the contact area is larger, the tensile stress concentration is suppressed (proppant G-C and H-C). Maximum compressive stresses at contacts are 450 – 550 MPa (figure 6.11d). In addition, σ_1 identifies curved tensile stress distributions (~ -20 MPa) along the surface between proppant contacts.

Figure 6.11f shows concentrations of shear stress. Maxima of σ_{XY} of 300 MPa at proppant-proppant contacts are observed. At the rock-proppant interface, the shear stress reaches maxima of 230 MPa (quartz) and 180 MPa (proppant), respectively.

Interestingly, the numerical calculation identifies high tensile stresses in the σ_1 and σ_2 computation, which are mainly horizontally distributed. These stress distributions tend from the contacts towards the surface or connect proppant contacts. The tensile stresses have maximum values of -80 MPa.

Proppant B in figure 6.11e illustrates an embedded proppant. Obviously, only compressive stresses of ~ 80 MPa occur at the contact. Besides the stresses in the proppant pack and at the interface, at a distance of approximately one quartz grain radius, large tensile stresses arise around the pores. These stresses have extremes between - 80 and -200 MPa.

In table 6.7, the maximum stress values observed in single nodes at the contact areas are shown in brackets. These single values are high, tensile stresses of about -300 MPa at PP-contacts and of about -100 MPa at PQ contacts. Compressive stresses of ~ 1000 MPa are observed.

		proppant-proppant contact	quartz-proppant contact stress in proppant	quartz-proppant contact stress in quartz
σ_2	max. tensile stress [MPa]	~ -70 (-300)	~ -20 (-100)	~ -40 (-100)
σ_1	max. compressive stress [MPa]	~ 550 (1000)	~ 450 (1000)	~ 450 (1000)
σ_{xy}	max. shear stress [MPa]	~ 300	~ 180	~ 230

Table 6.7.: *Maximum tensile, compressive and shear stresses observed in the 2D-model of the rock-proppant system. The maxima are differentiated in two types: the maximum values for the stress detected in single nodes is shown in parentheses brackets and the stress maxima distributed over a small area (> 10 notes).*

7 Discussion

7.1 *Diametral Loading of Spheres*

The theory of Hiramatsu & Oka [1966] is used to calculate the inhomogeneous stress distribution in idealised diametral load geometry. Small contact radii (Θ) and small Poisson ratios (ν) result in high tensile stresses beneath the contact area (by up to a factor of 90). In contrast, sufficiently large contact areas, as well as a large Poisson ratio, cause a homogeneous tensile stress distribution. These findings are compatible with observations by Chau & Wei [1998]. They expand the theory of Hiramatsu & Oka [1966] for anisotropic materials, and test the theory experimentally.

The diametral loading geometry is almost similar to the Brazilian disk test [Mellor & Hawkes 1971]. Mellor & Hawkes [1971] suggested that the contact radius should be at least 1/12 of the sphere radius, which corresponds to a contact angle of ~ 5°. Otherwise, the inhomogeneous stress distribution along the loading axis can initiate the fracture near the surface instead of in the centre of the disk. Figure 6.6 shows that the tensile stress is almost uniformly distributed for $\Theta = 5\,°$, where a tensile stress plateau over the inner 90 % of the sphere is observed.

The calculation of the inhomogeneous tensile stress distribution along the axis of loading results in the function of maximum tensile stress severity (S_{t_max}). S_{t_max} describes the maximum S as a function of Θ and ν, and can be employed for calculating the tensile stress for arbitrary contact angles. This approach is supported by the successful estimation of proppant tensile strength (ISP: 160 ± 30 MPa and HSP: 270 ± 80 MPa) in §6.1.5. The calculated tensile strength correlates well with values from the literature for mullite and corundum ceramics [Shackelford & Alexander 2000] (table 7.1). The tensile strength of ISP is slightly higher than the value from the literature. This is due to its composition: ISP consists of almost 50 % Al_2O_3 and 50 % SiO_2. Its main component is mullite, with some portion of corundum. This explains the higher tensile strength compared to pure mullite. HSP consist of 80 % corundum. The determined tensile strength correlates well to the values from the literature.

	quartz	mullite	corundum
tensile strength [MPa]	40 - 80	~ 110	~ 250
compressive strength [MPa]	~ 1100	~ 2000	~ 3000
critical fracture toughness [MPa $m^{-0.5}$]	~ 1	~ 2	~ 4

Table 7.1.: *Mechanical properties of quartz, mullite and corundum [Shackelford & Alexander 2000, Landolt & Börnstein 1987].*

7.2 *Findings from Analysis of Acoustic Emission*

7.2.1 Hypocenter Localisation

The clustering of AE hypocenters in figure 5.11 (§5.3) highlights that grain crushing and proppant embedment starts at the fracture faces at low stress. No crushing events within the proppant pack can be observed. With increasing differential stress (σ_{diff}), the AE activity increases and moves from the fracture face into the proppant pack. At maximum σ_{diff}, the main activity is located within the proppant pack. The experiments Bent 3.4 and FB 1.6 confirm the observations from experiment Bent 2.3. The small fracture width of experiment Bent 3.4 only allows a separation of the fracture faces in the first two loading stages.

The total number of located events is much smaller in experiment FB 1.6 compared to experiments Bent 2.3 and Bent 3.4. FB 1.6 shows less AE activity for the following four reasons:

- The HSP are tougher than the ISP. HSP features a maximum closure stress of nearly 100 MPa (compare to figure 4.4a). Conversely, the maximum closure stress for ISP is exceeded at 65 MPa (manufacturer’s data sheet).

- The damage at the fracture face and within the proppant pack is small compared to Bentheim sandstone experiments (see discussion 7.6.1).
- The grain size is smaller. If the released energy per event scales with the grain size, the released energy during single grain crushing is less.
- Ultrasonic transmission measurements have shown that the attenuation of the Flechtingen sandstone is at least 2 times higher compared to the Bentheim sandstone.

The micrographs in figure 5.16 highlight that the main damage is located at the fracture face, where the proppants are embedded. This observation is in accordance with the conceptual model of a mechanically induced fracture face skin (§2.62). The observed permeability reduction is an effect of the crushing of quartz grains and fines production at the fracture face. The fines produced block the pores and result in a compacted zone with reduced permeability.

7.2.2 Source Type Analysis

The mode of crack propagation of AE events can be determined by discriminating between AE source types using first motion polarities [Zang et al. 1998]. For this purpose, the number of positive and negative first motion polarities is counted and normalised by the number of sensors. The events are classified as follows:

tensile / T-type event:	if more than 75 % of the polarities are positive
collapse / C-type event:	if more than 75 % of the polarities are negative
shear / S-type event:	if the proportion of polarities is between the above

This classification shows that a T-type event can have some portion of shear displacement, and an S-type event can have some portion of tensile displacement. The C-type can consist of both types and reflects the collapse of a pore. The collapse of a pore is initiated by tensile or shear failure of the surrounding grains. The grain fragments move simultaneously into the free pore space, and the pore collapses. For the following interpretation, it is important to note that the accuracy of a single AE localisation is ~ 2.5 mm and no distinct separation between events from the proppant pack and the interface is possible. On the other hand, even the loading of a 2 mm small proppant pack allows the identification of AE clusters located at the fracture faces.

In all three AE experiments, the AE activity at the fracture face features about 50 – 90 % of C-type. The damage at the rock-proppant interface is C-type dominated (compare to figure 5.18). This reflects the collapse of pores at the fracture face. Additionally, 10 – 30 % of S-type and 0 – 15 % of T-type events are recorded. The experiment Bent 2.3 identifies a predominance of T-type events (~ 50%), recorded from the proppant pack; S- and C-type events are about 30 % and 20 %, respectively. In contrast, in the experiment Bent 3.4, only 1-2 % of AE events are T-type, although many proppants are fractured (compare to figure 5.16a). One logical explanation is that tensile fracture generation mainly occurs in a proppant loaded in diametral point load geometry, comparable to Brazilian disk test [Mellor & Hawkes 1971]. Such geometry would generate tensile stress along the loading axis. Referring to a proppant pack, this loading geometry corresponds to a proppant loaded between two other proppants. This loading geometry is rarely observed within proppant packs with only a few layers, but frequently in large multilayer proppant packs. In experiment FB 1.6, 95 % of events recorded from the HSP proppant pack are C-type. These collapse events can result from a proppant cleavage fracture followed by movement of the fragments into the adjacent pore space.

These results from spatial AE source type analysis lead to the assumption that the failure at the rock-proppant interface is C-type dominated. This finding is confirmed by the observed collapse of pores at the fracture face. The failure of ISP pack shows T-type domination; about 50 % of the AE events at maximum differential stress are T-type. In contrast, the deformation of the HSP pack seems to feature a dominance of C-type events. However, the total number of crushed high strength proppants is small (compare to figure 5.16c) and dominating fracture generation process in proppant cannot be identified.

rock-proppant interaction testing / results					
	Bent 2.2 max. diff. stress: 20 MPa	**Bent 2.3** diff. stress: 20 MPa	**Bent 2.3** max. diff. stress: 50 MPa	**Bent 3.4** max. diff. stress: 50 MPa	**FB 1.6** max. diff. stress: 50 MPa
permeability reduction ratio (FFS zone)	13.3 ± 1.7	- / -	- / -	18.9 ± 1.7	6.6 ± 0.3
permeability reduction	92 %	- / -	- / -	95 %	85 %
reduction of fracture width	12 %	12 %	23 %	54 %	18 %
total number of AE events > 0.3 Volts	- / -	- / -	42,000	44,000	16,700
dominant source type at the fracture face	- / -	- / -	C-type	- / -	C-type
dominant source type in the proppant pack	- / -	- / -	T-type	- / -	(C-type)

***Table 7.2**: Main results of rock-proppant interaction testing with the acoustic emission flow cell.*

The main results from four rock-proppant interaction (RPI) experiments with the acoustic emission flow cell (AEFC) are summarised in table 7.2.

7.2.3 Correlations between Source Types and Stress Distributions

The observed AE emissions in a loaded ISP pack are dominantly T-type (tensile). This experimental result correlates with the identification of high tensile stress concentrations with both modelling approaches. Wu & Chau [2006] conducted impact tests on plaster spheres in diametral compression experiments. They concluded that dynamic fragmentation of spheres is in tensile mode along the axis of compression.

The number of T-type AE-events at the rock-proppant interface is relatively small (1 – 10 %). Mostly C-type (collapse) events (~ 70 – 90 %) and a portion of S-type (shear) events (10 – 30 %) are observed (§5.3.6). Both modelling approaches highlight that the shear stresses at the contacts can be very high. The numerical model computes maximum shear stress of 300 MPa at PP-contacts and 230 MPa in quartz at QP-contacts. Hence, shear failure can play a role during disintegration of quartz and proppants. These findings agree with the AE-observations of S-type events in the proppant pack and at the interface.

In particular, the chipping (spalling) at the surface of proppants (compare to figure 6.5) might be a mixed mode failure type. Starting from contact points, tensile stress distributions (σ_1 and σ_2) are observed that trend towards the surface along curved stress trajectories. Near these concentrations, high shear stresses are observed (compare to figure 6.11). A chipping fracture can be initiated by a tensile fracture. The propagation of this initial crack can be driven by the high shear stress. This is a hypothesis and might be investigated in future experiments. Experiments with a specialised acoustic emission setup would be helpful in the future to identify the initiation and characteristics of different fracture types in loaded spheres.

7.3 Failure at the Rock-Proppant Interface

The investigations with AEFC highlight that the damage in a rock-proppant system starts at small stresses at the rock-proppant interface. With increasing stress, AE activity from the proppant pack is observed. ISP shows high activity, and HSP moderate activity at σ_{diff} = 50 MPa (compare to §5.3).

7.3.1 Initial Loading of Rock-Proppant Systems

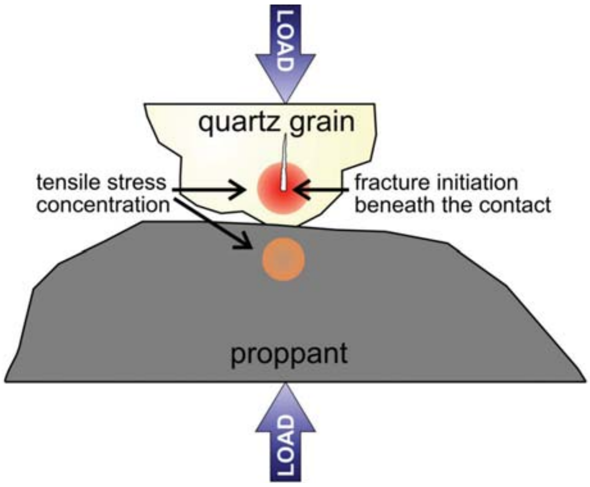
LOAD
quartz grain
tensile stress concentration
fracture initiation beneath the contact
proppant
LOAD

Figure 7.1: *Fracture initiation at the rock-proppant interface. The analytical approach for diametral loading of spheres predicts a high tensile stress concentration (red dot) beneath the contact. This tensile stress already exceeds the tensile strength of quartz at small externally applied differential stresses, and can explain the early onset of quartz grain crushing.*

In the initial phase of an experiment at isostatic pressure (10 MPa) or small differential loadings (5 MPa), a significant reduction in permeability can already be observed in the RPI experiments with both proppant types.

The numerical and the analytical approach identify highly localised tensile stress concentrations beneath contact areas if the contact angles are small.

The analytical approach explains the onset of quartz grain crushing at the rock-proppant interface. Even at low external stress (5 MPa), the tensile strength of quartz is exceeded (compare to figure 6.9). Fracture initiation and failure of quartz grains are to be expected during initial loading of rock proppant systems. In contrast, the tensile stress in proppants is too low to initiate failure. Figure 7.1 illustrates this relation.

The shape of the quartz grains can intensify the stress concentration. If the edge of a sub-angular quartz grain hits the proppant, the contact area will be very small; smaller than predicted by the Hertzian contact model used for analytical stress calculation. This intensifies the stress concentration and the quartz grain crushes at a very early stage of an RPI experiment. The Bentheim quartz grains in particular have a subrounded to subangular shape (compare to §4.1).

In general, the stresses at grain contacts in this granular system of quartz grains and proppants are significantly higher than the external stresses. The inhomogeneous stress distribution results in local failure, even if the externally applied stresses are significantly lower than the strength of the material.

Both modelling approaches identify tensile stresses in proppants at the rock-proppant interface below the tensile strength of ISP and HSP. Hence, the acoustic emission at the interface, and consequently the damage done to it, is attributed almost completely to quartz grain crushing. Proppant crushing starts at PP-contacts and not from PQ-contacts. The magnitude of tensile stress is too low to initiate fractures at PQ-contacts.

Tensile stresses calculated using the numerical approach are significantly smaller compared to the analytical approach. The analytical approach cannot explain the early onset of quartz grain crushing observed in the AEFC experiments.

7.3.2 Extent of the AE Cluster at the Rock-Proppant Interface

The AE investigations in §5.3 point out that the zone of AE activity at the rock-proppant interface extends to about 4 mm, which it is equal to roughly 12 grain radii. The accuracy of a single AE localisation is ~ 2.5 mm; the range of 4 mm might be an effect of dislocation. On the other hand, even the loading of a 2 mm proppant pack allows the identification of two separate AE clusters in the initial loading stage (compare to figure 5.14a). In addition, at low stresses (σ_{diff}: 0 – 20 MPa), the entire AE activity is recorded at the rock-proppant interface or the adjacent quartz grains (see figures 5.11 and 5.15). Almost no events are detected in the proppant pack.

One can assume that the entire activity is not caused by damage at the rock-proppant interface. Some of the recorded activity can be attributed to grain deformation and crushing along the grain-pore and grain-grain boundaries near the interface. The numerical model identifies tensile stresses near pores of -80 – -200 MPa. Hence, grain crushing can be expected at some distance from the grain-proppant contact (tensile strength of quartz: 40 – 80 MPa).

The area of investigation in this model is too small to differentiate between near field and far field effects of the rock-proppant interface. An additional study including a rock layer larger than 12 grain radii is necessary to clarify if these high stresses are caused by the point loading from rock-proppant interface. Blöcher et al. [2007] simulated the pore structure deformation of Bentheim sandstone with Rockflow/Geosys in an isostatic compression experiment with effective stresses up to 70 MPa. They found high stresses above 100 MPa near grain contacts and neighbouring pores.

7.4 Failure within the Proppant Pack

The theory of Hiramatsu & Oka [1966] was used to estimate the proppant tensile strength (§6.1.5). The intermediate strength proppants have a mean tensile strength of 160 ± 30 MPa and the high strength proppants of 270 ± 80 MPa.

The analytical approach estimates maximum tensile stresses of -95 MPa (ISP) and -175 MPa (HSP) at proppant-proppant contacts (compare to figure 6.9c). The contact radii are calculated using the Hertzian contact theory [Hertz 1882]. They are about 4° at the maximum external differential stress (σ_{diff}) of 50 MPa. This indicates that the contact angles between proppants might be even shallower, due to irregularities and asperities at the surface.

At σ_{diff} = 50 MPa, the numerical 2D-model observed maximum tensile stresses of ~ -300 MPa at PP-contacts (compare to table 6.7). These extremes are highly localised at the contact circle. Hence, the extremes correspond to the maximum tensile stress caused by Hertzian contact. The stress is high enough to initiate cracks, but it is significantly lower than the tensile stresses predicted by the Hertzian contact theory (compare to §6.1.2). Parallel to the discussion in §6.1.2, an internal material failure in the direct vicinity of the highly localised stress concentration is necessary to release an internal crack, which then effects proppant failure.

The tensile stress concentration beneath the contact (~ -70 MPa) is obviously too small to explain the proppant failure. In general, the 2D-numerical modelling approach predicts smaller stresses at contacts, compared to the analytical approach. This can be an effect of the mesh geometry. The stress concentrations occur along the axis of loading. If the mesh along the axis of loading is too coarse, the tensile stress might be underestimated.

Both approaches cannot explain the proppant failure observed at elevated differential stresses. Indeed, the analytical approach (compare to §6.1.5) shows that the minimum tensile strength of ISP (~ 95 MPa) and HSP (~ 150 MPa) is significantly smaller than the mean values. Hence, the analytical approach can predict the failure of some amount of proppants, but cannot explain the high AE activity observed from the ISP pack in experiment Bent 2.3.

This significant deviation of minimum tensile strength from the mean values as well as from the values in the literature for mullite and corundum might be due to the material failures found in proppants (compare to figures 4.4b and 6.9).

Fracture mechanics defines a Mode I crack. In Mode I, the crack faces are subjected purely to tensile stress; it is known as the tensile or opening mode [Whittaker et al. 1992]. The grade of stress concentration at the tip of a crack of length l and the applied stress σ_t, is defined by the stress intensity factor K_I [Atkinson 1987]:

$$K_I = \sigma_t \sqrt{\pi \cdot l} \qquad 7.1$$

This concept is only valid the case of fracture propagation in its own plane. If the stress intensity reaches the critical Mode I fracture toughness value (K_{Ic}), the fracture propagates. A small defect can increase the stress intensity factor and decrease the tensile strength of a particular material. If the crack length doubles, the tensile strength decreases by 1.41.

The micrograph in figure 4.4b identifies layers and small pores in intermediate strength proppants. These defects influence the tensile strength of an individual proppant. Table 7.1 lists values for K_{Ic} for quartz, mullite and corundum.

7.5 Stress Pattern and Fracture Pattern

In figure 7.2, the stress pattern (σ_2) computed at external differential stress of 50 MPa is compared to the fracture pattern observed in a micrograph of a rock-proppant system. The corresponding stress and fracture patterns in figure 7.2 are marked with the same number:

1) Highly localized tensile stresses are observed at proppant-proppant contacts. These tensile stresses can affect a proppant cleavage fracture, starting from both contacts and propagating towards the centre. The micrograph shows such cleavage fractures in proppants.
2) The numerical calculation identifies high tensile stresses, which trend from the contact towards the surface. These stress concentrations can explain the chipping of proppant fragments. Figure 7.2 clearly shows these chipping features at the surface. This explanation for chipping is not found in the analytical approach.
3) Curved fractures between contact points follow the tensile stress trajectories. Tensile stresses along curved lines between contact areas are identified in σ_1 and σ_2 (figure 6.11).
4) The 2D-model shows localised tensile stress maxima in the quartz grains (region α und β). At the rock-proppant interface, proppants are embedded and the quartz grains are disintegrated in the micrograph.

Proppant B illustrates an embedded proppant. Only compressive stresses occur at this rock-proppant contact. This proppant is well supported, and initiation of fracturing is unlikely. This observation is confirmed by the micrograph. Proppant fracturing is not initiated at quartz-proppant contacts.

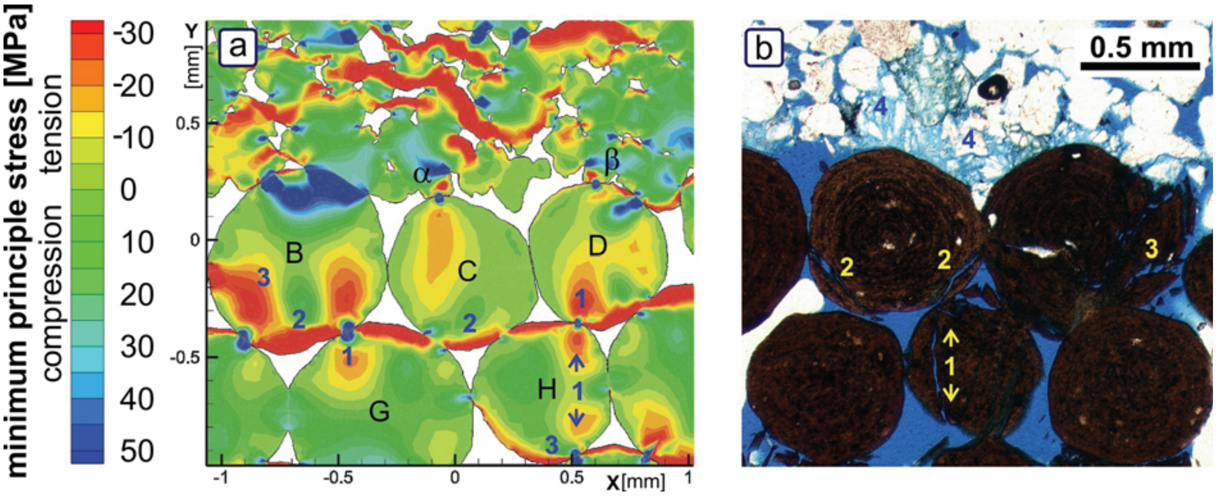

Figure 7.2.: *Comparison of stress pattern and fracture pattern in rock-proppant systems. The stress pattern determined using 2D modelling, mirrors the fracture pattern observed in a micrograph from the rock-proppant interface. 1: High tensile stress concentrations at proppant-proppant contacts can result in a cleavage fracture. 2: High tensile stresses at the surface are observed. These stresses explain the chipping near the contact region. 3: Curved stress patterns between contacts are detected; curved fractures between contacts can be seen. 4: High tensile stress concentrations in quartz grains at the interface are identified (α, β). The quartz grains at the interface are highly fractured.*

7.6 *Influences on FFS permeability*

7.6.1 Pore Structure of Sandstones

The Bentheim sandstone shows a large amount of damage and fines production at the fracture face (figure 5.16). In contrast, the damage at the rock-proppant interface of Flechtingen sandstone is small. Bentheim sandstone grains are sub-angular leading to small contact areas and high stress concentration at the rock-proppant interface. In addition, the Bentheim sandstone has a porosity that is about twice that of Flechtingen sandstone. In Bentheim sandstone, the grains are supported poorly within the granular structure (compare to figure 4.2a). The grade of cementation and consequently the contact areas between quartz grains are small. This causes stress concentration due to point loads at grain to grain contacts.

During failure, the induced fragments and fines move into the pore space and block the pores, explaining the observed reduction in permeability. Contrary, the Flechtingen sandstone grains are well supported by the about 20 % of cement (compare to figure 4.2c). Contact stresses at the rock-proppant interface are likely to be more distributed and stress concentration at grain contacts is expected to be much smaller.

Another explanation for the large amount of crushing at the Bentheim fracture face is the pore geometry. §4.3.1 investigates the distribution and geometry of pore sizes for Bentheim and Flechtingen rock. The Bentheim sandstone has a mean pore density of 21 pores / mm^2, and the mean pore radius (r^p_{50}) is 98 µm (optical measurement). The Flechtingen sandstone has smaller pores with r^p_{50} of 23.8 µm, and the number of pores is much higher with an average of 920 pores / mm^2. Both rock types have a large number of small pores that are nearly perfect spheres (compare to figure 4.6 & 4.7). With increasing pore radius, the circularity (C) of the pores in Bentheim rock decreases faster than in Flechtingen rock (figure 4.7). Bentheim sandstone has a fraction of approximately 15 % of large pores with a very low circularity ratio. If these "crack-like" pores with high aspect ratios are loaded, they will probably collapse at smaller loads compared to perfectly round pores.

7.6.2 Macroscopic Tensile Fracture Generation via 3-Point Bending Test

In preparation of a rock-proppant interaction test, the intact sandstone specimens are split by a macroscopic tensile fracture generation (3-point bending test) [Sun & Ouchterlony 1986]. The hypothesis is that the process zone around the tip of the tensile fracture may produce fines and may influence permeability. Backers [2005] optically estimated a width of 0.7 - 0.8 mm of the fracture process zone (FPZ) surrounding a tensile fracture in a Flechtingen sandstone. The FPZ estimated from acoustic emission was 6-9 times larger. Although an FPZ does exist, one would probably expect that the pore space is not as severely damaged as in a compressive test.

Experiment Bent 3.4 shows a significant reduction in permeability of the specimen with tensile fracture (~ 25 %); other experiments with Bentheim sandstone do not support this result. If this permeability reduction effect exists, the mechanically induced fracture face skin would result from two different permeability impairments: the macroscopic tensile fracture generation and the mechanical interaction of rock and proppant. This hypothesis should be investigated in further studies, which are beyond the scope of this work.

7.6.3 Determination of Damage Penetration of FFS zone

In §5.3 two methods of measuring the extent of the fracture face skin zone (penetration depth / w_S) were presented. The penetration depth has a direct influence on the permeability estimate for the fracture face skin (FFS) zone (k_S). The first method determines w_S from the cluster of hypocenters at the fracture face; the second method measures the thickness of a damaged layer at the fracture face from micrographs. Both methods have different resolutions and entail different uncertainties for estimating w_S.

A single AE location has an uncertainty of 2.5 mm. Hence, w_S determined from an AE cluster represents an upper limit for the extent of the mechanically induced FFS. This maximum leads to a minimum permeability reduction ratio (k_i/k_S). In contrast, the fracture face is only affected by crushing at the contact points (compare to figure 5.16). This results in a highly irregular shape of the damaged zone, and the optical estimate of w_S becomes somewhat arbitrary.

The triaxial shear failure experiments of Bentheim sandstone (compare to §5.1.) have delivered a permeability reduction ratio in the gouge zone of a shear band of between 180 and 1700 (§5.1.4). Fortin et al. [2005] estimated a permeability reduction ratio of 6 - 600 between initial permeability and permeability in the compacted zone in triaxial sandstone experiments. Vajdova et al. [2004] estimated the permeability of compaction bands and found a reduction ratio of 40 – 400. Fortin et al. [2005] have assumed a model that relates the initial porosity of a rock to the crack density and crack aspect ratio in the compacted zone. Vajdova et al. [2004] modelled the overall specimen permeability as a series of compacted layers in the non-damaged rock. Compared to these values, the permeability reduction ratios determined optically from the "gouge" at the rock-proppant interface between 350 and 430 (compare to table 5.7), are reasonable and provide a realistic approximation. Nevertheless, the lower limit of the estimation of Fortin et al. [2005] is within the range of the permeability reduction ratio determined from AE cluster analysis. Possibly, the penetration depth, as well as the fracture process zone, is not as clearly defined as assumed for the model calculations.

This means: The estimated values of k_S are equivalents to a homogeneous mechanically altered layer with reduced permeability at the fracture face. The determined permeability is an integral value for a given layer with a defined thickness. The amplitude of k_S and the k_i/k_S ratio are directly dependent on the given penetration depth w_S.

Two arguments contradict the general use of the optical gouge layer determination:

1) AE investigations of a shear fracture process zone (FPZ) (§5.1) point out that the acoustic FPZ is 15 times wider than the optical FPZ. The same trend holds for the RPI testing, where the acoustic FPZ is 26 times wider than the optical FPZ. On the one hand, this difference is owed to the accuracy of AE hypocenter location. On the other hand, it is possible that damage of grains occurs some distance from the rock-proppant interface, due to high contact loads, and this damage is not visible in micrographs.

2) The Flechtingen sandstone shows a significant reduction of k_T during RPI testing and an acoustic FPZ can be clearly identified in figure 5.15. An optical FPZ is hardly visible in the micrograph (figure 5.16c); only some isolated grains at the interface are fractured.

The consequence of these arguments is to define a penetration depth (w_S), which is used for all RPI experiments in order to compare the results. For all calculations w_S = 4 mm is used (estimated from the AE experiments). The calculation of the fracture face skin (equation 2.36) and the reservoir productivity (equation 2.39) are not influenced by this definition.

7.7 Influence of Proppant Pack Permeability

The permeability of the proppant pack (k_f) has a strong influence on the fracture conductivity and on the productivity of a reservoir. Table 7.3 compares the permeabilities, fracture width alterations and bulk deformation moduli for different RPI experiments. The reduction in permeability for ISP (60 – 75 %) is higher than the reduction for HSP (30 – 42 %). In general, the rock-proppant systems with Flechtingen sandstone show a higher k_f reduction. The permeability reduction coincides with a reduction of fracture width (w_f), of which Bentheim sandstone specimens have 16 – 20 %, and Flechtingen sandstone samples have 12 – 13 %. The Bentheim experiment with a low proppant concentration features the highest reduction of 52 %.

Wen et al. [2007] demonstrate that proppant concentration has a major impact on the conductivity of fractures at in-situ conditions. The fracture conductivity is the product of k_f and w_f. A lower concentration causes a higher percentage in reduction of conductivity. The larger reduction is an effect of proppant embedment into the fracture faces and the resulting loss of fracture width. Proppant embedment disproportionally affects proppant packs with a small number of proppant layers [Wen et al. 2007]. Figure 7.3 illustrates this interrelation. The micrograph in figure 5.16a shows that about half the proppant diameter at each fracture face is lost, due to embedment of ISP into the Bentheim rock matrix. The effect of proppant embedment explains the significantly higher reduction in fracture width in RPI experiment #1, as compared to experiment #2 (table 7.3). Both experiments were performed with the same rock and proppant type.

The numbers of localised events in the acoustic emission RPI experiments Bent 3.4 and Bent 2.3 are almost identical, although the proppant concentration is twice as high in the latter experiment (compare to §5.3). Most of the damage occurs at the fracture face where proppants get embedded. This supports the hypothesis that most of the reduction in fracture width is an effect of proppant embedment.

In weakly cemented rocks in particular, proppant embedment is an issue [Baree et al. 2003]. Hence, the reduction in fracture width for experiments #2 and #3 (Bentheim sandstone) is higher than the reduction for experiments #4 and #5 (Flechtingen sandstone). The micrograph in figure 5.16c supports this finding; damage and embedment at the fracture face are little for Flechtingen rock.

The inelastic bulk deformation modulus (E_{D_in}) identifies the degree of inelastic deformation in the rock-proppant system. Initially this value is small, i.e. the degree of inelastic deformation is high. The acoustic emission (AE) experiments (§5.3) locate only a small number of events from the proppant pack during initial loading; the AE activity occurs at the fracture faces. Hence, a proportion of the small E_{D_in} reflects the reorganisation and packing of the proppant pack, but only minor damage.

At maximum differential stress (σ_{diff}), E_{D_in} of ISP is significantly lower than E_{D_in} of HSP. The AE experiments show that the ISP fails in contrast to HSP at σ_{diff} > 35 MPa (compare to figures 5.11 and 5.16). The large amount of AE events from the proppant pack during loading from 35 - 50 MPa is accompanied by a decrease in E_{D_in} of ISP at this loading stage, as well as the high degree of inelastic deformation (compare to figures 5.19f and 5.20f). At the same loading stage, E_{D_in} of HSP increases and indicates a stiffening of the rock-proppant system.

The HSP proppant type is tougher. Hence, HSP possess a higher permeability and a lower reduction at maximum σ_{diff} (50 MPa), as compared to the ISP. (Both proppant types feature almost the same mesh size.) The permeability reduction observed at maximum σ_{diff} is higher than expected according to the manufacturer’s data (55 % for ISP and 35 % for HSP). Fredd et al. [2000] performed fracture flow experiments with split rock cores and concluded that conductivity experiments performed with flat, parallel core faces tend to overestimate the conductivity, compared to actual hydraulic fractures with rough fracture faces.

number	rock type / proppant type	proppant concentration	reduction in proppant pack permeability	reduction in fracture width	initial inelastic bulk deformation modulus	final inelastic bulk deformation modulus
		kg/m²	%	%	GPa	GPa
#1	Bent / ISP	5	- / -	52	- / -	- / -
#2	Bent / ISP	10	60	20	0.4	1.7
#3	Bent / HSP	10	30	16	0.2	3.6
#4	FB / ISP	10	75	13	0.5	0.9
#5	FB / HSP	10	42	12	0.5	10

Table 7.3: *Influence of rock type, proppant type and concentration on fracture width and permeability.*

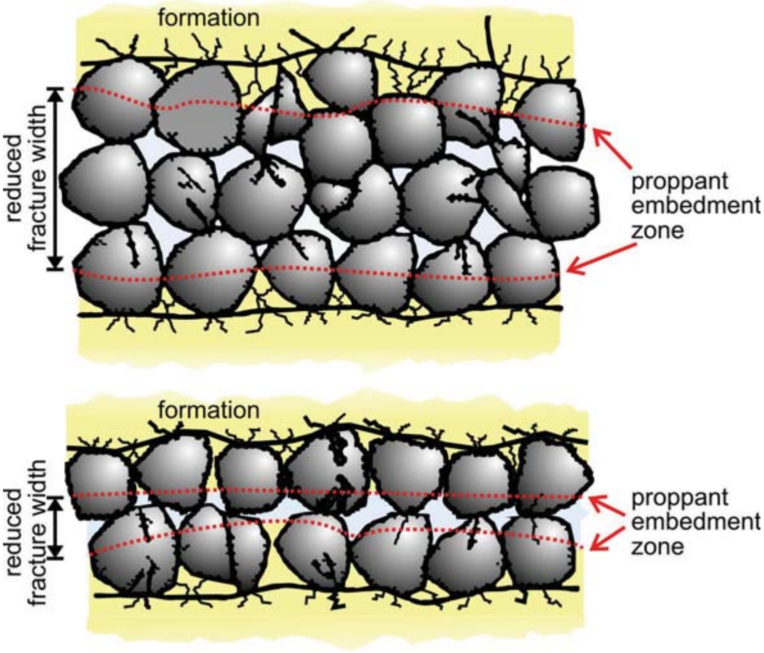

Figure 7.3: *Influence of proppant concentration on the fracture width at production conditions. The number of proppant layers strongly influences the fracture width during production. Fracture closure stress results in proppant embedment and reduces the fracture width of the lower fracture disproportionally high.*

Platens, quite often used in standard flow cells [Anderson et al. 1989, API 60 1989], inhibit the generation of fines from the fracture face. From a rough fracture face, the amount of fines produced can be significantly higher. These fines are transported into the proppant pack and affect permeability (compare to figure 5.22e). Indeed, optical inspection of proppant packs from Bentheim rock RPI experiments identified a large amount of crushing caused by quartz grains. In contrast, Flechtingen rock RPI experiments with ISP, result in a large amount of crushing caused by proppants. In this experiment, the proppant pack permeability is shown to be reduced much more.

At this point, it should be noted that permeability of a proppant pack is a representation of specific packing conditions and grain size distribution, not an intrinsic material parameter. The permeability measured will vary significantly, even if the experimental procedures and conditions are the same for each experiment. Baree et al. [2003] found variations of up to 50 % at 53 MPa fracture closure stress for a proppant pack of 20/40 frac sand. In contrast, the fracture width of these experiments varied by only about 4 %. To describe the fracture conductivity behaviour, a statistically significant number of experiments must be performed under the same conditions.

The experiments conducted with AEFC and BDFC show that final proppant pack permeability, fracture width and fines production are a function of the proppant type, the proppant concentration, and the rock type.

The influence of proppant embedment on fracture conductivity and width suggests that proppant concentration should be maximised in hydraulic stimulation operations. In the absence of proppants, the fracture conductivity is controlled by asperity and displacement [Fredd et al. 2000], and water fracturing treatments with low proppant concentrations can be impaired by fracture closure. Nevertheless, water fracturing treatments in tight reservoirs are conducted successfully and provide sufficient conductivity, even if the controlling mechanisms are not well-understood [Mayerhofer et al. 1997, Walker et al. 1998].

Further investigations into low proppant concentrations using the AEFC and BDFC would give insights into the mechanical and hydraulic interactions between rough surfaces and partial monolayers of proppants. In particular, the mechanically induced FFS might be reduced as a result of fewer contacts; but on the contrary, the stress on a single contact will drastically increase in partial proppant monolayers.

7.8 Long-Term Influences on Permeability at Reservoir Conditions

The permeability in all three long-term experiments reaches a constant level after sufficient experiment duration. In all experiments, the permeability is reduced by 50 – 85 % within 1 - 4 days. Long-term testing of the specimens (up to 40 days) results in a further permeability reduction of up to 95 %. The initial permeabilities and the long-term values are listed in table 7.4.

It is important to note that the reported reduction in permeability is somewhat arbitrary. The amplitude of permeability reduction is a function of the initial measurement. This initial value depends on the saturation process, fluid velocity and duration of fluid exposure. Hence, it does not reflect the intrinsic permeability of the rock type. The permeability reduction can be used to rate the different effects on permeability. Mechanical, chemical, as well as temperature influences can be considered as sources for the reduction in permeability observed for Flechtingen sandstone and the rock-proppant systems.

In contrast to experiments FB 10.11 and FB 10.12, the intervals between the modification of temperature and stress state were chosen to be sufficiently long in experiment FB 10.13, in order to equilibrate the flow system. Hence, the influence of the individual changes in experimental conditions, which influences the permeability of a rock-proppant system, can be determined from this experiment. Figure 7.4 shows the evolution of permeability.

Initially, the specimen is loaded with a small effective stress of 2 MPa and a temperature of 40 °C is applied to it (figure 7.4a). The initial permeability of the rock-proppant system is about 540 µD. A reduction in permeability by a factor of 2 is observed within the first four days of this experiment (figure 7.4b). This reduction is very likely to be attributed to the chemical-mechanical interaction between the rock and the 0.1 mol NaCl brine. Rotliegend sandstone contains about 6 % kaolinite and 9 % illite [Trautwein 2005]. In contact with the pore fluid, kaolinite is dispersed and migrates through the void space. Illite swells under favourable ionic conditions, and subsequently the illite phase is mobilised (compare to §2.6). The dispersed clay particles can accumulate at pore throats, thereby blocking the fluid pathways in the rock and causing decreased permeability. Clay swelling and mobilisation can be suppressed by adding a sufficient concentration of ions to the pore fluid. The concentration of 0.1 mol NaCl (~ 0.5 %) brine is too low to stabilise the clay minerals [Rahman et al. 1995].

Increasing the effective stress from 2 MPa to 10 MPa on day 7 (figure 7.4c) induces a further reduction in permeability from 320 µD to 170 µD. This further reduction by 50 % is an effect of consolidation. Blöcher et al. [2007] observed the same twofold permeability reduction during cyclic isostatic loading of Flechtingen sandstone.

Increasing the temperature to 150 °C (figure 7.4d) causes a reduction in permeability to 48 µD (day 8). It is unclear why a temperature rise has such a large effect on permeability. One possibility might be the alteration of clays with temperature. Another possibility is a chemical interaction and mineral conversion at given pT-conditions.

Weaver et al. [2009] found that proppants can dissolve due to pressure solution at favourable pT-conditions within weeks of fluid exposure. Microscopic observations (figures 5.24a&b) do not provide any indication for such dissolution of the ISP. In addition, the reduction in permeability takes place almost instantaneously. After sufficient time (constant conditions for 17 days), the permeability stabilises. In total, the permeability reduction of the rock-proppant system is about 93 %.

experiment	time [d]	permeability at beginning of experiment [µD]	time interval [d]	long term permeability [µD]
FB 10.11 / intact specimen	0.08	860 ± 40	8 - 15	120 ± 7
FB 10.12 / HSP	0.10	760 ± 30	21 - 27	109 ± 3
FB 10.13 / ISP	0.75	570 ± 30	25 - 35	38 ± 2

Table 7.4: *Initial and long-term permeabilities of Flechtingen sandstone experiments with ISP and HSP.*

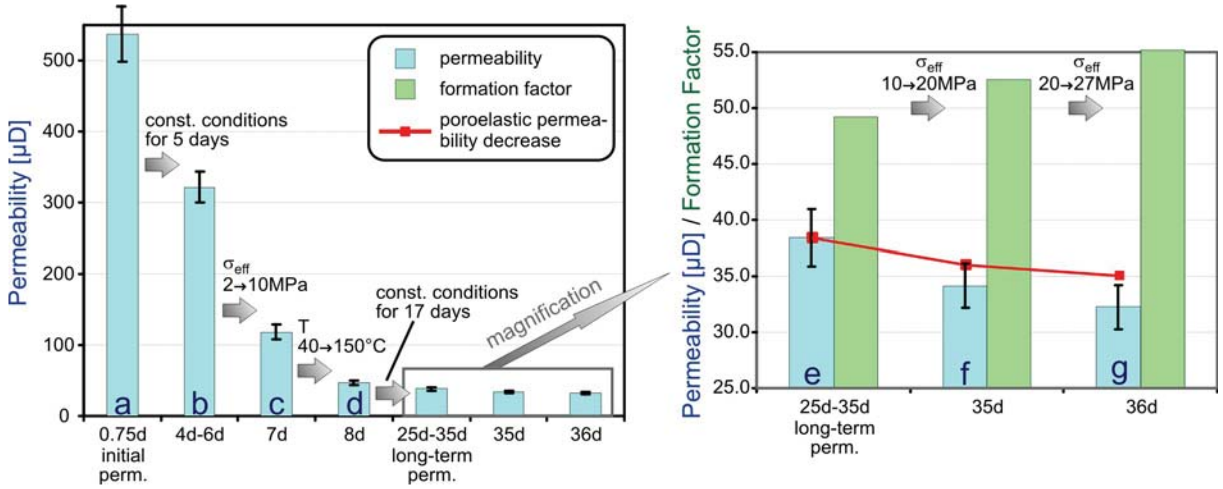

Figure 7.4: *Permeability evolution in a long-term experiment with Flechtingen sandstone and ISP proppant pack. The permeability of a rock-proppant system is altered due to chemical, mechanical and thermal influences. The initial permeability reduction (b) over 3 days is most likely an effect of electrochemical interactions between the pore fluid and the clay minerals in the Flechtingen rock (illite). Increasing the effective stress (c), as well as increasing the temperature (d) results in a further reduction in permeability. After sufficient time (25 days), the permeability reaches a constant level (e). From this level, the effective stress is increased up to 20 MPa (f) and 27 MPa (g) and a permeability reduction is observed, which is higher than the poroelastic permeably change (red line). This is an indication of flow impairment at the rock-proppant interface. The decrease in permeability is accompanied by an increase of the formation factor, i.e. the electrical conductivity of the rock-proppant system is reduced.*

A strict separation of time, stress and temperature effects was only performed for experiment FB 10.13. In addition, experiment FB 10.12 supports the findings from experiment FB 10.13. Consolidation as well as chemical-mechanical interaction results in a reduction in permeability of 80 %. Increasing the temperature causes a further reduction of 87 % (compare to table 5.13). Compared to experiment FB 10.13, the temperature's effect is less pronounced.

Increasing the effective stress to 20 MPa and 27 MPa at the end of experiment FB 10.13 (day 36 / figure 7.4g) leads to a permeability reduction of about 11 % and 16 %, respectively. The reduction is calculated relative to the long-term permeability of 38 ± 2 µD.

This reduction in permeability of 16 % is clearly higher than the poroelastic permeability change of Flechtingen sandstone. For illustration, the poroelastic permeability change is plotted as a red line in figure 7.4. In this comparison, a power law dependence of stress and permeability is used with a power law exponent of -0.093 (compare to §5.1.7). The comparison indicates that the mechanical interaction at the rock-proppant interface has affected the permeability in this long-term experiment, comparable to the experiments with AEFC and BDFC.

The experiments conducted with the AEFC and BDFC allow a direct calculation of the influence of rock-proppant interactions on permeability, because the same rock specimens are used to determine the permeability of the rock-proppant system (k_T) and of an intact sandstone specimen (k_i). For the long-term experiments, different specimens are used. This difference in experimental procedure inhibits a direct comparison of permeabilities of intact Flechtingen rock and rock-proppant systems. Experiment FB 10.12 shows a slightly reduced long-term k_T in comparison to permeability of the intact sandstone specimen in experiment FB 10.11 (k_i). The reduction in permeability is about 85 % in both experiments (compare to table 5.13), and no influence on the rock-proppant (HSP) interaction can be detected.

The reduction in permeability determined from experiment FB 10.13 is about 95 %. Increasing the temperature has the major impact, whereas mechanical stress at the rock-proppant interface has only a minor influence. These findings are supported by the small amount of grain crushing, fines production and pore blocking at the rock-proppant interface in Flechtingen sandstone (compare to figure 5.24).

Consequently, the reduction in permeability at the rock-proppant interface cannot be quantified with the LTFC, since the reduction observed that is due to mechanical interaction, is too small to form a clear contrast to other influences. Two reasons account for this:

1) A smaller stress than in the AEFC and BDFC experiments was chosen, because the reservoir conditions at the Gross Schoenebeck geothermal test site were simulated. Maximum effective stress was 27 MPa.

2) A sawed fracture was used for testing the rock-proppant systems. The specimens for the LTFC were too small to generate a controlled tensile fracture with a 3-Point bending test [Sun & Ouchterlony 1986]. The contact area between a proppant and a flat surface is larger than the contact area between an angular quartz grain and a proppant. This larger contact area results in lower stress and stabilises the rock-proppant system. Less damage at the interface is to be expected.

7.8.1 Correlation Between Hydraulic and Electrical Flow in Rock-Proppant Systems

The formation factor is defined as the ratio between electrical conductivity of the fluid (at a given temperature) and the conductivity of the rock specimen that is measured. A decrease in rock conductivity is an indicator of an impairment of the fluid pathways. At reservoir conditions, the formation factor (FF) of the intact specimen (FB 10.11) is about 44 (table 7.5). Other authors [Milsch et al. 2008, Engelmann 2007] found a similar formation factor of 40 for a very tight Flechtingen rock (k = 27 µD). The two rock-proppant systems feature a formation factor of 32 and 50, respectively.

The three experiments indicate that there is a rough correlation between the formation factor and the permeability. A decrease in permeability is accompanied by a decrease in electrical conductivity of the specimen, and an increase of the formation factor. During experiment FB 10.13, the permeability drops to 38 µD and the formation factor rises to 48. The magnification in figure 7.4 supports this finding; the decreasing permeability is accompanied by an increasing FF. Compared to the permeability, the alterations are smaller. FF increases by about 6 % and 11 %, at effective stresses of 20 MPa and 27 MPa, respectively.

Generally, measuring electrical rock conductivity (κ_R) and the formation factor (FF) is a powerful tool to characterise the fluid flow in the pore space of a type of rock. To use this tool, it is necessary to understand the k-κ_R - relationship and how to interpret they vary. Milsch et al. [2008] reported of an empirical correlation to describe this k-κ_R - relationship. They used an established empirical relation [Walsh & Brace 1984] to link k and FF:

$$k=c_F \cdot L_F^2 \frac{1}{FF^b} \qquad 7.2$$

where c_F is a shape factor, L_F is a characteristic length scale, and b is an empirical, rock-specific parameter. The physical meaning of both parameters c_F and L_F depends on the assumed pore space model. Investigations of Flechtingen rock in the LTFC in order to describe the k-κ_R-dependence yield [Milsch et al. 2008]:

$$k\ [\mu D]=1124 \frac{1}{FF^{1.0313}} \qquad 7.3$$

The formation factors determined in this study are used to estimate a permeability for the experiments FB10.11 – FB 10.13. For that purpose, mean values of FF are calculated and compared to the permeabilities measured (table 7.5). The time intervals are chosen in accordance with the long-term permeabilities.

This approach fails; the estimated permeabilities are considerably lower (factor 2 - 5) than the measured permeabilities. This holds for the intact specimen as well for the rock-proppant systems. The permeabilities of this Flechtingen rock specimen cannot be predicted from the k-κ_R –

dependence, although the formation factors of the Flechtingen sandstones are similar to measurements from Milsch et al. [2008].

The purpose of the electrical measurements was to detect precisely small alterations of the pore structure and fluid pathways due to rock-proppant interactions. It appears to have missed this goal. The evolution of the formation factor shows a correlation with the permeability (figure 7.4), but no conclusions can be drawn about the fluid impairments at the rock-proppant interface.

The interdependence of pore radius of electrical and hydraulic transport in a rock can explain the observed differences between evolution of FF and k. The permeability (k) is a quadratic function of the pore radius; the electrical conductivity is independent of the pore radius. This results in different flow paths for a given pore radius distribution. The hydraulic fluid flow will predominantly follow the path of least resistance, i.e. the path of maximum permeability. The electrical flow density is equally distributed over the pore space and the electrical flow follows the shortest path. Hence, the electrical tortuosity is always less than or equal to the hydraulic tortuosity.

The fines production at the rock-proppant interface leads to an alteration of hydraulic tortuosity, but not necessarily to an equal measure of alteration of electrical tortuosity. This correlation is obvious from figure 7.4; the formation factor increases by about 6 – 11 %, whereas the permeability decreases by 11 – 16 % at σ_{eff} of 20 MPa and 27 MPa, respectively.

Although the formations factor of the intact specimen determined by Milsch et al. [2008] and the formation factor of the intact specimen in FB 10.11 differ by only about 10 %, the permeability shows a deviation by a factor of 5. Hence, the k-κ_R - relation differs significantly between different sampling locations of the same rock type.

	measured long-term permeability [µD]	**formation Factor**	**estimated permeability [µD]**
FB 10.11 / intact specimen	120 ± 7	44 ± 5	23 ± 3
FB 10.12 / HSP	109 ± 3	32 ± 2	32 ± 2
FB 10.13 / ISP	38 ± 2	50 ± 3	20 ± 1

Table 7.5: *Comparison of measured permeabilities and permeabilities estimated from formation factor.*

7.9 Implications for Hydraulic Stimulations

7.9.1 Impact of long-Term Testing at Reservoir Conditions

The three long term tests show that the permeability of rock and rock-proppant systems reach a constant level after sufficient time. Having reached equilibrium conditions, no further long-term permeability alteration of the rock-proppant system is observed. Transferred to a reservoir at constant drawdown conditions, no long-term influences from mechanical interactions of the proppants with the fracture face can be expected. The permeability will stabilise at a constant level.

The specimen with intermediate strength proppants shows a threefold permeability reduction, compared to the other two experiments, due to a coupled thermal-hydraulic effect. This long-term experiment highlights that further effects, in addition to the mechanical effects, influence the evolution of permeability of a rock-proppant system. Further experiments are necessary to discover the nature of this thermo-hydraulic coupling in rock-proppant systems

7.9.2 Implications for Propping Agents

The tensile stress concentration beneath the contact area is a function the contact angle (Θ) and the Poisson ratio (ν). Hence, an implication for propping agents is the use of materials that provide a large contact angle and a large Poisson ratio. The contact angle is a function of ν and the Young modulus (E). A smaller value for E results in a larger Θ. For that reason, the contact angles of quartz grains are large compared to the angles of ceramic proppants. Sand used as a propping agent should decrease the embedment into the rock matrix.

proppant type	ceramic	sand	sand resin coated
fracture closure stress	25 MPa	25 MPa	50 MPa
relative size of proppant embedment	● 100 %	● ~75%	● ~25 %

Table 7.6: *Influence of material properties of proppants on the size of embedment. Penny [1987] demonstrated that the usage of sand and resin coated sand reduces the diameter of proppant embedment significantly compared to ceramic proppants.*

Schönert [2004] stated that the explosive type of fracturing in conjunction with abundant fines at the contact area is suppressed, if the sphere is plastically deformed at the contact face. This inelastic deformation increases the contact area and decreases the stress density in the sphere. A resin coating can provide the function of an inelastic deformable material and stabilise the proppant. In addition, the coating attenuates embedment effects at the rock-proppant interface. The larger contact area will suppress the explosive fracturing and will promote the cleavage into "larger" orange slices.

As well as sand, resin coated proppants should reduce embedment into the rock matrix. Weaver et al. [2005] and Penny [1987] demonstrated that sands and coated proppants generate significantly smaller "craters" in the rock matrix compared to ceramic proppants (table 7.6). The presented study is limited to ceramic proppants, which are the prime candidates for the hydraulic stimulation of the geothermal reservoir at Gross Schoenebeck. Other materials such as sand, specialised very light propping agents, or resin-coated proppant might have a smaller damage potential, i.e. the embedment will be reduced. Such investigations would be proposed for future experiments. With these proppant types, the AE-activity at the rock-proppant interface should be significantly reduced.

7.9.3 Influence of Mechanically Induced Fracture Face Skin on Productivity

The permeability reduction ratio (k_i/k_S) at maximum differential stress (σ_{diff}) varies between 7 and 11, depending on rock and proppant type (figure 7.5). The ratio of Bentheim sandstone is about 50 % higher compared to the ratio of Flechtingen sandstone. Between the two proppant types, no clear distinction can be made. For this calculation, the measurements from BDFC are taken into account exclusively. The BDFC was developed in order to simulate the geometric flow direction in a reservoir intersected by a fracture. In contrast, the k_i/k_S ratios determined using the AEFC are influenced by fines transport from the proppant pack into the lower rock section of the specimen (compare to figure 3.1).

The produced fines are transported through the proppant pack, accumulate at the lower fracture face and influence the permeability evolution for the rock-proppant system. This flow direction contradicts the flow direction in a hydraulically fractured reservoir during production. The fines accumulation at the lower fracture face leads to an additional permeability reduction. Hence, the measured permeability reduction is not only a function of the mechanically induced FFS. In fact, the reduction ratios gained from AEFC experiments are within the same order of magnitude; they range from 7 – 19. In particular, the ratios from Bentheim sandstone experiments conducted with the AEFC are higher in comparison to BDFC measurements.

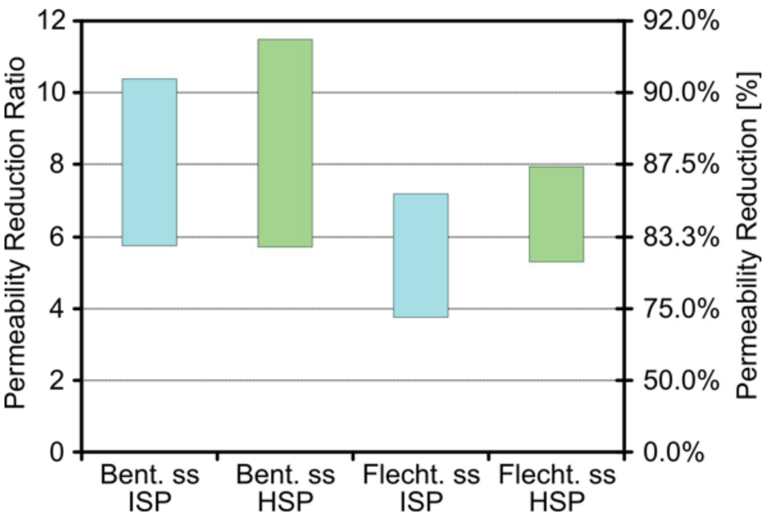

Figure 7.5: *Permeability reduction ratio of different RPI experiments. The reduction ratio of Bentheim sandstone (ss) is about 50 % higher compared to Flechtingen sandstone. Between the two proppant types (ISP and HSP), no clear difference can be ascertained. HSP seems to feature a slightly higher damage potential.*

The influence of permeability reduction on productivity index (PI_D) is computed for the pseudo steady-state flow regime (late times) using equation 2.36 and 2.39; the results are given in table 7.7. The calculation is conducted for a fracture half length (x_f) of 60m; this length corresponds to the fracture half length created during hydraulic stimulation in the injection well EGrSk3/90 [Legarth et al. 2005b] at the geothermal research site Gross Schoenebeck.

The calculation results in a reduction of the pseudo steady-state productivity by 0.1 – 0.2 % (table 7.7). The small reduction of 0.1 % gained from the Flechtingen sandstone experiments is relevant for Gross Schoenebeck reservoir, because the Flechtingen rock is an outcrop equivalent to the reservoir rock. Other effects like fluid-loss damage into the fracture face [Cinco-Ley & Samaniego V. 1981], filter cake build-up at the fracture face [Romero et al. 2003], or water blockage due to relative permeability changes [Holditch 1979] can lead to productivity reduction up to 90 %, due to alteration of the hydraulic transport properties at the fracture face. This comparison highlights that the direct influence of the mechanically induced fracture face skin is negligible compared to the listed productivity damage mechanisms.

Adegbola & Boney [2002] simulated fluid loss to the fracture face as a possible damage mechanism and reported that fracture face damage is very low for low permeable oil and gas wells in general. By contrast, fluid loss in highly permeable formations (reservoir permeability > 100 mD) can impair the well at early times of production, if FFS > 0.1. During late times, the effect on productivity is negligible. The different flow regimes and production periods of a produced reservoir intersected by a fracture are listed in table 7.8. Please refer to §2.6.1 for a description of the different flow regimes.

Figure 7.6 illustrates the influence of a FFS on the pressure distribution in a reservoir at early and late times of production, i.e. in formation linear flow and pseudo radial flow regimes. For a constant flow rate, the additional pressure drop adjacent to the fracture face caused by the FFS (red line / figure 7.6), is identical for both flow regimes. Compared to the linear flow regime, the radius of investigation and the drawdown in the wellbore is significantly larger in the pseudo radial flow regime.

	Bentheim sandstone			**Flechtingen sandstone**		
	max. k_i/k_S	FFS	PI_D reduction [%]	max. k_i/k_S	FFS	PI_D reduction [%]
ISP	10.6 ± 1.1	$2.0\ 10^{-3}$	0.20	7.2 ± 0.4	$9.2\ 10^{-4}$	0.09
HSP	11.3 ± 2.0	$2.2\ 10^{-3}$	0.22	7.9 ± 0.5	$1.1\ 10^{-3}$	0.11

Table 7.7: *Influence of mechanically induced fracture face skin on reservoir productivity in the pseudo steady-state flow regime. / FFS: fracture face skin, k_i: reservoir permeability, k_S: permeability of FFS zone, PI_D: dimensionless productivity index*

flow regime	production period
bi-bilinear	early times
bilinear	early times
formation linear	early times
pseudo radial	late times
pseudo steady-state	late times

Table 7.8: *Flow regimes and production periods of a reservoir intersected by a fracture.*

With increasing time of production, the relative influence of an FFS on the drawdown pressure and on productivity decreases considerably. In particular, in the pseudo radial or pseudo steady-state flow regime, the effect of a 4 mm layer with a tenfold reduction in permeability is negligible, compared to the radius of investigation of several hundred of meters and the total pressure gradient in the reservoir.

The pay zone of the reservoir at Gross Schoenebeck ranges in permeabilities of 10 - 100 mD. In consideration of a fracture half-length of 60 m and a permeability reduction ratio of 7 for Flechtingen rock, the penetration depth has to extend up to 0.5 m to influence the productivity at early times of production. In the pseudo steady-state flow period, this impaired layer would cause a productivity reduction of about 5 %.

Holdtich [1979] explored the issue of fracture face damage for gas production from low permeable reservoirs. One major conclusion from his paper is that the fracture face containing a 15 cm layer with a high permeability reduction of 99.9 % is necessary to have an effect on the productivity of a gas wells. In addition, Holdtich [1979] stated that combined effects (e.g. relative changes in permeability, an increase in capillary pressure, fluid loss) can cause such high permeability reduction. In particular, the decrease in porosity at the fracture face will result in an increase of capillary pressure, which can alter the water saturation in the fracture face and reduce the relative gas permeability.

Considering two-phase flow in gas reservoirs, Gdanski et al. [2005] found that 90 % of permeability loss could impair gas production due to its high impact on capillary pressure. Thus, interactions between different factors can severely impair the productivity, even in low permeable gas reservoirs.

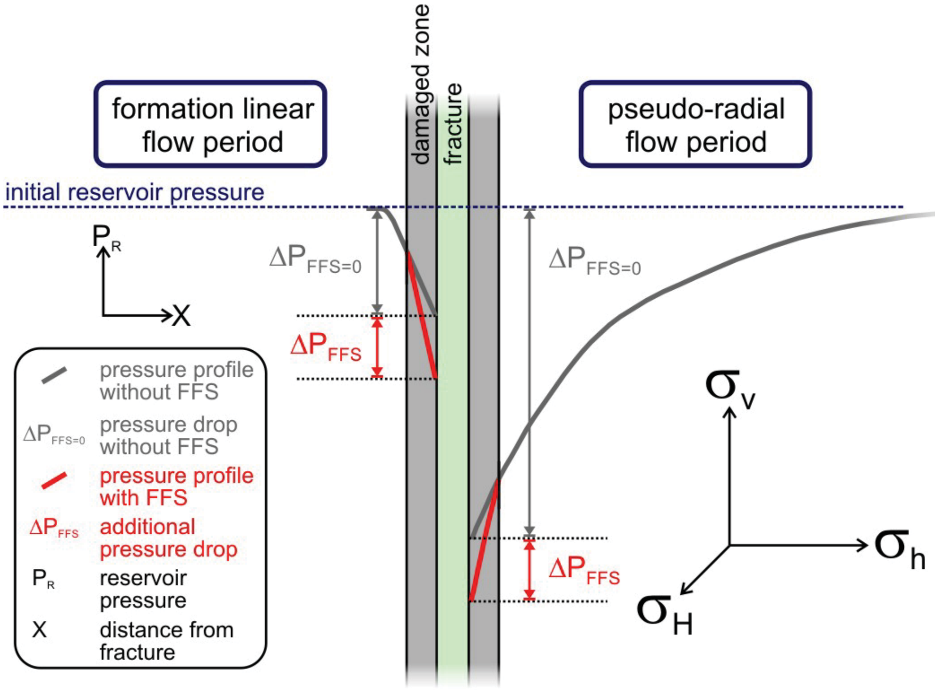
damaged zone
fracture
formation linear flow period
pseudo-radial flow period
initial reservoir pressure
P_R
X
$\Delta P_{FFS=0}$
ΔP_{FFS}
$\Delta P_{FFS=0}$
ΔP_{FFS}
pressure profile without FFS
$\Delta P_{FFS=0}$ pressure drop without FFS
pressure profile with FFS
ΔP_{FFS} additional pressure drop
P_R reservoir pressure
X distance from fracture
σ_v
σ_h
σ_H

Figure 7.6.*: Influence of a fracture face skin (FFS) on the reservoir pressure at early and late times of production. The additional pressure drop caused by the reduced permeability in the damaged zone adjacent to the fracture face, is equal in both flow periods (for constant flow rate). The radius of investigation is considerably larger in the late time (pseudo radial) flow period, compared to the early time (formation linear) flow period. Hence, the relative influence of an FFS decreases with increasing duration of production.*

The mechanically induced FFS produces a zone of reduced porosity and reduced pore size at the fracture face. This zone can trigger secondary effects like relative permeability changes and increase of capillary pressure. In addition, the reduced pore space can act as a filter, leading to internal filtering of migrating fines in the reservoir fluid during production.

Al-Abduwani et al. [2003] found from static internal filtration experiments with Bentheim sandstone that a suspension containing particles 12-times smaller than the pore throat radius, results in a considerable reduction in permeability of 90 %. Azarov et al. [2007] found similar results; they have modelled filter clogging affected by a suspension and stated that a ratio of 200 between effective pore size and suspension particle diameter is sufficient to clog efficiently a filter.

These two studies highlight the possible impact of a layer of reduced porosity at the fracture face. The deposit of fines transported from the reservoir rock to the fracture can cause a long-term impairment of a reservoir, due to the presence of a mechanical FFS. This hypothesis must be verified by future laboratory experiments and numerical studies. A deep bed filtration model as presented by Al-Abduwani et al. [2005] is a promising candidate to investigate deposition along the fracture face.

7.10 Field Observations of Fracture Face Skin

In tight gas reservoirs in particular, the production analysis indicates a post-fracture well productivity that is significantly lower than to be expected from the fracture characteristics simulation [Cramer 2005]. A fracture face skin (FFS), resulting from a dramatic reduction in relative permeability to gas adjacent to the fracture face, can affect the reduction in productivity. Identifying the FFS from wellbore pressure data is possible but difficult. The additional pressure drop caused by an FFS can be observed in the bi-linear and linear flow period, i.e. at early times of production. A new transient flow period has to be initiated in the reservoir, to make this kind of analysis possible. This can be achieved with a pressure build-up test. Wellbore storage effects superimpose the pressure response of a reservoir at early times. A downhole shut-in tool as well as downhole pressure gauge should be used to reduce the duration of wellbore storage. Plotting the dimensionless wellbore pressure as a function of dimensionless time (compare to §2.6.1), identifies the additional pressure drop as deviation from the ¼ slope, which is typical for an undamaged reservoir [Cinco-Ley & Samaniego V. 1981]. Important for this analysis is knowing the permeability, as well as reservoir thickness and fracture half-length of the reservoir.

Cramer [2005] identified a FFS of three from pressure build-up analysis of a well completed in a tight gas reservoir ($k \sim 30$ µD). A numerical simulation revealed a permeability reduction ratio of 70 in a 10 – 13 cm thick layer adjacent to the fracture. 80 % of the wellbore pressure drop at early stages was an effect of the fracture face skin.

Another source of FFS is reported by various authors [Butula et al. 2005, Dehane et al. 2000]. Gas condensation due to abrupt changes in pT-conditions can form a “bank” of condensate at the fracture face. This bank can extend for several meters and can severely reduce the productivity of a reservoir.

The effect of a mechanically induced FFS is too small to be detected in pressure build-up analysis. The secondary effects mentioned above can result in an increasing FFS and a long-term degradation of productivity. The pressure build-up analysis described here could identify this proposed long-term damage mechanism for fractured reservoirs. A clear identification of the damage mechanism in a reservoir is indispensable in order to develop efficient procedures for damage control.

8. Conclusions and Outlook

8.1. *Characterisation of Bentheim and Flechtingen Sandstone*

The triaxial compression and brittle failure of Bentheim sandstone demonstrate that grain crushing plays the dominant role in controlling mechanical and hydraulic properties during inelastic compaction. The permeability in the gouge layer decreases by a factor of 1700 resulting in a 10-fold permeability reduction of the investigated specimen. This highlights the impact of a very thin layer of fines material for fracture cross flow.

Concerning the elastic behaviour, the permeability of Bentheim sandstone shows no stress dependence. The permeability of Bentheim rock is in the range of 1300 – 2500 mD. A tube like pore model can be assumed for that rock type. In contrast, the Flechtingen rock shows significant poroelastic permeability dependence. The permeability varies from 80 to 550 µD. Differential stress power law (exponents: -0.07 - -0.09) matches the permeability behaviour properly. The exponents can be used to model the influence of stress changes on permeability in Rotliegend sandstone reservoirs.

8.2. *Rock-Proppant Interaction Experiments*

For rock-proppant interaction (RPI) testing, the bidirectional flow cell (BDFC) was developed, which simulates a cylindrical core of the fracture face and the adjacent proppant pack in the fracture. This setup allows a simultaneous determination of proppant pack and rock-proppant system permeability. In contrast to common fracture flow cells, the rock-proppant interaction experiments are conducted with specimens that feature a naturally rough fracture face. For that purpose, the specimens are fractured in tensile mode, comparable to an idealised hydraulic fracture generation.

This setup is employed to quantify the mechanically induced fracture face skin (FFS). This permeability reduction at the fracture face due to mechanical interactions of rock and proppants was proposed by Legarth et al. [2005a] as a potential damage mechanism. Up to now, no evidence has been given whether this mechanism exists and how it influences the productivity of a reservoir.

The localisation of the damaging events in a rock-proppant system was realised with the acoustic emission flow cell (AEFC). The experiments with this setup point out that crushing and fines production start at low differential stresses (~ 5 MPa) at the fracture face. With increasing differential stress, the AE activity moves into the proppant pack indicating proppant failure (~ 50 MPa).

An acoustic damage penetration of the mechanical FFS of 4 mm is estimated from the hypocenter clusters localised at the rock-proppant interface. In contrast, the optically determined FFS zone - determined from Bentheim sandstone RPI experiments - has an extent of 0.15 mm. This value is in good accordance with the optically determined width of the gouge layer (0.2 mm) from the triaxial shear experiment. The optically determined FFS zone leads to a permeability reduction at the fracture face by a factor of 350 – 430. Other authors [Fortin et al. 2005, Vajdova et al. 2004] estimated permeability reduction ratios for shear zones or compaction bands in the same order of magnitude.

For Flechtingen sandstone RPI experiments, an optical determination of the penetration depth is not applicable, because the amount of damage and fines generation at the fracture face is small, compared to Bentheim rock. In order to compare the permeability reduction of different experiments, a consistent damage penetration of 4 mm is defined.

The BDFC identifies a permeability reduction ratio at the fracture face between 7 and 11; the first one for Flechtingen and the latter one for Bentheim sandstone. The type of proppant (ISP or HSP) has no influence on the permeability reduction. Optical investigations identify abundant fines from crushed quartz grains at the rock-proppant interface. The fines block the pores, and porosity at the fracture face is significantly reduced. This observation is in accordance with the conceptual model of the mechanically induced FFS presented in the study at hand.

Hence, the existence of a mechanically induced fracture face skin due to rock-proppant interactions is proven. However, the direct influence of the mechanical FFS on the long-term productivity of a reservoir is negligible. Effects like fluid-loss into the fracture face, filter cake build-up at the fracture face or relative permeability changes generate a significantly higher FFS.

8.3. Long-Term Rock-Proppant Interaction Experiments

The long-term investigations under simulated in-situ conditions demonstrated that the hydraulic properties of rock-proppant systems reach equilibrium conditions after sufficient time. A long-term influence of the mechanical FFS cannot be ascertained with the LTFC. Prior to equilibrium, the permeability is influenced by mechanical, thermal and chemical interactions. In particular, the influence of temperature on permeability remains unclear and is therefore proposed for further investigations.

8.4. Modelling of Rock-Proppant Systems

The numerical modelling of a rock-proppant system with Rockflow/Geosys identified stress patterns, which are in good correlation with fracture patterns observed from micrographs of the RPI experiments. Based on the theory of diametral loading of spheres, a function was developed that predicts the maximum tensile stresses along the axis of loading. Analytical stress modelling of the rock-proppant interface using this function, explains the fracture initiation in quartz grains at the interface at small external stresses. The analysis of the inhomogeneous stress field in loaded proppants identifies failure types and highlights mitigation strategies. The small contact radii of stiff materials (e.g. ceramic proppants) promote tensile stress concentration and explosive type of failure accompanied with a large amount of fines due to high stress energy. The amount of produced fines has reduced the proppant pack permeability about 75 % at 50 MPa differential stress in the experiments. A plastically deformable coating (e.g. a resin coating) can distribute the stress, suppress the explosive type of failure and reduce the produced fines. Besides coating, materials with large Poisson rations carry the potential to reduce the tensile stress concentrations in proppants.

8.5. Implications for Geothermal Research Site Gross Schoenebeck

Concerning the hydraulic stimulation operations in the geothermal research well Gross Schoenebeck GtGrSk4/05, the high strength proppant type (HSP) is a good candidate for a sustainable long-term production from the reservoir. This proppant type provides a sufficient permeability even at high fracture closure stresses, which will possibly occur during production tests or work over operations. The direct influence of the mechanically induced fracture face skin is small, and the rock-proppant system with HSP shows no long-term degradation at in-situ conditions.

8.6. Outlook

The mechanical FFS creates a zone of reduced porosity and reduced pore size at the fracture face. This zone can trigger secondary effects, such as internal filtering of produced fines or relative permeability changes, and affects the long-term productivity. Further numerical and experimental studies are necessary to identify such coupled hydro-mechanical effects in reservoirs.

The presented study is limited to multi-layer ceramic proppant packs. Other propping agents, like sand or resin coated proppant, might have a smaller damage potential due to their mechanical properties. In the future, the investigation of small proppant packs (partially monolayers) is attractive since the mechanisms for sustainable production from self-propped fractures and waterfracs in low permeable reservoirs are not fully understood. A special end-plug of the BDFC is already designed for rock-proppant interactions tests with small proppant concentrations.

9. References

A

Adegbola, K. and Boney, C. (2002). *Effect of Fracture Face Damage on Well productivity*, SPE 73759

Aggour, T.M. and Economides, M.J. (1999), *Impact of Fluid Selection on High-Permeability Fracturing*. SPE 36902

Ahmed, U; Abou-Sayed, A.S., and Jones, A.H. (1979). *Experimental Evaluation of Fracturing Fluid Interaction with Tight Reservoir Rocks and Propped Fractures. SPE 7922*

Al-Abduwani, F.A.H.; Shirzadi, A.; van den Broek, W.M.G.T., and Currie, P.K. (2003). *Formation Damage vs. Solid Particles Deposition Profile during Laboratory Simulated PWRI.* SPE 82235

Al-Abduwania, F.A.H.; Hime, G.; Alvarez, A., and Farajzadeha, R. (2005). *New Experimental and Modelling Approach for the Quantification of Internal Filtration*. SPE 94634

Anderson, R.W.; Cooke, C.E., and Wendorff, C.L. (1989). *Propping Agents and Fracture Conductivity* in *Recent Advances in Hydraulic Fracturing*, SPE Monograph Series, Vol. 12, pp. 109-130

API RP-60 (1989). *API Recommended Practices for Testing High Strength Proppants in Hydraulic Fracturing Operations*, API Production Dept., Dallas

Archie, G.E., (1942). *The electrical resistivity log as an aid in determining some reservoir characteristics*. Trans. AIME 146, pp. 54–62

Atkinson, B.K. (1987). *Introduction to fracture mechanics and its geophysical applications*. In: Atkinson, B.K. (ed.). 1991. *Fracture mechanics of rock*. Academic press geology series. Academic Press, London: 1-26.

Azarov, A.; Radkowski, D., and Baron R. (2007). *Modeling of Filter Clogging During Suspension Filtering.* Proceedings of the COMSOL Conference 2007, Boston

B

Backers, T., (2005). *Fracture Toughness Determination and Micromechanics of Rock under Mode I and Mode II Loading*, PhD thesis, Universität Potsdam, Germany

Backers, T.; Fardin, N.; Dresen, G., and Stephansson, O. (2003). *Effect of loading rate on Mode I fracture toughness, roughness and micromechanics of sandstone.* Int. J. Rock Mech. Min. Sci., 40, pp. 425-433, Technical Note

Bariaa, R., Baumgartner J., Gerard A., Jung, R., and Garnish, J. (1999). *European HDR research programme at Soultz-sous-Forets (France) 1987–1996. Geothermics,* 28, pp. 655-669

Barree, R.D.; Cox, S.A., Barree, V.L., and Conway, M.W. (2003). *Realistic Assessment of Proppant Pack Conductivity for Material Selection.* SPE 84306

Basak, P. (1977). *Non-Darcy flow and its implications to seepage problems*. J. of the Irrigation and Drainage Div., ASCE, 103

Baud, P.; Klein, E., and Wong, T.-F. (2004). *Compaction localization in porous sandstones: spatial evolution of damage and acoustic emission activity.* Journal of Structural Geology. 26. pp. 603 - 624

Bear, J. (1988). *Dynamics of Fluids in Porous Media.* Dover Publications, Inc., New York

Behr, A., Mtchedlishvili, G., Haefner, F. (2002). *Consideration of Damage Zone in Tight Gas Reservoir Model with Hydraulically Fractured Well*, SPE 82298

Bennion, D.B.; Thomas, F.B., and Ma, T. (2000). *Formation Damage Processes Reducing Productivity of Low Permeability Gas Reservoirs.* SPE 60325

Bernabe, Y. (1991). *Pore geometry and pressure dependence of the transport properties in sandstones*. Geophysics 56(4), 436-446.

Bishop, S.R. (1997). *The Experimental Investigation of Formation Damage due to the Induced Flocculation of Clays Within a Sandstone Pore Structure by a high Salinity Brine*. SPE 38156

B Blöcher, G. (2008). *Pore space reconstruction of porous media*. Doctorial thesis, Technische Universität, Berlin, Germany

Blöcher, G., Bruhn, D., Zimmermann, G., McDermott, C., and Huenges, E. (2007). *Investigation of the undrained poroelastic response of sandstones to confining pressure via laboratory experiment, numerical simulation and analytical calculation*. Geological Society Special Publications.

Britt, L.K.; Smith, M.B.; Haddad, Z.; Lawrence, P.; Chipperfield, S., and Hellmann, T. (2006). *Water-Fracs: We Do Need Proppant After All.* SPE 102227

Butula, K.K., Maniere, J., Shandrrygin, A., and Rudenko, D. (2005). *Analysis of Production Enhancement Related to Optimization of Propped Hydraulic Fracturing in Gazprom's Yamburskoe Arctic Gas Condensate Field, Russia*. SPE 94727

Byrne, M. and Patey, I. (2003). *Formation Damage Laboratory Testing – A Discussion of Key Parameters, Pitfalls and Potential.* SPE 82250

C Calcagno P., and Sliaupa S. (Eds.) (2008). *Enhanced Geothermal Innovative Network for Europe*. In: Proceedings of the Engine Final Conference, 12-15 February 2008, Vilnius, Lithuania

Carman, P.C. (1937). *Fluid flow through granular beds*. Transactions of the Institute of Chemical Engineers 50, 150-166.

Chau, K.T. and Wei, X.X. (1998). *Spherically isotropic elastic spheres subject to diametral point load strength test*. International Journal of Solids and Structures 36, pp. 4474-4496

Cinco-Ley, H. and Samaniego V., F. (1977). *Effect of Wellbore Storage and Damage on the Transient Pressure Behaviour of Vertically Fractured Wells*, SPE 6752

Cinco-Ley, H. and Samaniego V., F. (1981). *Transient pressure analysis: Finite conductivity Fracture case versus damaged fracture case*. SPE 10179

Civan, F. (2000). *Reservoir Formation Damage.* Gulf Publishing Company, Houston, Texas USA

Cobb, S.L. and Farrell, J.J. (1986). *Evaluation of Long-Term Proppant Stability.SPE 14133*

Cornet*,* F.H. and P. Julien (1989). *Stress determination from hydraulic test and focal mechanisms of induced seismicity*. Int. J. *Rock* Mech. Min. Sci. Geomech. Abstr., 26(4), pp. 235-248

Coronado, J.A. (2007). *Success of Hybrid Fracs in the Basin.* SPE 106758

Costin, L.S. (1987). *Deformation and failure*. In: Atkinson, B.K. (ed.). 1991. *Fracture Mechanics of Rock*. Academic Press, New York: 167-215.

Coulomb, C. A. (1773). *Application des régles des Maxima et Minima á quelques Problmes des statique relatifs*. Acad. Roy. Sci. Mem. Math. Phys., 7.

Cramer, D.D. (2005). *Fracture Skin: A Primary Cause of Stimulation Ineffectiveness in Gas Wells.* SPE 96869

D Dacun, L. and Engler, T.W. (2001). *Literature Review on Correlations of the Non-Darcy Coefficient.* SPE 70015

Dake, L.P. (1978). *Fundamentals of Reservoir Engineering*. Elsevier, Amsterdam

Daneshy, A.; Blümling, P.: Marschall, P., and Zuidema, P. (2004). *Interpretation of Field Experiments and Observation of Fracturing Process.* SPE 86486

Darcy, H. (1856). *Les fontaines publiques de la ville de dijon. Dalmont*, Paris., The famous Appendix - Note D appears here.:647 & atlas

Dehane, A., Tiab, D., and Osisanya, S.O. (2000). *Comparison of the Performance of Vertical and Horizontal Wells in Gas-Condensate Reservoirs*. SPE 63164

Domenico, S. (1977). *Elastic properties of unconsolidated porous sand reservoirs*. Geophysics, 42: pp. 1339-68.

E Economides, M.J. and Nolte, K.G. (2000). *Reservoir Stimulation*, 3rd Edition, Wiley and Sons Ltd., United Kingdom

Engelmann, S. (2007). *Vergleichende petrophysikalische Untersuchungen an Sandsteinen – Korrelation der Gesteinseigenschaften und mikrostruktureller Parameter*, diploma thesis, Technische Universität Berlin, Germany

F Fand, R. M., Kim, B.Y.K., Lam, A.C.C., and Phan, R.T. (1987): *Resistance to the Flow if Fluids Through Simple and Complex Porous Media Whose Matrices Are Composed of Randomly Packed Spheres.* ASME J. Fluids Eng., vol. 109, pp. 268-274, 1987

Fischer G.J. (1992). *The determination of permeability and storage capacity: pore pressure oscillation method*. In: B. Evans and T-f Wong, (Ed), *Fault mechanics and transport properties of rocks*, Academic Press, New York, pp. 187–211.

Fjaer, E., Holt, R., Horsrud, P., Raaen, A., and Risnes, R. (1992). *Petroleum related rock mechanics*: Developments in petroleum science 33. Elsevier Science Publisher, Amsterdam.

Forchheimer, P. (1901). *Wasserbewegung durch Boden.* ZVDI (1901) 45, 1781

Fortin, G.; Schubnel, A., and Gueguen, Y. (2005). *Elastic wave velocities and permeability evolution during compaction of Bleurswiller sandstone.* International Journal of Rock Mechanics & Mining Sciences 42 (2005), pp. 873–889

Fredd, C.N., McConnell, S.B.; Boney, C.L., and England, K.W. (2000). *Experimental Study of Hydraulic Fracture Conductivity Demonstrates the Benefits of Using Proppants.* SPE 60326

G Gdanski, R., Weaver, J; Slabaugh, B., Walters, H., and Parker, M. (2005). *Fracture Face Damage – It Matters.* SPE 94649

Geandier G. and Denis, S., Mocellin, A. (2003). *Float glass fracture toughness determination by Hertzian contact: experiments and analysis.* Journal of Non-Crystalline Solids 318 (2003), pp. 284-295

Gérard, A., A. Genter, T. Kohl, P. Lutz, P. Rose, F. Rummel, (2006). The deep EGS (Enhanced Geothermal System) project at Soultz-sous-Forêts (Alsace, France). Geothermics, 35 (5-6), pp. 473-483

Geuzaine, C. and Remacle, J. F. (2006). *Gmsh: a threedimensional finite element mesh generator with built-in pre- and post-processing facilities*. Case Western Reserve University, Cleveland, OH.

Ghabezloo, S.; Sulem, J; Guedon, S., and Martineau, F. (in press). *Effective stress law for the permeability of a limestone.* International Journal of Rock Mechanics & Mining Sciences

Gidley, J.L. (1991). *A Method for Correcting Dimensionless Fracture Conductivity for Non-Darcy Flow Effects*. SPE 20710

Gómez, J.B., Glover P.W.J., and P. G. Meredith, P.G. (1997). *Damage of Saturated Rocks Undergoing Triaxial Deformation Using Complex Electrical Conductivity Measurements: Mechanical Modelling*. *Phys. Chem. Earth,* Vol. 22, No. 1-2, pp. 63-68,

Gueguen, Y and Dienes J. (1989). *Transport properties of rocks from statistics and percolation.* Math. Geol., 21, pp. 1-13.

H Haimson, B. and Lee, H. (2004). *Borehole breakouts and compaction bands in two high-porosity sandstones*. Int. J. Rock Mech. Min. Sci., 41, 7, pp. 287-301

Heiland, J. (2003). *Permeability of Triaxially Compressed Sandstone: Influence of Deformation and Strain-rate on Permeability*. Pure appl. geophys. 160 (2003), pp. 889-908

Heiland, J. and Raab, S. (2001). *Experimental investigation of the influence of differential stress on permeability of a lower permian (Rotliegend) sandstone deformed in the brittle deformation field*. Phys. Chem. Earth (A), Elsevier Science Ltd, 26(1,2), pp. 33-38

Hertz, H. (1882). *Ueber die Beruehrung fester elastischer Koerper*, J. Reine und Angewandte Mathematik 92, 156

H Hiramatsu, Y., Oka, Y. (1966). *Determination of the tensile strength of rock by a compression test of an irregular test piece*. International Journal of Rock Mechanics and Mining Science 3, pp. 89-99

Hirata, T.; Satoh, T., and Ito, K. (1987). *Fractal structure of spatial distribution of microfracturing in rock.* Geophys. J. R. Astr. Soc., 90, pp. 369-374

Hoek, E. and Franklin, J. A. (1968): *Simple triaxial cell for field or laboratory testing of rock.* Trans. Inst. Min. Metall, 77:A22 (Section A)

Holditch, S.A., 1979. Factors Affecting Water Blocking and Gas Flow from Hydraulically Fractured Gas Wells. JPT, 1515-1524

Hudson, J. A. and Harrison, J. P. (1997). *Engineering Rock Mechanics; An Introduction to the Principles.* Elsevier Science Ltd., Oxford

Huenges, E., Holl, H.-G., Bruhn, D., Brandt, W., Saadat, A., Moeck, I., and Zimmermann, G. (2007). *Current state of the EGS project Groß Schönebeck – drilling into the deep sedimentary geothermal reservoir*. European Geothermal Congress 2007, Unterhaching, Germany

I Igathinathane, C., Pordesimo, L. O., Columbus, E. P; Batchelor, W. D., and Methuku, S. R. (2008). *Shape identification and particles size distribution from basic shape parameters using ImageJ computers and electronics in agriculture* 63, pp. 168-182

J Jaeger, J. C., Cook, N. G. W., and Zimmerman, R.W. (2007). *Fundamentals of rock mechanics*. Science. Paperbacks. Chapman and Hall, London, 4th edition.

K Kaiser, J. (1950*). An Investigation into the Occurrence of Noises in Tensile Tests or a Study of Acoustic Phenomena in Tensile Tests*. PhD Thesis, Tech. Hoch. München, Munich, Germany

Katz, A.J. and Thompson, A.H. (1987). *Prediction of rock electrical conductivity from mercury injection measurements*. J. Geophys. Res. 92(B1), 599-607.

Keaney, G. M., Meredith, P.G., and Muriell, S.A.F. (1998). *Laboratory Study of Permeability Evolution in a 'Tight' Sandstone under Non-hydrostatic Stress Conditions*, SPE 47265

Klein, E. and Reuschlé, T. (2003). *A model for the mechanical behaviour of Bentheim Sandstone in the Brittle Regime*. Pure and Appl. Geophys, 160, pp. 833-849

Klein, E.; Baud, P.; Reuschlé, T., and Wong, T.-F. (2001). *Mechanical Behaviour and Failure Mode of Bentheim Sandstone Under Triaxial Compression.* Pure and Appl. Geophys., 160, pp. 833-849

Korsawe, J.; Starke, G.; Wang, W., and Kolditz, O. (2006). *Finite Element Analysis of Poro-Elastic Consolidation in Porous Media: Standard and Mixed Approaches.* Computer Methods in Applied Mechanics and Engineering. 195

L Landolt, H., Börnstein, R. (eds.) (1987). *Numerical data and functional relationships in science and technology*, Springer, Berlin Germany

Lawn, B. (1993). *Fracture of brittle solids*. Cambridge University Press, Cambridge.

Legarth, B., Huenges, E., Zimmermann, G. (2005b). *Hydraulic Fracturing in Sedimentary Geothermal Reservoirs*. Int. J. Rock Mech. Min. Sci., 42 (7-8), pp. 1028-1041

Legarth, B.; Raab, S., and Huenges, E. (2005a). *Mechanical Interactions between proppants and rock and their effect on hydraulic fracture performance*, DGMK-Tagungsbericht 2005-1, Fachbereich Aufsuchung und Gewinnung, 28.-29. April 2005, Celle, Deutschland, pp. 275-288

Leonhard, M. and Kinnet, B.L.N. (1999). *Multi-component autoregressive techniques for the analysis of seismograms.* Phys. Earth Planet. Int. 113(1–4), 247

Lockner, D. (1993). *The Role of Acoustic Emission in the Study of Rock Fracture*. Int. J. Rock Mech. Min. Sci., 30, pp. 883-899

Lockner, D. A.; Byerlee, J. D.; Kuksenko, V.; Ponoroarer, A., and Sidorin, A. (1992). *Observations of quasistatic fault growth from acoustic emissions.* In Fault Mechanics and Transport Properties of Rocks (Edited by B. Evans and T.-f. Wong), pp. 3-31, Academic Press, London

L Lockner, D.A. and Beeler, N.M. (2003). *Stress-induced anisotropic poroelasticity response in sandstone*. In: Proceedings of 16th ASCE Engineering Mechanics Conference, University of Washington, Seattle, WA, July 16–18, 2003.

Lurje, A.J. (1963). *Räumliche Probleme der Elastizitätstheorie*. Akademie-Verlag, Berlin, 1963

Lynn, J.D., Hisham, A., and Nasr-El-Din, H.A. (1998). *Evaluation of formation damage due to frac stimulation of a Saudi Arabian clastic reservoir.* J. of Petr. Sc.and Eng. 21, pp. 179-201

M Mack, D.J. and Myers, R.R. (2001). *Proppants: Is Bigger Better or is Placement the Key?* SPE 72381

Makurat, A. and Gutierrez, M. (1996). *Fracture Flow and Fracture Cross Flow Experiments*. SPE 36732

Matsunaga, I., Kobayashi, H., Sasaki, S., and Ishida, T. (1993). *Studying Hydraulic Fracturing Mechanism by Laboratory Experiments with Acoustic Emission Monitoring*. Int. J. Rock Mech. Min. Sci., 30, 7, pp. 909-912

Mayerhofer, M.J., Richardson, M.F., Walker Jr., R.N., Meehan, D.N., Oehler, M.W., Browing Jr., R.R., (1997). *Proppants? We Don't Need No Proppants*, SPE 38611

McDermott, C.I. and Kolditz, O. (2004). *Hydraulic-Geomechancial Effective Stress Model: Determination of Discrete Fracture Network Parameters from a Pump Test and Application to Geothermal Reservoir Modelling*. Proceedings of the 29 Workshop on Geothermal Reservoir Engineering, Stanford, California

Mellor, M. and Hawkes, I. (1971). Measurement of Tensile Strength by Diametral Compresson of Disks and Annuli, Eng. GeoL, 5: pp. 173-225.

Michael J. Mayerhofer, M.J. and Meehan, D.N. (1998). *Waterfracs – Results from 50 Cotton Valley Wells*. SPE 49104

Milsch, H.; Blöcher, G., and Engelmann, S. (2008). *The relationship between hydraulic and electrical transport properties in sandstones: An experimental evaluation of several scaling models.* Earth and Planetary Science Letters 275 (2008), pp. 355-363

Milsch, H., Spangenberg, E., Kulenkampff, J., and Meyhöfer, S. (2007). *A new Apparatus for Long-term Petrophysical Investigations on Geothermal Reservoir Rocks at Simulated In-situ Conditions*. Transp. Porous Med, 74, 1, 73-85.

Moeck I., W. Brandt, W., Blöcher, G., Holl, H.-G., Zimmermann, G., Huenges, E., Saadat, A., and Backers, T. (2008). *From gas to geothermal exploration: A case study from the NE-German Basin*. EAGE 70th Conference and Exhibition, Rome, Italy.

Moghadasi, J; Jamialahmadi, M.; Müller-Steinhagen, H.; Sharif, A., and Izadpanah, M. R. (2002). *Formation Damage in Iranian Oil Fields.* SPE 73781

Mohr, O. (1900). *Welche Umstände bedingen die Elastizitätsgrenze und den Bruch eines Materials?*. Z. Ver. dt. Ing., 44

Mondshine, T. C. (1973). *A new Potassium Based Mud System*. SPE 4516

Mungan, N. (1989). *Discussion of an Overview of Formation Damage.* JPT Vol. 41 No. 11, p. 1224

N Nasr-El-Din, H.A. (2003). *New Mechanisms of Formation Damage: Lab Studies and Case Histories.* SPE 82253

Nelder, J. A. and Mead, R. (1965). *A simplex method for function minimization.* Comput. J., 7, pp. 308-313

Norden, B., A. Förster, 2006. *Thermal conductivity and radiogenic heat production of sedimentary and magmatic rocks in the Northeast German Basin*. AAPG Bulletin, 90 (6), pp. 939 – 962

O Ohm, G. S. (1826). *Bestimmung des Gesetzes, nach welchem Metalle die Contaktelektricität leiten, nebst einem Entwurfe zu einer Theorie des Voltaischen Apparates und des Schweiggerschen Multiplicators.* In: Schweigger, J.S.C., Schweigger-Seidel, W. (Eds.), Jahrbuch der Chemie und Physik, vol. XVI, pp. 137-166.

P Paterson, M. S. and Wong, T-f. (2005) *Experimental Rock Deformation – The Brittle Field*. Springer-Verlag, Berlin, Germany

Penny, G.S. (1987*). An Evaluation of the Effects of Environmental Conditions and Fracturug Fluids upon long term Conductivity of Proppants.* SPE 16900

Pestman, B.J. and van Munster, J.G. (1996). *An Acoustic Emission Study of Damage Development and Stress-Memory Effects in Sandstone.* Int. J. Rock Mech. Min. Sci., 33, pp. 585-593

Preiss, S. (2000). *Experimentelle Untersuchungen zur Auswirkung der Porenraumstruktur auf das elektrische Strömungspotenzial von Sandsteinen*. PhD thesis, Universität Potsdam, Germany

R Rahman, S.S.; Rahman, M. M., and Khan, F. A. (1995). *Response of low-permeability, illitic sandstone to drilling and completion fluids.* Journal of Petroleum Science and Engineering 12, pp. 309-322

Reed, M. G. (1977). *Formation Permeability Damage by Mica Alteration and Carbonate Dissolution.* JPT, pp. 1056-1060

Reverberi, A., Ferraiolo, G., and Peloso, A. (1966). *Determination by Experiment of the Distribution Function of the Cylindrical Macropores and Ink bottles in Porous Systems*. Annali di Chimica, 56, 12.

Romero, D.J.; Valkó, P.P., and Economides, M.J. (2003). *Optimization of the Productivity Index and the Fracture Geometry of a Stimulated Well With Fracture Face and Choke Skins*, SPE 81908

Roodhart, L.P., Kulper, T.O.H., and Davies, D.R. (1988). *Proppant-Pack and Formation Impairment During Gas-Well Hydraulic Fracturing*. SPE 15629

Rushing, J.A. and Sullivan, R.B. (2003). *Evaluation of Hybrid Water-Frac Stimulation Technology in the Bossier Tight Gas Sand Play*. SPE 84394

S Schlichting, H. (1968). *Boundary Layer Theory*. McGraw-Hill, New York

Schön, J.H. (2004). *Physical properties of rocks: fundamentals and principles of petrophysics., volume 18. of Handbook of geophysical exploration*: Section I, Seismic exploration. Elsevier, Amsterdam, 1. edition.

Schönert, K. (2004). *Breakage of spheres and circular discs Institute of Mineral Processing.* Powder Technology 143-144, pp. 2-18

Schubnel, A., Nischizawa O., Masuda, K., Lei, X., Xue, Z., and Guenguen, Y. (2003), *Velocity Measurements and crack density determination during wet triaxial experiments on Oshima and Toki granites*, Pure Appl. Geophys. 160, 869–887.

Schutjens, P.M.T.M. and Ruig, H.d. (1997). *The influence of stress path on compressibility and permeability of an overpressurized reservoir sandstone: some experimental data*. Phys. Chem. Earth 22(1-2), 97-103.

Scott, T.; Ma, Q., and Roegiers, J-C. (1993). *Acoustic velocity changes during shear enhanced compaction of sandstone.* Rock Mech Min Sci & Geomech 1993;30: pp. 763-9

Shackelford, J.F. (Ed.) and Alexander, W. (Ed.) (2000). *The CRC Materials Science and Engineering Handbook.* CRC Press

Shaoul, J., Ross, M., Spitzer, W., Wheaton, S., Mayland, P., Singh, A.P. (2007). *Massive Hydraulic Fracturing Unlocks Deep Tight Gas Reserves in India*. SPE 107337

Sharma, M.M., Gadde, P.B., R. Sullivan, R., Sigal, R., Fielder, R., Copeland, D., Griffin, L., and Weijers, L. (2004). *Slick Water and Hybrid Fracs in the Bossier: Some Lessons Learnt*. SPE, paper 89976

Soni, J.P.; Islam, N., and Basak, P. (1978). *An experimental evaluation of non-darcian flow in porous media.* Journ. of Hydrology, 38, p. 231

S

Stammnitz, T. (1993). *Entwicklung einer Methode zur Untersuchung der Belastungsabhängigkeit von Porosität und Permeabilität sowie deren Beziehungen zur Gesteinsdeformation*. Dissertation, Technische Universität Clausthal.

Stanchits, S.; Backers, T.; Stephansson, O., and Dresen, G. (2003). *Comparison of Acoustic Emission Events and Micromechanics of granite under Mode I and Mode II loading.* Proceedings of EURO-Conference on Rock Physics and Geomechanics, 7-11 September 2003, Delft, Netherlands

Stanchits, S.; Vinciguerra, S., and Dresen, G. (2006). *Ultrasonic Velocities, Acoustic Emission Characteristics and Crack damage of Basalt and Granite.* Pure Appl. Geophys, 163, pp. 974-993

Sternberg, E. and Rosenthal, F. (1952). *The elastic sphere under concentrated loads*. J. Appl. Mech., pp. 413-421

Sun, Z.Q. and Quchterlony, F. (1986). *Fracture Toughness of Stripa Granite Cores*. Int. J. Rock Mech. Min. Sci, & Geomech. Abstr., 23, No. 6, pp. 399-409

T

Terzaghi, K. (1923). *Die Berechnung der Durchlassigkeitsziffer des Tones aus dem Verlauf der hydrodynamischen Spannungserscheinungen*. Sitzungsberichte der Akadamie der Wissenchaften in Wien, Mathematisch-Naturwissenschaftliche Klasse, IIa, 132, pp. 105-124.

Thiercelin M.C., and J.-C. Roegiers, J.-C. (2000). *Formation Characterization: Rock Mechanics*. in Economides, M.J. and Nolte, K.G. (2000). *Reservoir Stimulation*, 3rd Edition, Wiley and Sons Ltd., United Kingdom

Timoshenko S. P. and Goodier, J. N. (1970). *Theory of elasticity*. 3rd Edition, McGrawHill, Kogakusha, Tokyo.

Trautwein, U. (2005). *Poroelastische Verformung und petrophysikalische Eigenschaften von Rotliegend Sandsteinen*. Phd thesis, Technischen Universität, Berlin

Trautwein, U. and Huenges, E. (2003). *Pore pressure induced changes of transport properties reflecting microstructural deformation in Rotliegend sandstones*. EURO-Conference on Rock Physics and Geomechanics, 7. - 11. September 2003 Delft, The Netherlands.

U

Underwood, E. E. (1970). *Quantitative stereology*. Addison-Wesley series in metallurgy and materials. Addison-Wesley, Reading, Mass.

V

Vaydova, V.; Baud, P., and Wong, T.-F. (2004). *Permeability evolution during localized deformation in Bentheim sandstone*. J. Geophys. Res. 109

W

Walker, R.N.; Hunter, J.L.; Brake, A.C.; Fagin, P.A., and Steinsberger, N. (1998). *Proppants, We Still Don't Need No Proppants – A Perspective of Several Operators.* SPE 49106

Wallroth, T., Jupe, A.J. and Jones, R.H., (1996). *Characterisation of a fractured reservoir using microearthquakes induced by hydraulic injections*. Marine and Petroleum Geology, 13**,** pp. 447–455.

Walsh, J.B. and Brace, W.F. (1984). *The effect of pressure on porosity and the transport properties of rock*. J. Geophys. Res. 89 (B11), 9425–9431.

Wang, H.F. (2000). *Theory of linear poroelasticity with applications to geomechanics and hydrogeology*. Princeton University Press, Princeton, NJ.

Wang, W. and Kolditz, O. (2005). *Object-oriented finite element analysis of thermo-hydro-mechanical (thm) problems in porous media*. Center for Applied Geosciences, University of Tuebingen.

Wang, X.; Indriati, S.; Valko, P.P., and Economides, M.J. (2000). *Production Impairment and Purpose-Built Design of Hydraulic Fractures in Gas-Condensate Reservoirs*. SPE 64749

Warpinski, N.R. (2009). *Stress Amplification and Arch Dimension in Proppant Beds Deposited by Waterfracs*. SPE 119350

Warren, P. D. (1995). *Determining the Fracture Toughness of Brittle Materials by Hertzian Indentation.* Journal of the European Ceramic Society 15, pp. 201-207

Washburn, E. W. (1921). Phys. Rev. 17, pages 374–375.

W Weaver, J.; Rickmann, R., Luo, H., and Loghry, R. (2009). *A Study of Proppant-Formation Reactions.* SPE 121465

Weaver, J.D., Nguyen, P.D., Parker, M.A., van Batenburg, D., (2005). *Sustaining Fracture Conductivity*. SPE 94666

Webb, P.A. (2001). *An Introduction To The Physical Characterization of Materials by Mercury Intrusion Porosimetry with Emphasis On Reduction And Presentation of Experimental Data*. Micromeritics Instrument Corp., Norcross, Georgia.

Wen, Q., Zhang, S., Wang, L., Liu, Y., Li, X. (2006). *The effect of proppant embedment upon the long-term conductivity of fractures*. Journal of Petroleum Science and Engineering 55, 221–227

Whitaker, S. (1996). *The Forchheimer Equation: A Theoretical Development*. Transport in Porous Media 25, pp. 27-61

Whittaker, B.N., Singh, R.N. and Sun, G. (1992). *Rock Fracture Mechanics, Principles, Design and Applications*. Developments in Geotechnical Engineering, 71. Elsevier, Amsterdam.

Wu, S.Z. and Chau, K.T. (2006). *Dynamic response of an elastic sphere under diametral impacts. Mechanics of Materials*, 38, pp. 1039–1060

Wu, Y.S.; Xiong, W.; Lei, Q.; Shusheng Gao, S. (2008). *Behavior of Flow through Low-permeability Reservoirs.* SPE-113144

Y Yoshinaka, R.M., Osadat, T, and Tran, V. (1996). *Deformation Behaviour of Soft Rocks during Consolidated-Undrained Cyclic Triaxial Testing.* J. Rock Mech. Sci. & Geomech. Abstr., 33, pp. 557-572

Z Zang, A. (1997). *Akustische Emission beim Sprödbruch von Gestein*. Habilitation 1997 University of Potsdam, Potsdam, Germany

Zang, A., Wagner, F.C., Stanchits, S., Dresen, G., Andresen, R., and Haidekker, M.A. (1998) *Source analysis of acoustic emissions in Aue granite cores under symmetric and asymmetric compressive loads*, Geophys., J. Int., 135

Zang, A.; Wagner, F.C.; Stanchits, S.; Janssen, C., and Dresen, G. (2000). *Fracture process zone in granite*, J. Geophys. Res. 105

Zhang, J.; Wong, T.-F., and Davis, D.M. (1990). *Micromechanics of pressure-induced grain crushing in porous rocks*, J. Geophys. Res., 95, pp. 341-352

Zhu, W. and Wong, T-f. (1996). Permeability reduction in dilating rock: Netweork modelling of damage and tortuosity. Geophysical Research Letters, Vol. 23, No. 22, pp. 3099-3102

Zimmermann, G., Reinicke, A., Blöcher, G., Milsch, H., Gehrke, D., Holl, H.-G., Moeck, I., Brandt, W., Saadat, A., and Huenges, E. (2007). *Well path design and stimulation treatments at the geothermal research well GtGrSk4/05 in Groß Schönebeck*. Proceedings 32 Workshop on Geothermal Reservoir Engineering, Stanford, California

Zimmermann, G.; Reinicke, A.; Brandt, W.; Blöcher, G.; Milsch, H.; Holl, H.-G.; Moeck, I.; Schulte, T.; Saadat, A., and Huenges, E. (2008). *Results of stimulation treatments at the geothermal research well Groß Schönebeck/Germany*. Proceedings of the 33 Workshop on Geothermal Reservoir Engineering, Stanford, California

Zoback, M.D. and Byerlee, J.D. (1975). *Permeability and effective stress*. Amer. Assoc. Petrol. Geol. Bull. 59, 154-158.

Mottoes

Plinius Maior / Plinius der Ältere: *Naturalis historia / Naturgeschichte*. Ausgewählt, übersetzt und herausgegeben von Marion Giebel. Stuttgart 2005, S. 128

Jules Verne: *Voyage au centre de la terre*. 42. Ausgabe, Paris 2009, S. 186

Jules Verne*: Die Reise zum Mittelpunkt der Erde*. Aus dem Französischen übertragen und bearbeitet von Hans Eich. 2. Ausgabe, Würzburg 1990, S. 109

10. List of Figures

Figure 1.1: Flow directions in a reservoir with proppant filled fracture. 1

Figure 1.2:.Location of the geothermal research site Gross Schoenebeck and well path of the doublet system [modified from Moeck et al. 2008]. 3

Figure 2.1: Hertz contact model for two spherical bodies. 8

Figure 2.2: Diametral compression of a sphere. 8

Figure 2.3: Flow zones in porous media. 11

Figure 2.4: Propped fracture in a reservoir. 13

Figure 2.5: Influence of proppants on fracture conductivity (modified from [Fredd et al. 2001]). 15

Figure 2.6: Mechanisms impairing proppant pack conductivity (modified from [Legarth et al. 2005a]). 19

Figure 2.7: Conceptual model of a fracture face skin. 20

Figure 2.8: Transient pressure behaviour of a well influenced by a fracture face skin (FFS). 20

Figure 2.9: Influence of a FFS on dimensionless productivity (PI_D) in the pseudo steady-state flow regime. 21

Figure 2.10: Conceptual model of the mechanically induced FFS (modified from [Legarth et al. 2005a]). 22

Figure 3.1: Schematic view of an Acoustic Emission Flow Cell (AEFC). 23

Figure 3.2: Placing of piezoelectric ultrasonic P-wave transducers (PZT) and strain gages. 24

Figure 3.3: Schematic view of a Bidirectional Flow Cell (BDFC). 25

Figure 3.4: The Bidirectional Flow Cell (BDFC). 27

Figure 3.5: BDFC mounted on its carriage in MTS press. 27

Figure 3.6: Bottom and top plugs of BDFC used for proppant testing (plug 1) and rock testing (plug 2). 27

Figure 3.7: Photo collection of preparation and execution of a rock-proppant interaction test with the AEFC. 29

Figure 3.8: Photo collection of preparation and execution of a rock-proppant interaction test with the BDFC. 29

Figure 3.9: Schematic view of flow cycle and confining pressure system of the Long Term Flow Cell (LTFC) (modified from [Milsch et al. 2007]). 34

Figure 3.10: Photo collection of preparation and execution of a rock-proppant interaction test with the LTFC. 36

Figure 4.1: Mineral composition of Bentheim sandstone as determined by point counting 39

Figure 4.2: Micrographs and binary pictures of Bentheim and Flechtingen sandstone 39

Figure 4.3: Mineral composition of Flechtingen sandstone as determined by point counting 40

Figure 4.4: a) Fracture closure stress dependence of proppant permeability. ISP: intermediate strength proppant; HSP: high strength proppants. 20/40 mesh size corresponds to a diameter of 0.4 – 0.8 mm. b) Micrograph of an ISP pack 40

Figure 4.5: Pore and grain size distributions of Bentheim and Flechtingen sandstone determined with 2D optical scanning method (opt) and mercury intrusion porosimetry (HG). 41

Figure 4.6: Circularity ratio and axis ratio of ellipse for Bentheim and Flechtingen sandstone calculated from 2D image analysis. 44

Figure 4.7: Cumulative pore space of Bentheim and Flechtingen sandstone as function of circularity. 44

Figure 5.1: Stress-strain behaviour of triaxially loaded Bentheim sandstone. 48

Figure 5.2: Permeability reduction during triaxial compaction of Bentheim sandstone. 49

Figure 5.3: Vertical and horizontal p-wave velocity as function of time and differential stress. 49

Figure 5.4: AE hypocenter localisation of experiment Bent 1.2 and Bent 1.3. 50

Figure 5.5: Spatial AE distribution of experiment Bent 1.3. 51

Figure 5.6: Micrographs from the shear zone (Bent 1.1). 51

Figure 5.7: Evolution of Young's modulus due to cyclic loading. 53

Figure 5.8: Permeability of Bentheim and Flechtingen sandstone as a function of loading cycles, stress and flow rate. 54

Figure 5.9: Relative permeability changes due to fluid-rock interactions. 54

Figure 5.10: Estimation of flow rate interval for Bentheim sandstone permeability measurements. 57

Figure 5.11: Permeability evolution and AE hypocenters of experiment Bent 2.3. 60

Figure 5.12: Determination of β -factor. 60

Figure 5.13: Permeability evolution of Bent 2.2 specimen. 61

Figure 5.14: Permeability evolution and AE hypocenters of experiment Bent 3.4. 63

Figure 5.15: Permeability evolution and AE hypocenters of experiment FB 1.6 64

Figure 5.16: Micrograph of loaded rock-proppant systems in Bentheim and Flechtingen sandstone / Classification of fracture pattern. 65

Figure 5.17: Permeability reduction and permeability reduction ratio of experiments Bent 2.2, Bent 3.4, and Flecht 1.6. 65

Figure 5.18: Spatial AE distribution for Bentheim and Flechtingen RPI experiments. 67

Figure 5.19: Results from rock-proppant interaction testing of ISP and HSP with Bentheim sandstone. 70

Figure 5.20: Results from rock-proppant interaction testing of ISP and HSP with Flechtingen sandstone. 72

Figure 5.21: Continuous permeability change of a Flechtingen sandstone (FB 2.1) with ISP pack. 74

Figure 5.22: Photo collection of proppant packs and fracture faces after testing with the BDFC. 74

Figure 5.23: Permeability and formation factor from testing Flechtingen sandstone with ISP and HSP packs in the LTFC 78

Figure 5.24: Micrographs from long-term experiments with Flechtingen sandstone and ISP / HSP. 80

Figure 6.1: Idealised load geometry at the rock-proppant interface (true relative scale). 82

Figure 6.2: Maximum tensile stresses at the outer boundary of the contact circle. 83

Figure 6.3: Stress severity of principal stresses (σ_1, σ_2, σ_3) as well as shear stress σ_{xy} of a diametral loaded sphere. 84

Figure 6.4: Possible fracture pattern in a diametral loaded sphere. 86

Figure 6.5: Fractures in proppants. 86

Figure 6.6: Stress severity of σ_3 for two contact angles. 87

Figure 6.7: Tensile stress severity as function of contact angle (Θ) and Poisson ratio (ν). 88

Figure 6.8: Schematic view of single proppant testing load cell. 88

Figure 6.9: Maximum tensile stresses in quartz grains and proppant as a function of the external differential stress. 89

Figure 6.10: Artificial 2D-contact model of a rock-proppant system. 90

Figure 6.11: Stress distribution in a loaded rock-proppant system. 92

Figure 7.1: Fracture initiation at the rock-proppant interface. 98

Figure 7.2.: Comparison of stress pattern and fracture pattern in rock-proppant systems. 100

Figure 7.3: Influence of proppant concentration on the fracture width at production conditions. 104

Figure 7.4: Permeability evolution in a long-term experiment with Flechtingen sandstone and ISP proppant pack. 106

Figure 7.5: Permeability reduction ratio of different RPI experiments. 110

Figure 7.6.: Influence of a fracture face skin (FFS) on the reservoir pressure at early and late times of production. 111

Figure A1: Pressure calibration of AEFC sensor (Stellar Technologies GT1800-20000G-113). 131

Figure A2: Flow calibration of AEFC. The intrinsic pressure response of the AEFC as function of the applied flow rate. 131

Figure A3: Flow calibration of BDFC. The intrinsic pressure response of the BDFC as function of the applied flow rate. 131

Figure A4: Mohr-Coulomb diagram constructed from uniaxial and triaxial Bentheim sandstone experiments. 134

Figure A5: Comparison of stress-strain behaviour of intact specimen and rock-proppant system. 135

Figure A7: Differential pressure measurements of a Bentheim rock-proppant system and a proppant pack. 136

Figure A8: Differential pressure measurements of an intact Flechtingen rock and a Flechtingen rock-proppant system. 137

Figure A9: From an artificial 2D-contact model of a rock-proppant system to a 2D-mesh. 139

11. List of Tables

Table 2.1: Limits for flow regimes. Fand et al. [1987] define the flow regimes by upper and lower limits of Reynolds number. 11

Table 2.2: Comparison of three different types of hydraulic fracture stimulations. 16

Table 2.3: Categorisation of proppants based on maximum fracture closure stress. 18

Table 3.1: Quantities defining the hydraulic properties of rock-proppant systems. 30

Table 3.2: Procedures for evacuation, saturation and differential pore pressure measurements. 31

Table 3.3: Influence of different measurement and systematic errors on the permeability determination using the AEFC and BDFC. 32

Table 3.4: Parameters for permeability and electrical conductivity measurement using the long-term flow cell. 35

Table 3.5: Errors influencing the permeability determination using the LTFC. 35

Table 4.1: Chemical compounds of HSP and ISP (taken from manufacturer's data sheet). 40

Table 4.2: number of pores, micrographs and lower detection limits for 2D optical grain and pore size investigation. 41

Table 4.3: Parameters for characterisation of Bentheim and Flechtingen rock. 43

Table 5.1: List of all experiments of the present study conducted with Bentheim and Flechtingen sandstone. 45

Table 5.2.: Testing parameters for triaxial compression experiment with Bentheim sandstone. 47

Table 5.3: Parameters of different experiments for Young's modulus and permeability determination within the elastic stress interval. 52

Table 5.4: Differential stress functions of Flechtingen sandstone. 53

Table 5.5: Peak stress, onset of dilatancy, and Young's modulus of Bentheim sandstone experiments. 55

Table 5.6: Testing parameters of rock-proppant interaction (RPI) experiments with the Acoustic Emission Flow Cell (AEFC). 59

Table 5.7: Permeabilities and permeability reduction ratio computed from damage penetrations (w_S) determined from micrographs, as well as from acoustic emission hypocenter locations. 66

Table 5.8: Parameters for rock-proppant interaction testing of ISP and HSP with Bentheim sandstone. 69

Table 5.9: Parameters for rock-proppant interaction testing of ISP and HSP with Flechingen sandstone. 71

Table 5.10: Testing parameters of rock-proppant interaction experiment with continuous stress change. 73

Table 5.11: Reservoir parameters of Gross Schoenebeck pay zones and resulting effective stresses for long-term testing of Flechtingen sandstone and rock-proppant systems. 76

Table 5.12: Testing parameters for LTFC investigations. 77

Table 5.13: Evolution of permeability and formation factor of three long-term experiments conducted with Flechtingen sandstone, high strength (HSP) and intermediate strength proppants (ISP). 79

Table 6.1: Parameters of quartz grains and proppants (corundum) for Hertzian contact stress calculation. 83

Table 6.2: Parameter for stress calculation of diametral compressed spheres with the theory of Hiramatsu & Oka [1966]. 84

Table 6.3: Extremes of stress severity for two contact angles and resulting stress types in diametral loaded sphere. 85

Table 6.4: Parameters for the calculation of maximum tensile stresses in quartz grains and proppants. 89

Table 6.5: Contact angle interval used for the idealised 2D-contact model. 91

Table 6.6: Parameters for mechanical modelling of the 2D-contact model. 91

Table 6.7.: Maximum tensile, compressive and shear stresses observed in the 2D-model of the rock-proppant system. 93

Table 7.1.: Mechanical properties of quartz, mullite and corundum [Shackelford & Alexander 2000, Landolt & Börnstein 1987]. 95

Table 7.2: Main results of rock-proppant interaction testing with the acoustic emission flow cell. 97

Table 7.3: Influence of rock type, proppant type and concentration on fracture width and permeability. 103

Table 7.4: Initial and long-term permeabilities of Flechtingen sandstone experiments with ISP and HSP. 105

Table 7.5: Comparison of measured permeabilities and permeabilities estimated from formation factor. 108

Table 7.6: Influence of material properties of proppants on the size of embedment. 109

Table 7.7: Influence of mechanically induced fracture face skin on reservoir productivity in the pseudo steady-state flow regime. 110

Table 7.8: Flow regimes and production periods of a reservoir intersected by a fracture. 111

Table A1: Permeabilities and Young’s moduli for all specimens investigated with the AEFC and BDFC. 134

12. List of Symbols

symbol	unit	description
x_1 / x_2 / x_3	[m]	Cartesian coordinates
r / φ / θ	[m] / [°]	spherical coordinates
F	[N]	force
F_{PP} / F_{PQ} / F_{QP}	[N]	force at: proppant-proppant / proppant-quartz / quartz-proppant contact
σ_1, σ_2, σ_3	[MPa]	principle stress
σ_{xx}, σ_{yy}, σ_{zz}	[MPa]	normal stress
σ_{rr} / $\sigma_{\varphi\varphi}$ / $\sigma_{\theta\theta}$	[MPa]	normal stress in spherical coordinates
σ_{xy}, σ_{xy}, σ_{yz} / τ_{xy}, τ_{xy}, τ_{yz}	[MPa]	shear stress
σ_V, σ_H, σ_h	[MPa]	vertical, maximum horizontal, and minimum horizontal stress
σ_{diff}	[MPa]	differential stress
σ_{eff}	[MPa]	effective stress
σ_{eff_max}	[MPa]	maximum effective stress on proppant pack
$\sigma_{c\ max}$	[MPa]	maximum compressive Hertz stress
σ_{ra}	[MPa]	maximum tensile Hertz stress
σ_{tPP} / σ_{tPQ} / σ_{tQP}	[MPa]	tensile stress due to contact of: proppant-proppant/ proppant-quartz / quartz-proppant
σ_3 / P_C	[MPa]	confining pressure
P_P / ΔP_P	[MPa]	pore pressure / pore pressure gradient
p_H	[MPa]	uniform radial stress
ΔP_d	[MPa]	pseudo steady-state drawdown pressure
ΔP_{dd}	[MPa]	differential drawdown pressure during production
$\overline{\Delta P}_P$	[MPa]	differential mean pore pressure
S_0	[MPa]	coefficient of internal friction
E / E_R	[GPa]	Young's modulus
E^*	[GPa]	contact modulus
λ / μ	[GPa]	Lamé parameter
K	[GPa]	bulk modulus
E_D	[GPa]	bulk deformation modulus
E_{D_el} / E_{D_in}	[GPa]	bulk deformation modulus: elastic component / inelastic component
ε_1 / ε_2 / ε_V	[1]	axial, lateral, volumetric strain
ν	[1]	Poisson ratio / Poisson number
u	[m]	displacement
r / R	[m]	radius / radius of a sphere
r_s	[m]	specimen radius
a	[m]	radius of Hertz contact circle
d_0	[m]	mean free path
Δl	[m]	flow length
L_{Ri}	[m]	initial length of intact rock specimen
L / L_i / L_T	[m]	specimen length / length of intact rock sample / total length of rock-proppant system
w_f / w_S	[m]	fracture width / extent of fracture face skin zone (damage penetration)
x_f	[m]	fracture half length
h	[m]	effective reservoir thickness
d_r	[m]	distance of silver rims
P_E	[m]	perimeter of an ellipse

symbol	unit	description
r_{p_opt} / r_{g_opt}	[m]	equivalent pore radius / equivalent grain radius
$r^{50}_{p\_HG}$ / $r^{50}_{p\_opt}$	[m]	mean pore radius: mercury intrusion porosimetry / 2D image analysis
$r^{50}_{g\_opt}$	[m]	mean grain radius from 2D image analysis
L_F	[m]	characteristic length scale in a pore network
A_S	[m²]	specimen cross sectional area
A_E	[m²]	area of an ellipse
A_p / A_g	[m²]	area of pore / area of grain
$\mathbf{q}$ / q	[m³/s]	flow vector / flow
$\mathbf{v}$ / v_0 / v_D	[m/s]	flow velocity vector / characteristic flow velocity / Darcy flow velocity
$\mathbf{k}$ / k / k_a	[m²]	permeability tensor / permeability / apparent permeability
k_i / k_f / k_S / k_T	[m²]	initial rock permeability / fracture permeability / permeability of fracture face skin zone / total permeability of rock-proppant system
Θ	[°]	contact angle
Θ_{PP} / Θ_{PQ} / Θ_{QP}	[°]	contact angle between: proppant-proppant/ proppant-quartz / quartz-proppant
ϕ	[°]	angle of internal friction
T	[°C]	temperature
Φ_{HG} / Φ_{opt}	[%]	porosity from: mercury intrusion porosimetry / 2D image analysis
η	[Pa s]	dynamic fluid viscosity
ρ_f	[kg/m³]	fluid density
ρ_{bulk} / ρ_g	[kg/m³]	bulk density / grain density
R_{shunt}	[Ω]	shunt resistance
U_{shunt} / U_{Ag}	[V]	voltage across the shunt / voltage between rims
κ_f / κ_R	[S/m]	fluid conductivity / rock conductivity
γ_{HG}	[mN/m]	surface tension of mercury
ϑ_{HG}	[°]	wetting angle of mercury
D_p	[pores / mm²]	pore area density
δ_{ij}	[1]	Kronecker delta
P_{2n}	[1]	Legendre polynomials
A_{2n} / B_{2n}	[1]	constants
S / $S_{t\ max}$	[1]	stress severity / maximum tensile stress severity
Re	[1]	Reynolds number
α	[1]	Biot-Willis coefficient
β	[1]	Forchheimer beta-factor
γ	[1]	friction coefficient
B	[1]	formation volume factor
ψ	[1]	influence function
C_{fD}	[1]	dimensionless fracture conductivity
PI_D	[1]	dimensionless productivity index
c_F	[1]	shape factor
C	[1]	circularity
FF	[1]	formation factor
F_E	[1]	axis ratio of ellipse
FFS	[1]	fracture face skin

A1 Pressure and Flow Calibration

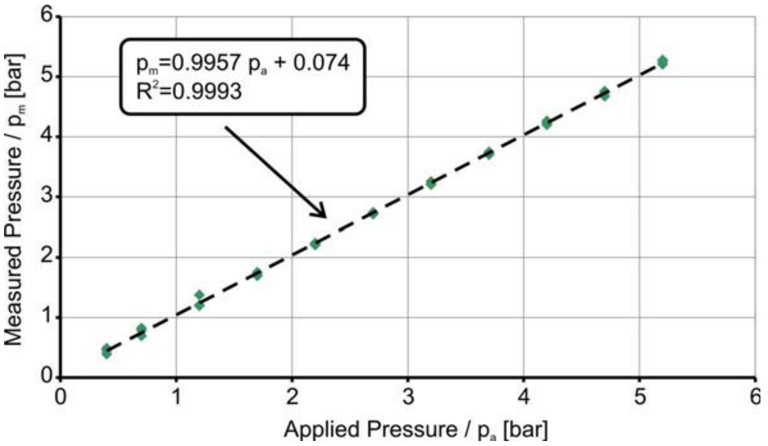

Figure A1: *Pressure calibration of AEFC sensor (Stellar Technologies GT1800-20000G-113). A pressure balance of the sensor in the range of 0-5 bar was conducted. For short-term measurements with a careful control of zero level, the measured pressure (p_m) fits the applied pressure (p_a) accurately.*

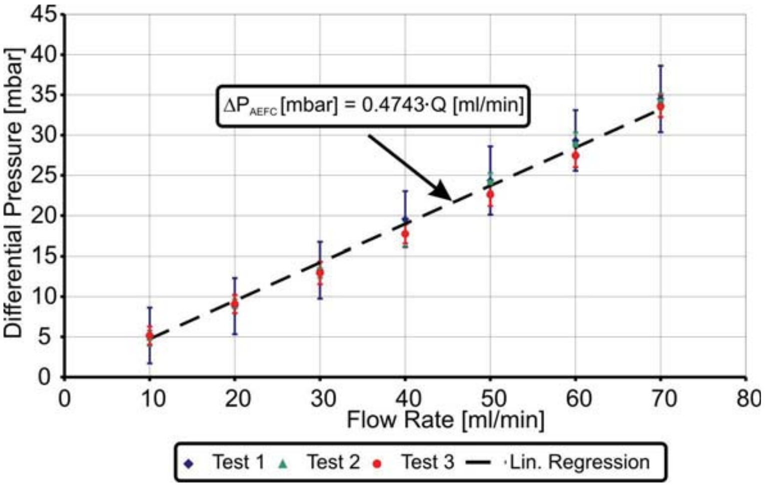

Figure A2: *Flow calibration of AEFC. The intrinsic pressure response of the AEFC as function of the applied flow rate.*

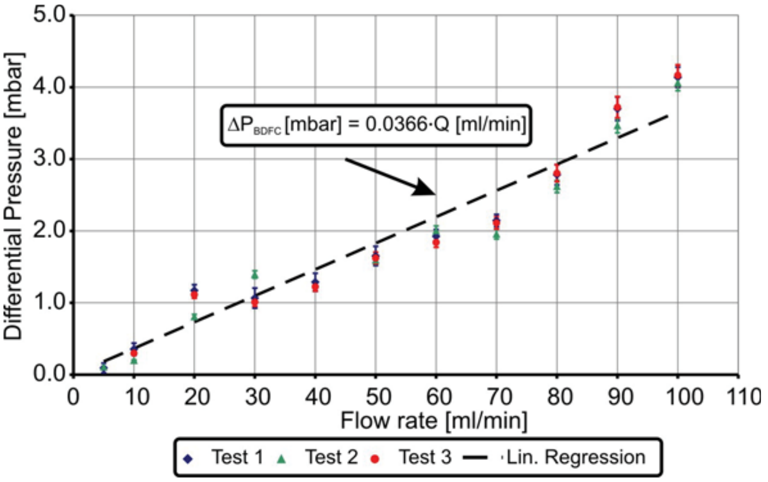

Figure A3: *Flow calibration of BDFC. The intrinsic pressure response of the BDFC as function of the applied flow rate.*

A2 Error Estimation

The accuracy of permeability determination (k_i, k_f, k_S) is affected by various potential measurement errors. Their influence on k_S is calculated using error propagation of Darcy's law (equation 2.30).

A2.1 AEFC & BDFC

The full span error of pressure transducers reflects the uncertainties of a long-term measurement, such as drift and the influence of the temperature. For short-term measurements, the accuracy of a pressure transducer is significant higher, if the zero level is carefully controlled. Thus, the effects on the accuracy in the differential pressure transducer and Quisix system pressure transducers are divided into effects on short and long-term measurements.

A2.1.1 Short Term Measurements

The influence of the mean differential pore pressure measurement ($\overline{\Delta P_P}$) on the permeability is calculated from the sum of zero level drift ($\Delta\overline{\Delta P_Z}$) and error of differential pressure measurement ($\Delta\overline{\Delta P_P}$):

$$\left(\frac{\Delta k}{k}\right)_{\Delta P} = \frac{\Delta\overline{\Delta P_P}}{\overline{\Delta P_P}} + \frac{\Delta\overline{\Delta P_Z}}{\overline{\Delta P_P}} \qquad \text{A1}$$

A2.1.2 Long Term Measurements

For permeability determination of tight Flechtingen sandstone, a long-term permeability measurement is conducted. The full span error of the differential pressure sensor $\overline{\Delta P_P}$ = 3.4 mbar is used for error estimation; the effect on permeability determination is:

$$\left(\frac{\Delta k}{k}\right)_{\Delta P} = \frac{\Delta\overline{\Delta P_P}}{\overline{\Delta P_P}} \qquad \text{A2}$$

A2.1.3 Influence of Temperature Measurement

The error of temperature measurement at ambient conditions is $\Delta T = 1$ K. The error propagation of equation 2.31 in combination with equation 3.6 with respect to ΔT results in:

$$\left(\frac{\Delta k}{k}\right)_{\Delta T} = 0.0232 \cdot \Delta T \qquad \text{A3}$$

This leads to an error of permeability measurement of 2.3 % per Kelvin.

A2.1.4 Rock Sample Length and Fracture Width Determination

The influence of the error of rock sample length determination (Δl_{Ri}) on FFS permeability (k_S) is:

$$\left(\frac{\Delta k_S}{k_S}\right)_{\Delta l_i} = \frac{k_S \Delta l_{Ri}}{k_i w_S} \qquad \text{A4}$$

This error depends on the ratio between rock and FFS permeability (k_i/k_S). For $2 < k_i/k_S < 10$; the error varies between 2.5 % and 0.5 %.

A2.2 LTFC

A2.2.1 Long Term Measurements

The differential pressure error $\Delta\overline{\Delta P_P}$ is estimated from standard deviation of upstream and downstream pressure, as it is calculated from the difference between them. The standard deviation is about 0.03 bar, which is equivalent to 1 % relative error. The effect on permeability determination is given as:

$$\left(\frac{\Delta k}{k}\right)_{\Delta P} = \frac{\Delta\overline{\Delta P_P}}{\overline{\Delta P_P}} \qquad \text{A5}$$

A2.2.1 Influence of Temperature Measurement

The accuracy of the temperature sensors ΔT is 2 °C. The error propagation for equation 3.14 results in the effect on permeability determination as:

$$\left(\frac{\Delta k}{k}\right)_{\Delta T} = \frac{35155 \cdot 1.0418}{T^{3.0418}} \cdot \Delta T \qquad \text{A6}$$

At a temperature of 150 °C, this causes a relative error for permeability measurement of 2 %.

A3 Characterisation of Bentheim and Flechtingen Rock

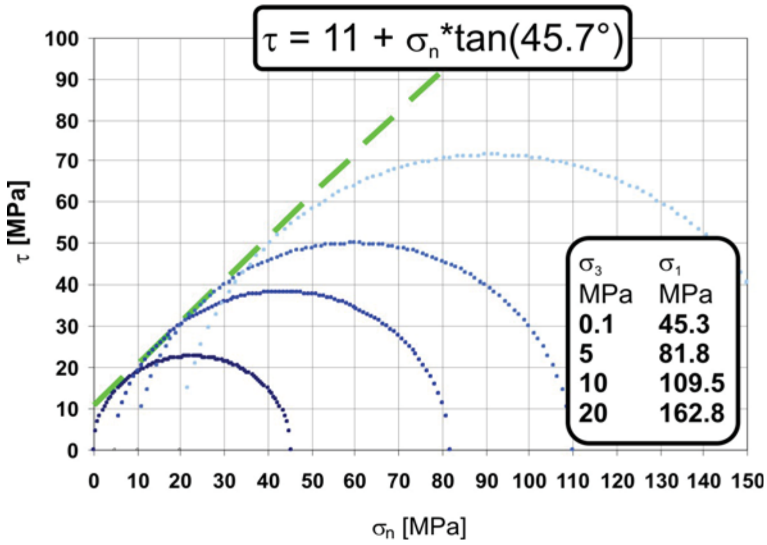

Figure A4: *Mohr-Coulomb diagram constructed from uniaxial and triaxial Bentheim sandstone experiments. Mean values of uniaxial and triaxial experiments (table 5.5) are used to determine the cohesion (S_0 = 11 MPa) and coefficient of internal friction (γ = 1.02). The coefficient of internal friction corresponds to an internal friction angle of 45.7°. / σ_n: normal stress; τ: shear stress*

specimen	Young's modulus GPa	confining pressure MPa	permeability unconsolidated mD	permeability consolidated mD
Bent 1.1	21.9 / u	10	2300 ± 230	- / -
Bent 1.2	22.8 / u	20	- / -	- / -
Bent 1.3	21.1 / u	10	1300 ± 130	- / -
Bent 1.4	20.0 / c	10	- / -	- / -
Bent 1.5	20.6 / c	10	1490 ± 90	1440 ± 70
Bent 1.6	22.0 / c	10	1330 ± 40	1260 ± 40
Bent 2.2	21.3 / c	10	2170 ± 170	2210 ± 150
Bent 2.3	20.7 / c	10	- / -	1630 ± 190
Bent 3.1	21.4 / c	10	1470 ± 70	1430 ± 90
Bent 3.3	22.1 / c	10	1220 ± 90	1170 ± 70
Bent 3.4	22.8 / c	10	- / -	2120 ± 60
Bent 3.5	21.7 / c	10	1410 ± 90	1480 ± 100
Bent 3.6	18.6 / u	10	2800 ± 200	2480 ± 70
Bent 4.14	18.8 / u	0.1	- / -	- / -
Bent 4.17	18.7 / u	0.1	- / -	- / -
specimen	**Young's modulus GPa**	**confining pressure MPa**	**permeability unconsolidated µD**	**permeability consolidated µD**
FB 1.5	20.4 / c	10	156 ± 4	86 ± 3
FB 1.6	21.3 / c	10	124 ± 3	100 ± 3
FB 2.1	13.0 / c	10	- / -	546 ± 14
FB 7.4	19.0 / c	10	262 ± 7	194 ± 5

Table A1: *Permeabilities and Young's moduli for all specimens investigated with the AEFC and BDFC. The notation "c" and "u" denotes "consolidated" and "unconsolidated". Consolidation means that the sample is triaxally loaded three times up to σ_{diff} = 65 MPa.*

A4 Stress-Strain Curves of RPI experiments

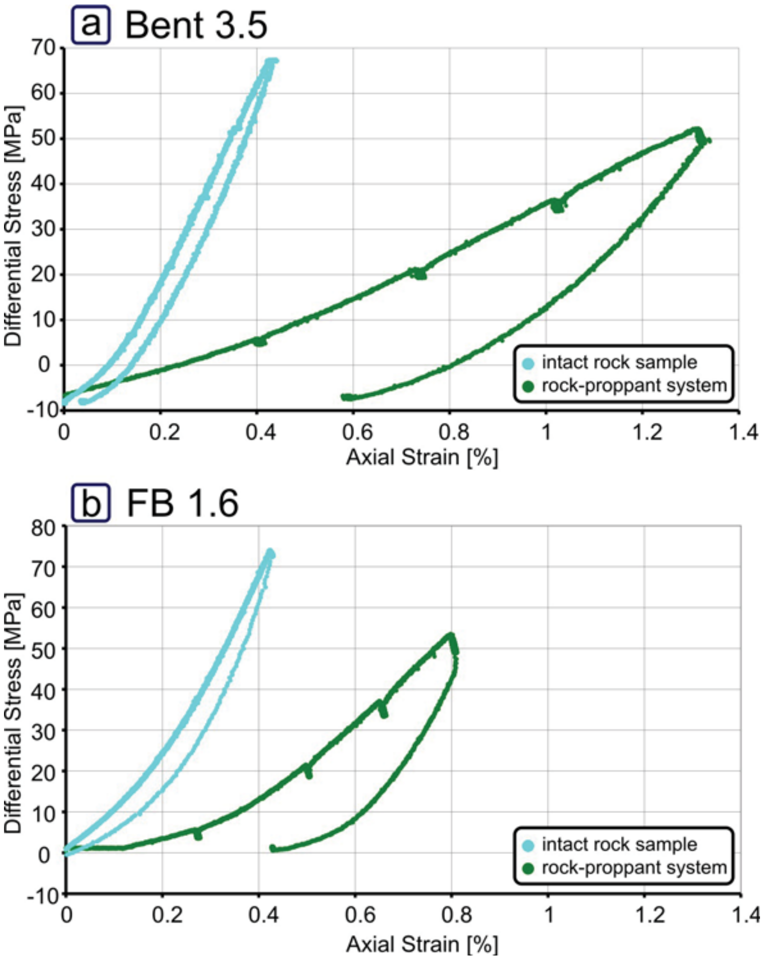

Figure A5: *Comparison of stress-strain behaviour of intact specimen and rock-proppant system. The stiffness of a rock-proppant system (green graph) is significantly reduced compared to the intact rock (blue graph). A Flechtingen rock-proppant system with high strength proppants (figure b) reacts stiffer than a Bentheim system with intermediate strength proppants (figure a).*

A5 Pore Pressure Curves

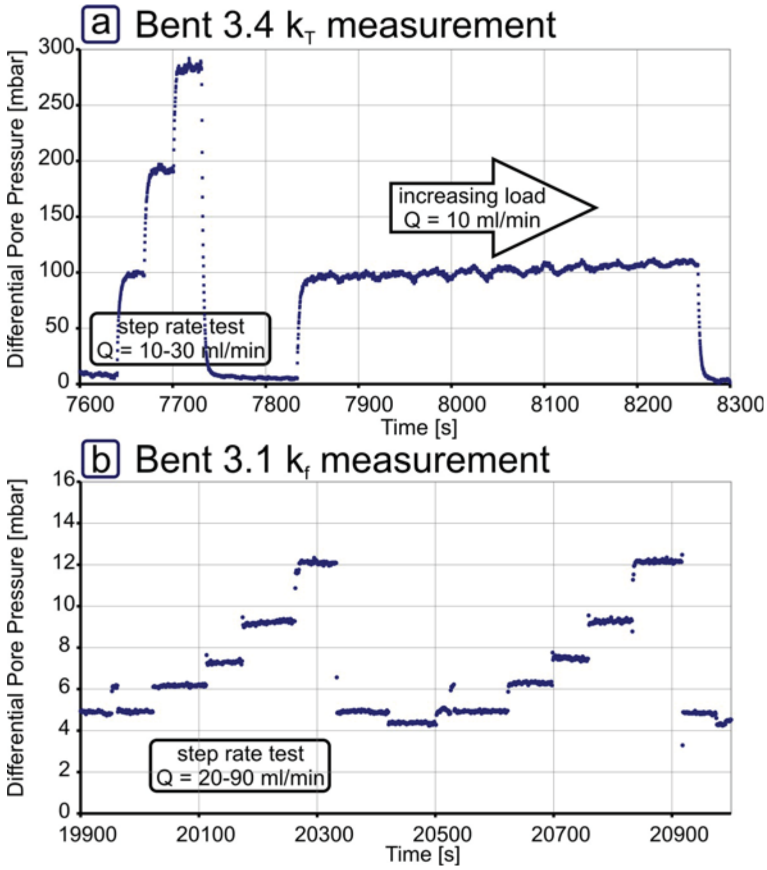

Figure A7: *Differential pressure measurements of a Bentheim rock-proppant system and a proppant pack.*

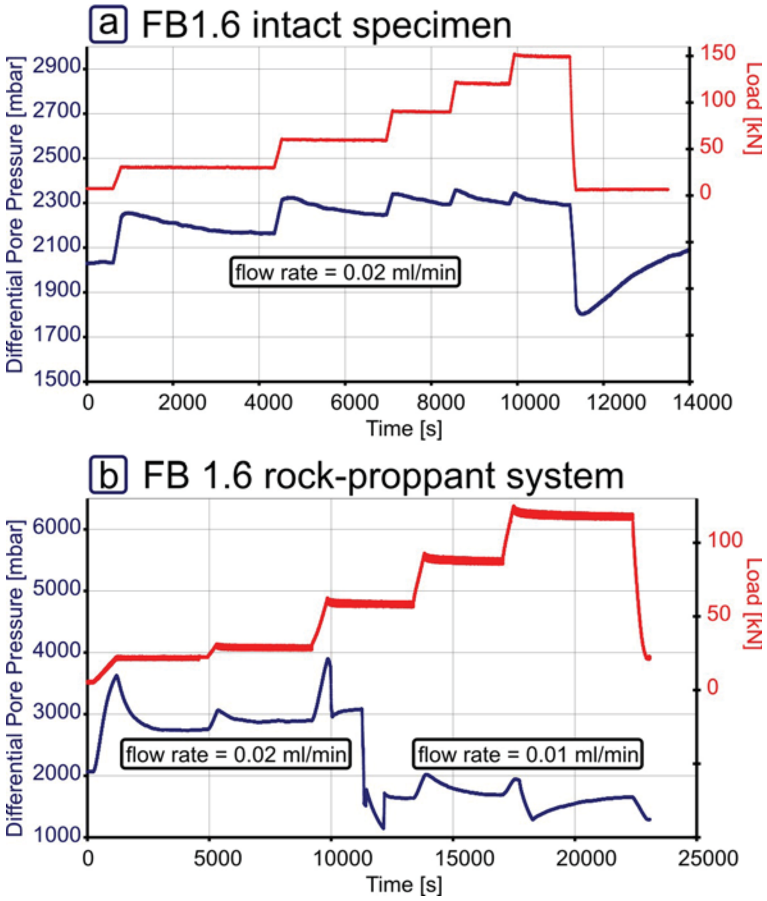

Figure A8: *Differential pressure measurements of an intact Flechtingen rock and a Flechtingen rock-proppant system. With increasing load, a significant increase in differential pore pressure is observed (figure a). The reduction of pore space during compaction results in a steep increase of pore pressure in the loading stage followed by a slow decrease. In the rock-proppant system experiment, the flow rate was reduced since the upper limit of the differential pressure transducers was exceeded (figure b).*

A6 From an Artificial Micrograph to a 2D-Mesh

The 2D-model is designed to simulate the experimental conditions and the mechanical behaviour of the rock-proppant interface and the proppant pack. A finite-element (FE) code is used that defines each proppant, grain, and pore including their mechanical properties in a discrete way. A six-step procedure is conducted in order to generate an FE-mesh from a micrograph.

1. The artificial micrograph is assembled from a micrograph of a tensile fracture and micrographs of single ISP. The contact radii are predefined (figure A9a).
2. The resulting picture is split into its three rgb (red green blue) channels. The red channel is divided by the green one and the blue channel, which mainly characterises the pore space, is subtracted. This procedure results in a grey scale picture; the pore space is light and the proppants and the grains are visible in dark grey levels (figure A9b).
3. The colour depth is reduced from 256 to 2 using a reasonable threshold, and a black and white picture is created (figure A9c). The definition of a reasonable threshold is somewhat arbitrary. A comparison of different thresholds demonstrates if the threshold level is set erroneously. A too high threshold results in black dots within the pore space; a too low threshold reduces the contact zones. The boarders of grains and proppants in the black-and-white picture are smoothed with graphic processing software.
4. This conversion into a black-and-white picture leads to misclassifications like isolated grains in the pore space. They are removed by a software tool, written by G. Blöcher [Blöcher 2008], which counts the number of black or white pixel clusters and removes them if they are below a defined threshold. In addition, this tool fills the outer boundary of the area of interest to enable the application of uniform load from all four outer boundaries (figure A9d). Large isolated grains (pixel clusters) are removed by hand.
5. A second algorithm of G. Blöcher [Blöcher 2008] is applied to vectorise the geometry and reference the picture to its original size. For that purpose, the coordinates of each black-white contact are saved in a geometric input file for the meshing tool Gmsh [Geuzaine & Remacle 2006]. Inside the Gmsh environment, the surface of the two materials – quartz grains and proppants – are defined (figure A9e). In addition, lines for mesh refinement (blue) are set in the direction of the material contacts (approximately normal to the contact radii). Without these lines, Gmsh increases the mesh size at some distance from the contact area. If the mesh is too coarse, localised tensile stress concentration near the contact region would be ignored in the calculation. Pores are not vectorised in the model because no pore pressure is applied – the pore space is empty in the simulation and is not included in the mesh. Within the Gmsh environment, the contact lengths are redefined. This step is necessary since the smoothing procedure in step 4 alters the predefined contact diameter.
6. Gmsh generates a triangle mesh based on the two defined material groups (light blue and pink meshes in figure A9f). The characteristic length along the material boundaries and blue lines are set to one pixel, resulting in a fine mesh along the boundaries and contacts. With increasing distance, the characteristic length decreases and the mesh becomes coarser. The grid has about 140,000 tetrahedrons.

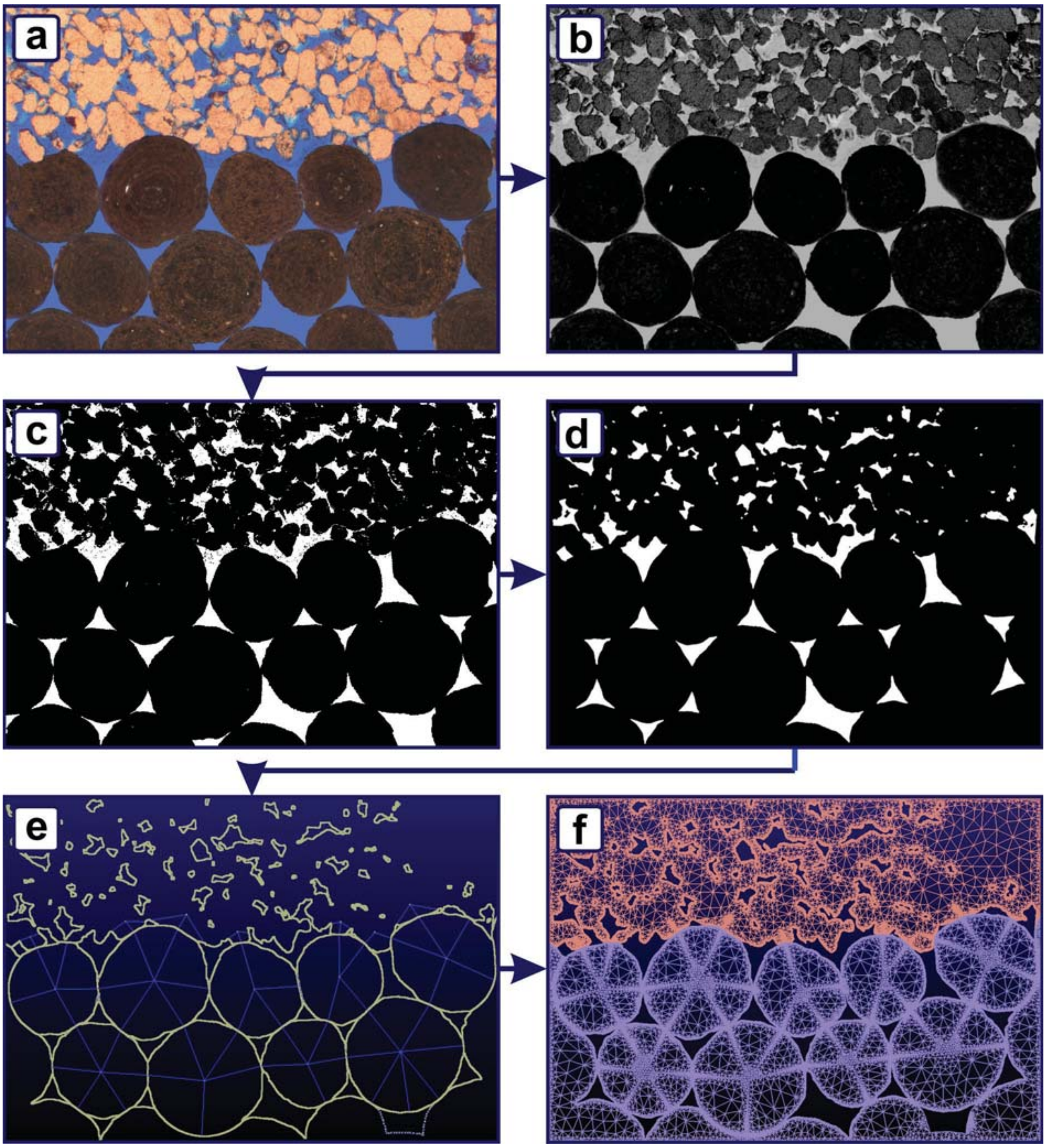

Figure A9: *From an artificial 2D-contact model of a rock-proppant system to a 2D-mesh. A six-step procedure is conducted in order to generate a finite element (FE) mesh (figure f) from the artificial micrograph a rock-proppant system (figure a). For that purpose a black-and-white picture is created (figure d) and imported in the meshing tool Gmsh [Geuzaine & Remacle 2006] (figure e). Inside the Gmsh environment, lines of refinement (blue) between contact points are set. The 2D-mesh is exported to the FE modelling software Rockflow/Geosys [Wang & Kolditz 2005].*

Relève-toi donc et reprend ta route.

Mach dich auf und setz deinen Weg fort!

Jules Verne, *Voyage au centre de la terre* (1864)

DOI: 10.2312/GFZ.b103-11098

ISSN 1610-0956